Imperial College London

Characterisation of Fibre Hybrid Thermosetting Composites for Automotive Applications

by

Tomas J. Katafiasz

Department of Aeronautics

Imperial College London

South Kensington Campus

London SW7 2AZ

United Kingdom

This thesis is submitted for the degree of Doctor of Philosophy

August 2018

"Experience without theory is blind, but theory without experience is mere intellectual play"

- Immanuel Kant

Abstract

The objective of the research presented in this PhD thesis is to improve the understanding of the failure modes and numerical modelling techniques associated with both interlayer and intralayer fibre hybrid composites and their monolithic constituent composite counterparts, with the overall objective of using the fibre hybrid composites for automotive components. The materials tested, as specified by the funding body Composites Innovation Cluster (Datacomp), were: a plain weave spread tow T700 carbon composite, a non-crimp 0°/90° S2-glass composite, an interlayer fibre hybrid of the two aforementioned monolithic composites, and an intralayer fibre hybrid 2x2 twill weave T700 carbon/Vectran composite, all within an MTM57 epoxy matrix and manufactured by Resin Film Infusion (RFI). Standardised and non-standardised testing was employed to determine the in-plane material properties of each material in tension, compression, and shear, as well as interlaminar fracture toughness in Mode I and Mode II. Subsequently, a novel Compact Tension (CT) specimen geometry was developed to alleviate premature out-of-plane buckling and premature compressive failure. This was imperative in capturing the materials translaminar fracture toughnesses since the monolithic S2-glass composite and the intralayer fibre hybrid T700 carbon/Vectran failed prematurely when utilising typical standard CT test geometries.

Once the in-plane material properties, and interlaminar and translaminar fracture toughnesses were measured, an existing energy-based bilinear plane stress traction-separation numerical modelling approach was used to provide insight into the complex failure processes associated with low velocity impacts. The fibre hybrid composites as well as their monolithic glass and carbon fibre composite counterparts were subjected to two discrete impact energy levels and their experimental load response curves and failure modes showed good agreement with the numerical modelling.

Finally, a 1:5 reduced scale car bonnet made from the interlayer and intralayer fibre hybrid composites was subjected to low velocity impacts at two discrete energy levels and compared to the same numerical modelling strategy as used with the plate impact study. A novel experimental test rig was developed which allowed for quantifiable boundary conditions to be numerically modelled, presenting good comparison to the impactor tup experimental load response curves as well as two experimental independent strain gauge readings.

Declaration of originality

The work presented hereafter is based on research carried out by the author at the Department of Aeronautics of Imperial College London and it is all the author's own work except where otherwise acknowledged. No part of the present work has been submitted elsewhere for another degree or qualification.

Tomas J. Katafiasz

The copyright of this thesis rests with the author and is made available under a Creative Commons Attribution Non-Commercial No Derivatives licence. Researchers are free to copy, distribute or transmit the thesis on the condition that they attribute it, that they do not use it for commercial purposes and that they do not alter, transform or build upon it. For any reuse or redistribution, researchers must make clear to others the licence terms of this work.

Acknowledgements

The author would like to thank the following individuals and organisations, for their help (both technically and supportively) throughout the course of this research:

- Supervisors: Professor Lorenzo Iannucci and Professor Emile Greenhalgh
    - For their tireless support, patience, and invaluable advice throughout the entire course of this research
- Colleagues: Dr Sang Nguyen, Mr Syed Abdullah, and Mr Atrash Mohsin (and many others throughout the years)
    - For their guidance and friendship
- Aeronautics departmental staff: Professor Paul Robinson, Professor Silvestre Pinho, Dr Koon-Yang Lee, Dr Dave Anthony, Dr Omar Bacarreza Nogales, Dr Frank Gommer, Mr Gary Senior, Mr Jon Cole, Mr Joseph Megyessi, Mr Keith Wolstenholme, Mr Roland Hutchins, and Dr Alexis Arnaudon (Centre for Mathematics of Precision Healthcare)
    - For their advice, as well as their jovial manner
- Organisations and associated parties: Composites Innovation Cluster (Datacomp project partners), University of Manchester (Dr Mohamed Saleh and Dr Adam Joesbury), Solvay (Mr Dan Thompson), Altair Engineering (Mr Peter Snape), Sigmatex (Mr Peter Sestic), Granta (Dr Donna Dykeman), Axon Automotive, Bentley Motors, Jaguar Land Rover, and DSTL
    - For their support (both technically and financially) and generosity
- Friends and family: My parents and grandparents, aunts and uncles, Lucie, Anil, Gareth, Jack, Jeff, Chloe, Chris, Alex, Sam, Leo, and Tamzin
- And a special acknowledgement to Professor Wesley Cantwell
    - Whose undergraduate final year project supervision and lectures at the University of Liverpool inspired my interest in composite materials

Table of contents

Abstract 5

Declaration of originality 7

Acknowledgements 9

1. Introduction 29

1.1. Background 29

1.2. Motivation and objectives 29

1.3. Outline of thesis 32

2. Literature survey and research plan 36

2.1. Literature survey 37

2.1.1. Spread tow composites 37

2.1.2. Characterising fibre hybrid composite material properties 39

2.1.3. Translaminar fracture toughness of fibre hybrid composites 46

2.1.4. Low velocity impact of fibre hybrid composites 49

2.1.5. Component scale impact modelling of fibre hybrid composite structures 53

2.2. Gaps in the literature and research plan 57

2.2.1. Characterising fibre hybrid composite material properties 57

2.2.2. Translaminar fracture toughness of fibre hybrid composites 57

2.2.3. Low velocity impact of fibre hybrid composites 58

2.2.4. Component reduced scale impact modelling of fibre hybrid composite structures 59

3. Characterisation of fibre hybrid composites and their monolithic composite counterparts 60

3.1. Introduction 60

3.1.1. Tension testing 62

3.1.2. Compression testing 64

3.1.3. In-plane shear testing 66
3.1.4. Volume fraction measurement 70
3.2. Using the rule of mixtures to estimate the tensile material properties of fibre hybrid composites 75
3.3. Interlaminar fracture toughness of fibre hybrid composites 76
3.3.1. Mode I: DCB testing 78
3.3.1.1. Test set-up 78
3.3.1.2. Data reduction 79
3.3.1.3. Results 80
3.3.1.4. Post-test analysis 82
3.3.2. Mode II: 4-ENF testing 87
3.3.2.1. Test set-up 87
3.3.2.2. Data reduction 87
3.3.2.3. Results 88
3.3.2.4. Post-test analysis 90
3.4. Summary 92
4. Translaminar fracture toughness of fibre hybrid composites and their monolithic composite counterparts 93
4.1. Introduction 93
4.2. Preliminary standard CT geometry tests 94
4.3. Development of a novel compact tension specimen 100
4.3.1. Model development 100
4.3.2. Specimen manufacture 105
4.4. Test set-up 108
4.5. Data reduction 109
4.6. Results 112

4.6.1. Compliance curves 112
4.6.2. Critical strain energy release rates 114
4.7. Post-test analysis 117
4.8. Summary 121
5. Low velocity impact response characterisation of fibre hybrid composites 123
5.1. Introduction 123
5.2. Mechanical testing 123
5.2.1. Manufacture 123
5.2.2. Test set-up 124
5.2.3. Data reduction 125
5.3. Finite element numerical modelling 125
5.3.1. Numerical model theory 125
5.3.2. Numerical model set-up 131
5.4. Non-destructive testing 143
5.5. Experimental testing and numerical modelling of flat plate impacts 144
5.5.1. Monolithic S2-glass composite 149
5.5.2. Monolithic T700 carbon composite 152
5.5.3. Interlayer fibre hybrid T700 carbon/S2-glass 155
5.5.4. Intralayer fibre hybrid T700 carbon/Vectran 158
5.6. Quantifying the numerical model's accuracy 161
5.7. Summary 165
6. Low velocity structural impact response of fibre hybrid composites on a reduced scale car bonnet 167
6.1. Introduction 167
6.2. Mechanical testing 167
6.2.1. Manufacture using a Bentley bonnet mould 167

6.2.2. C-scanning of cured bonnets 170
6.2.3. Test rig development and set-up 172
6.3. Numerical model set-up 177
6.4. Experimental testing and numerical modelling of structural bonnet impacts 183
6.4.1. Interlayer fibre hybrid T700 carbon/S2-glass 183
6.4.2. Intralayer fibre hybrid T700 carbon/Vectran 190
6.5. Quantifying the numerical model's accuracy 193
6.6. Summary 196
7. Discussion 198
7.1. Introduction 198
7.2. Key findings 198
8. Conclusions and future work 204
8.1. Introduction 204
8.2. Conclusions 204
8.3. Future work 206
9. Bibliography 209
10. Appendices 230
10.1. Numerical model monolithic S2-glass composite impact plate fracture toughness sensitivity, 140J 230
10.2. Numerical model monolithic S2-glass composite impact plate strain rate 'kappa' sensitivity, 140J 231
10.3. Numerical model intralayer fibre hybrid T700 carbon/Vectran impact plate fracture toughness sensitivity, 70J 232
10.4. Numerical model interlayer fibre hybrid T700 carbon/S2-glass structural bonnet impact damping factor sensitivity, 20J 233
10.5. VUMAT material cards 234

10.6. Numerical cohesive interaction cards 238

10.7. Bonnet rig test fixture drawings 240

List of figures

Figure 1.1: The pyramid of tests [9] 30

Figure 2.1: Fibre arrangement in spread tow compared to typical tow [30] 37

Figure 2.2: Tow spreading due to air passing through individual fibres during pneumatic method [31] 37

Figure 2.3: Continuous spread tow tape placement incorporating unequal angles [36] 38

Figure 2.4: Common fibre hybrid configurations (interlayer, intralayer, and intrayarn) [5] .. 40

Figure 2.5: Definitions of the hybrid effect: (a) Typical load displacement curve of a 50/50 fibre hybrid composite, (b) hybrid deviation from the rule of mixtures [5] 40

Figure 2.6: Pseudo-ductility during fibre hybrid tensile loading leading to irreversible damage [52] 41

Figure 2.7: The tensile hybrid effect as a function of fibre plies within a unidirectional interlayer fibre hybrid [55] 42

Figure 2.8: UD high modulus carbon/E-glass fibre hybrid composite: (a) linear rule of mixtures for elastic modulus, (b) bilinear rule of mixtures for tensile strength [64] 44

Figure 2.9: Diagram showing effect of doubler plates [78] 45

Figure 2.10: Diagram of a conventional CT specimen with the locations of possible failure mechanisms [93] 47

Figure 2.11: Anti-buckling guide for a standard Compact Tension specimen [103] 48

Figure 2.12: Modified OCT specimen (dimensions in mm) [105] 49

Figure 2.13: Overview of low velocity impact modelling approaches [109] 50

Figure 2.14: Post-test C-scans for plate impact of fibre hybrid with various interlayer carbon/glass configurations L6-L9 (see [115] for more information) 51

Figure 2.15: Global automotive CO_2 regulations, critical emission or gas mileage [131] 54

Figure 2.16: BMW 7-series chassis consisting of both metallic and fibre reinforced polymer composite structures [134] 54

Figure 2.17: Comparison of dynamic strain for experiment and numerical model for fibre hybrid plate impact: (a) glass-carbon-glass layup, (b) carbon-glass-carbon layup [6] 56

Figure 2.18: Strain comparison for hood slam test [141] 56

Figure 3.1: Representative composite tension test results, stress versus strain results 63

Figure 3.2: Representative failure modes for tension tests 64

Figure 3.3: Representative composite compression, stress versus strain results 65

Figure 3.4: Representative failure modes for compression tests 66

Figure 3.5: In-plane shear response of monolithic S2-glass composite 68

Figure 3.6: In-plane shear response of monolithic T700 carbon composite 68

Figure 3.7: In-plane shear response of intralayer fibre hybrid T700 carbon/Vectran 68

Figure 3.8: In-plane shear response of interlayer fibre hybrid T700 carbon/S2-glass 69

Figure 3.9: Representative failure modes for in-plane shear tests 69

Figure 3.10: Monolithic S2-glass composite thermogravimetric burn-off, weight % 71

Figure 3.11: Monolithic T700 carbon composite thermogravimetric burn-off, weight % 71

Figure 3.12: Interlayer fibre hybrid T700 carbon/S2-glass burn-off, weight % 72

Figure 3.13: Intralayer fibre hybrid T700 carbon/Vectran burn-off, weight % 72

Figure 3.14: Microscopic through-thickness unit cell of interlayer fibre hybrid T700 carbon/S2-glass, Fiji/ImageJ binary threshold processing carbon fibres 74

Figure 3.15: Microscopic through-thickness unit cell of intralayer fibre hybrid T700 carbon/Vectran, Fiji/ImageJ binary threshold processing carbon fibres 75

Figure 3.16: T700 carbon spread tow doublers on a portion of an intralayer fibre hybrid T700 carbon/Vectran DCB specimen 78

Figure 3.17: Test set-up for the double cantilever beam of interlaminar fibre hybrid T700 carbon/S2-glass 79

Figure 3.18: Typical load versus displacement plot for the interlayer fibre hybrid T700 carbon/S2-glass DCB tests 80

Figure 3.19: Typical compliance$^{1/3}$ versus crack length plot for the interlayer fibre hybrid T700 carbon/S2-glass DCB tests 80

Figure 3.20: Interlayer fibre hybrid T700 carbon/S2-glass double cantilever beam results, critical strain energy release rate versus crack length (red ellipse indicates invalid failure) .. 81

Figure 3.21: Typical load versus displacement plot for the intralayer fibre hybrid T700 carbon/Vectran DCB tests 81

Figure 3.22: Typical compliance$^{1/3}$ versus crack length plot for the intralayer fibre hybrid T700 carbon/Vectran DCB tests 81

Figure 3.23: Intralayer fibre hybrid T700 carbon/Vectran double cantilever beam results, critical strain energy release rate versus crack length 82

Figure 3.24: Electron micrograph of T700 carbon fibre bond at Mode I fracture surface (x650) 83

Figure 3.25: Interlayer fibre hybrid T700 carbon/S2-glass DCB specimen #2, *R*-curve..... 83

Figure 3.26: Interlayer fibre hybrid T700 carbon/S2-glass DCB specimen #3, *R*-curve..... 84

Figure 3.27: Electron micrograph of interlayer fibre hybrid T700 carbon/S2-glass out-of-plane crack relocation across carbon weave within a DCB specimen (x32) 84

Figure 3.28: T700 carbon spread tow doubler buckling failure due to bending on an intralayer fibre hybrid T700 carbon/Vectran DCB specimen..... 85

Figure 3.29: Electron micrograph of intralayer fibre hybrid T700 carbon/Vectran, Mode I fracture surface (x7)..... 86

Figure 3.30: Electron micrograph of intralayer fibre hybrid T700 carbon/Vectran, shows Mode I riverlines at the resin rich regions (x17) 86

Figure 3.31: Test set-up for the 4-end notched flexure 87

Figure 3.32: Typical compliance versus crack length plot for the interlayer fibre hybrid T700 carbon/S2-glass 4-ENF tests..... 88

Figure 3.33: Interlayer fibre hybrid T700 carbon/S2-glass 4-end notched flexure results, critical strain energy release rate versus crack length 88

Figure 3.34: Typical compliance versus crack length plot for the intralayer fibre hybrid T700 carbon/Vectran 4-ENF tests 89

Figure 3.35: Intralayer fibre hybrid T700 carbon/Vectran 4-end notched flexure results, critical strain energy release rate versus crack length 89

Figure 3.36: Electron micrograph of intralayer fibre hybrid T700 carbon/Vectran, Mode II fracture surface (x270) 90

Figure 3.37: Interlayer fibre hybrid T700 carbon/S2-glass 4-ENF specimen #5, R-curve 91

Figure 3.38: Interlayer fibre hybrid T700 carbon/S2-glass 4-ENF specimen #8, R-curve 91

Figure 4.1: Diagram of a conventional CT specimen with the locations of possible failure mechanisms [93] 93

Figure 4.2: Typical compact tension specimen design with 0.5mm mesh around the notch tip and 1mm at the rear (4mm thick) 95

Figure 4.3: Mesh sensitivity study: mesh size versus internal energy 96

Figure 4.4: Compact tension specimen type for monolithic S2-glass composite and intralayer fibre hybrid T700 carbon/Vectran, load versus displacement 98

Figure 4.5: Two-tapered compact tension specimen type for monolithic S2-glass composite and intralayer fibre hybrid T700 carbon/Vectran, load versus displacement 99

Figure 4.6: Extended compact tension specimen type for monolithic S2-glass composite and intralayer fibre hybrid T700 carbon/Vectran, load versus displacement 99

Figure 4.7. Nominal CCT specimen geometry profile dimensions (all dimensions in mm) .. 100

Figure 4.8: Buckled CCT geometry without through-thickness groove: a) profile view b) front view c) back view 101

Figure 4.9: NCCT specimen type 102

Figure 4.10: NCCT specimen geometry: (a) Specimen FE model (b) Eigenvalue first buckling mode (the contour shows the absolute out-of-plane displacement and is unitless, red represents the maximum and blue represents the minimum) (c) Maximum strain criterion at 50% of buckling load (contour other than blue indicates values greater than unity, where red represented the criterion's maxima) 102

Figure 4.11: NCCT specimen FE optimisation methodology 103

Figure 4.12: ENCCT thick-side specimen dimensions (all dimensions in mm) 104

Figure 4.13: ENCCT specimen type 105

Figure 4.14: Monolithic S2-glass composite NCCT material layup, post-cure, prior to waterjet cutting: (a) with PTFE inserts, (b) with PTFE inserts removed 105

Figure 4.15: Monolithic S2-glass composite NCCT specimens, post waterjet cutting and notching 106

Figure 4.16: Monolithic S2-glass composite NCCT specimen prior to testing 107

Figure 4.17: Intralayer fibre hybrid Vectran/T700 carbon ENCCT specimen with PTFE inserts still intact 107

Figure 4.18: Intralayer fibre hybrid Vectran/T700 carbon ENCCT specimen with PTFE inserts removed and scale bar labelled for optical crack measurement 108

Figure 4.19: C-scan and X-ray of ENCCT intralayer fibre hybrid T700 carbon/Vectran specimen prior to testing (colour scale in dB) 108

Figure 4.20: NCCT and ENCCT test set-up 109

Figure 4.21: Illustration of the data reduction methodology using the area method 110

Figure 4.22: Optical crack growth through a representative monolithic S2-glass composite NCCT specimen (red indicates crack propagation) 111

Figure 4.23: Monolithic S2-glass composite MCC method compliance calibration curve (FE derived) for the NCCT specimen type 113

Figure 4.24: Intralayer fibre hybrid T700 carbon/Vectran CC method compliance calibration curve (experimentally derived) for the ENCCT specimen type 113

Figure 4.25: Representative critical strain energy release rate (G_{IC}) versus crack length (a) for the monolithic S2-glass composite NCCT specimens 114

Figure 4.26: Representative critical strain energy release rate (G_{IC}) versus crack length (a) for the intralayer fibre hybrid T700 carbon/Vectran ENCCT specimens 115

Figure 4.27: Representative composite *R*-curves using the area method for critical strain energy release rate versus crack length 116

Figure 4.28: Post-test radiograph of NCCT specimens: (a) Monolithic T700 carbon composite, (b) Monolithic S2-glass composite, (c) Interlayer fibre hybrid T700 carbon/S2-glass..... 118

Figure 4.29: Post-test radiograph of ENCCT intralayer fibre hybrid T700 carbon/Vectran118

Figure 4.30: Electron micrograph of NCCT specimen, monolithic S2-glass composite 119

Figure 4.31: Electron micrograph of NCCT specimen, monolithic T700 carbon composite . 119

Figure 4.32: Electron micrograph of NCCT specimen, interlayer fibre hybrid T700 carbon/S2-glass composite (S2-glass fibres highlighted in green) 120

Figure 4.33: Electron micrograph of ENCCT specimen, intralayer fibre hybrid T700 carbon/Vectran composite (Vectran fibres highlighted in green) 120

Figure 5.1: Impact panel representative pre-test C-scans plots, monolithic S2-glass composite, monolithic T700 carbon composite, interlayer fibre hybrid T700 carbon/S2-glass, intralayer fibre hybrid T700 carbon/Vectran (colour scale in dB) 124

Figure 5.2: ASTM D7136 test fixture [25] 124

Figure 5.3: Low velocity impact plate test set-up: (a) photograph, (b) diagram 125

Figure 5.4: Bilinear energy-based stress-strain law with damage..... 127

Figure 5.5: Non-linear in-plane shear curve fitting parameters [163] 128

Figure 5.6: Impact plate FE quarter model set-up..... 131

Figure 5.7: Mesh refinement and location in plate impact models (one quarter of the experimental test) 134

Figure 5.8: Mesh sensitivity study, 70J impact on monolithic S2-glass composite, load versus deflection 135

Figure 5.9: Mesh sensitivity study, 70J impact on monolithic S2-glass composite, velocity versus time 135

Figure 5.10: Mesh sensitivity study on cohesive thickness, 70J impact on monolithic S2-glass composite, load versus deflection 136

Figure 5.11: Mesh sensitivity study on cohesive thickness, 70J impact on monolithic S2-glass composite, velocity versus time 136

Figure 5.12: Strain rate enhancement, rate enhancement factor versus strain rate [148]..... 138

Figure 5.13: Single element boundary conditions 139

Figure 5.14: Loading and unloading of a single continuum shell element with permanent strain constants β=1 and β=18, in-plane stress versus strain 140

Figure 5.15: Ultrasonic C-scan of failed experimental specimens, back face delamination analysis 143

Figure 5.16: Monolithic S2-glass composite load response at 70J impact: (a) load versus deflection, (b) load versus time..... 149

Figure 5.17: Monolithic S2-glass composite at 70J impact, through-thickness microscopic image of failed experimental specimen 150

Figure 5.18: Monolithic S2-glass composite load response at 140J impact: (a) load versus deflection, (b) load versus time..... 151

Figure 5.19: Damage progression on the back face of a monolithic S2-glass composite plate at 140J impact 151

Figure 5.20: Monolithic S2-glass composite at 140J impact, through-thickness microscopic image of failed experimental specimen..... 152

Figure 5.21: Monolithic T700 carbon composite load response at 70J impact: (a) load versus deflection, (b) load versus time..... 153

Figure 5.22: Damage progression on the back face of a monolithic T700 carbon composite plate at 70J impact 153

Figure 5.23: Monolithic T700 carbon composite at 70J impact, through-thickness microscopic image of failed experimental specimen..... 154

Figure 5.24: Monolithic T700 carbon composite load response at 140J impact: (a) load versus deflection, (b) load versus time..... 154

Figure 5.25: Monolithic T700 carbon composite at 140J impact, through-thickness microscopic image of failed experimental specimen..... 155

Figure 5.26: Interlayer fibre hybrid T700 carbon/S2-glass load response at 70J impact: (a) load versus deflection, (b) load versus time 155

Figure 5.27: Interlayer fibre hybrid T700 carbon/S2-glass at 70J impact, through-thickness microscopic image of failed experimental specimen 156

Figure 5.28: Interlayer fibre hybrid T700 carbon/S2-glass load response at 140J impact: (a) load versus deflection, (b) load versus time 157

Figure 5.29: Damage progression on the back face of a interlayer fibre hybrid T700 carbon/S2-glass plate at 140J impact 157

Figure 5.30: Interlayer fibre hybrid T700 carbon/S2-glass at 140J impact, through-thickness microscopic image of failed experimental specimen 158

Figure 5.31: Intralayer fibre hybrid T700 carbon/Vectran load response at 70J impact: (a) load versus deflection, (b) load versus time 158

Figure 5.32: Intralayer fibre hybrid T700 carbon/Vectran at 70J impact, through-thickness microscopic image of failed experimental specimen 159

Figure 5.33: Intralayer fibre hybrid T700 carbon/Vectran load response at 140J impact: (a) load versus deflection, (b) load versus time 159

Figure 5.34: Intralayer fibre hybrid T700 carbon/Vectran at 140J impact, through-thickness microscopic image of failed experimental specimen 160

Figure 5.35: 70J composite plate impact, peak loads per unit mass 162

Figure 5.36: 70J composite plate impact, peak loads per through-thickness 162

Figure 5.37: 140J composite plate impact, peak loads per unit mass 162

Figure 5.38: 140J composite plate impact, peak loads per through-thickness 163

Figure 5.39: 70J composite plate impact, absorbed energies per unit mass 164

Figure 5.40: 70J composite plate impact, absorbed energies per through-thickness 164

Figure 5.41: 140J composite plate impact, absorbed energies per unit mass 165

Figure 5.42: 140J composite plate impact, absorbed energies per through-thickness 165

Figure 6.1: Bentley Continental Supersports Convertible [181] 167

Figure 6.2: Bentley Continental car bonnet mould: (a) female side, (b) male side 168

Figure 6.3: Dry fibre plies cut to bonnet shape, T700 carbon and S2-glass 169

Figure 6.4: C-scanning gimble: (a) Isometric view, (b) bottom view with 3 PTFE contact points 170

Figure 6.5: Bonnet C-scan configurations and approximate scanning locations: (a) Intralayer fibre hybrid T700 carbon/Vectran, (b) Interlayer fibre hybrid T700 carbon/S2-glass..... 171

Figure 6.6: Representative C-scan plots pre-test (colour scale in dB): (a) Intralayer fibre hybrid T700 carbon/Vectran, (b) Interlayer fibre hybrid T700 carbon/S2-glass..... 171

Figure 6.7: Preliminary bonnet impact testing exhibiting uncontrolled boundary conditions [160] 172

Figure 6.8: Base rig boundary conditions 173

Figure 6.9: End block locale..... 174

Figure 6.10: End block bonding set-up 174

Figure 6.11: Natural adhesive chamfer between end block and bonnet surface (rear of bonnet) 175

Figure 6.12: FLA-3-11-1LJC strain gauge dimensions [184]..... 176

Figure 6.13: Bonnet impact test set-up 176

Figure 6.14: Part sectioning and mesh refinement zones, coloured red 177

Figure 6.15: Bonnet mesh sizing 178

Figure 6.16: Bonnet impact model, MPC control points with boundary conditions 179

Figure 6.17: Structural bonnet model (exploded into two halves), cohesive surface locations 180

Figure 6.18: Interlayer fibre hybrid T700 carbon/S2-glass numerical FE (undamped) load response at 15J structural bonnet impact, load versus time 184

Figure 6.19: Discrete Fourier transform of the load versus time response curve (Figure 6.18), red dashed line encapsulates the frequency of interest = 329Hz, amplitude versus frequency 184

Figure 6.20: Interlayer fibre hybrid T700 carbon/S2-glass 20J structural bonnet impact deflection magnitude (m) at: (a) 5.0ms, (b) 7.4ms 185

Figure 6.21: Interlayer fibre hybrid T700 carbon/S2-glass load response at 15J structural bonnet impact: (a) load versus deflection, (b) load versus time 187

Figure 6.22: Interlayer fibre hybrid T700 carbon/S2-glass load response at 20J structural bonnet impact: (a) load versus deflection, (b) load versus time 188

Figure 6.23: Interlayer fibre hybrid T700 carbon/S2-glass strain gauge response at 15J structural bonnet impact 189

Figure 6.24: Interlayer fibre hybrid T700 carbon/S2-glass strain gauge response at 20J structural bonnet impact 189

Figure 6.25: Micrographs of interlayer fibre hybrid T700 carbon/Vectran bonnet cross-section along the plane x-z at impact site: (a) 15J, (b) 20J 189

Figure 6.26: Representative C-scans for interlayer fibre hybrid T700 carbon/S2-glass bonnet experimental impacts: (a) 15J, (b) 20J 190

Figure 6.27: Intralayer fibre hybrid T700 carbon/Vectran load response at 15J structural bonnet impact: (a) load versus deflection, (b) load versus time 191

Figure 6.28: Intralayer fibre hybrid T700 carbon/Vectran load response at 20J structural bonnet impact: (a) load versus deflection, (b) load versus time 191

Figure 6.29: Micrographs of intralayer fibre hybrid T700 carbon/Vectran bonnet cross-section along the plane x-z at impact site: (a) 15J, (b) 20J 191

Figure 6.30: Intralayer fibre hybrid T700 carbon/Vectran strain gauge response at 15J structural bonnet impact 192

Figure 6.31: Intralayer fibre hybrid T700 carbon/Vectran strain gauge response at 20J structural bonnet impact 192

Figure 6.32: Representative C-scans for interlayer fibre hybrid T700 carbon/S2-glass bonnet experimental impacts: (a) 15J, (b) 20J 193

Figure 6.33: 15J structural composite bonnet impact, peak load per unit mass 194

Figure 6.34: 20J structural composite bonnet impact, peak load per unit mass 194

Figure 6.35: 15J structural composite bonnet impact, maximum deflection per unit mass . 195

Figure 6.36: 20J structural composite bonnet impact, maximum deflection per unit mass . 195

Figure 10.1: Monolithic S2-glass composite plate impact at 140J for various fracture toughness values (131.6kJ/m^2 used), load versus deflection 230

Figure 10.2: Monolithic S2-glass composite plate impact at 140J for various fracture toughness values (131.6kJ/m^2 used), load versus time..... 230

Figure 10.3: Monolithic S2-glass composite plate impact at 140J for various strain rate 'kappa' values (k=100 used), load versus deflection 231

Figure 10.4: Monolithic S2-glass composite plate impact at 140J for various strain rate 'kappa' values (k=100 used), load versus time 231

Figure 10.5: Intralayer fibre hybrid T700 carbon/Vectran plate impact at 70J for various fracture toughness values (G_{IC}=142.0 used), load versus deflection 232

Figure 10.6: Intralayer fibre hybrid T700 carbon/Vectran plate impact at 70J for various fracture toughness values (G_{IC}=142.0 used), load versus time..... 232

Figure 10.7: Interlayer fibre hybrid T700 carbon/S2-glass structural bonnet impact at 20J for various Rayleigh material damping (ζ=0.3 used), load versus deflection 233

Figure 10.8: Interlayer fibre hybrid T700 carbon/S2-glass structural bonnet impact at 20J for various Rayleigh material damping (ζ=0.3 used), load versus time 233

List of tables

Table 2.1: A selection of current spread tow manufacturers 39

Table 3.1: Base level tests performed on fibre hybrid composites and constituents 60

Table 3.2: Materials tested 61

Table 3.3: Tension material properties 63

Table 3.4: Compression material properties 65

Table 3.5: Nominal in-plane shear properties as fitting parameters for numerical modelling 69

Table 3.6: Thermogravimetric analysis results, volume fractions and density 72

Table 3.7: Experimental versus theoretical tensile properties for the interlayer and intralayer fibre hybrids 76

Table 3.8: Mode I interlaminar critical strain energy release rates for fibre hybrid composites 82

Table 3.9: Mode II interlaminar critical strain energy release rates for fibre hybrid composites 89

Table 4.1: Compact tension test types, experimental and numerical suitability study 97

Table 4.2. NCCT FE model analysis thickness optimisation 103

Table 4.3: NCCT and ENCCT ply counts and nominally cured thicknesses 106

Table 5.1: VUMAT material input deck [163] 130

Table 5.2: FE impact plate model thicknesses and continuum shell/cohesive element stacking sequences 132

Table 5.3: Interlaminar material properties used for FE modelling cohesive elements 141

Table 5.4: Material properties used for impact plate FE modelling, continuum shell elements 142

Table 5.5: Back face damage for 70J plate impacts, experimental versus numerical 145

Table 5.6: Back face damage for 140J plate impacts, experimental versus numerical 146

Table 5.7: Delamination (interlaminar) failure for 70J plate impacts, experimental versus numerical (not to scale) 147

Table 5.8: Delamination (interlaminar) failure for 140J plate impacts, experimental versus numerical (not to scale) 148

Table 6.1: Bonnet nominal cured thicknesses and stacking sequences 169

Table 6.2: Cohesive surface properties 180

Table 6.3: Material properties used for structural bonnet impact FE modelling, continuum shell elements 182

Table 6.4: Natural frequencies of the interlayer fibre hybrid T700 carbon/S2-glass numerical model 186

1. Introduction

1.1. Background

The use of composite materials within the commercial automotive sector has been identified as a potential emerging market in the UK. The government led research consortium 'Composites UK' published a document outlining the importance of composite material development and the projected growth targets for major engineering markets such as aerospace, defence, automotive, rail, construction, marine, oil and gas, and renewables [1]. They reported that by 2030, the automotive industry would grow by 16%, behind only the oil and gas industry at 33%, and the aerospace industry at 19%.

The research involved in this PhD was undertaken in conjunction with an industrial consortium (Composites Innovation Cluster (CiC) [2]), aimed at promoting the streamlining of composite materials into the UK automotive industry. The consortium involved several composite manufacturing and automotive companies, both nationally and internationally. The role of Imperial College London, being stakeholders in the subprogram of the CiC known as 'Datacomp', was aimed at providing composite material data to be used effectively with up-to-date finite element model solvers. The material properties were to be determined through both standard and non-standard test regimes to provide a comprehensive data set for each material type. The material property data was collected and stored within an easily accessible online database managed by Granta [3]. The industrial partners associated with the project were then able to utilise the composite material data in the design of future composite automotive components.

1.2. Motivation and objectives

The motivation for this research originated at the automotive industry's demand for lighter and more fuel efficient cars, where fibre hybridisation could save up to 25% of a cars weight and thus reduce consumption of 250 million barrels of crude oil per year [4]. Fibre hybrid composites have proven to have beneficial properties over 'monolithic fibre' composites, such as exhibiting pseudo-ductility [5] to avoid sudden catastrophic component failure, as well as improved impact performance [6].

A variety of composite materials were tested as part of this research, namely two fibre hybrid composites (interlayer fibre hybrid T700 carbon/S2-glass and intralayer fibre hybrid T700 carbon/Vectran) and their monolithic constituent composites (fibres supplied by Sigmatex [7] and MTM57 resin by Solvay [8]), discussed further in Chapter 3. The fibres were chosen by the Composites Innovation Cluster (CiC) [2] for their favourable in-plane mechanical properties and impact resistance. The resin (MTM57) was chosen due to its high toughness, resistance to high temperatures, and good surface finish. The experimental testing at the material property level utilised both standardised and non-standard tests for the various composite materials and fibre architectures. Figure 1.1 presents this level at the bottom, under the 'coupons' label, taken from the Department of Defense (United States of America) Military Composite Materials Handbook [9], originally proposed by Rouchon [10]. Chapter 4 addresses premature compression and buckling failure during translaminar fracture toughness testing, where a novel specimen design is presented.

Upon capturing the in-plane, interlaminar, and translaminar material properties through both standard and non-standard test regimes, drop tower impact testing was employed to provide an insight into how composite laminates respond to low velocity impact damage, a likely occurrence within bodywork of automotive components (such as dropped tools to a car bonnet or debris strike). This type of testing is labelled under the 'details' subsection of Figure 1.1. The materials' failure modes were investigated experimentally and compared to energy-based bilinear plane stress interlaminar and translaminar fracture numerical models to further understand the complex failure associated with low velocity impact of fibre hybrid composites.

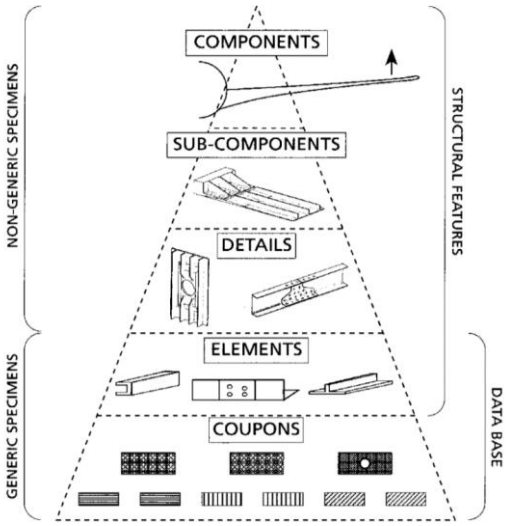


Figure 1.1: The pyramid of tests [9]

Finally, a reduced scale industrial component was subjected to low velocity impact experimentally and numerically modelled, utilising the properties determined from the previous subsections. Doing so therefore supported the numerical modelling strategy through accurate experimental correlation. This final phase of experimental testing prior to a full scale component test would be within the 'sub-components' category of the test pyramid presented in Figure 1.1. By mechanically testing the materials from coupon level through to the sub-component level, the research within this thesis provides an insight into the feasibility of fibre hybrid composites for use within industrial automotive components by furthering the understanding of their associated failure modes.

To summarise, the main objectives of the research presented are as follows:

i. Experimentally measure a comprehensive set of material properties through both standard and non-standard testing of novel fibre hybrid composite materials for employment within the Composites Innovation Cluster Datacomp database [2], primarily for use by the automotive industry in component design.
ii. Develop a new Compact Tension specimen geometry to determine the translaminar fracture toughness of the novel fibre hybrid composite materials, where current standard test specimens were unsuitable due to premature compressive failure and out-of-plane buckling.
iii. Utilise an existing energy-based bilinear plane stress numerical model using the measured material properties under low velocity impact of flat plate laminates and compare them to experimental testing. Doing so would provide insight into the unique failure processes associated with the two fibre hybrid composites.
iv. Numerically model (using the same modelling approach as with the plate impacts) a reduced scale industrial component subjected to low velocity impact. This would also prove the conceptual feasibility of the numerical model to capture the structural response of fibre hybrid composite components.

1.3. Outline of thesis

The main body of this thesis is divided into seven Chapters. The following paragraphs outline the content of each Chapter and their relevance and progression to the following Chapters.

Chapter 2: Literature survey and research plan

This Chapter outlines the current state of the art within the literature for each of the topics within the following Chapters. The state of the art regarding the topics in each Chapter is summarised and the gaps in the literature are discussed. The identified gaps hence informed the presented research plan.

Chapter 3: Characterisation of fibre hybrid composites and their monolithic composite counterparts

The research in this Chapter outlines the base level testing shown in Figure 1.1, where largely standardised testing was employed on the fibre hybrid composites and their monolithic composite counterparts. The in-plane material properties were fully characterised under the tensile, compressive, in-plane shear, and interlaminar fracture in Mode I and Mode II, as well as their volume fraction by use of Thermogravimetric Analysis (TGA) and analytical microscopy. The data generated in this Chapter provided a sound baseline of data for further, more complex non-standardised material testing in the subsequent Chapters, where the nominal material properties were required for numerical modelling. The novelty presented in this Chapter lies within the in-plane and interlaminar material properties of the fibre hybrid composites, therefore providing insight into their unique failure modes.

Chapter 4: Translaminar fracture toughness of fibre hybrid composites and their monolithic composite counterparts

This Chapter provides a clearly novel output from this thesis, where a new Compact Tension (CT) specimen design was developed. This was due to the inadequacy of

typical CT specimen geometries when testing composites with low compressive to tensile strength ratios, which commonly lead to premature compressive failure at the rear of the specimen. Such materials also tended to buckle out-of-plane with typical CT specimen geometries due to their thin through-thickness. Therefore, a novel CT specimen design was developed through numerical optimisation and experimental testing, and the fracture toughness values could be captured for both the fibre hybrid composites and their monolithic composite counterparts.

Chapter 5: Low velocity impact response characterisation of fibre hybrid composites

Using the in-plane, interlaminar, and translaminar material properties measured within the preceding Chapters, an energy-based bilinear plane stress traction-separation VUMAT (Abaqus Finite Element user subroutine) was used to compare low velocity impact numerical models to experimental test results. The purpose of this low velocity impact testing was to provide insight into the failure processes involved with both the interlayer and intralayer fibre hybrid composites and also support the accuracy of the VUMAT material model for use with fibre hybrid composite laminates. Two impact energy levels were employed and post-test fractographic analysis was used to inform the associated failure processes. The novelty in this Chapter is the utilisation of an energy-based bilinear plane stress numerical modelling approach in conjunction with the low velocity impact of fibre hybrid composites, hence providing insight into their resulting complex failure modes.

Chapter 6: Low velocity structural impact response of fibre hybrid composites on a reduced scale car bonnet

The research in this Chapter involved the development of a novel test-rig to mount a reduced scale (1:5) Bentley Continental car bonnet (courtesy of Solvay [8]). Interlayer and intralayer fibre hybrid composites were tested at two discrete energy levels and since the test rig provided known boundary conditions, numerical modelling was used to support the Abaqus VUMAT subroutine for structural component level testing. Strain gauging was employed on both sides of the scaled bonnet at 80mm from the

impact site and then compared to virtual strain gauges in the numerical models. The development of the experimental test rig, providing nominal points of constraint and thus quantifiable boundary conditions, allowed accurate implementation of the energy-based bilinear plane stress numerical modelling approach for low velocity impact. Conducting this study on a doubly curved structural component provided inherent novelty regarding the state of the art.

Chapter 7: Discussion

This Chapter draws upon and discusses the key outcomes from the preceding Chapters, their novelty, and their relevance given the current state of literature.

Chapter 8: Conclusions and future work

This Chapter outlines and summarises the key findings from the preceding Chapters. Drawing from these, suggestions for future work are made, indicating where the research may be developed further.

Publications and dissemination:

- **Journal papers:**
  - T. J. Katafiasz, L. Iannucci, and E. S. Greenhalgh, "Development of a novel compact tension specimen to mitigate premature compression and buckling failure modes within fibre hybrid epoxy composites," *Composite Structures*, vol. 207, 2019 [11]
- **Conference oral presentations:**
  - T. Katafiasz, "Hybrid Fibre Composites for Delamination Resistance and Cost Saving," in Cyclitech 2015: The first international conference on bicycle technology, Brussels, Belgium, 2015 [13]
  - T. J. Katafiasz, "Interlaminar and Intralaminar Properties of Carbon Spread Tow and Glass Fibre Hybrid Composites for Cost Saving in the Mass Production of Automotive Components," in ECCM17 - 17th European Conference on Composite Materials, Munich, Germany, 2016 [14]
  - T. J. Katafiasz, "Development of a Novel Compact Tension Specimen for Fibre Hybrid Composites," in CompTest 2017: 8th International Conference on Composites Testing and Model Identification, Leuven, Belgium, 2017 [15]
- **Invited webinar presentations:**
  - T. Katafiasz, "Bridging Characterization and Simulation: Materials Information Needs for Design," in *Granta Webinar,* Cambridge, UK, 2017 [16]

2. Literature survey and research plan

The automotive industry has recently begun pursuing more complex composite material systems for structural components, where vibrational and acoustic damping, surface finish, cost, and performance are prioritised. The UK government has identified the emergence of fibre hybrid composite materials for automotive components as a priority for research and development and invested into companies such as CARBIO [17] and Composites Innovation Cluster [2], aimed at streamlining the delivery of composites into the commercial automotive markets. This Chapter therefore outlines the current state of the art for the characterisation of fibre hybrid composites, primarily related to the automotive industry. The carbon spread tow is first discussed, highlighting its benefits, followed by the basic mechanical characterisation of fibre hybrid composites. This presents the current understanding of the effect that fibre hybridisation has upon the interlaminar and in-plane composite laminate properties.

The fracture toughness of composites has become increasingly important regarding numerical modelling approaches of composite impact behaviour, particularly penetrative, where the failure modes are largely dominated by fibre fracture. Research by Pinho [18], Lopes et al. [19], Ehrich [20], and Gonzalez [21]–[23] amongst others have discussed the benefits of an energy-based translaminar fibre fracture approach when numerically modelling low velocity impacts of composites, with its' importance within the automotive industry highlighted by Altair Engineering [24]. Subsequently, the literature regarding the translaminar testing of fibre hybrid composites is explored, highlighting the shortfalls in the current test methods.

Due to the emergence of energy-based fracture numerical modelling aiding design of components, the literature regarding fibre hybrid composites under low velocity impact is explored. Standard test regimes such as the ASTM D7136 [25] flat laminate plate impact standard is presented as well as non-standard test methods used primarily within the automotive industry.

The following Chapter outlines the current state of the art for each subsequent Chapter. The gaps within the literature are then highlighted along with a research plan to address these gaps.

2.1. Literature survey

2.1.1. Spread tow composites

Spread tow (also interchangeably referred to as 'thin ply' [26]) is a relatively new form of carbon fibre architecture developed to utilise elliptical carbon fibre tow cross sections as opposed to traditional circular cross sections (Figure 2.1) and so, laminate thicknesses within the order of 0.02mm can be achieved in woven architectures [27]. Due to its improved in-plane mechanical properties compared to traditional tow composites, and now ubiquitous throughout the Formula One industry, spread tow manufacturing is becoming affordable for the commercial automotive sector and fibre processing companies are increasingly providing tow spreading capabilities (Table 2.1). Inherently, the volume fraction of a fibre reinforced polymer utilising spread tows is higher than those comprised of traditional circular fibre tows due to lower crimp angles, resulting in a lower percentage of matrix which is not being utilised [28]. This leads to spread tow composites exhibiting favourable material properties due to less matrix voidage [29] as well as lower angles of crimp.

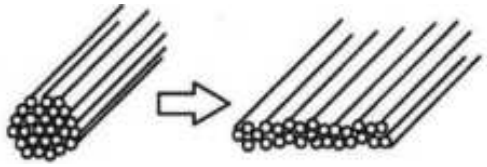


Figure 2.1: Fibre arrangement in spread tow compared to typical tow [30]

A method of fibre dispersion was first proposed in 1996 by Kawabe, K. et al. [30] through the use of a pneumatic loading on traditional circular carbon fibre tows. When a transverse flow of air is inflicted upon a sagged tow of fibres at a specific tautness, a uniform and stable spreading of the fibres is achieved [30]. At this point in the spreading process, where the fibres are sagged, tension across the fibre tows is alleviated momentarily and the air is free to pass through the tow, in-between the individual fibres, therefore inducing fibre spreading (Figure 2.2).

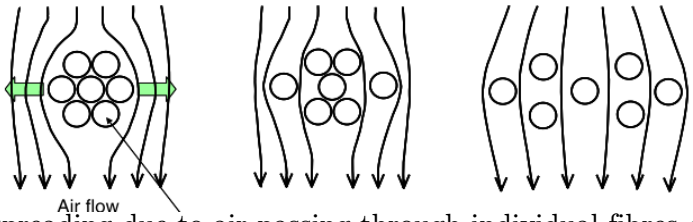


Figure 2.2: Tow spreading due to air passing through individual fibres during pneumatic method [31]

The pneumatic method can be supplemented with roll spreading, where the tows are drawn off the bobbin on to rolls moving in a traversing motion. By combining the roll spreading method with the pneumatic method, the dispersion of the fibres is increased up to a critical level of fibre tension, above which fibre breakage is likely to occur [32]. A combination of the two spreading methods has been developed, where the traversing roll spreaders vibrate over the tow while hot air at 200°C is effectively blown transverse to the fibre direction (through the presence of a vacuum below the sagged fibres) [30], [32], [33]. It is suggested that the roll method is useful for initially overcoming the adhesion due to fibre sizing and then the pneumatic method allows for further spreading [33].

Several manufacturers have accomplished successful spreading of thick tows through pneumatic and rolling methods. Table 2.1 lists a selection of these manufacturers along with their publicised capabilities. Spread tow tape has itself been incorporated by Tsai, S. W. and Cognet, M. [34] into NCF with a nominal ply thickness of 0.08mm [35]. By doing so, the detrimental mechanical properties associated with crimped woven fabrics such as resin rich regions and increased fibre crimp are suppressed, whilst maintaining thin laminates. Like thick tows, spread tow tapes are not constricted to 0°/90° relative weave patterns and a manufacturing technique has been developed to account for this. An automated process that allows continuous placement of spread tow tapes at any angle to be interleaved with one another to satisfy specific design requirements commonly dictated by strength has been developed (Figure 2.3). This is particularly useful for manufacturing strength-to-weight optimised components where certain regions require higher load capacities than others.

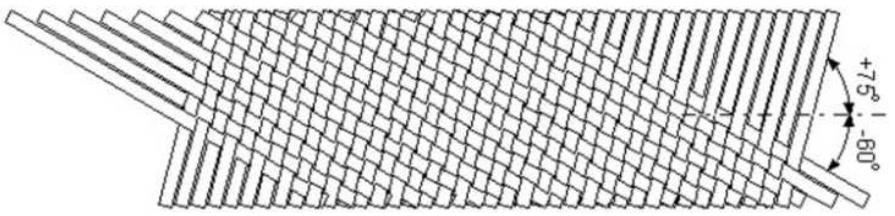


Figure 2.3: Continuous spread tow tape placement incorporating unequal angles [36]

Table 2.1: A selection of current spread tow manufacturers

Manufacturer	Capabilities	Areal density	Country
Chomarat (chomarat.com) [37]	Spreading up to 50K for NCF 'C-Ply', Weaving at 0°, 90°, 45°, 25° and 20° angles	75 gsm	France, North Africa, USA, China
Harmoni Industry Co. Ltd. (harmoni.co.jp) [38]	Spreading single-tow up to 12K to 80mm width at 20m/min and multi-tow 24K at 5m/min, Plain, twill and 'any style' weaving	100 gsm	Japan
North Thin Ply Technology (thinplytechnology.com) [39]	Spreading, Automated Tape Laydown (ATL) up to 3.4x12m preform areas at 7.5m/min	30 gsm (for PAN-based fibres)	Switzerland, USA
Oxeon AB (oxeon.se) [40]	Spreading up to 12K to 50mm width, Weaving at a variety of angles	40 gsm	Sweden, USA
Sakai Ovex Co. Ltd. (sakaiovex.co.jp) [41]	Spreading up to 48K to 40mm width, Weaving at 0°/90° relative angles	80 gsm	Japan
Sigmatex Ltd. (sigmatex.com) [7]	Spreading, Weaving at 0°/90° relative angles	88 gsm	UK, USA, China
Teknomax Corp. (teknomax.jp) [42]	Tow spreading machinery, Weaving machinery	160 gsm	Japan

2.1.2. Characterising fibre hybrid composite material properties

A review in 2014 by Swolfs et al. [5] highlighted the three most common categories of fibre hybrid composites as interlayer, intralayer, and intrayarn, where hybridisation was defined by the fibre architecture, as shown in Figure 2.4. The interlayer approach has typically been the most common in the last thirty years of research within the field [43] due to its ease of manufacture and the ability to vary the fibre volume fractions without the need for the intricate weaving machines required when manufacturing intralayer or intrayarn fibre blankets. As the commercial availability of fibre weaving looms have become more accessible, recent years have seen the emergence of research into intralayer and intrayarn fibre hybridisation [44]–[47], for automotive applications, where not only structural, but pseudo-ductility and impact performance are prioritised. Thermogravimetric Analysis (TGA) has been utilised for

fibre hybrid composites, a method commonly used with monolithic composites, to determine their relative volume fractions and constituent quantities, regardless of fibre architecture [48].

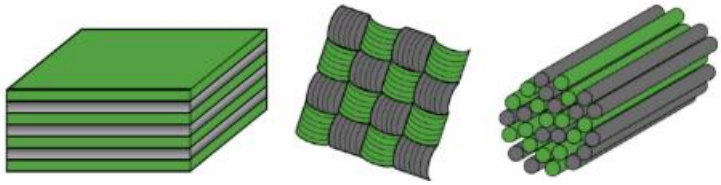


Figure 2.4: Common fibre hybrid configurations (interlayer, intralayer, and intrayarn) [5]

The experimental characterisation of fibre hybrid composites has largely entailed the same test standards as those associated with monolithic composites to allow comparison to their monolithic composite counterparts as a performance baseline. Swolfs et al. [5] highlighted the failure modes currently observed within the literature. Fibre hybrid composites tended to follow a rule of mixtures in their tensile modulus, whereas their tensile failure strength and strain did not typically comply with such a model. This was attributed by Swolfs et al. to the fibre architecture, fibre alignment, and crimp within the woven plies. Figure 2.5 presents the typical definitions of the hybrid effect, where Low Elongation (LE) fibres are hybridised with High Elongation (HE) fibres within a common matrix system.

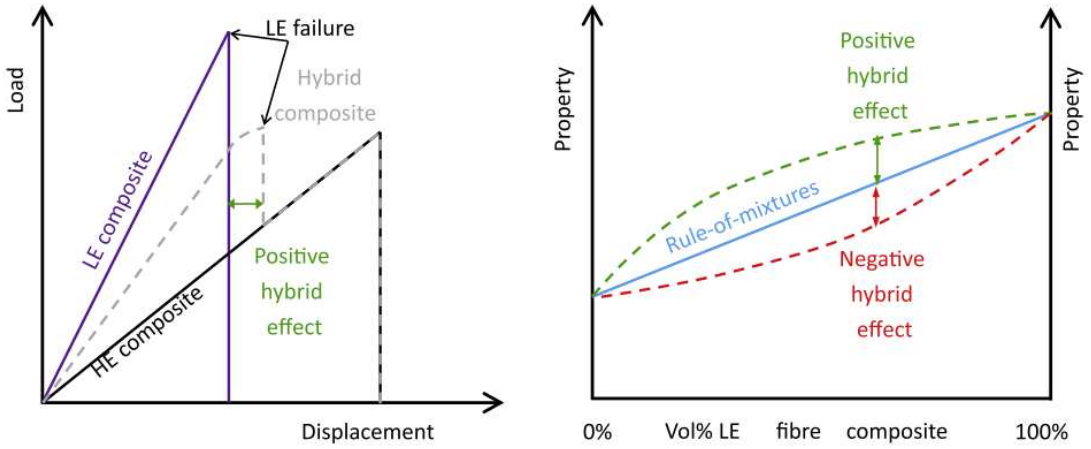


Figure 2.5: Definitions of the hybrid effect: (a) Typical load displacement curve of a 50/50 fibre hybrid composite, (b) hybrid deviation from the rule of mixtures [5]

Much research has been conducted regarding the tensile effect of fibre hybridisation within the collaborative High Performance Ductile Composite Technology ('HiPerDuCT') project undertaken by the University of Bristol and Imperial College London in the UK [49]. Resulting from this project, a number of academic papers have been published regarding the hybrid effect upon the tensile failure of fibre hybrid composites [50]–[54]. Among these, the most succinct theory of pseudo-ductility during tensile loading of fibre hybrid composites is shown diagrammatically in Figure 2.6. It was proposed that there are four predominant types of tensile failure in interlayer fibre hybrid composites, which in turn affect the stress versus strain response of the material through the combination of translaminar and interlaminar failure modes. Pseudo-ductility can be achieved through the careful dispersion of fibre hybrids resulting in both interlaminar and translaminar fracture of the composites. It is therefore apparent that both the interlaminar fracture toughness as well as the translaminar fracture toughness, and their relative failure loads are vital to achieving such a pseudo-ductile response, favoured by industry where CFRP (Carbon Fibre Reinforced Polymer) composites typically fail in a brittle and catastrophic manner.

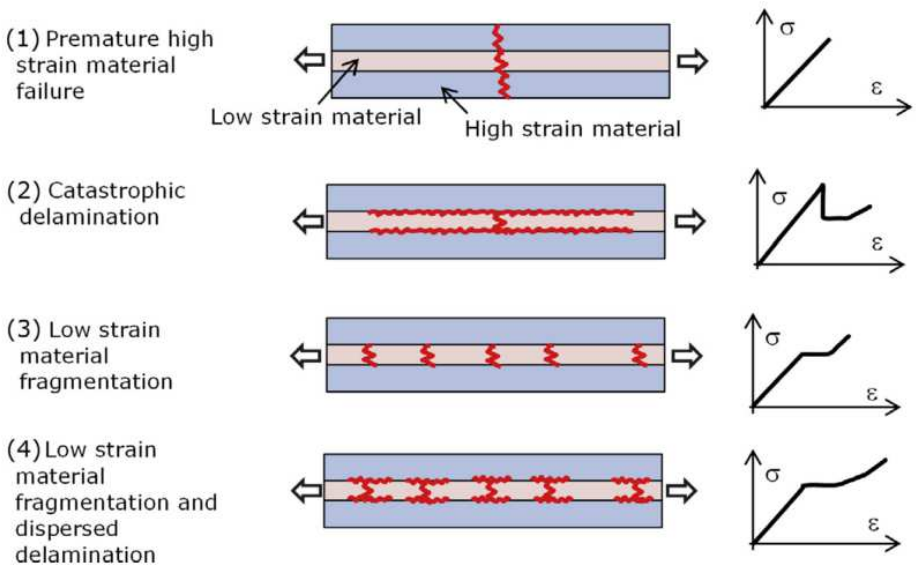


Figure 2.6: Pseudo-ductility during fibre hybrid tensile loading leading to irreversible damage [52]

Regarding the stacking sequence of interlayer fibre hybrids and fibre placement within intrayarn fibre hybrids, Swolfs et al. [55] proposed a unidirectional tensile strength-based

numerical model. By modelling the stress intensity factors around each of the fibre clusters, they concluded that a carbon/glass interlayer fibre hybrid with spread tow plies produced the most favourable hybrid effect (higher strain to failure compared to a monolithic carbon composite), due to the suppression of fibre cluster breaks across neighbouring plies, Figure 2.7, and a similar phenomenon was also reported by Zhang et al. [56]. In the same paper, Swolfs et al. also conducted a similar numerical study on commingled fibre hybrids (intrayarn, Figure 2.4) and found the interlayer fibre hybrids to present superior hybrid effects when containing the same fibre volume fractions.

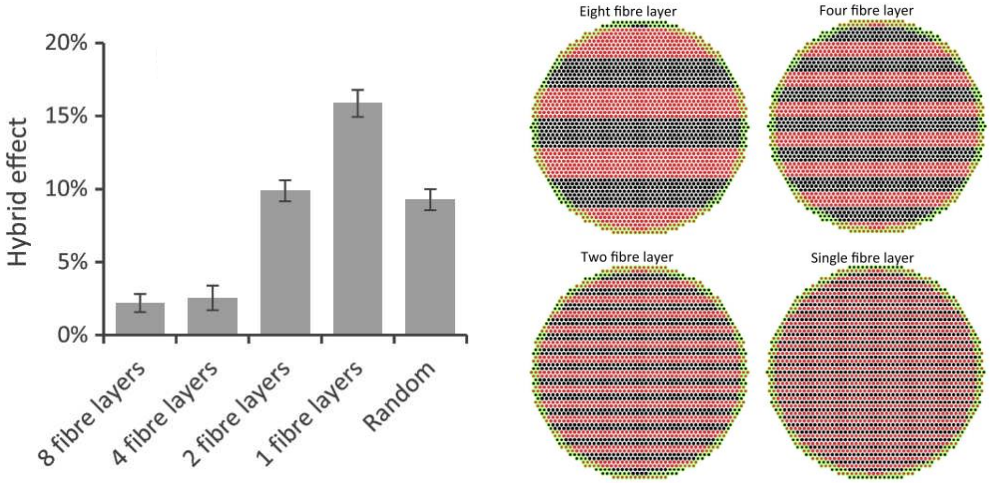


Figure 2.7: The tensile hybrid effect as a function of fibre plies within a unidirectional interlayer fibre hybrid [55]

To calculate fibre hybrid laminate strength and stiffness using an analytical approach, Summerscales, J. [57] proposed in his PhD thesis a rule of mixtures for fibre hybrid systems containing two fibre types to the relative Low Elongation (LE) fibres and the High Elongation (HE) fibres. Assuming there is a common matrix system between the two (or more) fibre types (and no interaction between the fibres);

$$E = E_{LEf} v_{LEf} + E_{HEf} v_{HEf} + E_m v_m \tag{2.1}$$

where E is the composite modulus, E_{LEf} is the low elongation fibre modulus, v_{LEf} is the low elongation fibre volume fraction, E_{HEf} is the high elongation fibre modulus, v_{HEf} is the high elongation fibre volume fraction, E_m is the matrix modulus, and v_m is the matrix volume fraction.

Summerscales also summarised from previous literature [58] that the total elastic strain energy for a hybrid system consisting of three fibre types was given by the following equation (note that this assumes that at $\epsilon = \epsilon_a$, all the 'a' type fibres will fail, at $\epsilon = \epsilon_b$, all the 'b' type fibres will fail and at $\epsilon = \epsilon_c$, all the 'c' type fibres will fail):

$$U = {}^1\!/_2\, E_A v_A \in'_A{}^2 + {}^1\!/_2\, E_B v_B \in'_B{}^2 + {}^1\!/_2\, E_C v_C \in'_C{}^2 \tag{2.2}$$

where U is the total composite elastic strain energy, E is the modulus for each fibre type, v is the volume fraction for each fibre type, and $\in'$ is the failure strain for each fibre type.

Other researchers largely followed this linear rule of mixtures [5], [59]–[62] and furthering this, it was surmised by Summerscales [58] that the total strength of a fibre hybrid composite, comprising of low (L) and high (H) elongation fibres, is given by the following formula:

$$\sigma' = V_L E_L \in'_L + V_H E_H \in'_H + V_L V_H (E_L - E_H)(\in'_H - \in'_L) \tag{2.3}$$

Where (given that $\in'_H > \in'_L$):

$V_L E_L \in'_L + V_H E_H \in'_H$ = overall strain of the composite (constant strain)

$V_L E_L (1 - V_L)(\in'_H - \in'_L)$ = upper bound strength (enhancement of LE fibres)

$V_H E_H (1 - V_H)(\in'_L - \in'_H)$ = degradation of strength (maintaining constant strain)

The tensile, compressive, and flexural properties of fibre hybrid composites were discussed in a review by Kretsis in 1987 [43]. The review confirmed that both the tensile and compressive moduli largely followed a rule of mixtures. A higher flexural stiffness was also noticed when the highest modulus fibres were placed on the outside of the specimens. Although the elastic modulus of fibre hybrid composites have largely followed a linear rule of mixtures approach, the same cannot be said for their strength. Researchers have therefore proposed a bilinear rule of mixtures [59], [60], [63], where a critical volume fraction governs the bilinearity, summarised succinctly by Ribeiro et al. [64] as follows:

$$\sigma_{hybrid} = \begin{cases} V_L S_L + V_H E_H \varepsilon_L \,;\; V_H < V_{crit} \\ V_H S_H \,;\; V_H > V_{crit} \end{cases} \tag{2.4}$$

where S_L and S_H are the reference strengths of the Low Strength (LS) and High Strength (HS) one layer composites, E_H is the elastic modulus of the monolithic HS composite, V_L is the relative LS fibre volume fraction, V_H is the relative HS fibre volume fraction, ε_L is the strain to failure of the monolithic LS one layer composite, and V_{crit} is the critical value of the HS fibre volume fraction (given as follows, where the relative fibre volume fractions, homogenising the matrix: $V_L + V_H = 1$, and substituted into (2.4)):

$$V_{crit} = \frac{S_L}{S_L + S_H - E_H \varepsilon_L} \tag{2.5}$$

Using the linear rule of mixtures (Equation (2.1)), Ribeiro et al. [64] proved reasonable correlation between the analytical modulus against experimental data for a range of carbon/glass (denoted as CHM/G), carbon/basalt, and carbon/carbon fibre hybrid epoxy composites (Figure 2.8a). They also proved some correlation between the same materials' hybrid strength using the bilinear rule of mixtures approach (Equation (2.4)), Figure 2.8b. Other researchers have however reported poor correlation whilst using the bilinear rule of mixtures approach in both carbon/glass [62] and carbon/polyethylene [65] fibre hybrids.

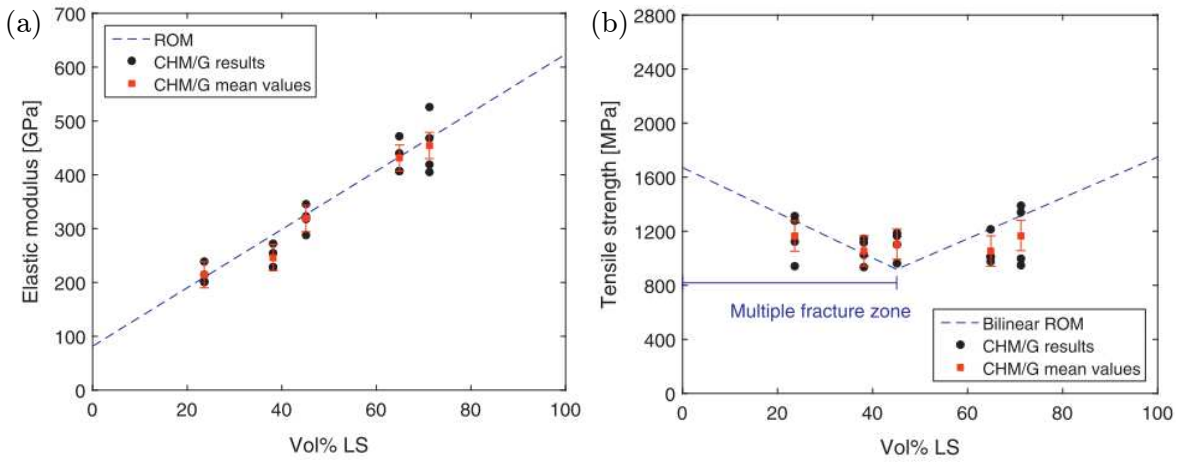


Figure 2.8: UD high modulus carbon/E-glass fibre hybrid composite: (a) linear rule of mixtures for elastic modulus, (b) bilinear rule of mixtures for tensile strength [64]

There have been Mode I and Mode II interlaminar tests of fibre hybrid composites which contain carbon nanotubes dispersed through the neighbouring fibre hybrid plies [45], [66]–[71]. The testing associated with such interlaminar properties have largely been conducted using Double Cantilever Beam (DCB) and 3 or 4-point End Notched Flexure (3-ENF or 4-ENF) testing. Interlayer fibre hybrids are likely to present lower interlaminar fracture toughnesses in both Mode I and Mode II compared to intralayer fibre hybrids due to the undulations caused by the crimp resulting in a tortuous fracture surface [72], as well as the thicker resin layer between plies noticed in the nesting of un-woven fabrics [73]. Fibre bridging has also been reported to increase the Mode I fracture toughness in glass/flax fibre hybrid composites [56]. Testing by Hwang and Shen [74] in Mode I, and Hwang and Huang [75] in Mode II for a carbon/glass fibre hybrid epoxy composite also concluded that the fibre hybrid composites presented higher interlaminar toughness than monolithic composites. Aside from one other paper by Miyairi and Wakabayashi in 1984 [76] (which was published in Japanese), data regarding the interface between carbon and glass fibres within the same epoxy system was scarce. There was, however, interlaminar testing conducted on commingled fibre hybrid yarn thermoplastic and epoxy composite systems by Thanomsilp and Hogg [77]. They utilised DCB and 4-ENF testing for both a thermoplastic and epoxy matrix systems encapsulating glass/polypropylene, glass/nylon, and glass/modified polyethylene terephthalate. They found that doublers were required for the testing to alleviate unwanted compressive failure on the laminate surfaces during bending. This was also used by other researchers including Reeder and Whitley [78] for non-hybrid composites, who showed the purpose of the doublers used in a DCB test specimen diagrammatically in Figure 2.9.

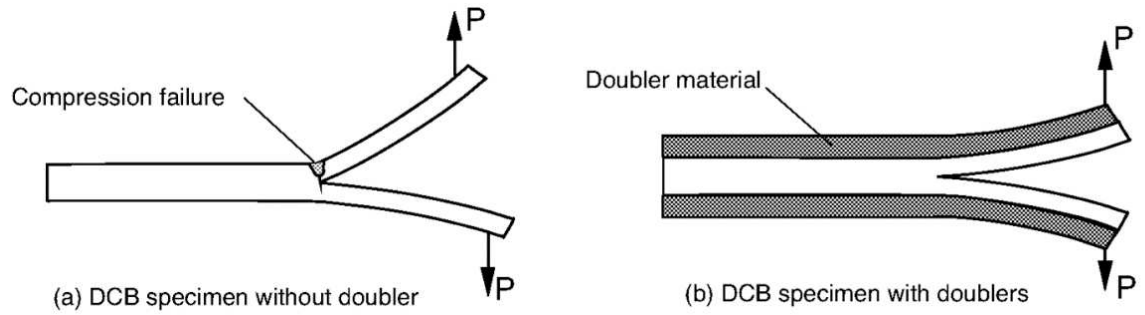


Figure 2.9: Diagram showing effect of doubler plates [78]

Since the interlaminar fracture toughness Mode I and Mode II testing of an interlayer fibre hybrid inherently presents through-thickness compliance discontinuity, due to the off-mid-plane delamination, research has been conducted to take this into account when calculating the fracture toughness. Most notably the interface between polymeric composite and metallic surfaces has been studied for both Mode I [79]–[81] and Mode II [82]–[84]. Due to the drastic variation in stiffness between these neighbouring materials correction factors in calculating the fracture toughnesses for Mode I and Mode II are presented by Ouyang et al. [85] and Ouyang and Li [86] respectively. Research has however been published where the stiffness variation between the Mode I DCB arms is minimal, and therefore neglected when characterising the interlaminar properties of fibre hybrid composites [56].

2.1.3. Translaminar fracture toughness of fibre hybrid composites

The need to characterise a material's translaminar fracture toughness relates directly to numerical impact modelling and component design of industrial components, where loading scenarios such as OHT (Open Hole Tension) due to fastener holes and debris-based impact events are often present. Researchers [87]–[90] have characterised the fracture toughness of CFRP composites using the Compact Tension (CT) specimen design similar to the ASTM E399 [91] standard but its success has relied heavily upon the relatively similar tensile and compressive strength of the material systems. A common unwanted failure that occurred during CT testing has been that while opening the CT arms, the un-notched rear side of the specimen underwent compressive forces leading to premature failure through compression (FM1, Figure 2.10), as well as out-of-plane buckling (FM6, Figure 2.10) [87], [92]–[95]. Premature compressive failure tended to occur for woven materials with high levels of crimp and materials with low compressive strengths compared to their tensile strengths, when using test methods summarised succinctly by Blanco et al. [93] and Laffan et al. [90]. Composites commonly exhibit lower compressive strengths due to the presence of microbuckling which leads to fibre kinking [96]–[98]. Fibre crimp due to the fibre architecture notably causes this premature compressive failure, since composites typically have crimp angles of around 3° [97]. The interfacial properties between two neighbouring fibre types within an interlayer fibre

hybrid composite have also been reported to affect the translaminar fracture toughness, although in a CC (Compact Compression) specimen, by Tsampas et al. [99].

Blanco et al. [93] proposed a novel '2TCT' (Two Tapered Compact Tension) specimen geometry which contained four tapered edges to minimise compressive failure at the rear of the specimen (FM1, Figure 2.10). Parametric modelling was employed to achieve the desired specimen geometry, where various unwanted failure modes were considered along with various geometrical manipulations. They found that a specimen thickness of 5.6mm was optimal for reducing the unwanted premature buckling (FM6) and compressive failure (FM1) modes, albeit for only one material system. The parametric study involved seven specimen types, drawing inspiration from the standard CT and Extended Compact Tension (ECT) geometries from the ASTM E399 [91] standard, and the Widened Compact Tension (WCT) and Tapered Compact Tension (TCT) geometries from a report by Cher [100]. It should be noted that increasing the thickness of standard CT specimens were also found to affect the measured translaminar fracture toughness, as presented by Teixeira et al. [88].

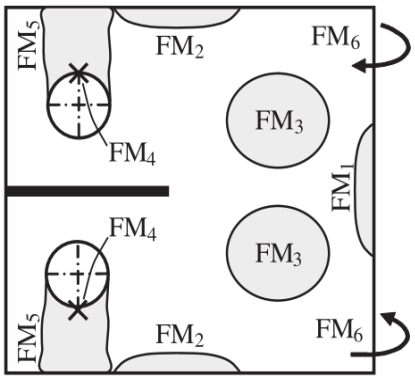


Figure 2.10: Diagram of a conventional CT specimen with the locations of possible failure mechanisms [93]

A 2017 study by Swolfs [101] highlighted the effect of fibre hybridisation between carbon and glass fibres on the translaminar fracture toughness, where the interlayer fibre hybrid was seen to exhibit values in-between the two monolithic composite counterparts, indicating a possible rule of mixtures. Ortega et al. [102] also found similar results with interlayer carbon-glass fibre hybrids, although their CT specimen failed at the rear due to compression (characterised as failure mode FM1 by Blanco et al. [93], Figure 2.10). To counteract premature buckling

within this specimen, Swolfs used a steel anti-buckling guide and verified that the load was not interfered with by removing it before crack initiation and noted 'no noticeable change in load' [101]. Other researchers have also employed anti-buckling devices (Figure 2.11) with susceptible composites, utilised to artificially prohibit the out-of-plane buckling and premature compression failure at the rear of the CT specimen [35], [101], [103], [104]. The issue with this approach relates to the unknown lateral forces acting upon the specimen. Because the out-of-plane force at the rear of the specimen is inherently unquantifiable (due to the internal through-thickness stress fields), anti-buckling guides were not used for the materials presented within this thesis.

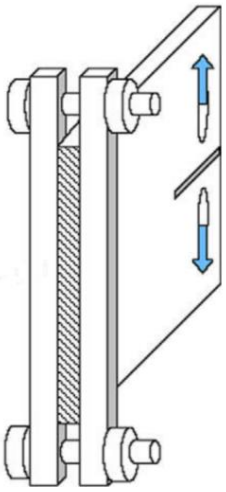


Figure 2.11: Anti-buckling guide for a standard Compact Tension specimen [103]

Another attempt to reduce the unwanted buckling and compressive effects without utilising an anti-buckling guide has been presented by Donadon et al. [105]. A side 'groove' was cut into the Over-height Compact Tension (OCT) specimen to allow for a lower crack driving force across a thinned portion of the laminate containing fibres orientated at 90°, Figure 2.12. An issue arising from this design however lies in the notching process, which does not take into account any broken fibres arising from the grooving process (undertaken post-cure), hence reducing confidence in the thickness measurement of the fractured region. The associated *R*-curves also proved to be insufficiently long at a crack length of 15mm, and a stable propagation toughness was not reached.

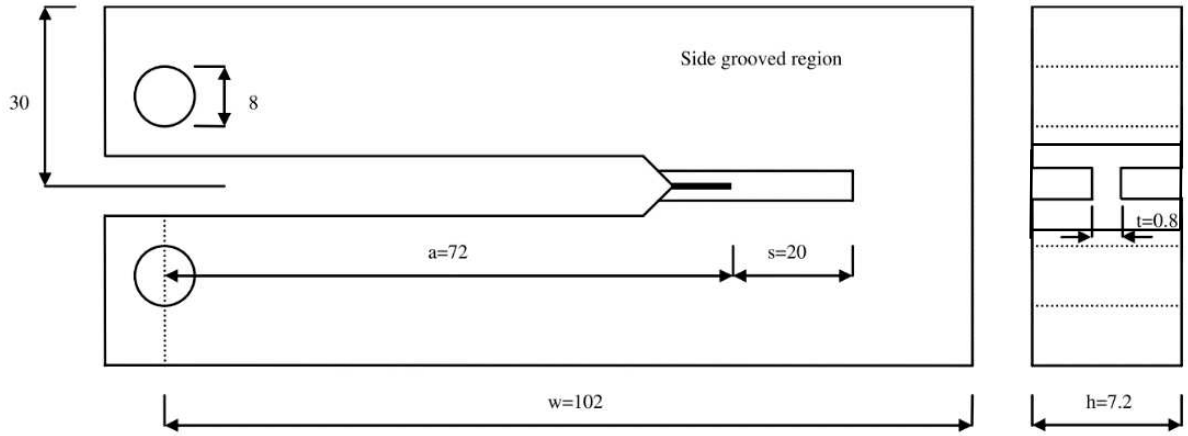


Figure 2.12: Modified OCT specimen (dimensions in mm) [105]

2.1.4. Low velocity impact of fibre hybrid composites

Swolf's review [5], as previously mentioned, considered the impact performance of fibre hybrid composites present in the literature. A large proportion of the studies were focussed upon the effect of fibre type dispersion within the composite, and a 30% improvement when carbon plies were blocked at the impacted surface of the panel was highlighted [106]. These results were however contradicted by another study [107], where the authors claimed that delamination between the neighbouring fibre types absorbed more energy than the effect of the fibre placement and thus the interfacial properties were critical to the energy absorption capabilities of the fibre hybrid. The placement of aramid fibres on the opposite side to the impact (where tensile loading is highest) was also noticed to improve penetration resistance under impact since the tensile fracture toughness of such fibres is known to be higher than that of carbon fibres [108].

Regarding numerical modelling, a 2018 review by Bogenfeld et al. [109], funded by BMWi (the German Federal Ministry of Economic Affairs and Energy) [110] and Airbus Helicopters Door Systems [111], highlighted the numerical approaches regarding low velocity impact on composite laminates along with their capabilities and level of detail, Figure 2.13. By increasing the level of detail within the modelling, the computational effort was increased. Early models included the spring-mass model that provided a quasi-analytical solution for laminate impact damage through a series of springs with bending. Subsequently, a layered shell model provided a kinematic response that took into account the natural frequencies of the plate but did not

typically include ply-by-ply failure characterisation. More recently, a stacked layer model included both solid shell laminate elements, as well as solid cohesive layer elements to capture both translaminar and interlaminar damage respectively. Research by Gonzalez et al. [21] used this approach with some success but concluded that the non-linear in-plane shear response of the composite laminate must be modelled, as proposed by Maimí et al. [112], to correctly capture the load response under low velocity impact.

Varying levels of detail can be drawn from the stacked layer method, depending upon the material modelling approach used and whether an energy-based or stress-based failure model is incorporated. Typically cohesive layer (COH3D8) elements (capturing interlaminar damage) are placed between continuum shell elements (capturing intralaminar and translaminar damage) using an Abaqus-based model [113] and Sun et al. [114] quantified that a minimum of six cohesive layers are required throughout a modelled laminate to accurately capture delamination. Bogenfeld concluded [109] that a user-defined material must be utilised to include the non-linear in-plane shear response and permanent plastic deformation, since commercial FE code does not offer such capabilities.

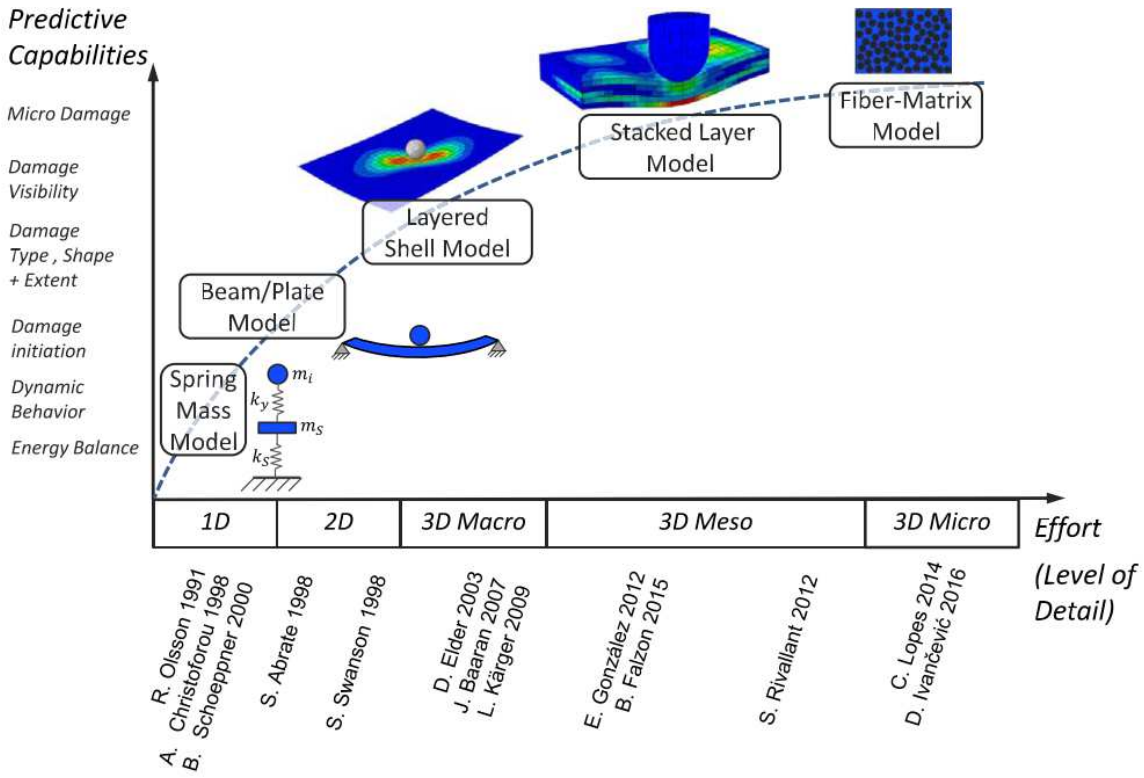


Figure 2.13: Overview of low velocity impact modelling approaches [109]

Gonzalez et al. [115] conducted an experimental study on the effects that dispersion and placement of carbon and glass fibre plies within an interlayer epoxy fibre hybrid produced through Resin Transfer Moulding (RTM) had upon the low velocity impact of composite panels. Non-destructive C-scanning was employed to characterise the damage severity of the impacted panels (Figure 2.14). They found that placing the glass fibre plies at the mid-plane of the laminate improved the energy dissipation. They also concluded that the presence of carbon fibre plies reduced the overall impact resistance of the fibre hybrid composites under impact loading, but improved the in-plane properties, highlighting an apparent trade-off between impact resistance and in-plane properties.

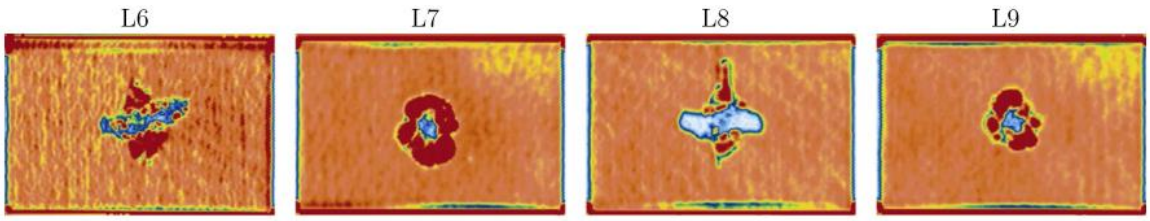


Figure 2.14: Post-test C-scans for plate impact of fibre hybrid with various interlayer carbon/glass configurations L6-L9 (see [115] for more information)

Sevkat et al. [6] conducted a similar experimental study, where carbon-glass fibre hybrids were subjected to low velocity impact. They showed that the monolithic glass fibre composite absorbed the most energy over a range of impact energies, whereas the monolithic carbon composite absorbed the least. They also concluded that although the peak load and absorbed energy were similar, the delaminated area would be reduced where the glass fibre plies were located furthest from the mid-plane of the laminate. Enfedaque et al. [116] also showed that placing the glass fibres on the outer surfaces improved the impact resistance of interlayer carbon-glass fibre hybrid composites, which was attributed to the higher strain to failure of the glass fibres.

Concerning the fibre architecture of low velocity impact on composite laminates, Potluri et al. [117] studied the effect of the fibre weave type upon the damage area prior to six energy level impacts ranging from 5J to 30J. They noticed a reduction in in-plane damage with an increase within the three-dimensionality of the fibre weave. The impact damage from these studies were confined by a 40mm diameter hole clamp on the laminate during testing to reduce plate

bending. They concluded that at low velocities (where penetration did not occur), uni-directional laminates failed mostly through interlaminar failure, whilst 3D laminates failed more locally, with through-thickness penetration. They also concluded that the compression-after-impact strength was reduced with higher fibre crimp angles, proving less desirable for component design.

Corum et al. [118] conducted multiple impact studies upon chopped glass, cross-ply carbon, and quasi-isotropic carbon epoxy composite laminates for automotive bodywork structures for the US department of Energy Office of Advance Automotive Technologies [119]. They chose a pendulum impact test to represent 'relatively large objects' such as a dropped tool, a gas gun impact test to represent small objects such as roadway debris, and brick drop impact to represent larger, and more globally destructive impacting bodies [118], [120]. They concluded that an impactor head of 12.7mm diameter for the pendulum and gas gun tests was suitable to bound other impact studies of 6.4mm to 101.6mm diameter heads found within the literature, where a larger hemispherical diameter led to an increase in damage [121].

Numerical modelling has been carried out on the low velocity impact of interlayer fibre hybrid composites using LS-DYNA MAT-43 and then compared to experimental results [6], showing reasonable correlation between peak loads. Since the numerical modelling did not utilise any energy-based damage however, the energy absorption of the models did not compare well to the experimental results and no indication of a quantified displacement correlation was reported. Superior accuracy is noted when the mesh density does not affect translaminar fracture within numerical modelling. This can be achieved by means of crack smearing the translaminar fibre fracture using a bilinear energy-based failure model, where the energy dissipated is made a function of the element volume resulting in a mesh-independent failure model [122].

Research by Ying et al. [123] presents the low velocity impact response of intralayer fibre hybrid composites, where attempts have been made to categorise the associated failure modes. This research identified the damage morphology of both intralayer and interlayer carbon-aramid/epoxy fibre hybrid composites under impact. They concluded that the although the 'ductility index' of the fibre hybrid composites were higher than that of the non-fibre hybrid

composites, further optimisation and research must be done to exploit these lightweight materials, particularly for the automotive industry.

Donckels et al [124] reported 'dent relaxation' effects within low velocity impact of biaxial composite plates. They noticed that the plastic deformation of the surrounding material at an impact site was not permanent and returned to its original state after a prolonged period of time (24 hours) after the impact event. This may be explanatory for some discrepancies between experimental test data and numerical modelling that do not incorporate this phenomenon. Research by Tan et al. [125] utilised a non-linear shear cracking three-dimensional material model to accurately capture the permanent indentation with good accuracy. They concluded that its accuracy is highly relevant for CAI (Compression After Impact) modelling, where permanent strain deformation affects the post-test compression strength.

The friction coefficient between austenitic stainless steel and glass fibre polymer composites was reported to be less than 0.1 [126], whereas between 3000-series aluminium and carbon fibre epoxy to be approximately 0.3 [127]. This data would be used in numerical modelling, where the test fixtures and impactor tup heads are commonly metallic.

2.1.5. Component scale impact modelling of fibre hybrid composite structures

Full structural impact testing and numerical modelling of fibre hybrid composites has not been a wide-reaching topic of interest in the literature, largely due to the expense and the need to fully characterise the material properties and base level failure modes before designing or manufacturing the components. Since fibre hybridisation has seen a recent resurgence within the research community as a whole however, there have been a few attempts at producing full structural components for testing [128], [129]. The emergence of lightweight structural composite bodywork has been expedited in recent years within the automotive industry due to international governmental regulations promoting the reduction of CO_2 output from vehicles, summarised succinctly by Ishikawa et al. [130], Figure 2.15.



Figure 2.15: Global automotive CO_2 regulations, critical emission or gas mileage [131]

Due to this change in legislation, companies such as BMW are driving material development by using composite bodywork within their 7-series production model chassis, which contains both monolithic metallic as well as composite structures, Figure 2.16. Within the UK, composite manufacturers such as FAR UK [132] and CARBIO [17] have also entered the market with automotive components. FAR UK [132] have developed a carbon fibre chassis with Axon Automotive [133] targeting small car manufacturers who require a crashworthy chassis design. CARBIO [17] is developing an automotive structure manufactured by hybridising both carbon and flax fibres, which they claim enhances vibrational damping whilst maintaining relatively low weight and high bending stiffness, compared to a monolithic composite structure.



Figure 2.16: BMW 7-series chassis consisting of both metallic and fibre reinforced polymer composite structures [134]

In 2018 Safri et al. published a review on the impact behaviour of fibre hybrid composites for structural applications [4], but few examples of fibre hybrid composites used for structural impact components were mentioned. An automotive bumper beam manufactured from carbon and glass fibre hybrid composite with a thermoplastic matrix was presented and shown to improve impact performances whilst reducing 33% weight relative to its monolithic glass fibre composite counterpart [135]. Another example of fibre hybridisation was an intrayarn pultruded I-beam manufactured from carbon and glass fibres in a polyester resin [136]. Numerically modelled using Abaqus' Hashin failure, then compared to experimental bending tests, the results compared well. It should be noted however that the fracture toughnesses used were experimentally characterised from the area under the standard tensile test curves, and not through traditional translaminar toughness testing [137].

A global-local numerical modelling strategy was used to capture low velocity impact damage on laminate plate impact [138], [139] with the global section containing only shell-based elements with elastic deformation. This methodology has also been scaled up to full-scale curved structural panel simulation [109]. The computational times were then compared to an identical model comprised of stacked-solid elements containing damage criteria throughout the structure. The global-local approach was proven to provide calculation time of 1.8% compared to the fully modelled counterpart. It is therefore reasonable to assume that local impact damage must be modelled inherently within a specific region of a components' structure using a global-local method. Research by Zhang [140] proved that a shell-based model for a very similar full-scale structural panel provides good elastic correlation with experimental testing, but does not provide the extent of damage that a fracture based material modelling approach provides.

Virtual strain gauges have been used with some success in low velocity impact of fibre hybrid panels for comparison to experimental testing. The following correlation between the experimental and numerical gauges upon a standard plate impact specimen were reasonably accurate, but exhibited a clear delay in signal transmission due to the 'inherent stiffness of finite element formulation' [6], Figure 2.17.

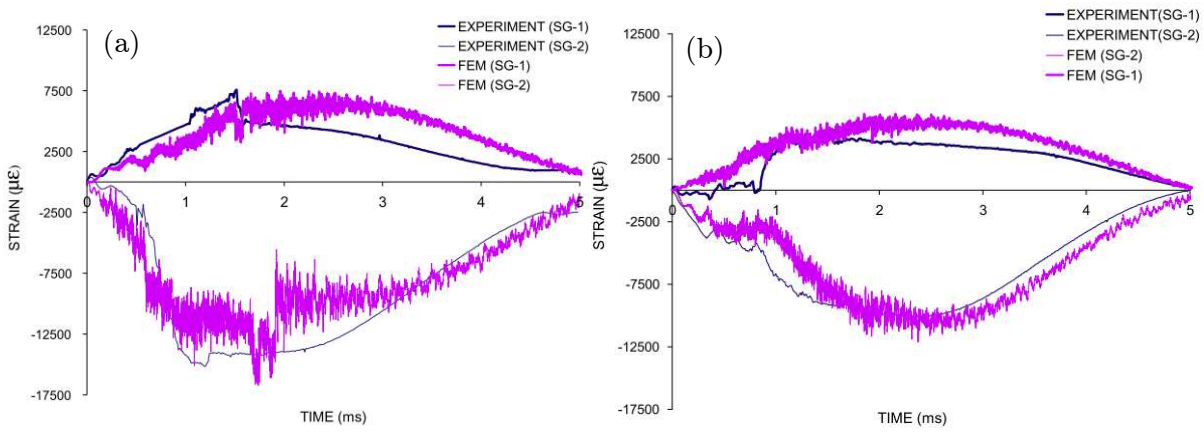


Figure 2.17: Comparison of dynamic strain for experiment and numerical model for fibre hybrid plate impact: (a) glass-carbon-glass layup, (b) carbon-glass-carbon layup [6]

Another example of strain gauge to virtual strain gauge comparison was presented by SAE (Society for Automotive Engineers) [141], although not for a fibre hybrid composite. Their research presented reasonable correlation between experimental testing and a numerical model of a 'hood slam test', where a car bonnet was slammed shut and virtual gauges compared reasonably well to their experimental counterparts at a region close to a high stress location. The numerical solution underwent resonance throughout the event, probably due to underdamping of the material model. Therefore, the maximum strain presented at 'Point B' is likely to be higher than the correct strain that a sufficiently damped model would exhibit, Figure 2.18.

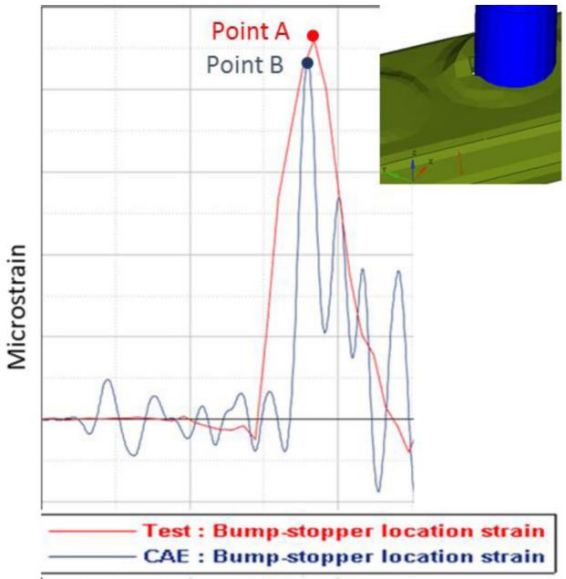


Figure 2.18: Strain comparison for hood slam test [141]

2.2. Gaps in the literature and research plan

2.2.1. Characterising fibre hybrid composite material properties

It was apparent that there was little if any data available regarding the hybridisation of Vectran with carbon fibres in the literature, although the Formula One racing industry widely utilise other aramid-based fibres such as Zylon, Kevlar, Nomex, Spectra, and Dyneema in their debris impact absorbing fibre hybrid composite structures [142], [143]. The use of thin ply carbon and glass within fibre hybrid composites have been studied [144], [145], but not within the specific architecture of spread tow T700 carbon with non-crimp S2-glass, and within an MTM57 epoxy matrix. By testing these materials, through both standard and non-standardised test regimes, the material properties alone would present novelty in the field. Furthermore, fractographic analysis of the failed specimens would provide insight into the complex failure modes associated with fibre hybrid composites.

Although the use of doublers is common within the literature for materials exhibiting poor in-plane compressive properties, data is sparse regarding the interlaminar fracture toughness in Mode I or Mode II between interlayer or intralayer fibre hybrid composites within a common matrix system and without the presence of carbon nanotubes. Because of this, the use of such a test regime would provide a novel application of traditional Mode I and Mode II fracture toughness testing for the fibre hybrid composite systems in this research. By characterising the monolithic constituent composite properties as well as the fibre hybrid composites, further insight into the interlaminar fracture associated with the fibre hybrid constituents and their fibre architectures can be made.

2.2.2. Translaminar fracture toughness of fibre hybrid composites

The use of anti-buckling guides in translaminar testing were discussed and there were few solutions in the literature to reduce the unwanted buckling of composites when utilising typical CT specimen geometries such as those specified in ASTM E399 [91]. Some solutions not involving anti-buckling guides were suggested however, such as increasing the specimen thickness or introducing tapered corners to the specimen geometry, as proposed in the parametric geometrical CT study by Blanco et al. [93]. Since aramid-based fibres are to be utilised in this research (as directed by the funding body due to their high energy absorption

properties) and exhibit low compressive strengths [143], a novel Compact Tension specimen geometry will be developed, negating the need for over-thick specimens (which in turn affect the measured toughness values [88]), or anti-buckling guides [101] (where the out-of-plane stress fields' effect upon the resulting toughness value is difficult to quantify).

2.2.3. Low velocity impact of fibre hybrid composites

There has been experimental research into the effects that the dispersion of two types of fibres have upon the low velocity impact resistance of interlayer fibre hybrid composites, as previously discussed. Currently, no research has been conducted into incorporating monolithic fibre composite properties (including their translaminar fracture toughnesses) into an interlayer fibre hybrid ply-by-ply numerical model under low velocity impact. This has been partly due to the scarcity of both in-plane, translaminar, and interlaminar data for the monolithic constituents of interlayer fibre hybrid systems. Swolfs et al. [101] highlighted the importance of translaminar fracture toughness in the penetration of fibre hybrid composite impact, stating that there are 'large synergetic effects of up to 40% compared to the linear rule-of-mixtures', meaning that the a stress-based formulation may be inadequate in capturing the associated hybrid effect.

There has been no research into utilising the translaminar fracture toughness of intralayer fibre hybrid composites within low velocity impact modelling. Although this approach would incorporate homogenisation of the material across the in-plane properties, it presents advantages such as scalability to full scale industrial components where numerical models would typically contain millions of elements. Without modelling each fibre ply individually, the modelling time and cost can be reduced for full scale components, highlighted by Bogenfeld et al. [109].

The rate dependence (due to material viscoelasticity, see [146]) associated with GFRP (Glass Fibre Reinforced Polymer) composites is available within the literature [147]. The loading rate can be seen to affect the moduli and strength of composites and capturing this phenomenon can lend to accurate numerical modelling. There is only one set of data available for the in-plane shear response of an S2-glass epoxy system however. Tsai and Sun published

this data [148] and similar data was not found elsewhere, highlighted by Singh's 2018 literature review on strain rate effects [149]. In composites (particularly GFRP), the loading rate has an effect upon the impact performance and thus will be taken into account when numerically modelling low velocity impact.

2.2.4. Component reduced scale impact modelling of fibre hybrid composite structures

The research into fibre hybrid composites for structural component low velocity impact testing has been discussed, where the few relevant literature studies have been identified. Therefore, any component scale impact testing conducted will be highly novel, particularly when comparing to an energy-based bilinear plane stress numerical modelling approach which has not been presented in the literature previously. This type of material modelling, which provides extent of damage as well as damage onset, has not yet been utilised with fibre hybrid composite laminates, nor on structural components manufactured from fibre hybrid composites. Endeavouring to do so will provide insight into the feasibility of such modelling techniques for fibre hybrid composite structures, and therefore their suitability for use in automotive structure design, where numerical modelling is heavily relied upon [24].

3. Characterisation of fibre hybrid composites and their monolithic composite counterparts

3.1. Introduction

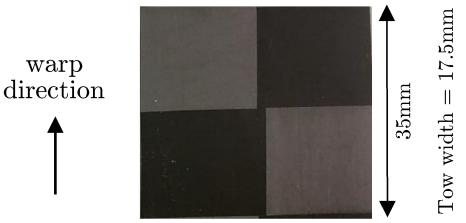
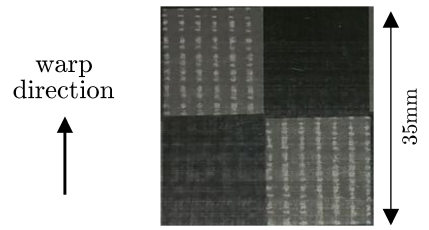
To accurately numerically model fibre hybrid composites, the constituent materials must first be fully characterised. It was therefore necessary for an array of both standard and non-standard tests be performed, where the monolithic and hybrid composite properties could be determined. Table 3.1 summarises the tests used to quantify the material data, and any relevant information about the processes used where test standards were not utilised. All tests in this Chapter were carried out at room temperature using a quasi-static (where any rate effects can be applied post-test for scaling to higher rate numerical modelling), mechanically screw-drive actuated Instron 5969 test machine, fitted with a calibrated 50kN load cell.

Table 3.1: Base level tests performed on fibre hybrid composites and constituents

Mode	Test standard	Reasoning
Tension	BS ISO 527-4: 1997 [150] BS ISO 527-2: 2012 [151] (resin only)	Well established test method, used extensively throughout the literature
Compression	Haeberle and Matthews test rig [152] and BS ISO 604: 2003 [153] for monolithic resin	Test fixture developed at Imperial College London, similar to BS ISO 14126:1999 [154]
In-plane shear	BS ISO 14129:1998 [155]	Long-standing test method, standardised throughout literature studies
Interlaminar fractrure toughness: Mode I	ASTM D5528: 2014 [156]	'Double-cantilever beam' method, cited and well established in the literature
Interlaminar fracture toughness: Mode II	Non-standard: 4-End Notched Flexure 'Martin and Davidson method' [157]	Experimental data reduction technique taking into account beam bending theory
Volume fraction	Non-standard: 'McDonough et al. thermal gravimetric analysis method' [48] + analytical microscopy	ASTM Journal paper [48], not yet a standard available for fibre hybrid volume fraction measurement
Density	AccuPyc II 1340 Pycnometer [158] + standard test-lab weighing scales	Accurate measurement of volumes through nitrogen purge cycling

In total three discrete monolithic composites were investigated, along with one interlayer fibre hybrid and one intralayer fibre hybrid composite (see Figure 2.4). The materials tested are listed and their respective cured images of their tow architectures are shown in Table 3.2.

Table 3.2: Materials tested

Material description	**Image**
Monolithic S2-glass non-crimp composite (0°/90°) (312gsm fibre blanket density) Fibre supplier: Sigmatex [7] MTM57 resin supplier: Solvay [8]	
Monolithic T700 carbon spread tow 12K plain weave composite (0°/90°) (88gsm fibre blanket density) Fibre supplier: Sigmatex [7] MTM57 resin supplier: Solvay [8]	
Monolithic Vectran non-crimp composite (0°/90°) (212gsm fibre blanket density) Fibre supplier: Sigmatex [7] MTM57 resin supplier: Solvay [8]	
Interlayer fibre hybrid: T700 carbon spread tow 12K plain weave (0°/90°)/S2-glass non-crimp (0°/90°), alternate carbon (C) and glass (G) ply blocks of [C-G-C-G-C-G-C] = 1mm thick (ie, 2mm thick mirrors this block for symmetry) Fibre supplier: Sigmatex [7] MTM57 resin supplier: Solvay [8]	
Intralayer fibre hybrid 2x2 twill weave: 50% T700 carbon/ 50% Vectran (520gsm fibre blanket density) Fibre supplier: Sigmatex [7] MTM57 resin supplier: Solvay [8]	

All the composites were manufactured using RFI with MTM57 resin film, vacuum bagged at a ramp rate of 100°C/hour to 125°C, dwelled for 1 hour before a non-controlled cool down to room temperature, as specified by the manufacturer (Solvay) [159]. A fibre volume fraction for each material was nominally 0.55, although the true fibre volume fractions were determined through both TGA and analytical microscopy (Section 3.1.4). All tests were conducted with five specimens to provide reasonable statistical scatter within the results.

For all layup sequences displayed, 0° relates to the warp direction for the woven fabrics and 0° for the non-crimp fabrics. Due to cost and time constraints within the Datacomp project [160], the materials were all tested solely in the warp (0°) direction. This was considered acceptable since previous studies regarding non-crimp carbon fabrics showed that the influence of loading direction (ie warp or weft) had little effect on the resulting mechanical properties, with low scatter between the two directions (within the normal scatter of the test specimens) [161]. Furthermore, although the tow width for the carbon spread tow composites was large with respect to the specimen dimensions (namely in the compression and tension specimen dimensions), the surface ply location was not noticed to affect the mechanical properties, with low levels of scatter noticed throughout the test regimes. It should be noted that the unit cell locations of the laminates were not controlled.

3.1.1. Tension testing

Tensile characterisation utilised the BS ISO 527-4: 1997 [150] test standard where end-tabbed specimens of nominal dimensions 25mm x 2mm x 250mm were loaded axially in tension at a stroke of 2mm/min. To determine the Poisson's ratio, an Imetrum optical gauge measurement system was used to capture the axial and transverse strains one side of the specimen's surface using two points 40mm axially and two points 14mm transverse to the loading direction. The interlayer T700 carbon/S2-glass specimens utilised strain gauging due to lack of equipment at the time of testing. The BS ISO 527-2: 2012 [151] test standard was used for the monolithic MTM57 resin tensile testing. Figure 3.1 shows this data in terms of representative stress versus strain curves for each material, and Table 3.3 summarises the resulting material properties. Figure 3.2 displays the representative failed specimens post-test. Any numerical

modelling would idealise that the stress versus strain curves are linear to failure, regardless of the experimental load responses. The non-linearity of the tensile responses are due to matrix crazing during damage onset, hence reducing the recorded moduli in the S2-glass, interlayer fibre hybrid, and monolithic MTM57 resin.

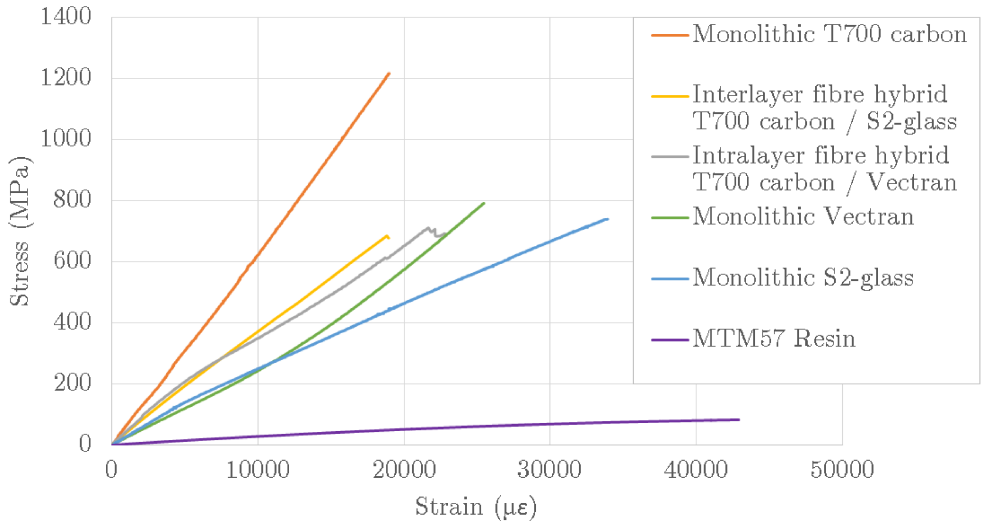
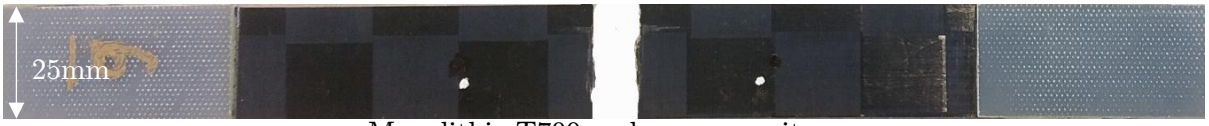


Figure 3.1: Representative composite tension test results, stress versus strain results

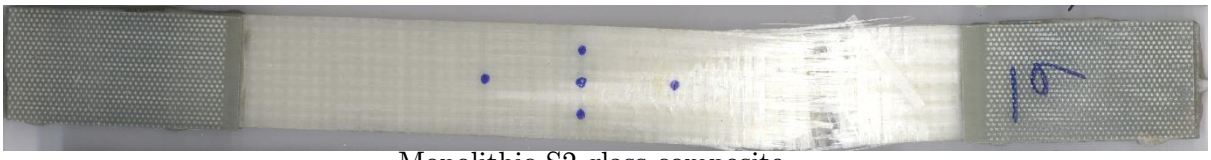
Table 3.3: Tension material properties

Material	**Young's modulus (GPa) (CV%)**	**Tensile strength (MPa) (CV%)**	**Poisson's ratio, ν_{12} (CV%)**
Monolithic S2-glass composite	22.00 (5.51)	719.77 (3.37)	0.085 (-)
Monolithic T700 carbon composite	65.11 (2.26)	1183.27 (2.75)	0.035 (43.93)
Monolithic Vectran* composite	24.23 (2.67)	778.49 (4.33)	-
Interlayer fibre hybrid T700 carbon/S2-glass	40.56 (5.01)	661.78 (6.62)	0.049 (6.97)
Intralayer fibre hybrid T700 carbon/Vectran	29.68 (12.40)	671.83 (7.38)	0.27 (21.36)
MTM57 Resin	2.68 (1.01)	80.07 (5.80)	-

*monolithic Vectran composite data courtesy of S. Abdullah, Imperial College London [162] using BS ISO 527-4:1997 [150]



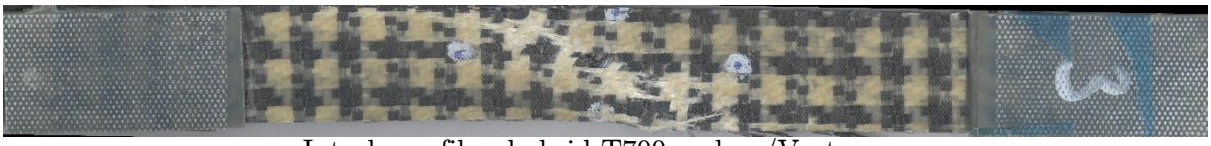
Monolithic T700 carbon composite



Monolithic S2-glass composite



Interlayer fibre hybrid T700 carbon/S2-glass



Intralayer fibre hybrid T700 carbon/Vectran

Figure 3.2: Representative failure modes for tension tests

The monolithic carbon composite failed in a brittle and highly localised manner whereas the monolithic S2-glass composite and the intralayer fibre hybrid T700 carbon/Vectran specimens failed less locally, across a larger gauge region. The monolithic S2-glass composite presented signs of matrix crazing around the fracture site prior to fibre fracture, evident from the failed specimen.

3.1.2. Compression testing

Compressive composite material characterisation utilised a non-standard test rig, developed at Imperial College London [152]. End-tabbed specimens of nominal dimensions 10mm x 4mm x 90mm were end and shear-loaded axially in compression at a stroke of 1mm/min. Two strain gauges were placed either side of the gauge area to determine the overall strain, and whether premature bending occurred (>10% difference between the two gauges). The BS ISO 604: 2003 [153] test standard was used for the monolithic MTM57 resin compressive strength, considering the resin as a plastic rather than a fibre-reinforced composite, thus failing in a more ductile manner than a fibre reinforced composite. Figure 3.3 presents this data in terms of representative stress versus strain curves for each material, whilst Table 3.4 summarises the

resulting material properties. It should be noted that the compressive properties of the interlayer fibre hybrid T700 carbon/S2-glass were not characterised because such test specimens were all seen to fail outside of the gauge region and presented a discrepancy between the two strain gauges above the 10% threshold, indicative of premature bending. Due to this, the homogenised compressive strength for that material was calculated through a rule of mixtures (Section 3.2) for the homogenised material modelling in Chapter 6.

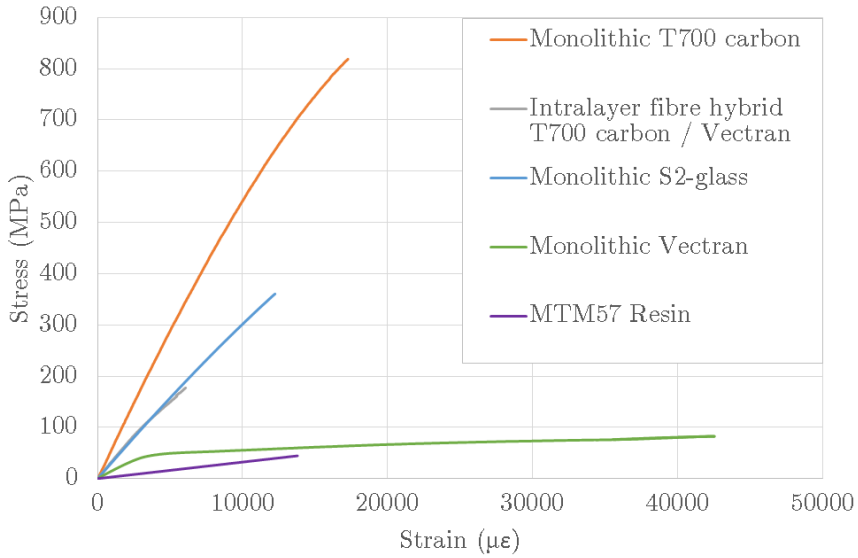


Figure 3.3: Representative composite compression, stress versus strain results

Table 3.4: Compression material properties

Material	Young's modulus (GPa) (CV%)	Compressive strength (MPa) (CV%)
Monolithic S2-glass composite	32.97 (2.34)	371.81 (6.22)
Monolithic T700 carbon composite	55.71 (11.74)	761.98 (12.60)
Monolithic Vectran* composite	13.92 (2.45)	82.82 (5.34)
Intralayer fibre hybrid: T700 carbon/Vectran	29.97 (8.18)	165.78 (6.88)
MTM57 Resin	3.08 (1.65)	116.08 (1.16)

*monolithic Vectran composite data courtesy of S. Abdullah, Imperial College London [162] using the Imperial College test rig [152]

Figure 3.4 presents the representative failure modes associated with the compression specimens. It can be seen that mid-plane delamination dominated the compression failure within the monolithic T700 carbon composite specimen and brooming was noticed in the intralayer fibre hybrid T700 carbon/Vectran specimens. The monolithic S2-glass composite

showed through-thickness shear at approximately 45°, indicative of an acceptable failure mode [154].

The compression moduli are seen to vary to the tensile moduli. For the monolithic Vectran composite this reduction in compressive modulus can be attributed to the fibrillous nature of the fibres, promoting micro-buckling. The monolithic carbon composite compression modulus is lower than its tensile modulus due to the crimp in the spread tow weave (promoting fibre kinking). The tensile modulus of the monolithic S2-glass composite was perceived to be lower than its compressive modulus due to matrix crazing during the onset of loading, hence reducing the modulus was calculated within the (latter) linear portion of the tensile loading (1000-3000με).

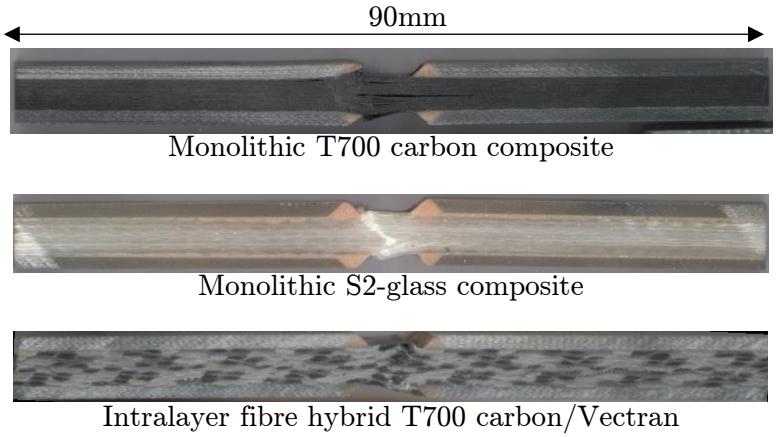


Figure 3.4: Representative failure modes for compression tests

3.1.3. In-plane shear testing

In-plane shear composite characterisation utilised the BS ISO 14129:1998 [155] test standard, where end-tabbed specimens laid-up at ±45° fibre orientations of nominal dimensions 25mm x 2mm x 250mm were loaded axially in tension at a stroke of 2mm/min. An Imetrum optical measurement system was used to capture the axial and transverse strains one side of the specimen's surface, which was required to calculate the shear strain within the gauge region of the specimen. The shear response of axially loaded ±45° fibre orientations was largely non-linear beyond the initial modulus and therefore the full in-plane shear response curves were required to accurately numerically model low velocity impact testing (as recommended by [21],

[112]), as opposed to a single modulus and chord or strain offset strength (as suggested within the test standard [155]). The function utilised within the Abaqus VUMAT subroutine [163] (Chapters 5 and 6) to populate this non-linear behaviour utilised the following formula to generate a best curve fit for the test data (see Section 5.3.1 for further details). The instantaneous strain γ is applied to this function at every time step to govern the resulting in-plane modulus G_{12}.

$$G_{12} = maximum\begin{Bmatrix} G_{ult} \\ G_{12init}e^{-\lambda(\gamma-\gamma_0)} - \lambda(\gamma-\gamma_0)G_{12init}e^{-\lambda(\gamma-\gamma_0)} \end{Bmatrix} \quad (3.1)$$

where γ is the shear strain, λ is a fitting constant, G_{12init} is the initial (linear) modulus, G_{ult} is the final (linear) modulus, S_{C0} is stress at which the response transitions from linear to non-linear, and $\gamma_0 = G_{12init}/S_{C0}$ is the strain at the linear-to-non-linear transition.

Figures 3.5 to Figure 3.8 present the experimental stress versus strain data plotted alongside the FE curve fits (fit parametrically) used in the numerical modelling, and Table 3.5 summarises the in-plane shear properties along with the parameters used for numerical modelling. From the stress versus strain graphs, the majority of FE curve fits, and hence properties, can be seen to fit within the scatter of the experimental test data. It should be noted that due to logistical restraints strain gauges were used for the interlayer fibre hybrid T700 carbon/S2-glass specimens and thus the entire response was not recorded due to premature strain gauge failure. Scissoring was noticed in the failed specimens (Figure 3.9) and as the fibres aligned axially in the loading direction, the test deviated from a pure in-plane shear response. This phenomenon was accounted for however, since the numerical modelling in Chapters 5 and 6 utilised the entire curve fit.

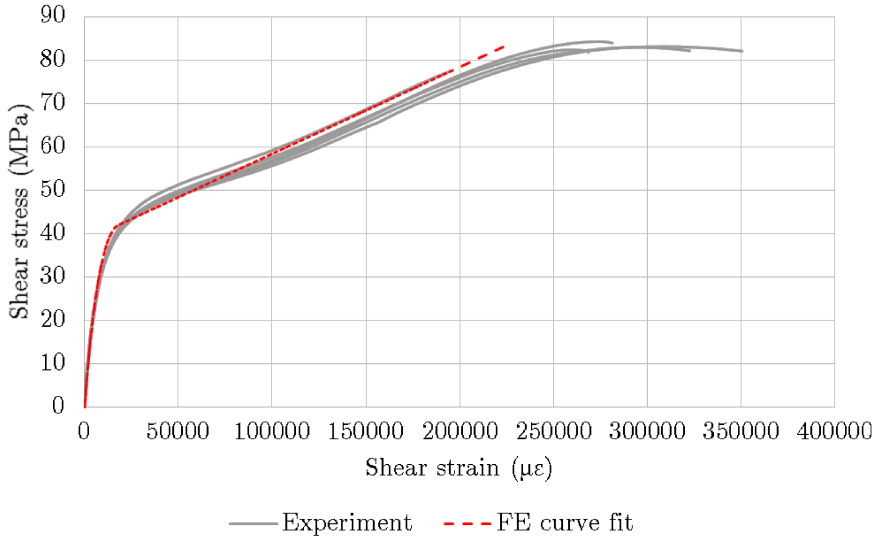


Figure 3.5: In-plane shear response of monolithic S2-glass composite

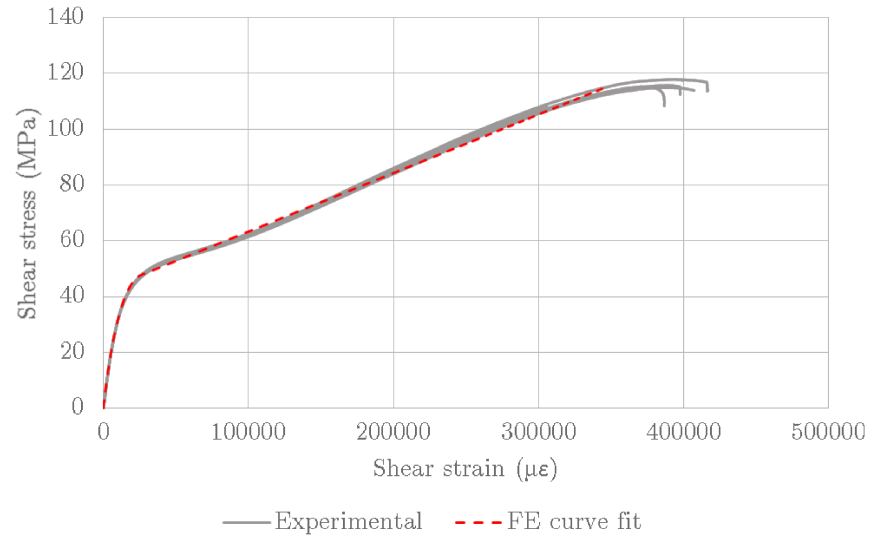


Figure 3.6: In-plane shear response of monolithic T700 carbon composite

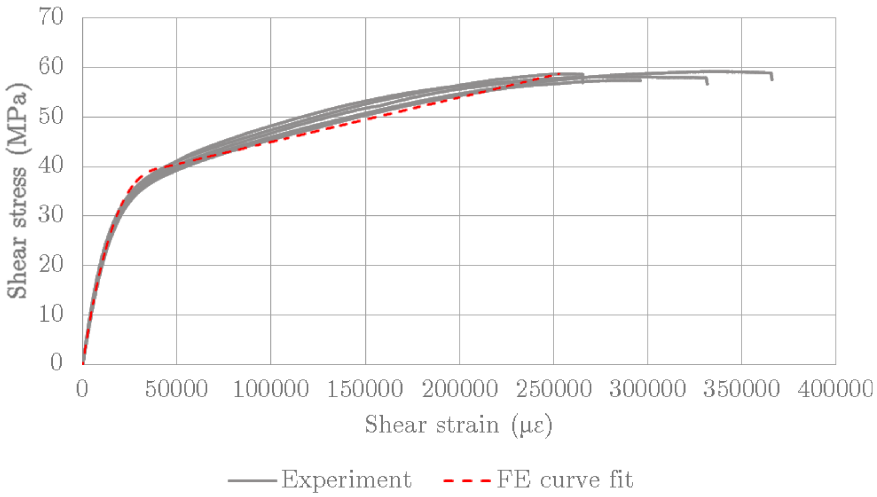


Figure 3.7: In-plane shear response of intralayer fibre hybrid T700 carbon/Vectran

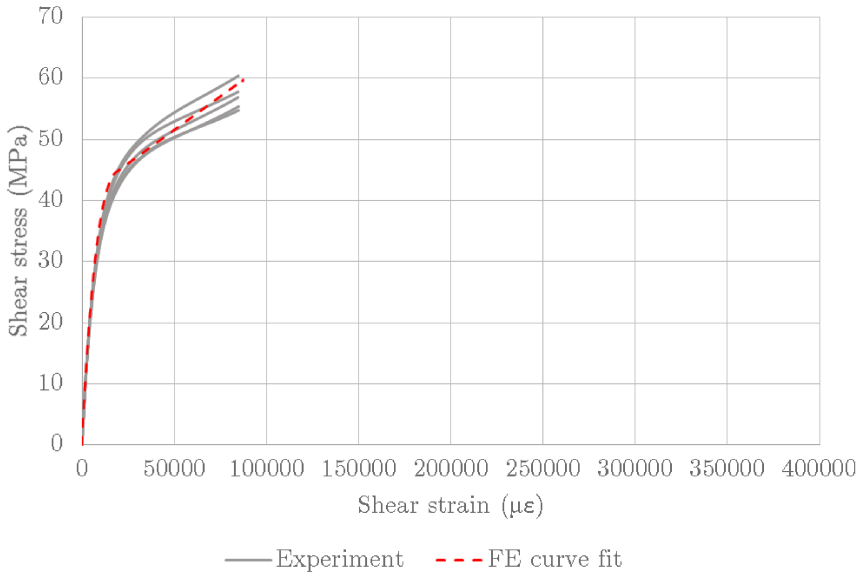
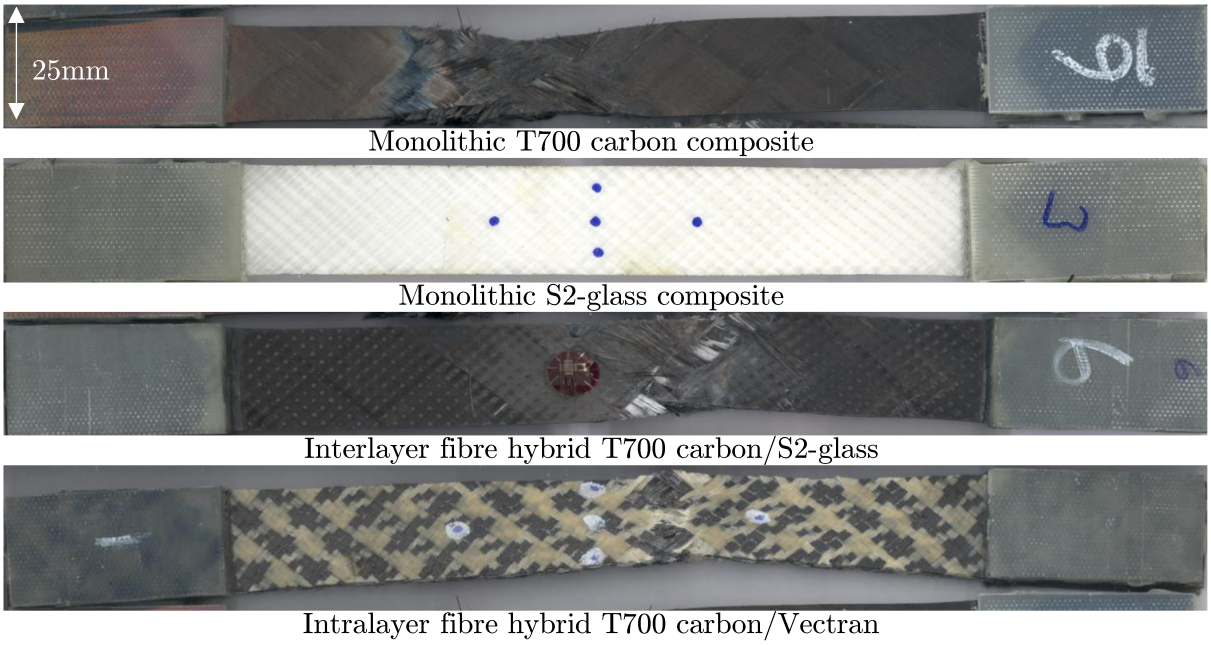


Figure 3.8: In-plane shear response of interlayer fibre hybrid T700 carbon/S2-glass

Table 3.5: Nominal in-plane shear properties as fitting parameters for numerical modelling

Material	**G_{12init} (GPa)**	**G_{12ult} (GPa)**	**S_C (MPa)**	**S_{C0} (MPa)**	**λ**
Monolithic S2-glass composite	5.68	0.20	83.66	2.67	51.0
Monolithic T700 carbon composite	4.25	0.21	114.41	0.74	33.5
Intralayer fibre hybrid: T700 carbon/Vectran	2.47	0.09	57.74	1.77	24.0
Interlayer fibre hybrid: T700 carbon/S2-glass	5.57	0.22	84.56	4.00	50.0



Monolithic T700 carbon composite

Monolithic S2-glass composite

Interlayer fibre hybrid T700 carbon/S2-glass

Intralayer fibre hybrid T700 carbon/Vectran

Figure 3.9: Representative failure modes for in-plane shear tests

The monolithic T700 carbon and intralayer fibre hybrid T700 carbon/Vectran specimens showed signs of significant scissoring prior to ultimate fibre fracture. Similar to the tensile testing, the monolithic S2-glass specimen presented matrix crazing throughout the gauge region prior to ultimate failure with little scissoring. The interlayer fibre hybrid presented less scissoring than the monolithic T700 carbon specimen due to the presence of the S2-glass fibres, and the S2-glass fibres remained intact after the fracture of the T700 carbon fibres.

3.1.4. Volume fraction measurement

To characterise the composites regarding their constituent fractions, a TGA (Thermogravimetric Analysis) burn-off method as well as an analytical microscopic approach was undertaken. Since the degradation temperatures (Table 3.6) vary between the MTM57 resin, T700 carbon fibre, S2-glass fibre, and Vectran fibres it was possible to burn off each of the constituents individually to obtain their weight fraction (and therefore volume fractions) without affecting the other constituents. The TGA method heated each composite sample and recorded the sample weight during constant ramp rates to elevated temperatures. This was then used to calculate the composite's volume fraction for each of their constituents, where individual densities for the constituents had been previously determined. The AccuPyc II 1340 pycnometer was used to measure the bare fibre densities as well as the resin only density, for the weight to volume fraction calculation as follows, following a similar approach to that published in reference [48]:

For carbon/Vectran hybrid:	For carbon/glass hybrid:
$W_0 = W_r + W_c + W_v$	$W_0 = W_r + W_c + W_g$
$W_{T1} = W_c + W_v$	$W_{T1} = W_c + W_g$
$W_{T2} = W_c$	$W_{T2} = W_g$

$$v_x = {W_x}/{(\rho_x V_x)} \tag{3.2}$$

where W_0 is the dry mass of the sample, W_r is the mass of the resin, W_c is the mass of the carbon fibres, W_v is the mass of the Vectran fibres, W_g is the mass of the glass fibres, W_{T1} is the mass of the sample after the first temperature exposure, W_{T2} is the mass of the sample

after the second temperature exposure, v_x is the volume fraction of 'x' constituent, and ρ_x is the density of the 'x' constituent.

The burn-off tests were carried out within a nitrogen environment to alleviate any unwanted oxidisation leading to unstable burn-off. Repeatable volume fractions for each material were calculated using this approach and supported using analytical microscopy. The following Figures (Figure 3.10 to Figure 3.13) present the weight percentage fractions of each material during the TGA analyses. Table 3.6 presents the volume fraction results for each of the materials tested from the TGA, as well as the measured densities from the Pycnometer recordings. The weight percentage was considered to have plateaued once a rate change of -0.1%/min was reached. It should be noted that one of the intralayer fibre hybrid T700 carbon/Vectran burn-off tests was shortened in time and therefore presents the variation to the other specimens, noticed in Figure 3.13.

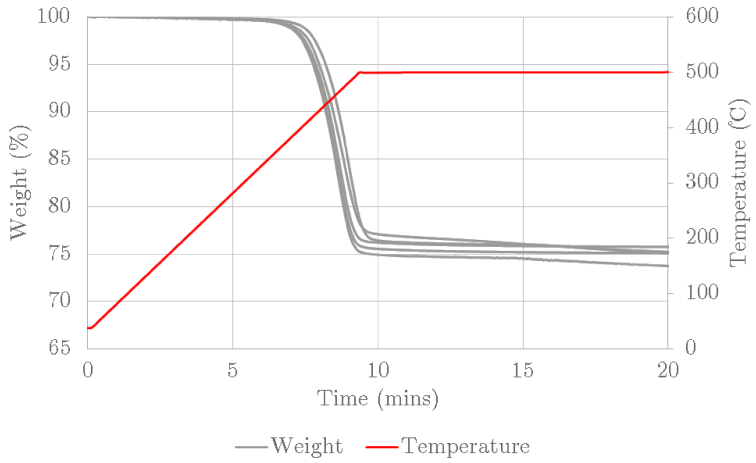


Figure 3.10: Monolithic S2-glass composite thermogravimetric burn-off, weight %

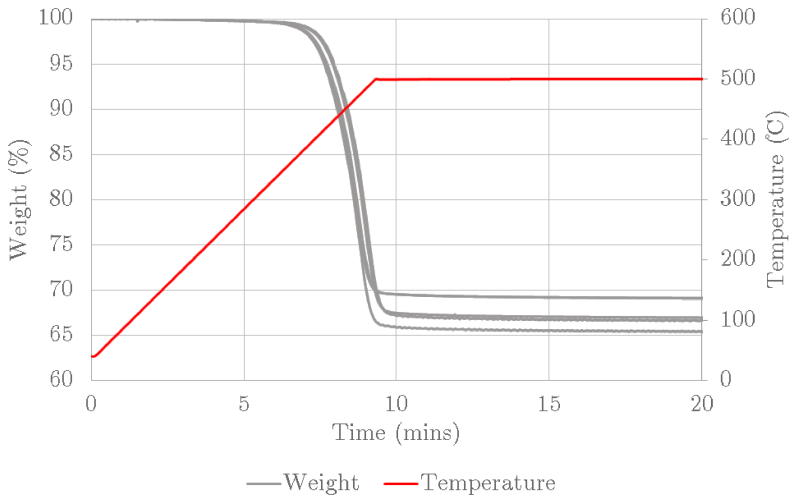


Figure 3.11: Monolithic T700 carbon composite thermogravimetric burn-off, weight %

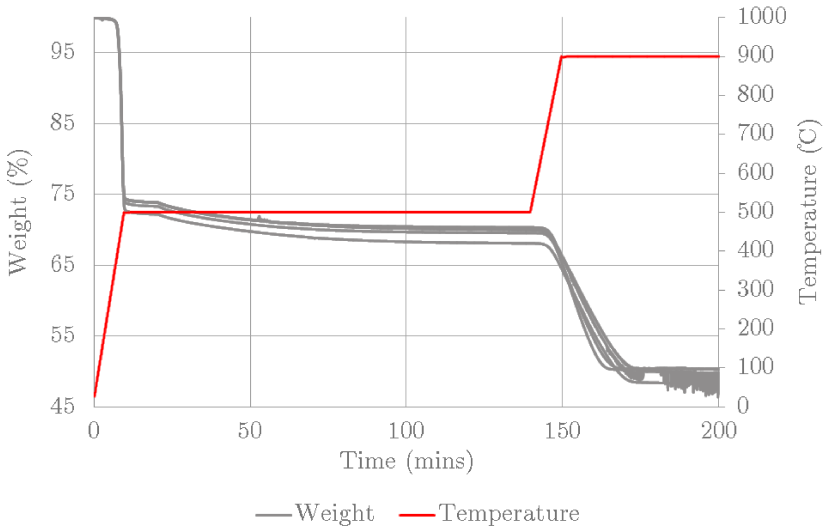


Figure 3.12: Interlayer fibre hybrid T700 carbon/S2-glass burn-off, weight %

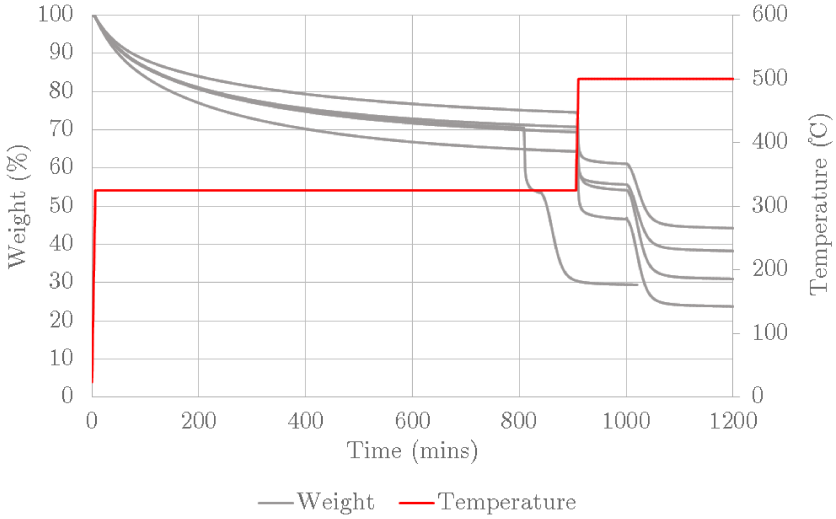


Figure 3.13: Intralayer fibre hybrid T700 carbon/Vectran burn-off, weight %

Table 3.6: Thermogravimetric analysis results, volume fractions and density

Material	**Degradation temperature (°C)**	**$v_{g/v}$ (CV%)**	**v_c (CV%)**	**v_r (CV%)**	**ρ, kg/m³ (CV %)**
Monolithic S2-glass composite	1056 Ref: [164]	0.559 (1.47)	-	0.441 (1.87)	1904.6 (0.84)
Monolithic T700 carbon composite	900 Ref: [48]	-	0.532 (3.65)	0.468 (4.15)	1532.9 (0.14)
MTM57 resin	300 Ref: [159]	-	-	-	1202.8 (0.05)
Interlayer fibre hybrid: T700 carbon/S2-glass	-	0.365 (2.22)	0.194 (2.34)	0.441 (2.32)	1772.2 (0.34)
Intralayer fibre hybrid: T700 carbon/Vectran	- (Vectran: ~450 Ref: [165])	0.343 (23.33)	0.297 (15.94)	0.360 (12.24)	1574.9 (4.78)
		Total v_f: 0.640 (6.87)			

It can be seen that the scatter associated with the intralayer fibre hybrid T700 carbon/Vectran was considerably higher than that of the other materials. This was attributed to the sample size required by the TGA being small (˜4mm x 4mm x 4mm) compared to its unit cell (approximately 10mm x 10mm, in-plane, see Table 3.2). Therefore the TGA presented large variations in the volume fractions due to the smaller specimen sizes for the intralayer fibre hybrid T700 carbon/Vectran.

To further determine a more accurate evaluation of the fibre volume fraction for the intralayer fibre hybrid T700 carbon/Vectran and the interlayer fibre hybrid T700 carbon/S2-glass, image processing software Fiji/ImageJ (ver. 1.51h) [166] was used to analyse microscopic images of the fibre hybrid cross sections. The cured specimens were potted and then cut to through-thickness cross sections. The resulting specimens were then polished so that the contrast differences between the fibre types could be identified. An automatic zoom Zeiss camera was then used to capture the polished through-thickness cross section of the fibre hybrid composites.

Firstly, as shown in Figure 3.14, the microscopic images were imported into the image processing software and converted into an 8-bit binary format. The image was then passed through a threshold analysis to numerically identify between the pixels associated with the carbon fibres types due to their lighter hue. The threshold was set in such a way as to incorporate the resin equally into the non-identified fibre category so that only the carbon fibres were highlighted. From this, the carbon fibres were set to a black format (binary: 1) and the other composite constituents were set to white (binary: 0).

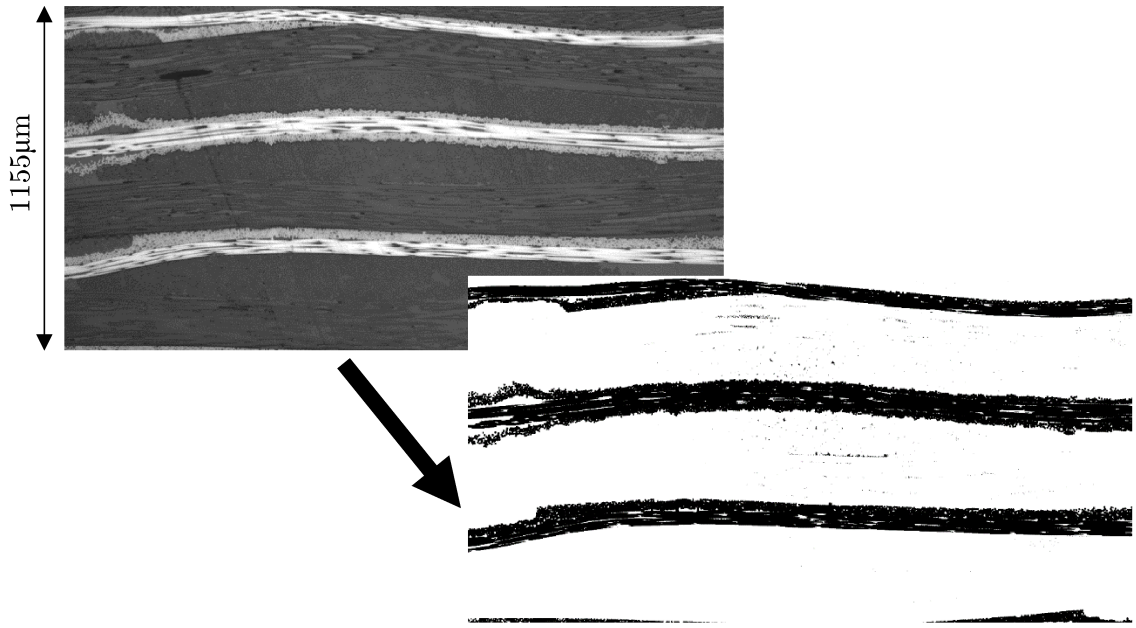


Figure 3.14: Microscopic through-thickness unit cell of interlayer fibre hybrid T700 carbon/S2-glass, Fiji/ImageJ binary threshold processing carbon fibres

Figure 3.14 shows this conversion from raw microscopic image into the binary threshold for the interlayer fibre hybrid T700 carbon/S2-glass and the same for the intralayer fibre hybrid T700 carbon/Vectran (Figure 3.15), where the carbon fibres were set to black in both cases. The pixels were then counted according to their binary identifier and an area percentage was determined. Both fibre hybrid systems exhibited fibre waviness in these cross-sectional micrographs likely leading to low compressive strengths [97]. The interlayer fibre hybrid showed less waviness than the intralayer fibre hybrid, due to the carbon spread tow plain weave architecture exhibiting less crimp than the 2x2 twill intrawoven carbon and Vectran fibres.

Assuming that the scatter associated with the unit cell was adequately captured through the presence of multiple randomly oriented plies across a large enough cross-section, the analytical microscopy gave carbon fibre volume fractions (v_c) of 0.20 (theoretically 0.27 [7]) for the interlayer fibre hybrid T700 carbon/S2-glass and 0.43 (theoretically 0.50 [7]) for the intralayer fibre hybrid T700 carbon/Vectran. The interlayer fibre hybrid T700 carbon/S2-glass showed close correlation to the TGA analysis. The intralayer fibre hybrid T700 carbon/Vectran presented a closer to anticipated 50% carbon to Vectran ratio, since the material blanket was a 2x2 twill weave of theoretically equal tow volumes [7].

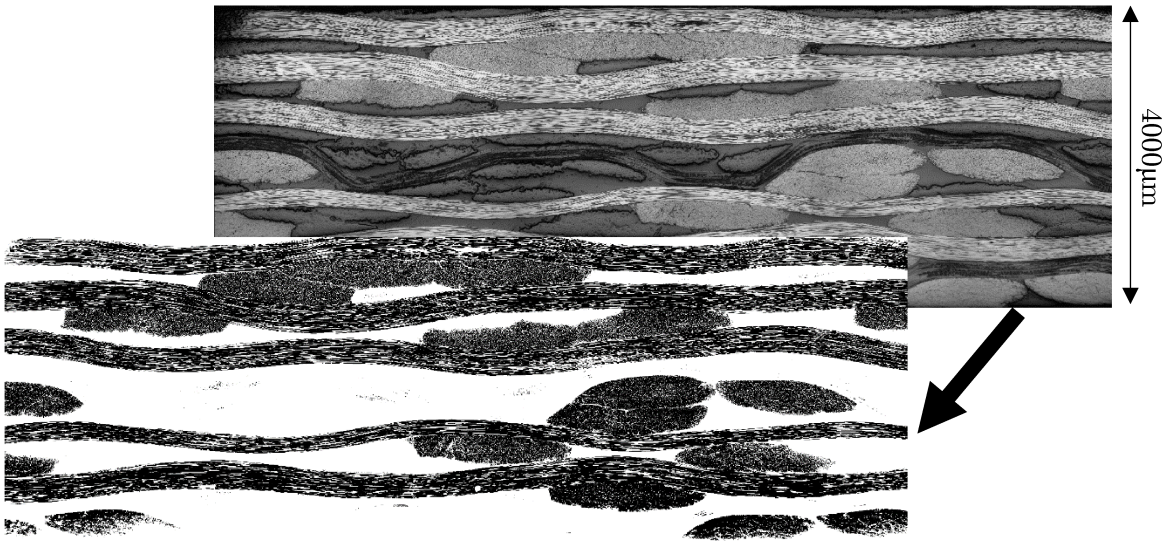


Figure 3.15: Microscopic through-thickness unit cell of intralayer fibre hybrid T700 carbon/Vectran, Fiji/ImageJ binary threshold processing carbon fibres

3.2. Using the rule of mixtures to estimate the tensile material properties of fibre hybrid composites

Utilising the analytical linear rule of mixtures approach proposed by Summerscales [57] for the elastic modulus and strength, as well as the bilinear rule of mixtures from other researchers [64] (Section 2.1.2), the tensile strength and modulus of the fibre hybrid composites could be estimated from the monolithic composite constituents and the volume fractions measured from the TGA burn off testing (Table 3.6). Table 3.7 shows these experimental and theoretical values for the interlayer fibre hybrid T700 carbon/S2-glass and intralayer fibre hybrid T700 carbon/Vectran tensile properties. Since the individual (dry, without a surrounding matrix) fibre properties were not known, the composite properties were used for the calculations of the theoretical modulus and strength.

Table 3.7: Experimental versus theoretical tensile properties for the interlayer and intralayer fibre hybrids

	Interlayer fibre hybrid T700 carbon/S2-glass		**Intralayer fibre hybrid T700 carbon/Vectran**	
	Experimental	**Theoretical**	**Experimental**	**Theoretical**
Tensile modulus (GPa) (CV%)	40.56 (5.01)	36.96	29.68 (12.40)	43.20
Tensile strength (MPa) (CV%)	661.78 (6.62)	Linear: 1044.12 Bilinear: 410.65	671.83 (7.38)	Linear: 956.87 Bilinear: 549.11

The reason for the discrepancies between the experimental and theoretical intralayer fibre hybrid tensile material properties most likely originate from the fibre architecture, namely the high level of crimp within the intralayer fibre hybrid weave, resulting in both low experimental modulus and strength. The interlayer fibre hybrid showed a theoretical modulus close to the lower bound of the experimental modulus. The interlayer fibre hybrid strength however was vastly overestimated when using the linear rule of mixtures and underestimated with the bilinear rule of mixtures. The bilinear rule of mixtures presented lower theoretical strength for both fibre hybrid systems, compared to the experimental data, likely due to the incorrect location of the transition between the critical volume fractions.

Within the intralayer fibre hybrid this could be attributed to the overestimation of the monolithic carbon composite strength, which was taken from the spread tow carbon composite strength, hence idealising its influence on the fibre hybrid due to the lower crimp and higher volume fraction of the spread tow. Therefore, it could be surmised that relying solely upon the theoretical moduli for both interlayer and intralayer fibre hybrids was not feasible for structural (stiffness) component design. The measured fibre hybrid composite properties were therefore utilised in the structural component numerical modelling of the interlayer fibre hybrid composite presented in Chapter 6.

3.3. Interlaminar fracture toughness of fibre hybrid composites

When numerically modelling a composite laminate under impact loading, the interlaminar behaviour between the plies can be characterised and modelled using cohesive elements. Thus, it was important to fully characterise the Mode I and Mode II fracture properties between the

neighbouring plies for both fibre hybrid composites being tested. Mode I interlaminar testing utilised the DCB (Double Cantilever Beam) method, following the ASTM D5528: 2014 [156] test standard, with nominal specimen dimensions 20mm x 170mm x 4mm. Mode II interlaminar testing utilised the non-standard 'Martin and Davidson' [157] approach to a 4-ENF (4-End Notched Flexure) test set-up, with nominal specimen dimensions 20mm x 140mm x 4mm.

The interlayer fibre hybrid T700 carbon/S2-glass layup was $[CGCGCGC]_2[D][GCGCGC][CGCGCGC]$ (where D denotes the delamination plane, C denotes a 0°/90° spread tow plain weave T700 carbon ply, and G denotes a 0°/90° S2-glass NCF ply), resulting in a mid-plane interface between the two fibre types. Due to the relatively low compressive strength of Vectran (Table 3.4), the intralayer fibre hybrid T700 carbon/Vectran DCB and 4-ENF specimens were stiffened and strengthened with T700 carbon spread tow doublers, since this material exhibited the highest compressive modulus and strength. This resulted in a layup of $[C]_{10}[V]_2[C]_{10}$ (where C denotes a 0°/90° spread tow plain weave T700 carbon ply, and V denotes an intrawoven 0°/90° Vectran/T700 carbon fibre hybrid 2x2 twill weave ply). Premature compressive failure occurred due to bending on the outer face of the DCB and 4-ENF test specimens which did not contain doublers. Reeder et al. [78] presented this as a feasible method for improving the effective compressive strength on the outer surface due to bending. The doublers were made from 10 plies of carbon spread tow, providing a nominally cured thickness of 1.3mm for each side. This proved to be adequately thick since local compression on the surface of the specimens and warping of the specimen arms was not noticed post-test.

The delamination plane within the interlayer fibre hybrid T700 carbon/S2-glass interlaminar fracture Mode I and Mode II specimens was considered, since the delamination cannot inherently be mid-thickness when between two plies of differing fibre types. Correction factors presented by Ouyang et al. [85] and Ouyang and Li [86] for Mode I and Mode II respectively take into account this difference when characterising composite to metallic interfacial properties, which have relatively different flexural rigidities. The difference in compliance between the two arms of the interlayer fibre hybrid was assumed to be zero, since a single T700 carbon spread tow ply was negligibly thin at 95μm cured in comparison to the total

cured laminate thickness of 4mm. Using classical laminate theory for one of the DCB arms, the offset of a carbon ply at the mid-plane (i.e. $[CGCGCGC]_2$) resulted in a flexural stiffness of 24.4GPa compared to 23.7GPa without the carbon ply at the mid-plane (i.e. [CGCGCGC][CGCGCG]). Research by Zhang et al. [56] has also reported the redundance of a correction factor when utilising a DCB specimen for the Mode I fracture toughness between a glass and flax fibre hybrid polymer composite.

The *Resistance*-curves (*R*-curves) for the fracture toughness testing were plots of the critical strain energy release rate versus the optically measured crack length. Upon plotting the *R*-curves for both fibre hybrids, the initiation and propagation fracture toughnesses were deduced and compared to the fracture surface for further information on the failure processes. By doing so, fractographic analysis of these interlaminar failure surfaces could be used to better understand the delamination process that occurs during low velocity impact events on the fibre hybrid composites.

3.3.1. Mode I: DCB testing

3.3.1.1. Test set-up

The DCB test was set-up as shown in Figure 3.17, where end blocks were bonded using Araldite 2011 2-part epoxy to the specimen surface, and thus allowed free rotation across the width axis of the specimen. The specimen was pre-cracked at a stroke of 1mm/min to a known crack length and then returned to the origin. The specimen was then loaded in tension at a stroke of 0.5mm/min to allow the sporadic stick-slip behaviour of the crack propagation to be monitored carefully using a travelling microscope, and then correlated to the force versus displacement data captured from the test machine. T700 carbon spread tow doubling was cured at the same time as the intralayer fibre hybrid T700 carbon/Vectran to prohibit compressive failure on the outer face of the arms, as shown in Figure 3.16. No warping was noticed post-test since the carbon doublers dominated the stiffness of each specimen arm.



Figure 3.16: T700 carbon spread tow doublers on a portion of an intralayer fibre hybrid T700 carbon/Vectran DCB specimen

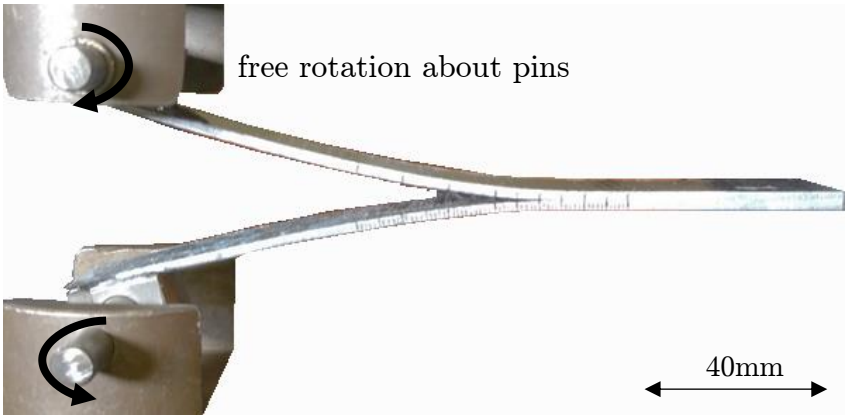


Figure 3.17: Test set-up for the double cantilever beam of interlaminar fibre hybrid T700 carbon/S2-glass

3.3.1.2. Data reduction

The MBT (Modified Beam Theory) method [167] was utilised in calculating the critical strain energy release rate for the Mode I tests. Simple beam theory assumes that the DCB arms are clamped (without rotation at the crack tip), which is unrepresentative of the true loading case. Therefore, the MBT method accounts for the bending within the arms by using a crack length correction (Δ) (typically -4.22mm for the interlayer fibre hybrid T700 carbon/S2-glass, and typically -3.42mm for the intralayer fibre hybrid T700 carbon/Vectran). This takes into account the rotation about the crack tip, leading to the following equation for the critical strain energy release rate [167]:

$$G_{IC} = \frac{3P\delta}{2B(a+\Delta)} \tag{3.3}$$

where P is the applied force, δ is the crack opening displacement, B is the specimen width, a is the crack length, and Δ is the crack length correction (determined as the negative intercept of crack length axis upon plotting the cube root of the machine head compliance versus known crack length [167]). The starter crack was nominally 1mm-2mm prior to the first data point.

Due to the constraints of the numerical model, which requires an initiation and propagation fracture toughness, the results were interpreted as such, hence simplifying a somewhat complex process. The spread tow carbon fibre architecture promoted high levels of scatter and therefore the use of a single propagation toughness values should be treated with caution. The doublers used for the intralayer fibre hybrid T700 carbon/Vectran composite failed prematurely before a meaningful propagation toughness value could be discerned. The propagation toughness

values were calculated as an average of the data points beyond where the *R*-curves tended to plateau. To capture the fibre architecture (and the local architecture dependant toughness) multiple cohesive layers would be required in the numerical model and was not considered due to time constraints.

3.3.1.3. Results

Figure 3.18, Figure 3.19, and Figure 3.20 present the typical load versus displacement, compliance$^{1/3}$ versus crack length, and Mode I interlaminar *R*-curve for the interlayer fibre hybrid T700 carbon/S2-glass respectively. Figure 3.21, Figure 3.22, and Figure 3.23 present the typical load versus displacement, compliance$^{1/3}$ versus crack length, and Mode I interlaminar *R*-curve for the intralayer fibre hybrid T700 carbon/Vectran respectively. Table 3.8 shows the initiation and propagation values taken from these *R*-curves.

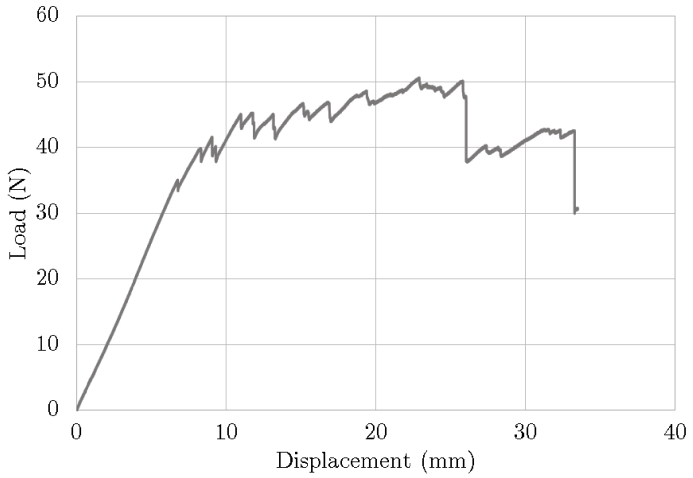


Figure 3.18: Typical load versus displacement plot for the interlayer fibre hybrid T700 carbon/S2-glass DCB tests

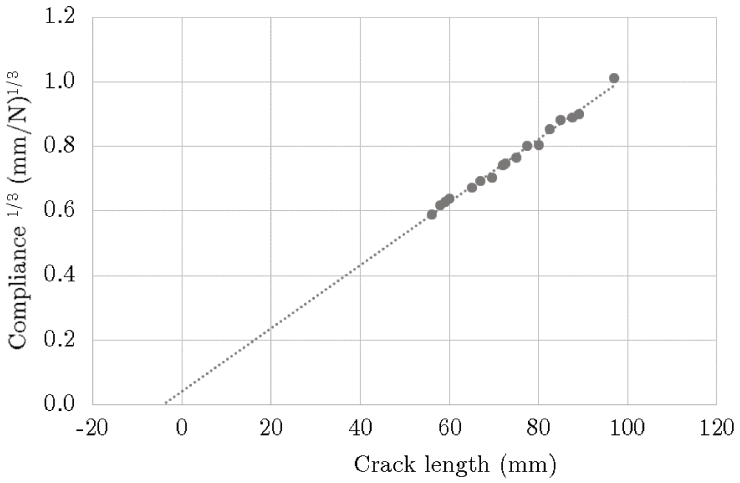


Figure 3.19: Typical compliance$^{1/3}$ versus crack length plot for the interlayer fibre hybrid T700 carbon/S2-glass DCB tests

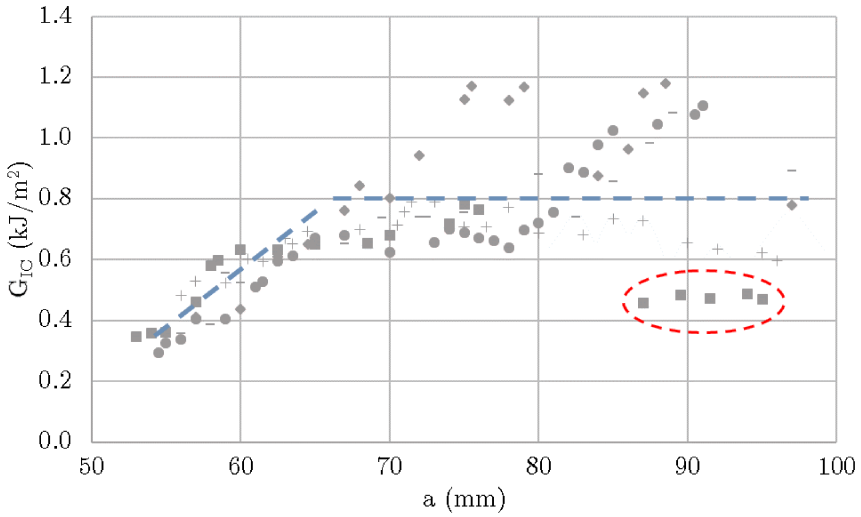


Figure 3.20: Interlayer fibre hybrid T700 carbon/S2-glass double cantilever beam results, critical strain energy release rate versus crack length (red ellipse indicates invalid failure)

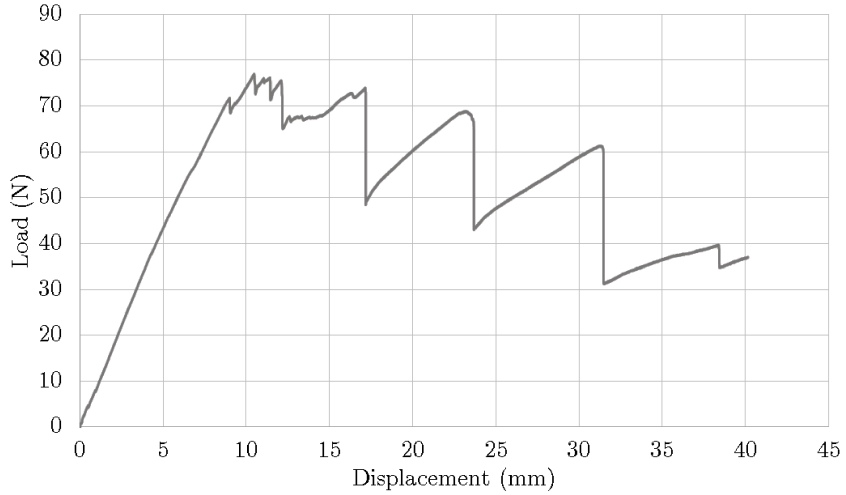


Figure 3.21: Typical load versus displacement plot for the intralayer fibre hybrid T700 carbon/Vectran DCB tests

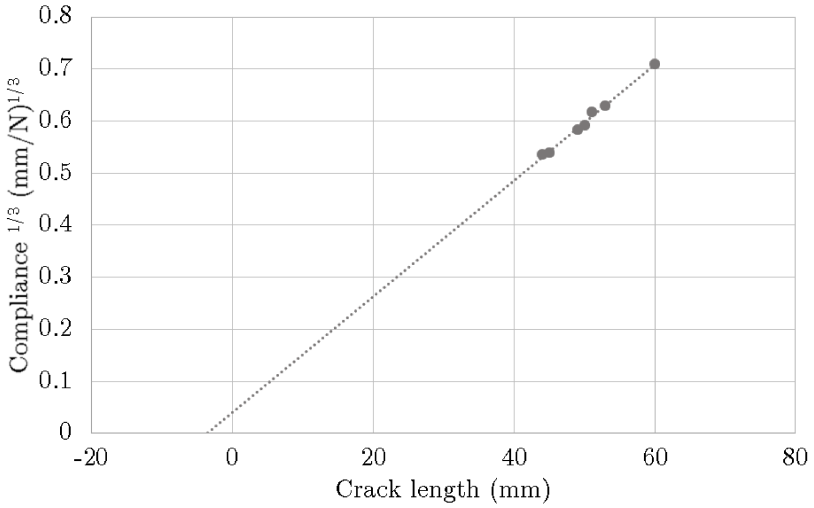


Figure 3.22: Typical compliance$^{1/3}$ versus crack length plot for the intralayer fibre hybrid T700 carbon/Vectran DCB tests

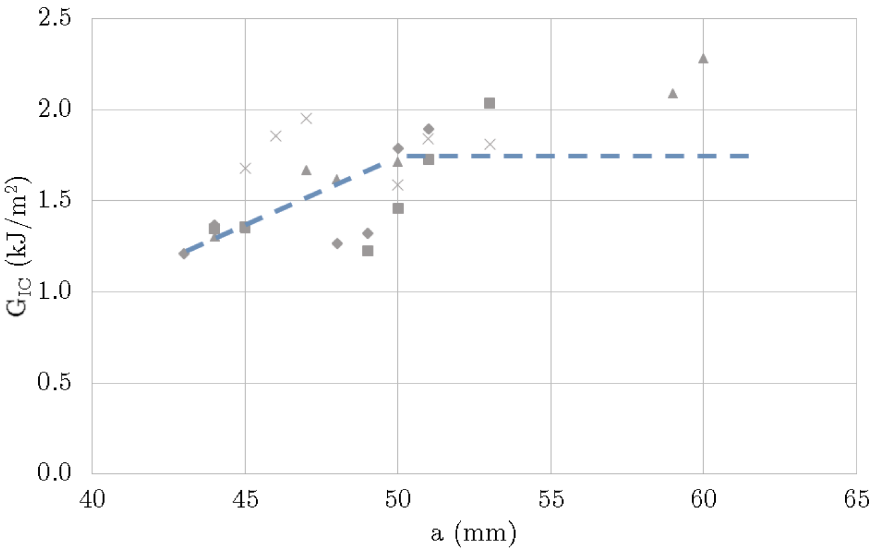


Figure 3.23: Intralayer fibre hybrid T700 carbon/Vectran double cantilever beam results, critical strain energy release rate versus crack length

Table 3.8: Mode I interlaminar critical strain energy release rates for fibre hybrid composites

Material	Initiation critical strain energy release rate G_{IC} (kJ/m²)	Propagation critical strain energy release rate G_{IC} (kJ/m²) (CV%)
Interlayer fibre hybrid T700 carbon/S2-glass	0.35	0.80 (20.30)
Intralayer fibre hybrid T700 carbon/Vectran	1.21	1.74 (21.64)

3.3.1.4. Post-test analysis

The *R*-curve associated with the interlayer fibre hybrid T700 carbon/S2-glass presented distinct initiation, increasing with crack length and subsequent plateauing, which indicated both clear initiation and propagation toughnesses. However, there were some anomalous values below 0.6kJ/m², and above 85mm crack length where compressive failure had occurred on the outer surface of the specimen arms, highlighted in Figure 3.20. The *R*-curves were investigated by examining the sites on the specimens and comparing them directly to the toughnesses for the given crack length. It was noticed that since the unit cell of the T700 carbon spread tow is almost equal to the width of the test specimen, the weave location strongly governed the crack path and subsequent fracture toughness. Upon further examination, it was noticed that the crack path had relocated out of plane in across all specimens causing a ply-split of the centremost carbon ply, and then continued to follow the

0° spread tow, indicating that the variation in stiffness between the two DCB arms governed the crack path. This was seen to have affected the resulting toughnesses in Figure 3.25 and Figure 3.26, where fibre bridging and out-of-plane crack propagation was identified. The carbon fibre/matrix bond was noticed to have been poor due to the lack of plastic deformation observed in the matrix, resulting in bare fibres, Figure 3.24. Fractographic analysis shown in Figure 3.27 further verifies this phenomenon, where lifting of 90° carbon fibres led to a carbon-carbon ply-split interface crack, resulting in reduced toughness.

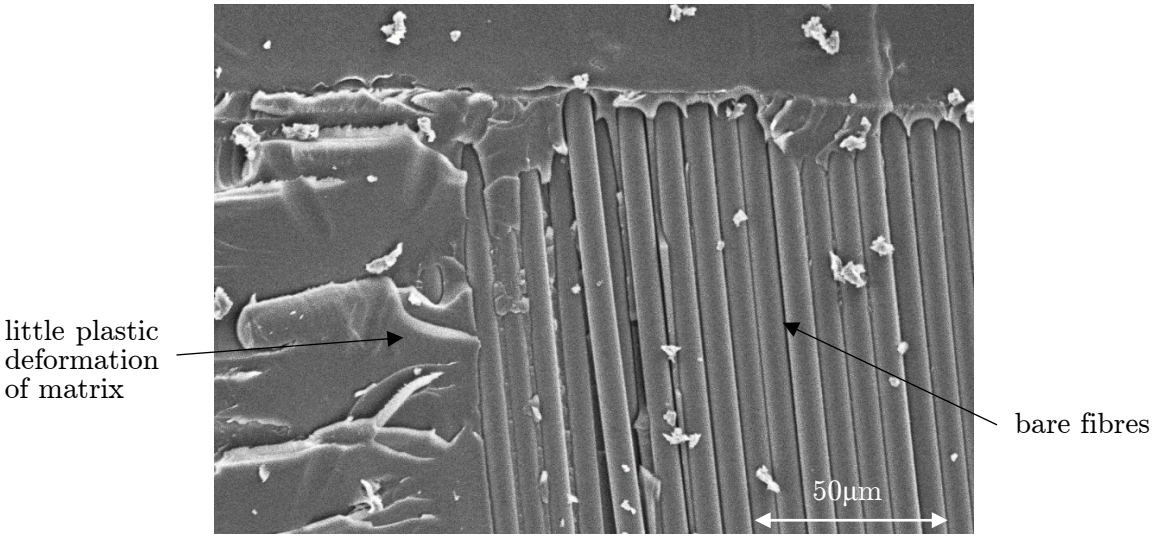


Figure 3.24: Electron micrograph of T700 carbon fibre bond at Mode I fracture surface (x650)

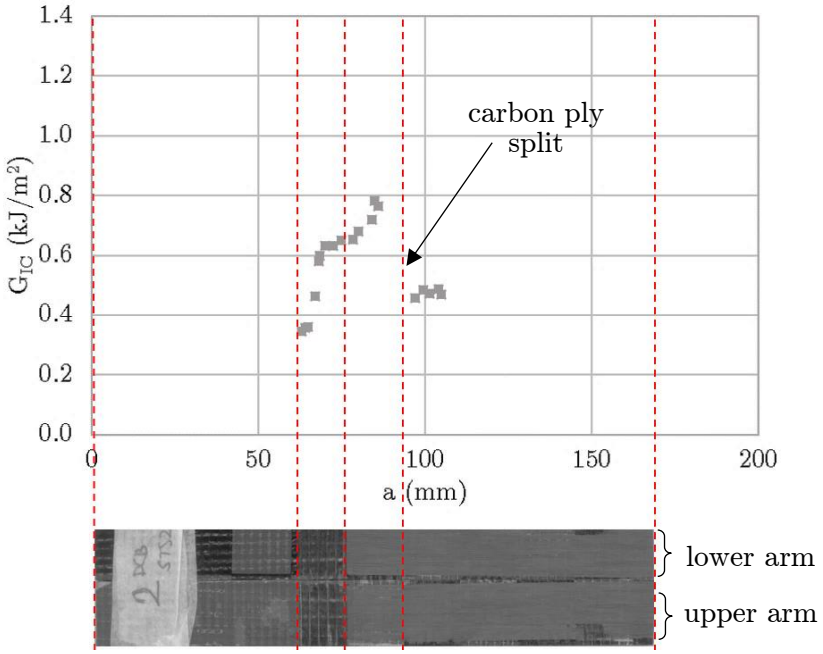


Figure 3.25: Interlayer fibre hybrid T700 carbon/S2-glass DCB specimen #2, *R*-curve

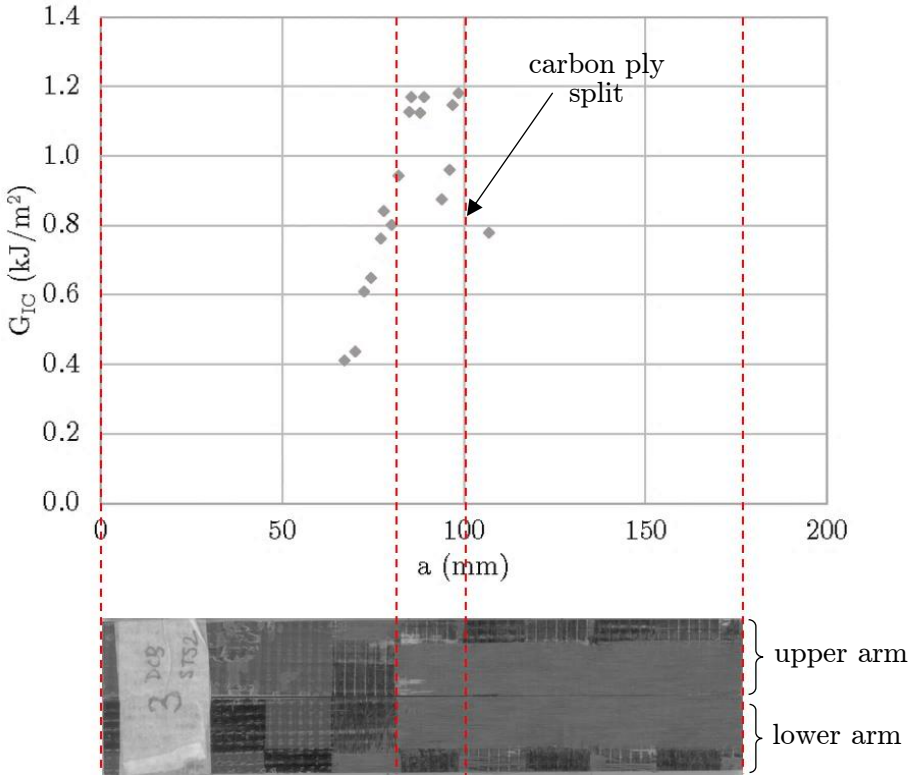


Figure 3.26: Interlayer fibre hybrid T700 carbon/S2-glass DCB specimen #3, *R*-curve

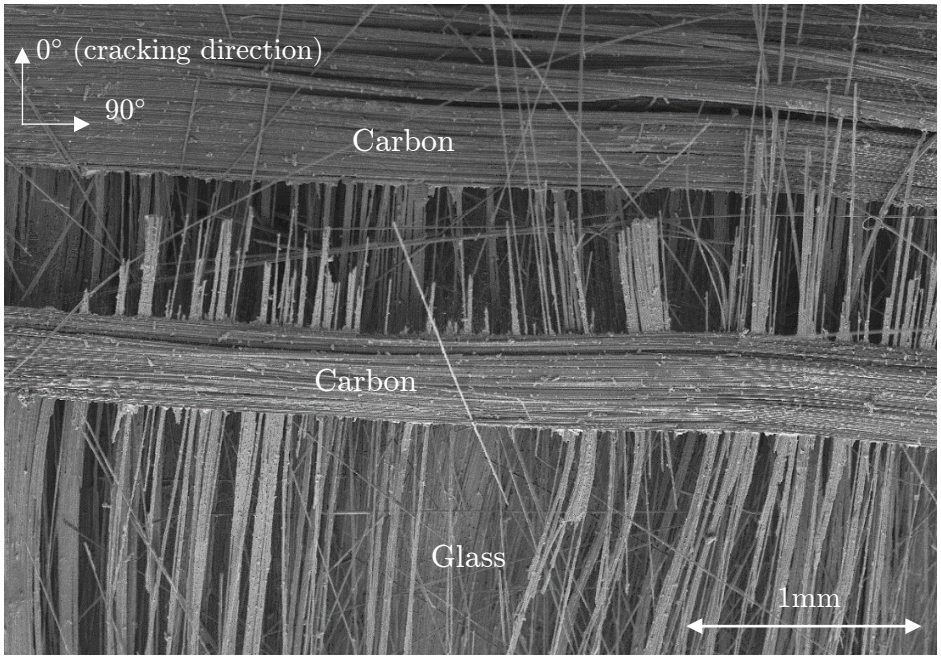


Figure 3.27: Electron micrograph of interlayer fibre hybrid T700 carbon/S2-glass out-of-plane crack relocation across carbon weave within a DCB specimen (x32)

No data for crack lengths >60mm is presented for the intralayer fibre hybrid T700 carbon/Vectran (Figure 3.23) because the T700 carbon doubler delaminated and locally buckled away from the fibre hybrid, resulting in invalid data, as shown in Figure 3.28.

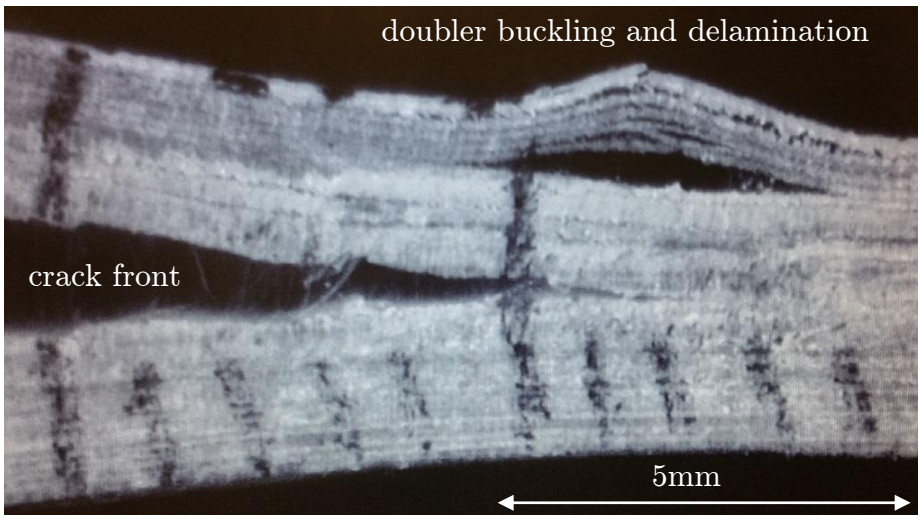


Figure 3.28: T700 carbon spread tow doubler buckling failure due to bending on an intralayer fibre hybrid T700 carbon/Vectran DCB specimen

There were visually clear differences between the fracture morphologies associated with the Vectran fibres and carbon fibres within the 2x2 twill weave of the intralayer fibre hybrid T700 carbon/Vectran specimens. The Vectran was seen to have been very fibrous, promoting fibre bridging between the specimens arms, whereas the carbon fibre exhibited a much smoother fracture surface, Figure 3.29. At the tow boundaries resin-rich regions were noted, presenting typical Mode I features associated with crimped fabrics such as riverlines within the resin [73], Figure 3.30. It is not surprising that the intralayer fibre hybrid exhibited higher fracture toughness values to the interlayer fibre hybrid due to the higher level of undulations between neighbouring plies caused by the tow crimp (noticed visually) as well as a thicker resin layer usually noticed in woven composites [73], although the latter point was not quantified.

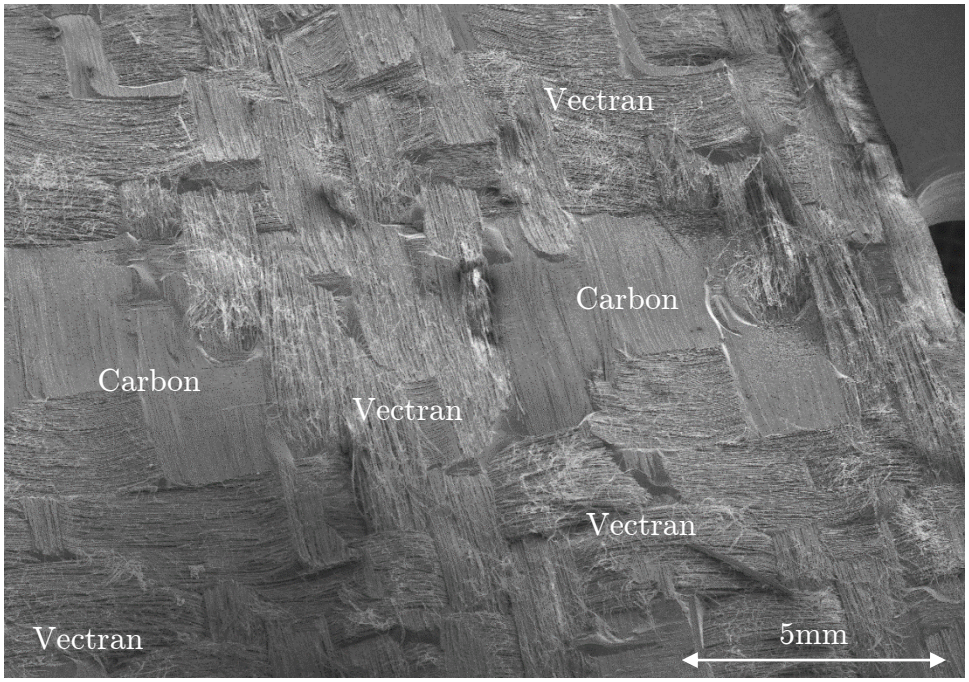


Figure 3.29: Electron micrograph of intralayer fibre hybrid T700 carbon/Vectran, Mode I fracture surface (x7)

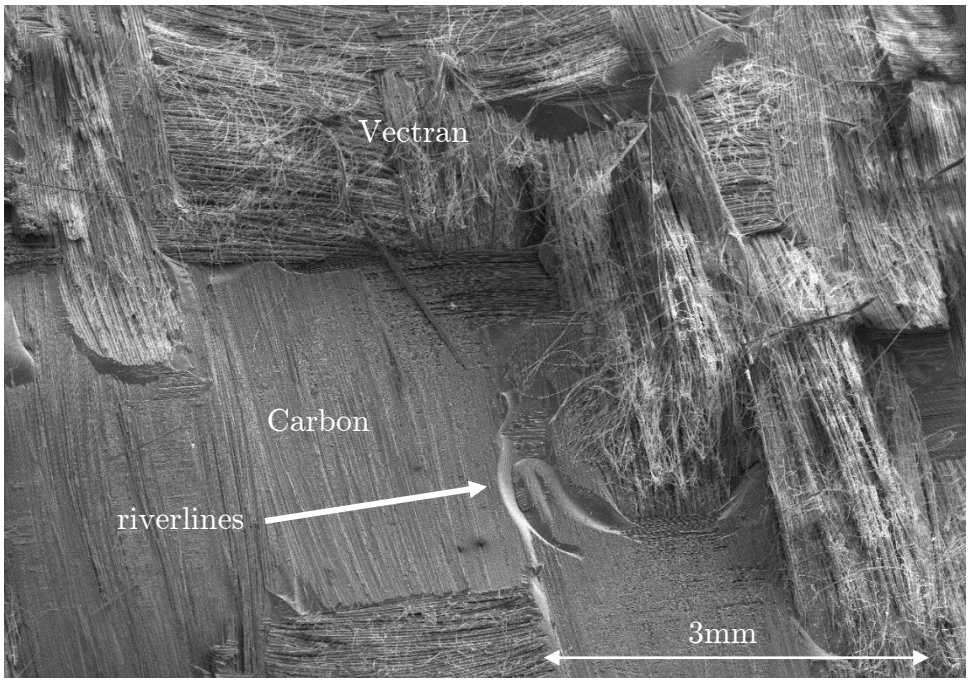


Figure 3.30: Electron micrograph of intralayer fibre hybrid T700 carbon/Vectran, shows Mode I riverlines at the resin rich regions (x17)

3.3.2. Mode II: 4-ENF testing

3.3.2.1. Test set-up

The 4-ENF (4-End Notched Flexure) test was set-up as shown in Figure 3.31, where the bottom support pins (9mm nominal diameter) were fixed at a nominal distance of 120mm and the loading pins (9mm nominal diameter) were set to a separation of 80mm [157]. The loading pins were free to rotate about a central pin across the specimen width. The test was loaded in compression at a stroke of 0.5mm/min to allow for the sporadic stick-slip behaviour of the crack propagation to be monitored carefully using a travelling microscope and then correlated to the force versus displacement data captured from the test machine. The delamination was initiated using a PTFE film between the centremost glass and carbon plies as follows: [CGCGCGC][CGCGCG][D][CGCGCGC]$_2$ (where D denotes the PTFE delamination starter, C denotes a 0°/90° spread tow plain weave T700 carbon ply, and G denotes a 0°/90° S2-glass NCF ply). The 4-ENF specimens were tested with the thicker arm on the bottom only, due to time and resource (material) constraints. The first (initiation) data points were captured approximately 1mm-2mm after the starter cracks.



Figure 3.31: Test set-up for the 4-end notched flexure

3.3.2.2. Data reduction

Similar to the MBT method [167] used in the Mode I testing, the Martin and Davidson method [157] was utilised, where the compliance gradient of the beam across the optically recorded crack lengths generated Mode II critical strain energy release toughnesses as follows:

$$G_{IIC} = \frac{P^2}{2B} m \tag{3.4}$$

where P is the driving force, B is the specimen width, and m is the linear gradient of the compliance with respect to the crack length.

3.3.2.3. Results

Figure 3.32 and Figure 3.34 show the typical Mode II interlaminar compliance versus crack length plots for the interlayer fibre hybrid T700 carbon/S2-glass and the intralayer fibre hybrid T700 carbon/Vectran respectively. Figure 3.33 and Figure 3.35 show the Mode II interlaminar *R*-curve for the interlayer fibre hybrid T700 carbon/S2-glass and the intralayer fibre hybrid T700 carbon/Vectran respectively. Table 3.9 presents the initiation and propagation values taken from these *R*-curves, as well as the discrete value used for numerical analysis.

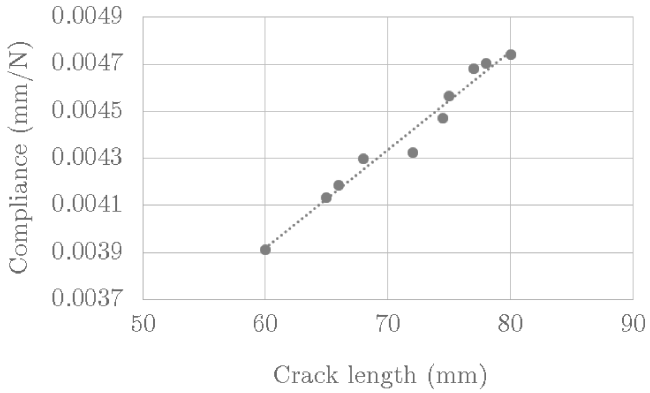


Figure 3.32: Typical compliance versus crack length plot for the interlayer fibre hybrid T700 carbon/S2-glass 4-ENF tests

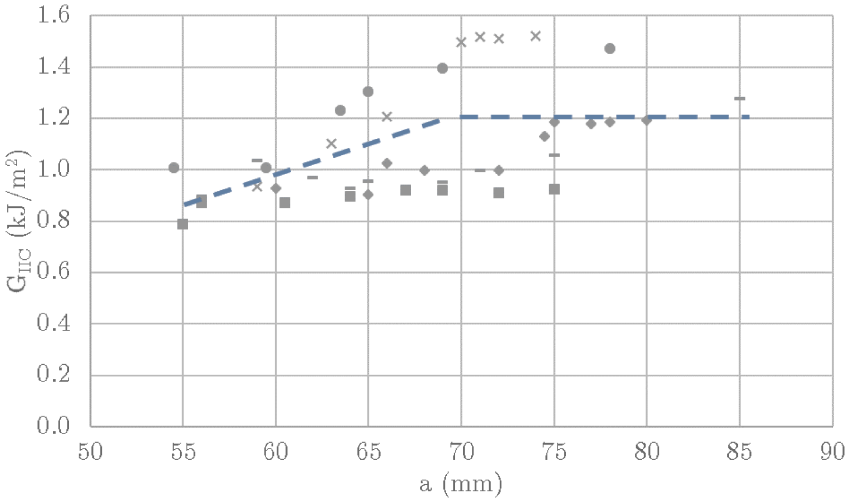


Figure 3.33: Interlayer fibre hybrid T700 carbon/S2-glass 4-end notched flexure results, critical strain energy release rate versus crack length

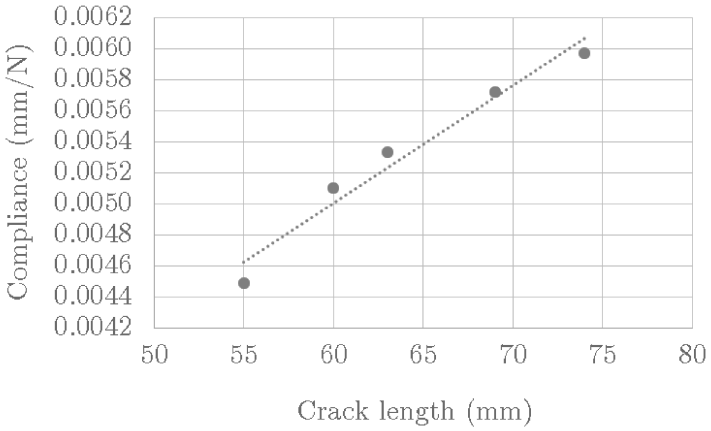


Figure 3.34: Typical compliance versus crack length plot for the intralayer fibre hybrid T700 carbon/Vectran 4-ENF tests

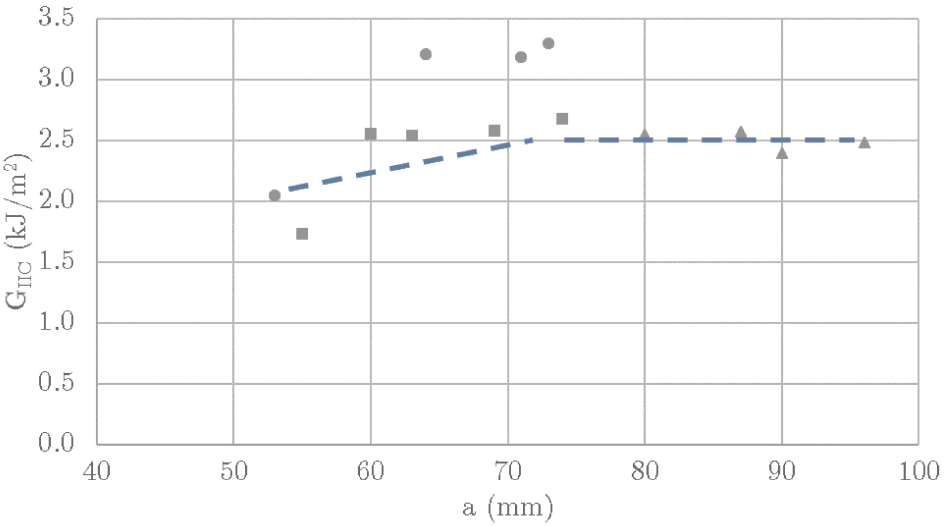


Figure 3.35: Intralayer fibre hybrid T700 carbon/Vectran 4-end notched flexure results, critical strain energy release rate versus crack length

Table 3.9: Mode II interlaminar critical strain energy release rates for fibre hybrid composites

Material	**Initiation critical strain energy release rate G_{IIC} (kJ/m²)**	**Propagation critical strain energy release rate G_{IIC} (kJ/m²) (CV%)**
Interlayer fibre hybrid T700 carbon/S2-glass	~0.85	1.22 (18.00)
Intralayer fibre hybrid T700 carbon/Vectran	~2.00	2.50 (3.23)

3.3.2.4. Post-test analysis

Due to the premature failure of the doublers (debonding and buckling locally), a clear propagation fracture toughness was difficult to determine. The fibre architectures, as well as the mismatch in stiffness between the 4-ENF arms resulted in spurious results, which should be treated with caution. Due to the numerical model requiring an initiation and propagation toughness value, the average of the data points upon a reasonably acceptable plateau of the *R*-curves was utilised for a propagation toughness value.

Upon comparing the Mode II interlaminar *R*-curves alongside the failed specimen surfaces for the fibre hybrid T700 carbon/S2-glass, unlike the Mode I tests, splitting of the centremost 0 ° carbon spread tow caused an increase in the critical strain energy release rate (Figure 3.37 and Figure 3.38). Electron micrographs of the intralayer fibre hybrid T700 carbon/Vectran provided clear Mode II fracture features at the carbon interface in the form of cusps [73] (Figure 3.36). Conversely, the Vectran interface presented a much more fibrous surface, similar to that of the Mode I tests, where the fibres could be seen to have undergone shearing, resulting in smaller defibrillated strands. Similar to the Mode I testing, the intralayer fibre hybrid presented higher Mode II fracture toughness due to the fibre crimp and resin thickness between the plies [73].

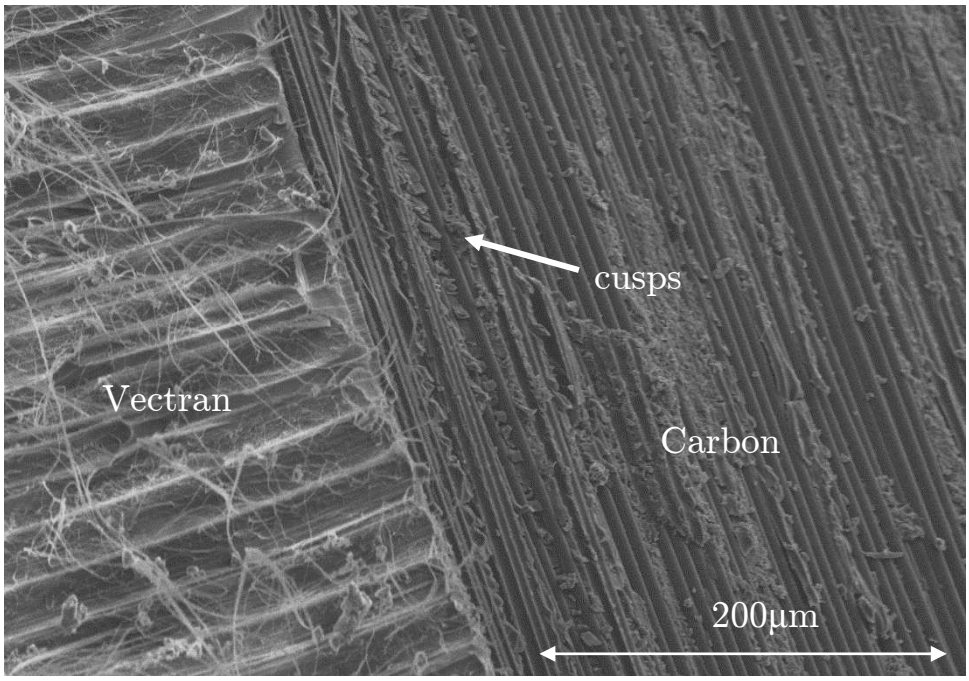


Figure 3.36: Electron micrograph of intralayer fibre hybrid T700 carbon/Vectran, Mode II fracture surface (x270)

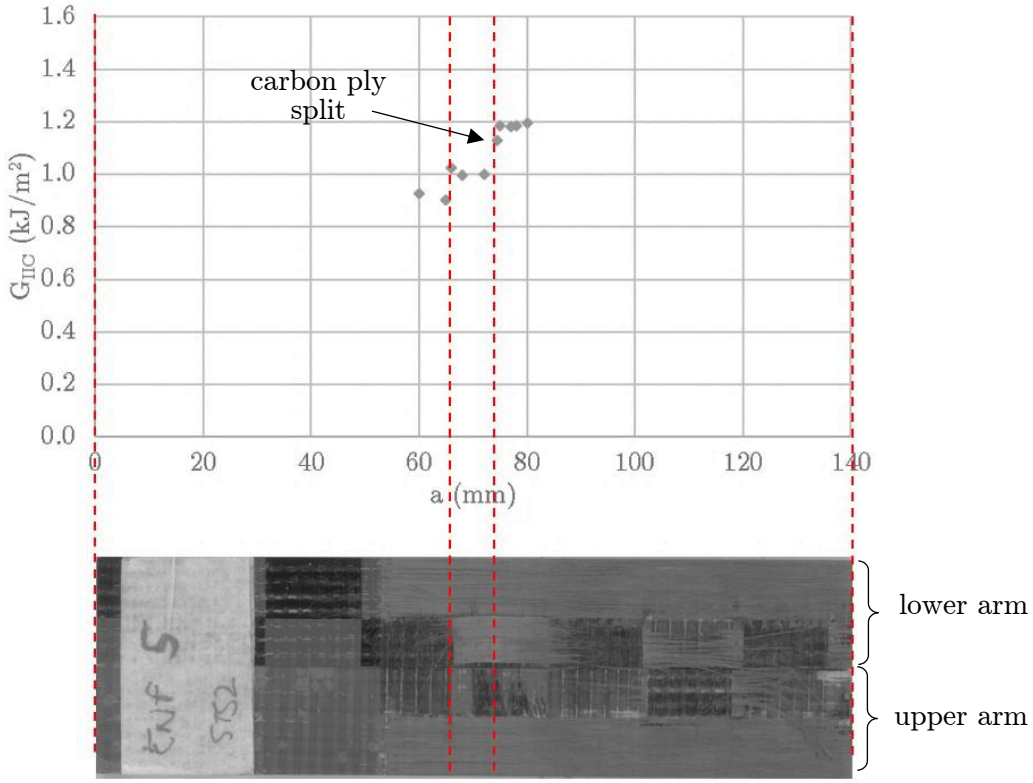


Figure 3.37: Interlayer fibre hybrid T700 carbon/S2-glass 4-ENF specimen #5, R-curve

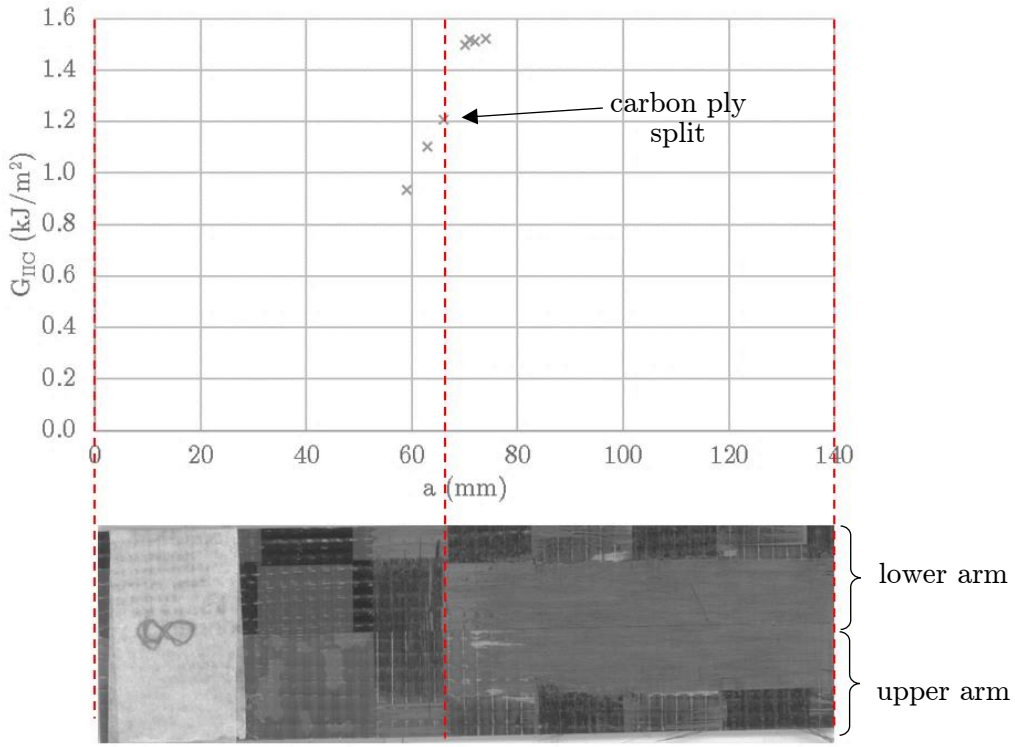


Figure 3.38: Interlayer fibre hybrid T700 carbon/S2-glass 4-ENF specimen #8, R-curve

3.4. Summary

The research presented in Chapter 3 highlighted the base level testing of two novel fibre hybrid composites and their monolithic composite counterparts. Upon measuring the material property data through standard and non-standard test regimes, a full set of in-plane and interlaminar properties have been collated. The composite constituent volume fractions for each material have also been identified through TGA burn-off as well as analytical microscopy.

Novelty within the Chapter is presented in the Mode I and Mode II interlaminar testing of both the interlayer and intralayer fibre hybrids, where the current literature had failed to provide this data. The material properties determined within the Chapter are also inherently novel, given that the material systems have not been characterised fully in such a comprehensive manner.

By accurately characterising these material properties, standardised low velocity drop tower impact testing (Chapter 5) and non-standard structural impact testing (Chapter 6) could be compared to numerical models of each impact event, hence providing a credibility to the interlaminar fracture toughnesses measured.

Chapter 3 publications and dissemination:

- **Conference oral presentations:**
  - T. Katafiasz, "Hybrid Fibre Composites for Delamination Resistance and Cost Saving," in Cyclitech 2015: The first international conference on bicycle technology, Brussels, Belgium, 2015 [13]

4. Translaminar fracture toughness of fibre hybrid composites and their monolithic composite counterparts

4.1. Introduction

This Chapter addresses the gaps in the state of the art on translaminar fracture toughness of fibre hybrid composites as discussed in Section 2.1.3. Standardised Compact Tension (CT) specimen designs were tested but were found to have been unsuitable for the fibre hybrid material systems. Therefore, a new specimen geometry was developed and is presented.

Research highlighted in the literature survey (Chapter 2) was undertaken to inhibit invalid failure modes within a typical CT specimen through parametric geometrical FE modelling [93]. Figure 4.1 shows the failure modes considered in this parametric study of typical CT specimen geometries and labelled them as follows: FM1/FM2: local compression, FM3: in-plane shear, FM4: bearing, FM5: shear-out, and FM6: buckling.

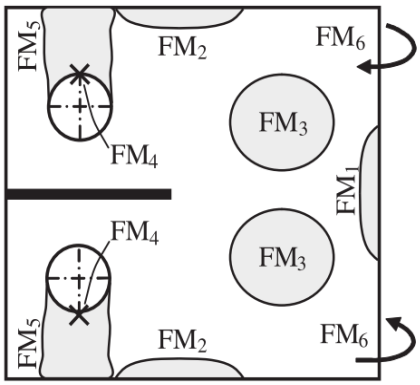


Figure 4.1: Diagram of a conventional CT specimen with the locations of possible failure mechanisms [93]

For the materials tested in this research, premature compressive failure occurred within the composites containing S2-glass and Vectran, where considerably lower (about 50%) compressive strength relative to tensile strength was observed (Table 3.3 and Table 3.4). The initiation load required to propagate a crack within a CT specimen was approximately proportional to the tensile strength of the material and therefore a material with a relatively low compressive to tensile strength ratio tended to lead to premature compressive failure at the rear of the specimen (FM6 in Figure 4.1).

Preliminary tests carried out on the monolithic S2-glass composite and intralayer fibre hybrid T700 carbon/Vectran composite showed that an array of typical CT specimen geometries failed through modes FM1 and FM6 (Figure 4.1) due to the low compressive strength and modulus of this system. A novel specimen geometry, named the 'Notched Curved Compact Tension' (NCCT) specimen (due to its geometrical features, see Section 4.3), was developed by means of optimising a numerical modelling approach along with experimental testing. The NCCT specimen allowed large crack lengths, of up to 20mm, without premature failure or the need for an anti-buckling device for the monolithic S2-glass composite (Section 2.1.3). The specimen geometry was then refined and a more repeatable manufacturing process was developed, allowing translaminar fracture toughness testing of the intralayer fibre hybrid T700 carbon/Vectran composite. Named the Extended Notched Curved Compact Tension (ENCCT) specimen (Section 4.3), this new design was an improvement on the NCCT due to extending the specimen length aiding in capturing longer *R*-curve crack lengths, increasing the in-plane cracking area (for larger unit cell architectures), as well as introducing a resinous chamfer between the thickened and thin section, hence reducing the stress concentrations around the fractured region.

4.2. Preliminary standard CT geometry tests

Both experimental and numerical testing were employed across various CT geometries towards measuring the translaminar fracture toughness of the monolithic and fibre hybrid composites for impact modelling. All numerical models for the various CT specimen geometries were run using Abaqus 6.14 in both implicit linear static and eigenvalue buckling to determine the failure strains and the critical buckling loads respectively.

The numerical FE models were comprised of continuum shell elements (SC8R), cohesive elements (COH3D8), and rigid body elements (R3D4). The continuum shell elements (SC8R), which were assigned the composite laminate properties determined in Chapter 3, utilised the Abaqus composite material property for each ply (where one element through-thickness contained two plies, and each ply had three integration points to allow for bending). The cohesive elements (COH3D8) were assigned the MTM57 resin material properties (Chapter 3) and were located at three regions spaced 1mm equally through the thickness of the specimen

to capture the interlaminar stresses between neighbouring continuum shell ply stacks. Rigid body elements (R3D4) were used to model the loading pins with frictionless tangential and hard normal penalty contact properties with the specimen. Using a typical CT specimen geometry (Figure 4.2), a mesh sensitivity study was employed (Figure 4.3) where the total internal energy of the model was tabulated against the mesh size around the notch tip. Six discrete element sizes at the notch tip and up to a 5mm radius from the notch tip between 2mm and 0.05mm were investigated. Elements at the rear of the specimen were set to 1mm (since the tow size for the S2-glass composite was within this order of magnitude) for each model and the remaining elements were set globally to 2.5mm in size.

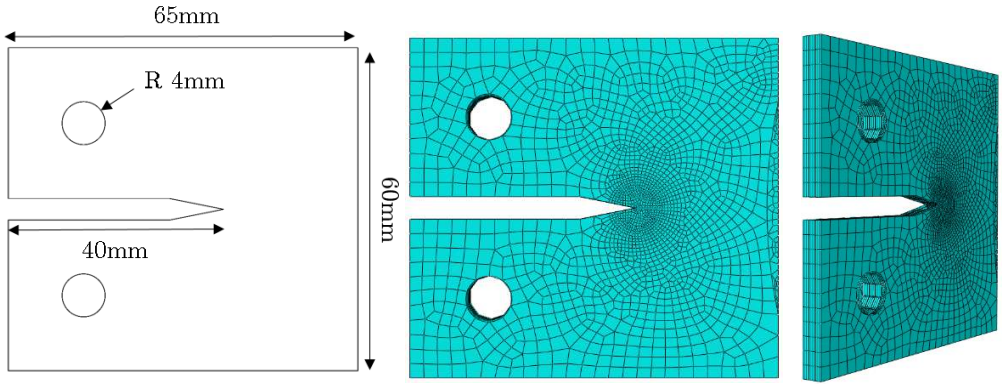


Figure 4.2: Typical compact tension specimen design with 0.5mm mesh around the notch tip and 1mm at the rear (4mm thick)

The internal energy within the model was seen to converge where the mesh size around the notch tip was approximately 0.5mm, quantified as a convergence of 0.03% difference to the trending value at 0.05mm. Therefore, to aid in computational time and efficiency, a mesh size of 0.5mm was used around the notched region (in tension) and 1mm at the pins and rear of the specimen (in compression, where high compressive stresses were likely to occur; failure modes FM1 & FM5, Figure 4.1). The CT model ASTM E399 [91] shown in Figure 4.2 contained a total of 62676 nodes and 42420 elements, comprising of 31986 SC8R, 3360 R3D4 and 7074 COH3D8 type elements.

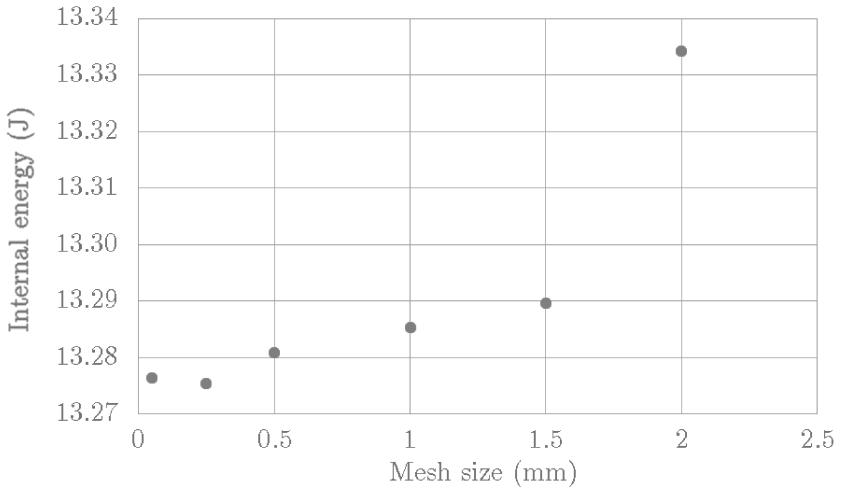


Figure 4.3: Mesh sensitivity study: mesh size versus internal energy

By running multiple linear static models at discrete crack lengths, an approximate crack length (if at all) could be determined before buckling failure at the rear of the specimen occurred. This was achieved by first conducting linear static analysis on a specimen with a discrete crack length and determining the (decreasing with crack length) driving force responsible for a Abaqus maximum strain criterion greater than unity at 1mm vertically from the notch tip, as follows [168]. This criterion was utilised as an initial first pass for the tensile fibre fracture around the notch tip and thus a safety factor of two was introduced into the design phase (Figure 4.11).

$$I_F = max \begin{cases} \epsilon_1/\epsilon_{1t} & if\ \epsilon_1 > 0\ or\ -\epsilon_1/\epsilon_{1c}\ if\ \epsilon_1 < 0 \\ \epsilon_2/\epsilon_{2t} & if\ \epsilon_2 > 0\ or\ -\epsilon_2/\epsilon_{2c}\ if\ \epsilon_2 < 0 \\ \epsilon_3/\epsilon_{3t} & if\ \epsilon_3 > 0\ or\ -\epsilon_3/\epsilon_{3c}\ if\ \epsilon_3 < 0 \\ & abs(\gamma_4)/\gamma_{4u} \\ & abs(\gamma_5)/\gamma_{5u} \\ & abs(\gamma_6)/\gamma_{6u} \end{cases} \tag{4.1}$$

where: ϵ is the strain in the given direction and γ is the shear strain in the given direction; note that ultimate compressive strains are deemed positive.

This driving force was then employed within an eigenvalue buckling mode analysis to quantify whether buckling would occur for each particular crack length given the required damage initiating force. This data is summarised in

Table 4.1 for the monolithic S2-glass composite and intralayer fibre hybrid T700 carbon/Vectran composite properties regarding four 5.6mm thick CT specimen geometries (consisting of 26 plies of NCF S2-glass 0°/90° fibre blankets, and 8 plies of 2x2 twill weave T700 carbon/Vectran fibre blankets) (thickness as recommended by Blanco et al [93], as a result of their parametric study). The numerical FE studies were undertaken at 5mm discrete crack length intervals.

Table 4.1: Compact tension test types, experimental and numerical suitability study

CT Specimen type: Reference	**Critical crack length prior to buckling/compression failure**			
	Experimental		**Numerical**	
	Monolithic S2-glass composite	**Intralayer fibre hybrid T700 carbon/Vectran**	**Monolithic S2-glass composite**	**Intralayer fibre hybrid T700 carbon/Vectran**
Compact Tension (CT): [91]	8mm	0mm	<10mm	<5mm
Disk Compact Tension (DCT): [91]	-	-	<5mm	0mm
Two-Tapered Compact Tension (2TCT): [93]	3mm	0mm	<5mm	<5mm
Extended Compact Tension (ECT): [93]	4mm	1mm	<5mm	0mm

The Compact Tension geometries were tested for the S2-glass and intralayer fibre hybrid T700 carbon/Vectran composites (manufactured using RFI (see Section 3.1) using the same test procedure as stated in Section 4.4. The corresponding load versus displacement graphs for these tests undertaken at a stroke of 1mm/min, are presented for the CT (Figure 4.4), 2TCT

(Figure 4.5), and ECT (Figure 4.6) type specimens. Post-test X-ray images (using Dibromomethane, 99% penetrant) are also presented alongside these graphs, highlighting the relevant premature failure mode denoted in Figure 4.1 [93]. Buckling (FM6) was noticed within the CT and 2TCT specimens as well as compressive failure at the rear end of the specimen (FM1) occurring in both the CT and ECT specimens. This indicated that either a thicker specimen or an anti-buckling device was required to counteract this out-of-plane buckling, both of which have drawbacks. The thickness of CT specimens have been found to affect the measure fracture toughness, as investigated by Teixeira et al. [88] when using monolithic spread tow carbon composite, as well as increasing the manufacturing cost. Anti-buckling devices inherently lead to unknown through-thickness stress variations and concentrations through the specimens being tested as well as obscuring the field of view when utilising Digital Image Correlation (DIC), and thus have been disregarded.

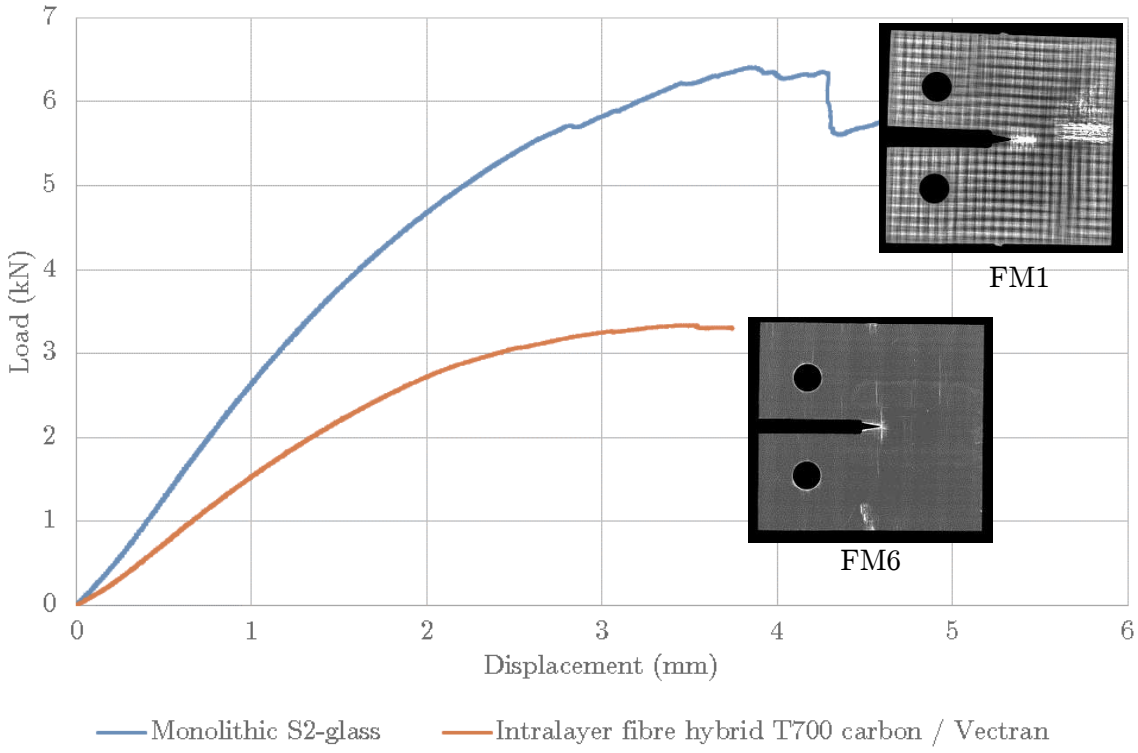


Figure 4.4: Compact tension specimen type for monolithic S2-glass composite and intralayer fibre hybrid T700 carbon/Vectran, load versus displacement

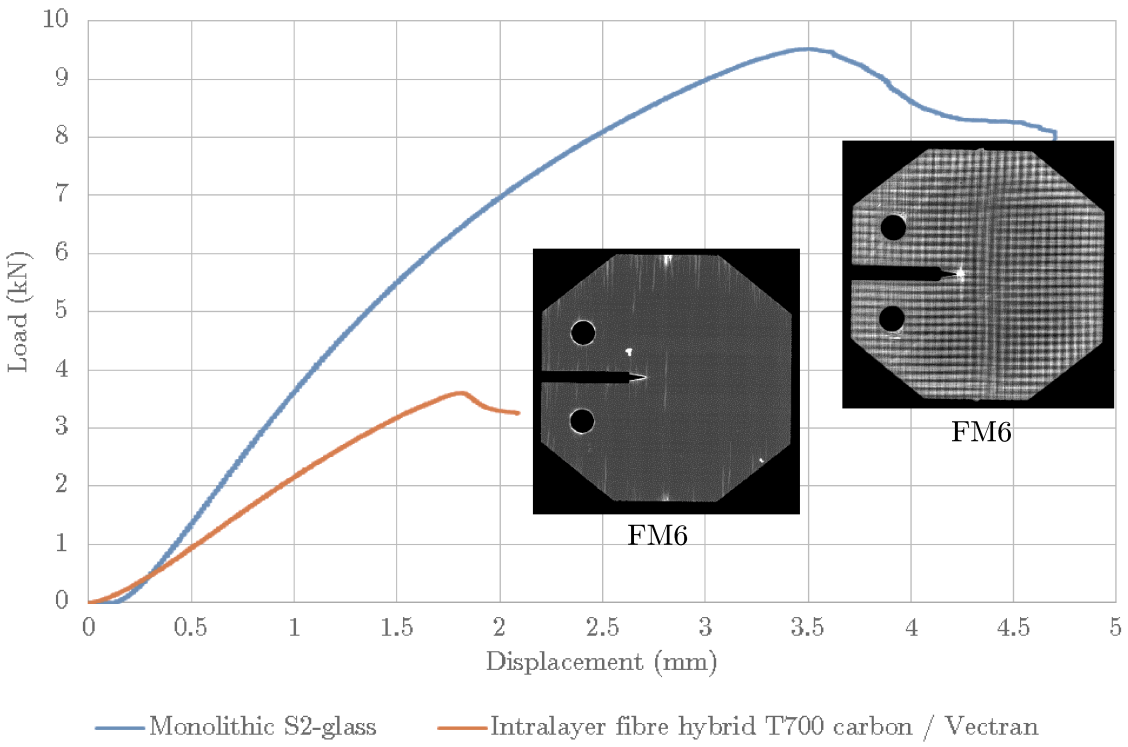


Figure 4.5: Two-tapered compact tension specimen type for monolithic S2-glass composite and intralayer fibre hybrid T700 carbon/Vectran, load versus displacement

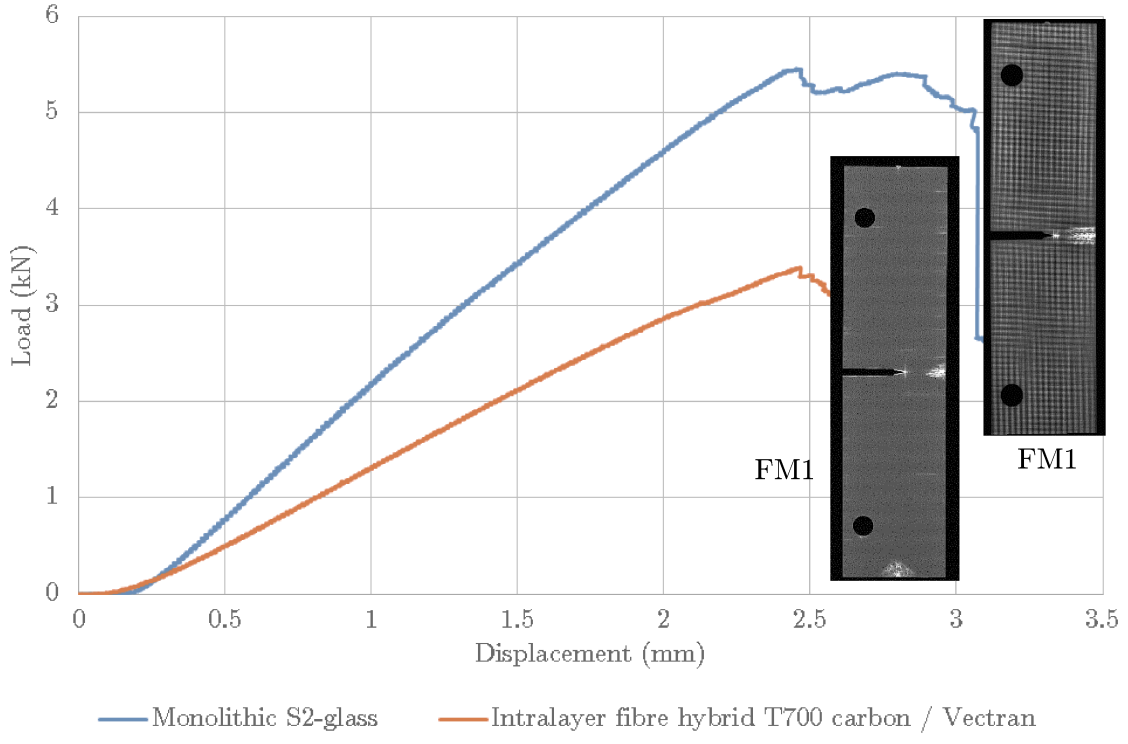


Figure 4.6: Extended compact tension specimen type for monolithic S2-glass composite and intralayer fibre hybrid T700 carbon/Vectran, load versus displacement

4.3. Development of a novel compact tension specimen

4.3.1. Model development

A Curved Compact Tension (CCT) geometry (Figure 4.7) was developed by introducing a 30mm radii at the rear of the typical compact tension specimen [91], tangential to the connecting horizontal sides so as to eliminate unnecessary stress concentrations at the rear of the specimen (FM1, Figure 4.1). A curvature in the specimen 'arms' was also introduced to reduce the stress concentrations associated with FM2 (Figure 4.1). Despite the reduction in compressive stresses at the rear of the specimen, experimental tests showed that buckling led to compressive failure regardless of the curvature. Crazing was also seen around the notch and the through-thickness crack was barely visible (Figure 4.8).

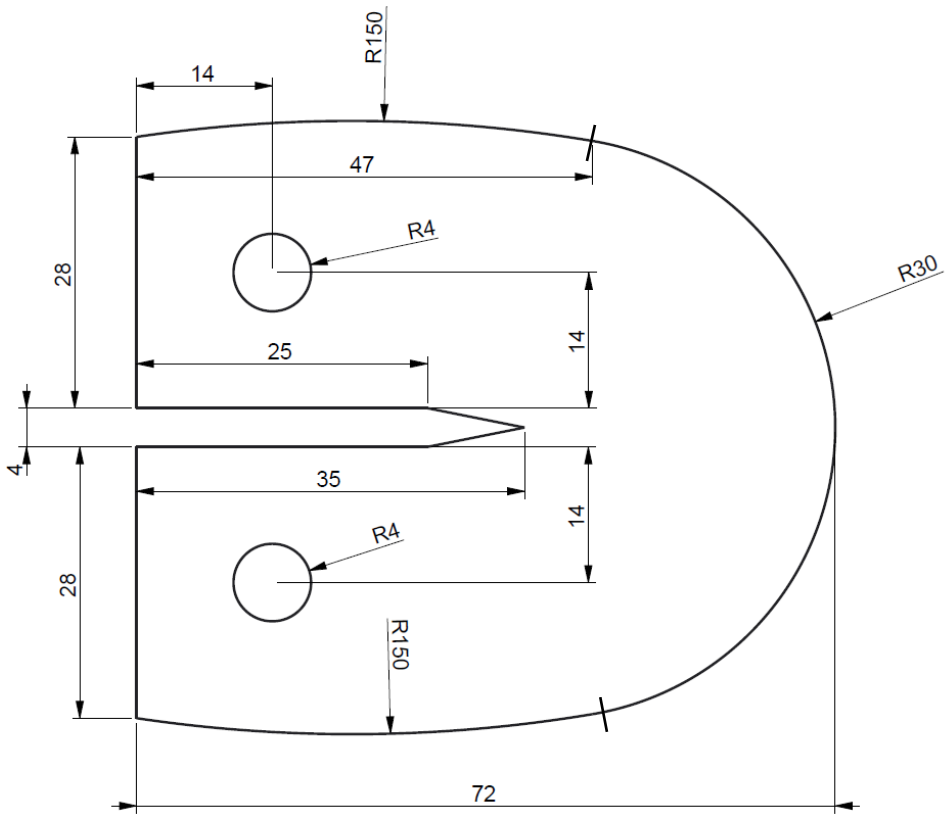


Figure 4.7. Nominal CCT specimen geometry profile dimensions (all dimensions in mm)

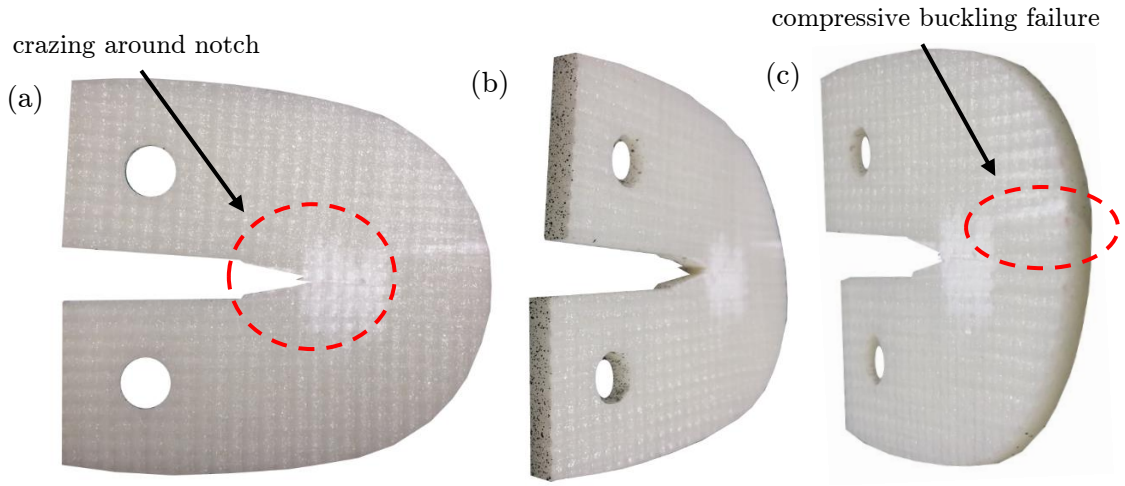


Figure 4.8: Buckled CCT geometry without through-thickness groove: a) profile view b) front view c) back view

To mitigate this type of buckling failure, the 4mm curved CT specimen shown in Figure 4.8 was modelled numerically at a thickness of 10mm, where eigenvalue buckling modes analysis was carried out. The load required to propagate the crack was below the critical buckling load up to a crack length of 12mm. An R-curve of 12mm crack length was not likely to be long enough to capture a propagation fracture toughness, and thus a new design iteration was required.

It was apparent that the solution to mitigate premature buckling was to reduce the CT geometry's 'cracking' driving force, whilst also increasing the critical buckling load. To achieve this, and also capture long crack lengths whilst maintaining a high buckling-to-crack propagating load ratio, the thickness of the crack growth area was reduced by introducing a 4.7mm thick rectangular notched section 4mm x 60mm either side of the specimen along the crack growth region, located 12mm from the rear (see Section 4.3.2 for the manufacturing details). This reduced the load required to propagate the crack whilst maintaining a high critical buckling load due to a relatively thick rear of the specimen. This specimen geometry was named the 'Notched Curved Compact Tension' (NCCT) specimen due to its dimensional features (Figure 4.9) and a study to optimise the ratio between the critical buckling load and the load required for crack growth was undertaken (Figure 4.10 and Figure 4.11). Eigenvalue buckling mode analysis was performed to determine the critical buckling load (Figure 4.10b), and a linear static model utilising the maximum strain criterion was used to determine the load required for crack propagation (Figure 4.10c).

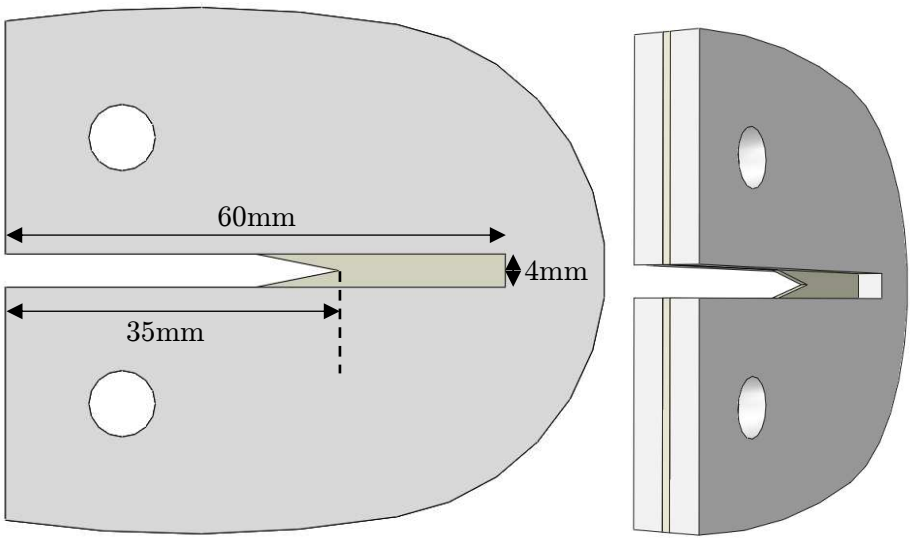


Figure 4.9: NCCT specimen type

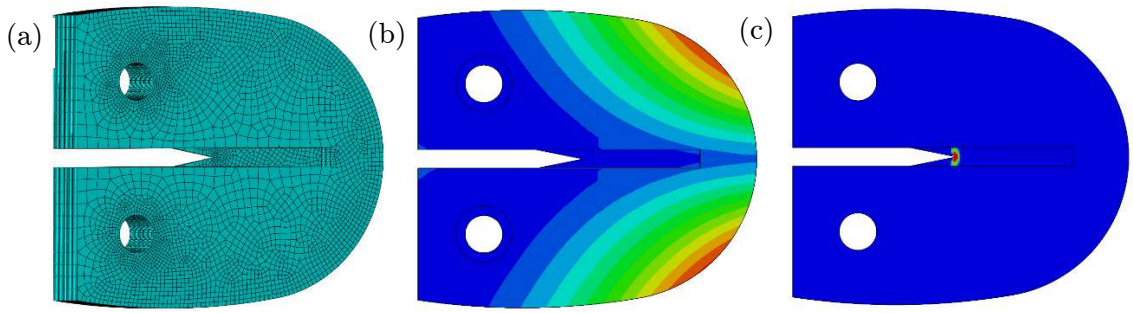


Figure 4.10: NCCT specimen geometry: (a) Specimen FE model (b) Eigenvalue first buckling mode (the contour shows the absolute out-of-plane displacement and is unitless, red represents the maximum and blue represents the minimum) (c) Maximum strain criterion at 50% of buckling load (contour other than blue indicates values greater than unity, where red represented the criterion's maxima)

The eigenvalue buckling mode FE model shown in Figure 4.10a defined the critical buckling load of the specimen geometry at five linear static FE models containing discrete crack lengths of 21mm to 41mm, at 5mm intervals. The critical buckling load taken from the eigenvalue analysis was then scaled by a 50% safety factor (to ensure the minimisation of buckling, since there was scatter in the material properties utilised) and applied directly to the corresponding linear static FE model with the same crack length (Figure 4.10b).

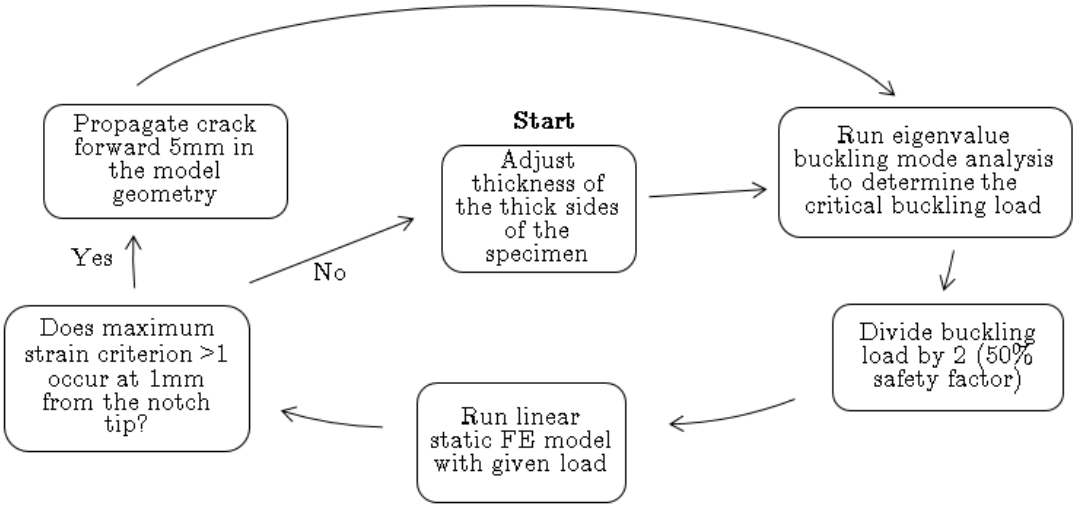


Figure 4.11: NCCT specimen FE optimisation methodology

From the linear static model, it was clear that for all discrete crack lengths, the critical buckling load (with a 50% safety factor) applied to the linear static model produced a strain criterion >1 around the crack tip, whilst the rest of the model remained undamaged. The maximum strain criterion data at the notch tip is summarised in Table 4.2.

Table 4.2. NCCT FE model analysis thickness optimisation

Δa, change in crack length (mm)	**50% buckling load (kN)**	**Maximum strain criterion at the notch tip for given buckling load**
0	4.24	2.66
5	3.42	2.06
10	2.72	1.78
15	2.26	1.43
20	2.03	1.20

The materials listed below were successfully characterised when using the NCCT test specimen design:

- Monolithic S2-glass non-crimp composite (0°/90°);
- Monolithic T700 carbon spread tow 12K plain weave composite;

- Interlayer fibre hybrid: T700 carbon spread tow 12K plain weave/S2-glass non-crimp (0°/90°), alternate carbon (C) and glass (G) ply blocks of [C-G-C-G-C-G-C].

The intralayer fibre hybrid T700 carbon/Vectran did not however perform as intended due to considerable fibre pull-out from the thickened region of the specimen (where failure occurred not only in the thinned region, as required), leading to erroneous loads and thus the associated fracture energy. The unit cell size of this fibre hybrid was larger than the 4mm thinned region height. Because of this, an update to the NCCT specimen design was made where the thinned area was increased to accommodate the larger unit cell of the 2x2 twill weave (10mm x 10mm), as well as extending the specimen length to capture a longer crack and hence a more comprehensive *R*-curve. Although not shown graphically in Figure 4.13, the thinned region was also chamfered to the thicker region to lower the stress concentrations around the transition by sanding the corners of the PTFE insert hence allowing resin build-up (see Section 4.3.2). The notch tip was reduced from 35mm to 25mm from the end of the specimen and the design was named 'Extended Notched Curved Compact Tension' (ENCCT) (Figure 4.13). By comparing the NCCT (Figure 4.9) and ENCCT (Figure 4.13) type specimens, it can be seen that the maximum crack length is 25mm for the NCCT and 50mm for the ENCCT type specimens due to the thinned region and notch tip location, allowing for a longer *R*-curve to be captured when using the ENCCT specimen type.

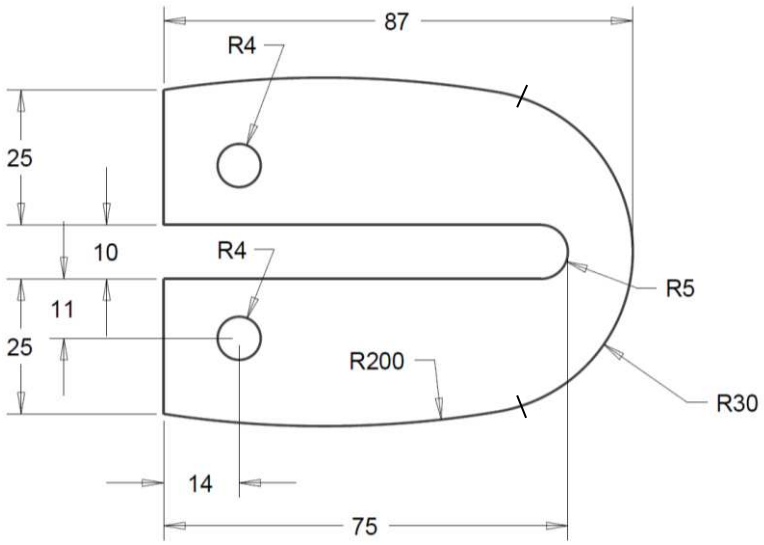


Figure 4.12: ENCCT thick-side specimen dimensions (all dimensions in mm)

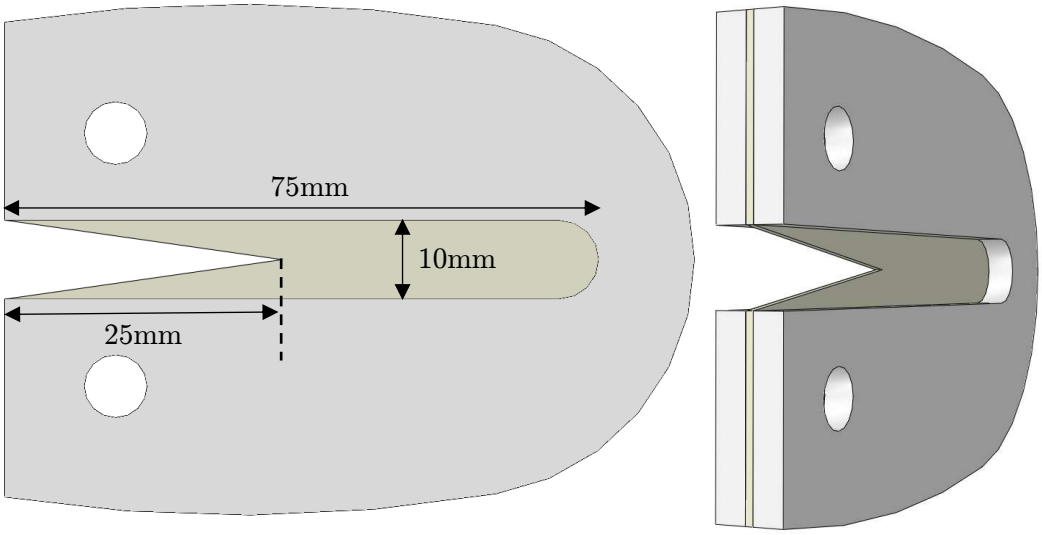


Figure 4.13: ENCCT specimen type

4.3.2. Specimen manufacture

The materials used for the NCCT specimen type were laid-up in panels of dimensions 120mm x 480mm, as shown in Figure 4.14. PTFE (Polytetrafluoroethylene) inserts of dimensions 4.7mm x 4mm x 60mm were inserted at cuts made either side of the panel before curing to achieve the thinned cracking region of the NCCT specimen. Care was taken to ensure that the inserts lined up with each other either side. Resin rich regions around the cut could be seen where the fibres, which were cut by hand using a surgical scalpel, slightly exceeded the dimensions of the inserts by about 1mm.

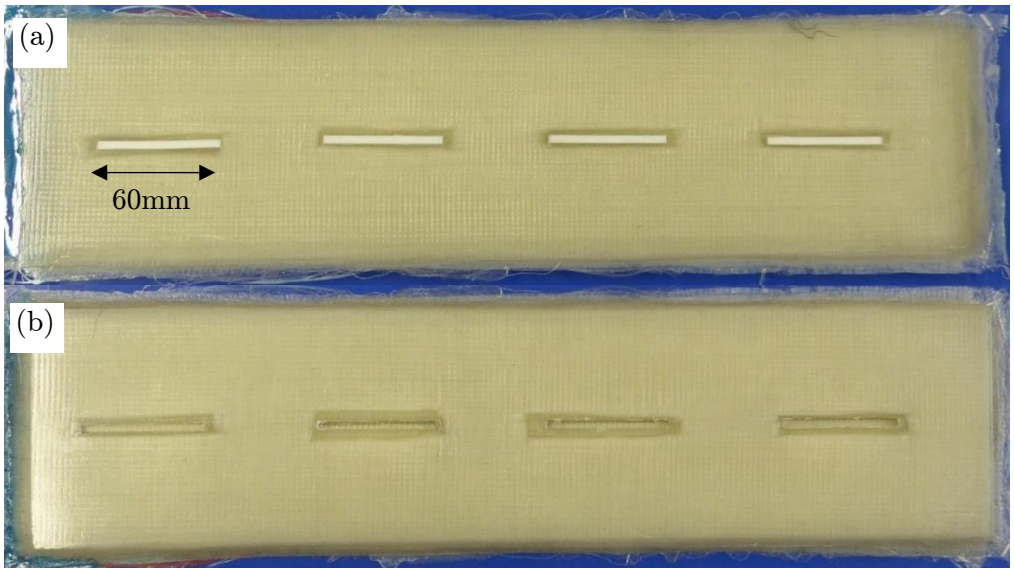


Figure 4.14: Monolithic S2-glass composite NCCT material layup, post-cure, prior to waterjet cutting: (a) with PTFE inserts, (b) with PTFE inserts removed

The materials were manufactured using the same method as for the base level testing (Chapter 3). By doing so, the material properties determined from all tests could be used in conjunction with one another for impact modelling (Chapters 5 and 6). The ply counts and nominal cured thicknesses are shown in Table 4.3.

Table 4.3: NCCT and ENCCT ply counts and nominally cured thicknesses

Material, specimen type	**Thick side: ply count (nominally cured thickness)**	**Thin middle: ply count (nominally cured thickness)**
Monolithic S2-glass composite (G), NCCT	$[G]_{20}$, 4.7mm	$[G]_{4}$, 1.0mm
Monolithic T700 carbon composite (C), NCCT	$[C]_{50}$, 4.7mm	$[C]_{10}$, 0.9mm
Interlayer fibre hybrid T700 carbon (C)/S2-glass (G), NCCT	$[C\text{-}G\text{-}C\text{-}G\text{-}C\text{-}G\text{-}C]_{4}$, 4.2mm	[C-G-C-G-C-G-C], 1.0mm
Intralayer fibre hybrid T700 carbon/Vectran (CV), ENCCT	$[CV]_{7}$, 4.2mm	[CV], 0.8mm

Upon curing, one side of the inserts were removed and the specimen shapes were cut using a waterjet cutter to their desired dimensions. The specimens were then notched using a circular diamond saw with one of the PTFE inserts in place, providing some support for the thinned region during the cutting process. The insert was then removed and the notch tip was sharpened by hand three times using a surgical scalpel to create a sharp crack tip prior to testing, as recommended by Pinho [169] since the notch tip radius has been observed to affect the fracture toughness [170].

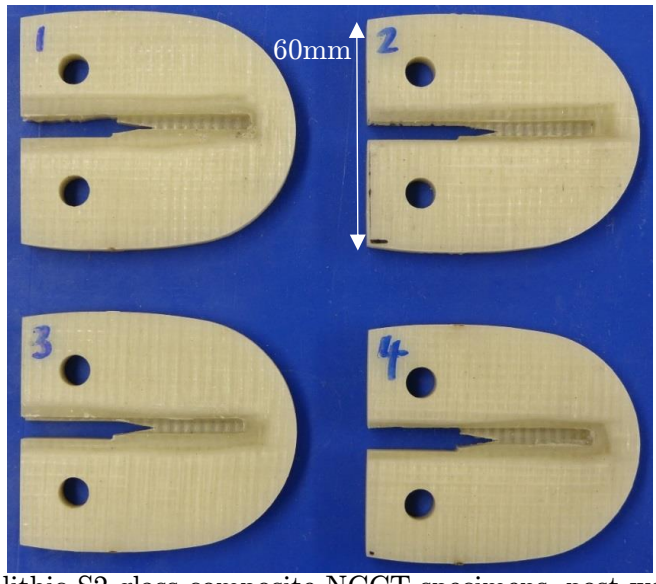


Figure 4.15: Monolithic S2-glass composite NCCT specimens, post waterjet cutting and notching

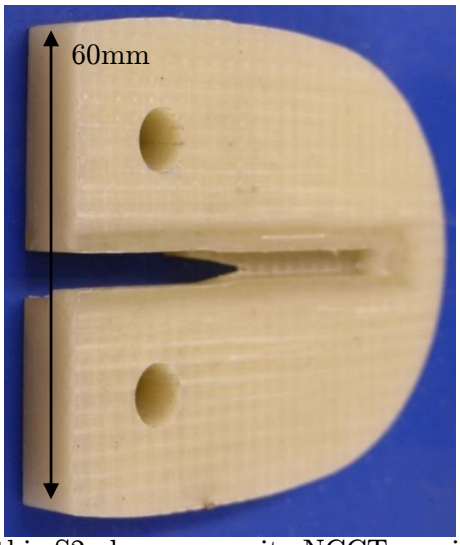


Figure 4.16: Monolithic S2-glass composite NCCT specimen prior to testing

The ENCCT specimens were manufactured in the same manner as the NCCT specimens except the PTFE inserts were chamfered using sandpaper to create a sloping transition between the thick sides of the specimen and the thin cracking region. This was employed to minimise stress concentrations occurring at the sharp inside edge of the thinned region, which could have affected the crack path. The specimens were arranged in a row of three by a column of two to reduce the curvature on the caul plate, which had a slight thinning effect on the edges of the NCCT specimens under vacuum of the autoclave cycle. Figure 4.17 and Figure 4.18 show the ENCCT specimen for the intralayer fibre hybrid T700 carbon/Vectran before and after the PTFE inserts had been removed and scale bar drawn respectively. The ENCCT specimens were C-scanned and one specimen X-rayed (using Dibromomethane, 99% penetrant) prior to testing (Figure 4.19), to identify any delaminations, discontinuities, and inclusions which could affect the crack driving force and thus lead to erroneous fracture toughness data.



Figure 4.17: Intralayer fibre hybrid Vectran/T700 carbon ENCCT specimen with PTFE inserts still intact



Figure 4.18: Intralayer fibre hybrid Vectran/T700 carbon ENCCT specimen with PTFE inserts removed and scale bar labelled for optical crack measurement

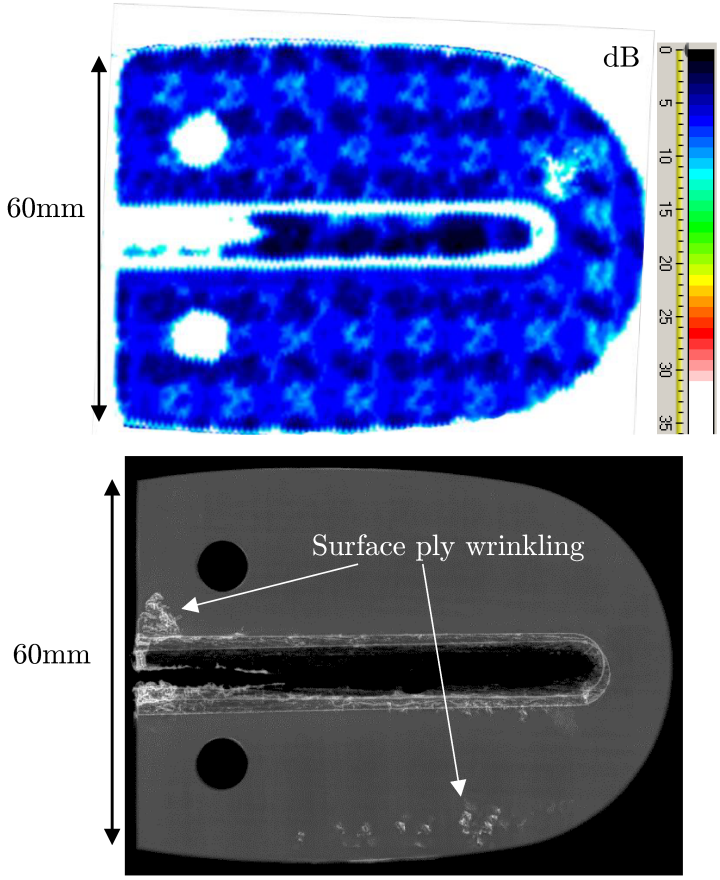


Figure 4.19: C-scan and X-ray of ENCCT intralayer fibre hybrid T700 carbon/Vectran specimen prior to testing (colour scale in dB)

4.4. Test set-up

The NCCT and ENCCT testing was carried out at room temperature (20 ° C) using an Instron 5969 test machine at a constant stroke of 0.5mm/min in tension, where the crosshead displacement (mm), load (N) and time (s) were recorded (Figure 4.20). Video recording was employed to capture the crosshead displacement (mm) from markers on the specimen surface

using an Imetrum optical strain system at 10Hz and the crack growth (mm) against the scale bars drawn on each specimen. The Imetrum optical strain and the Instron 5969 sources were correlated automatically via an analogue to digital converter and thus the load from the crosshead and the optical displacement curves could be plotted purely from the pin locations, eliminating the test machine and instrumentation compliance errors. A backlight was used to show clear crack growth through the specimen thickness for the translucent monolithic S2-glass composite and for the other opaque materials front lighting sufficed. The crack was followed optically using the same Imetrum optical strain gauge video.

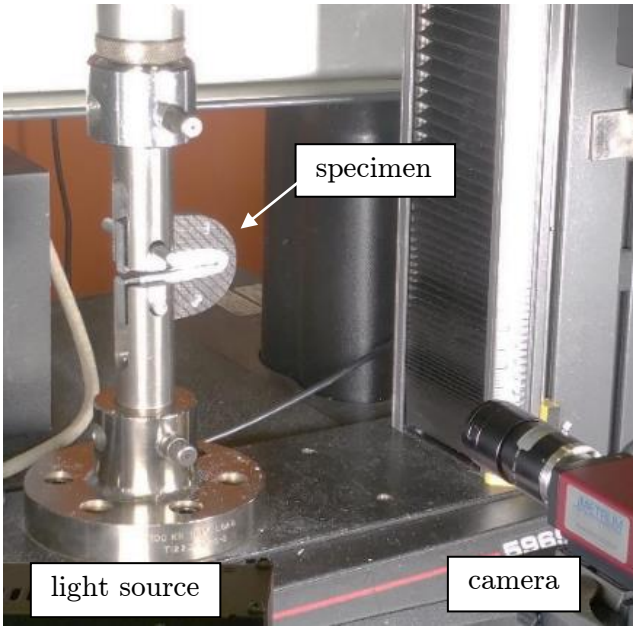


Figure 4.20: NCCT and ENCCT test set-up

4.5. Data reduction

An area method [171] was used to calculate the critical strain energy release rate at various crack lengths to populate the *R*-curve. This method was easily employed due to the thinned region providing clear optical through-thickness crack length measurement. The following formula was used to determine the critical strain energy release rate G_{IC} (J/m^2) of the material:

$$G_{IC} = \frac{\Delta E}{\Delta a.\, t} \tag{4.2}$$

where ΔE is the change in energy expended propagating the crack (J), Δa is the change in crack length (m), and t is the specimen thickness at crack (m)

The energy required to propagate the crack was calculated as the integral of the load versus displacement curve, ignoring the elastic energy stored within the specimen (Figure 4.21). The energy 'E' was correlated with the crack length taken from the video capture in the test at specific points to determine the critical strain energy release rates along the crack length. The benefits of this approach include its simplicity and independence from compliance calibration curves. The major drawback of the area method is the assumption of stable crack growth, where in reality the load drop during crack growth is an unstable event and therefore not necessarily a straight line, as presented in Figure 4.21. The reliance on the user's measurement of the crack length, which can be subjective to both parallax and human errors can also lead to uncertainty. It also assumes that upon unloading at any point, the load response curve would return to the origin, with negligible permanent plastic strain. This was proven true for the ENCCT specimen whilst undertaking the compliance curve calibration for the CC (Compliance Calibration) method. The S2-glass material however presented compliances during the 'stick' phases of loading that did not intersect the origin and may be attributed to the matrix crazing noticed. To determine whether plastic deformation did not occur outside of the translaminar crack front, non-destructive testing was employed post-test (see Section 4.7).

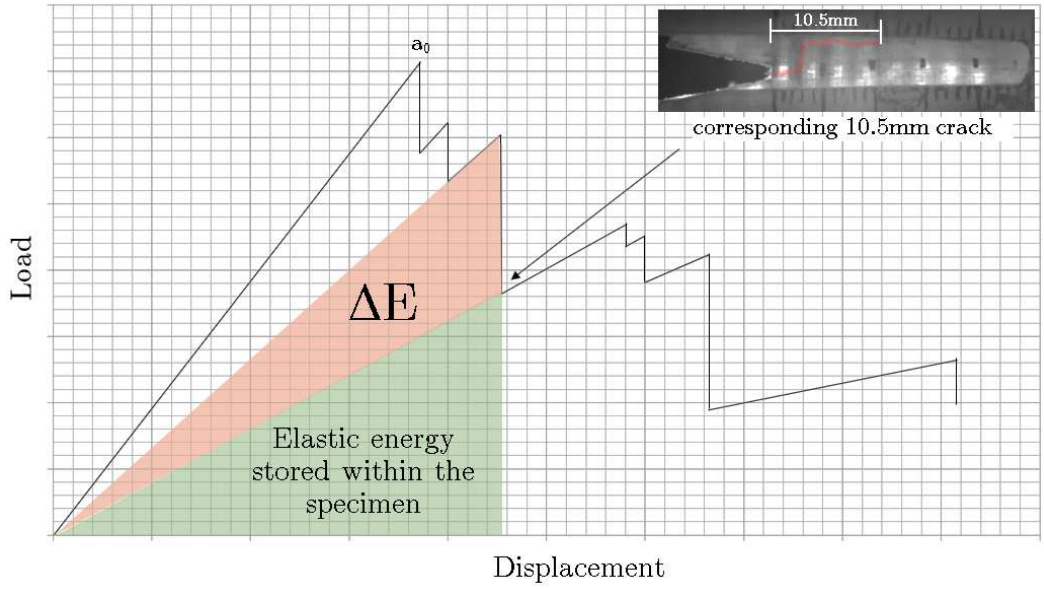


Figure 4.21: Illustration of the data reduction methodology using the area method

Figure 4.22 shows a typical crack growth made visible through the use of a backlight for the monolithic S2-glass composite NCCT specimens. The crack in this particular specimen could be seen to have propagated directly along the thinned region and jumped vertically in-plane along a tow to then continue its translaminar development at the boundary at the change of thickness. The monolithic S2-glass composite exhibited crazing along the thinned region prior to crack formation. It should be noted that it was important to distinguish the difference between matrix crazing (discolourment and change in translucency) and crack propagation by the slip stick behaviour of the crack growth.

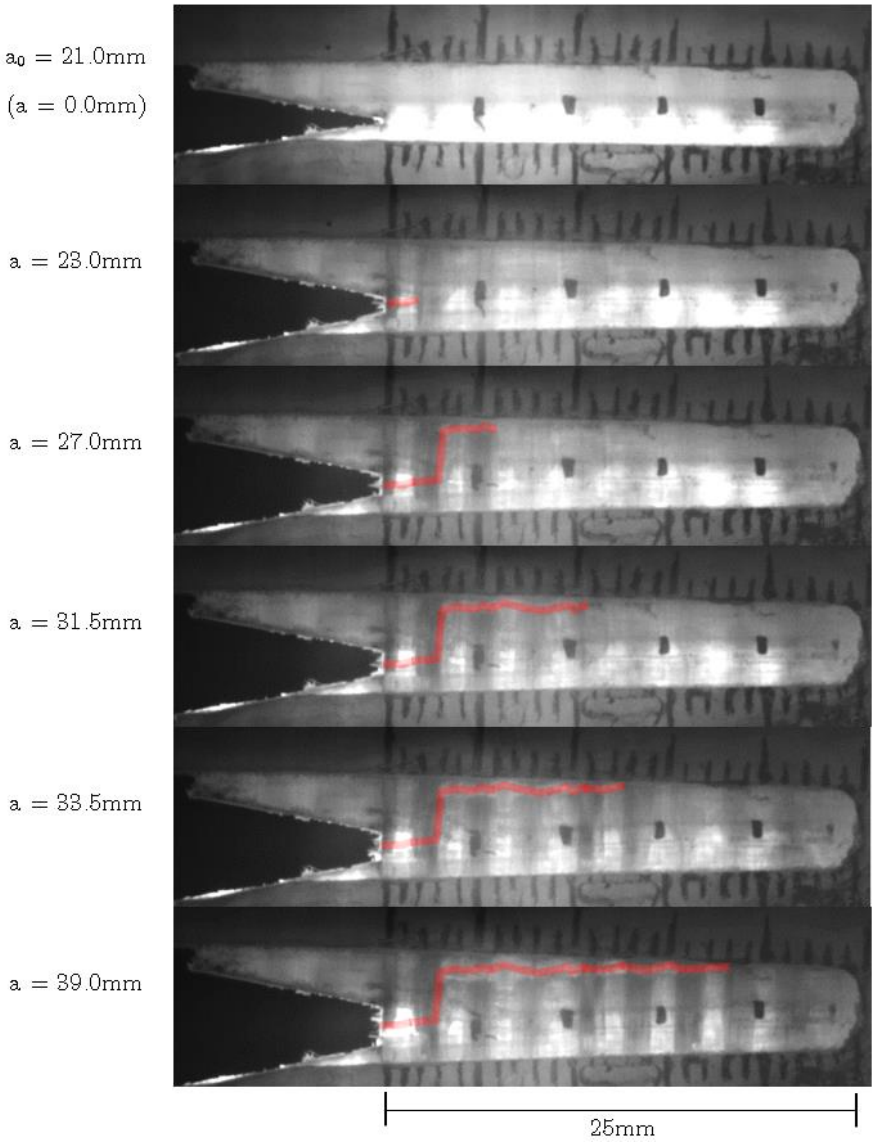


Figure 4.22: Optical crack growth through a representative monolithic S2-glass composite NCCT specimen (red indicates crack propagation)

As well as the area method, the MCC (Modified Compliance Calibration) method [171] was also used to calculate the critical strain energy release rates for the monolithic S2-glass composite, supporting the area method as an accurate means of data reduction for the NCCT specimen type. The MCC method involved determining a compliance calibration curve from the range of discrete crack lengths under linear elastic FE modelling. By plotting compliance (mm/N) versus crack length (mm), the compliance calibration curve for the monolithic S2-glass composite NCCT specimens were fit using the following function:

$$C = (\alpha a + \beta)^{\chi} \tag{4.3}$$

where a is the crack length, and α , β , and χ were calculated to best fit the experimental data [171]. The critical strain energy release rate was then calculated using the following formula:

$$G_{IC} = \frac{{P_c}^2}{2t}\frac{dC}{da} \tag{4.4}$$

where Pc is the critical load prior to crack growth for a given crack length, t is the thickness of cracked region at that crack length, and dC/da is the derivative of the compliance (C) with respect to crack length (a)

Similarly to the MCC method, a compliance calibration (CC) method [171] was carried out alongside the area method for the ENCCT intralayer fibre hybrid T700 carbon/Vectran specimens. The CC procedure followed the same data reduction as MCC except the compliance curve was derived experimentally by cutting to known crack lengths and measuring the initial elastic compliance before fracture initiation after each discrete cut to extend the crack.

4.6. Results

4.6.1. Compliance curves

Figure 4.23 shows the FE derived compliance calibration curve for the monolithic S2-glass composite NCCT specimens used in calculating the MCC method critical strain energy release

rates. Figure 4.24 shows the experimentally derived compliance calibration curve for the intralayer fibre hybrid T700 carbon/Vectran ENCCT specimens used in calculating the CC method critical strain energy release rates. It should be noted that due to the geometry, the possible crack length is much larger for the ENCCT compared to that of the NCCT test type.

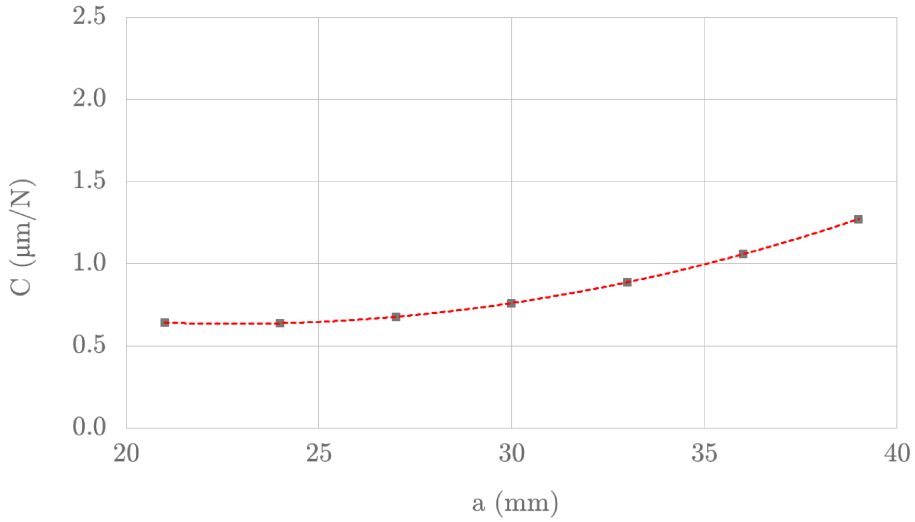


Figure 4.23: Monolithic S2-glass composite MCC method compliance calibration curve (FE derived) for the NCCT specimen type

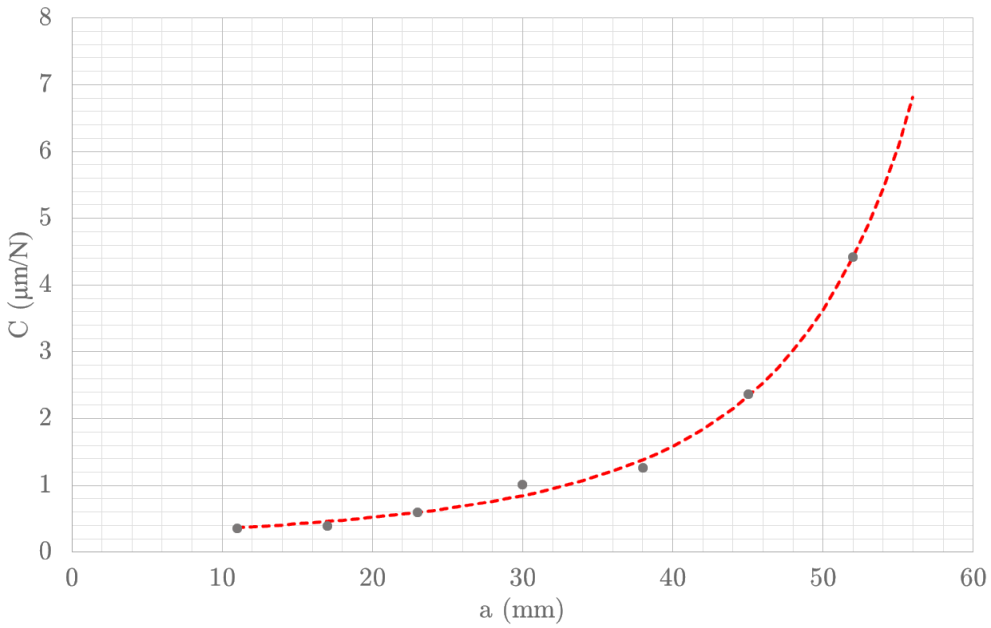


Figure 4.24: Intralayer fibre hybrid T700 carbon/Vectran CC method compliance calibration curve (experimentally derived) for the ENCCT specimen type

4.6.2. Critical strain energy release rates

Figure 4.25 shows the critical strain energy release rate calculated using the area method compared with that of the MCC method [171] for the monolithic S2-glass composite NCCT specimens. The initiation critical strain energy release rate was approximately 20 kJ/m^2. The propagation critical strain energy release rate can be seen to have been on average 156.5kJ/m^2 (CV=8.8%) for the MCC method and 131.6kJ/m^2 (CV=10.8%) for the area method. Propagation values were determined where the *R*-curves tended to plateau towards a constant value, where Δa>11mm.

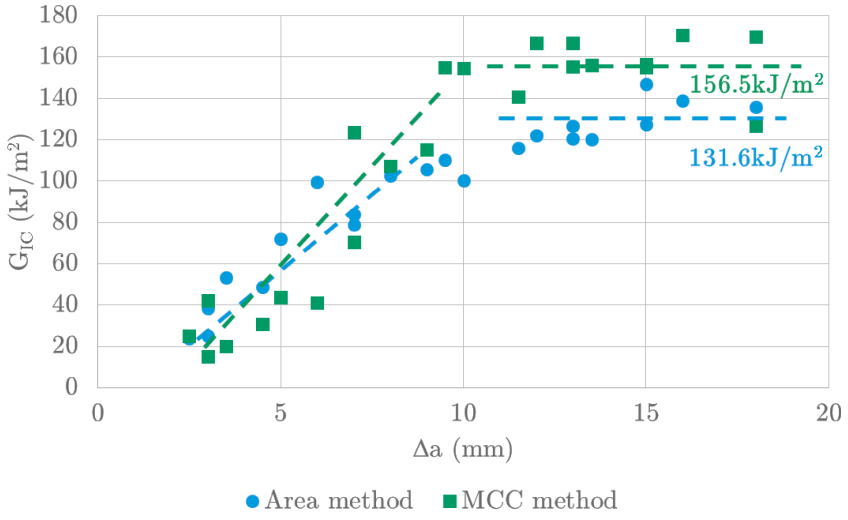


Figure 4.25: Representative critical strain energy release rate (G_{IC}) versus crack length (a) for the monolithic S2-glass composite NCCT specimens

Figure 4.26 shows the critical strain energy release rate calculated using the area method as compared with that of the CC method [171] for the intralayer fibre hybrid T700 carbon/Vectran ENCCT specimens. The initiation critical strain energy release rate can be seen to have been approximately 60 kJ/m^2 for the CC method and 30 kJ/m^2 for the area method. The propagation critical strain energy release rate can be seen to have been on average 173.2kJ/m^2 (CV=44.9%) for the CC method and 154.7kJ/m^2 (CV=15.4%) for the area method, both measured upon plateauing, where Δa>15mm.

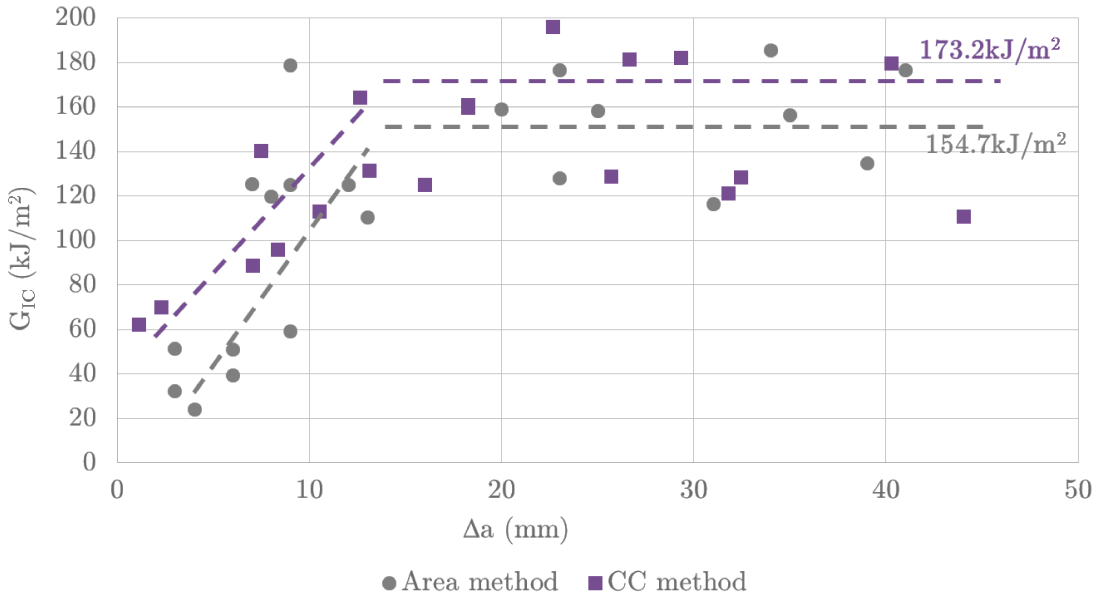


Figure 4.26: Representative critical strain energy release rate (G_{IC}) versus crack length (a) for the intralayer fibre hybrid T700 carbon/Vectran ENCCT specimens

Figure 4.27 shows the full *R*-curves for the monolithic S2-glass composite, monolithic T700 carbon composite, and interlayer fibre hybrid T700 carbon/S2-glass using the NCCT specimen type. Figure 4.27 also displays the intralayer fibre hybrid T700 carbon/Vectran *R*-curve using the ENCCT specimen type.

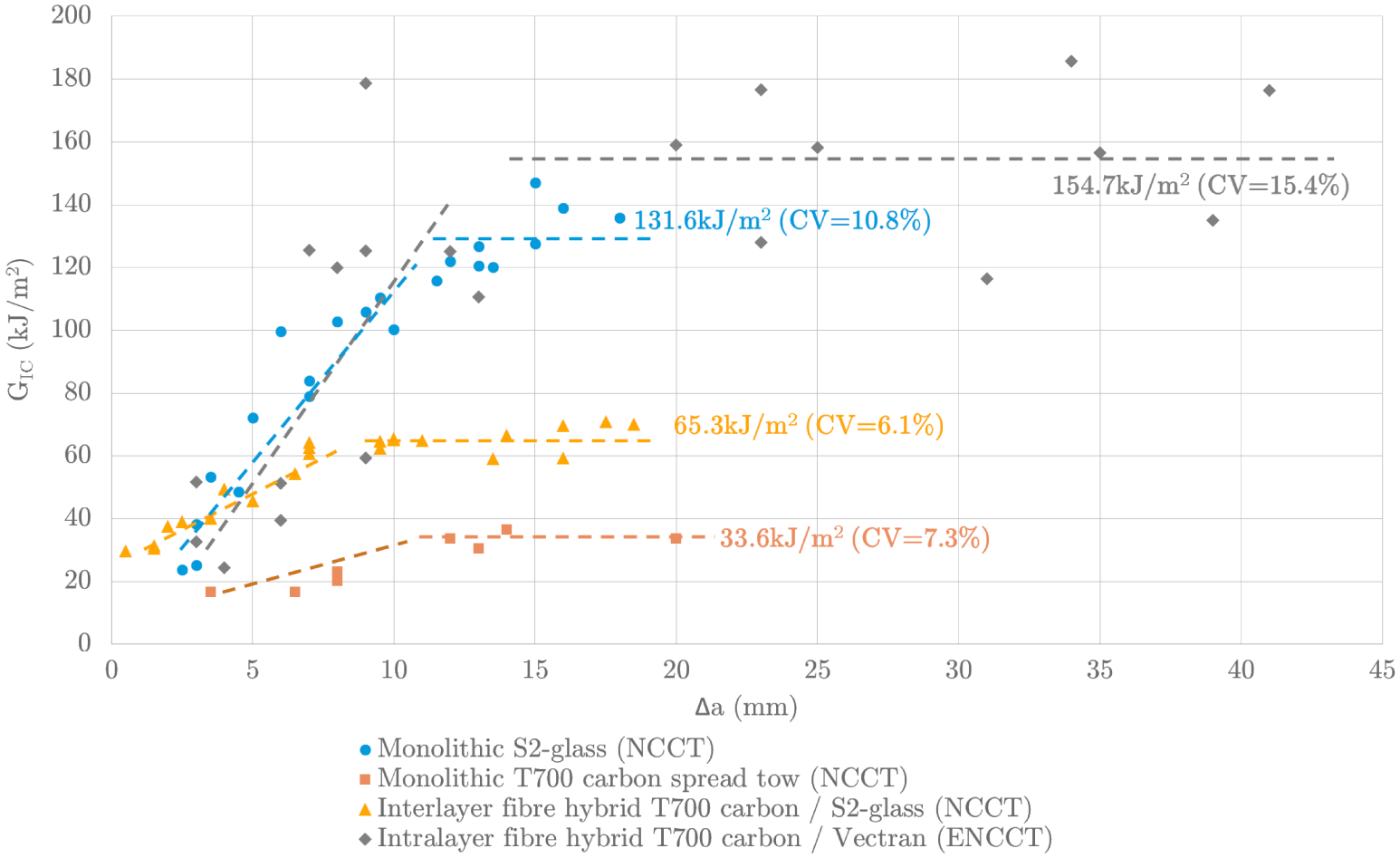


Figure 4.27: Representative composite *R*-curves using the area method for critical strain energy release rate versus crack length

4.7. Post-test analysis

The NCCT and ENCCT test specimens showed reasonable and repeatable critical strain energy release rates despite possible limitations associated with the difficulty in specimen manufacture, namely the alignment of the PTFE inserts and the hand-cutting of fibre plies. Comparing the results to other compact tension tests in the literature, the novel specimen designs exhibited a similar, if not lower, coefficient of variation across a range of data reduction methods [87], [171], [172]. The MCC method [171] (which determines a compliance calibration curve through FE models) and CC method [171] (which determines a compliance calibration curve through experimental testing) were compared to the area method in the form of *R*-curves and showed good correlation for the critical strain energy release rates in both initiation and propagation.

Post-test X-radiography (using Dibromomethane, 99% penetrant) was undertaken to determine any regions of unwanted damage remote from the crack, which could have led to erroneous results due to damage occurring outside of the crack growth region and through failure modes other than translaminar fracture. Figure 4.28 shows the post-test radiograph of the NCCT specimens (although the thinned region was not captured by the X-ray), indicating that all of the fracture energy had been dissipated through the translaminar crack, as required. Note than the white region within the monolithic T700 carbon composite specimen occurred at the latter stages of the test and at large crack lengths, where the specimen had fractured invalidly at the corner of the thinned region. Figure 4.29 shows the post-test x-radiograph of the ENCCT specimen, where penetrant impregnation could be seen within the thickened region due to fibre fracture. Due to there being no observed presence of delamination or fibre pull-out between the thick and thinned region of the specimens from the radiographs, a realistic fracture toughness value was considered to have been measured. It should be noted that the two arms of the ENCCT specimen were drawn apart completely to allow easier inspection post-test, hence the through-thickness fracture separating the specimen into two pieces at the rear of the specimen (Figure 4.29).

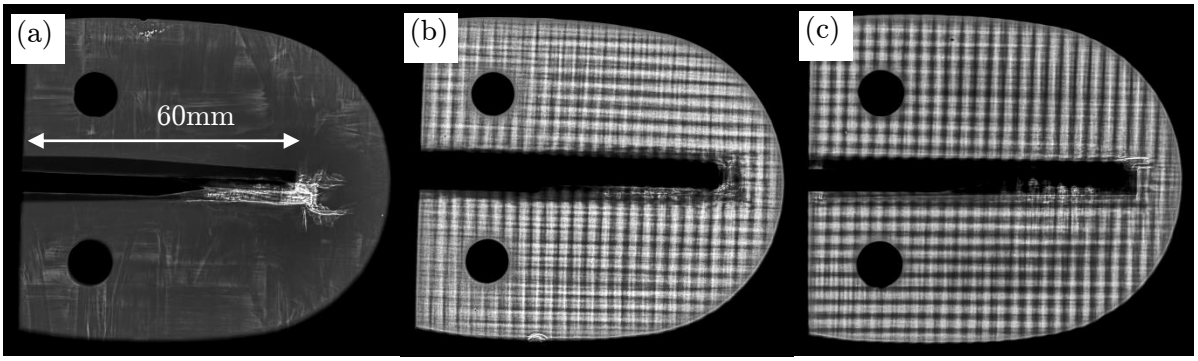


Figure 4.28: Post-test radiograph of NCCT specimens: (a) Monolithic T700 carbon composite, (b) Monolithic S2-glass composite, (c) Interlayer fibre hybrid T700 carbon/S2-glass

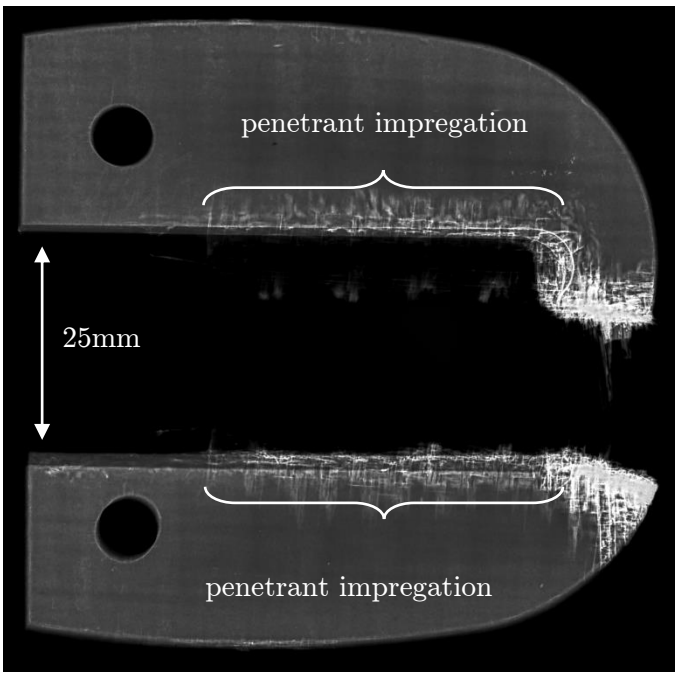


Figure 4.29: Post-test radiograph of ENCCT intralayer fibre hybrid T700 carbon/Vectran

Post-test SEM images were taken of the NCCT and ENCCT specimens and their corresponding pull-out lengths displayed (Figure 4.30 through to Figure 4.33). The resulting images were used to determine the mechanisms that controlled both the shape and magnitude of the R-curves presented in Figure 4.27. Firstly, the failed monolithic S2-glass composite NCCT specimen (Figure 4.30) showed uniform and regular fracture of the NCF fibre tows (hence the low scatter), with prominent fibre pull-out (hence the high fracture toughness). Whereas, the monolithic T700 carbon composite specimen (Figure 4.31) showed very little fibre pull-out (indicative of a low fracture toughness), and few data points were captured due

to its sporadic slip-stick crack behaviour. The fibre hybrids exhibited similar behaviour, with the interlayer T700 carbon/S2-glass NCCT specimen (Figure 4.32) showing large S2-glass pull-out, tending to control the crack path and hence reduce the slip-stick carbon spread tow behaviour noticed within the monolithic carbon composite. The *R*-curve for the interlayer hybrid could be seen to be midway between its monolithic composite counterparts, indicating that a 'rule of mixtures' approach may be applicable to fibre hybrid fracture toughness, although further work is required to demonstrate this conclusively. The ENCCT specimen intralayer fibre hybrid T700 carbon/Vectran presented sparsely separated Vectran tow pull-out lengths (since a 2x2 twill weave was used), leading to large scatter in the fracture toughness having been presented in the *R*-curve.

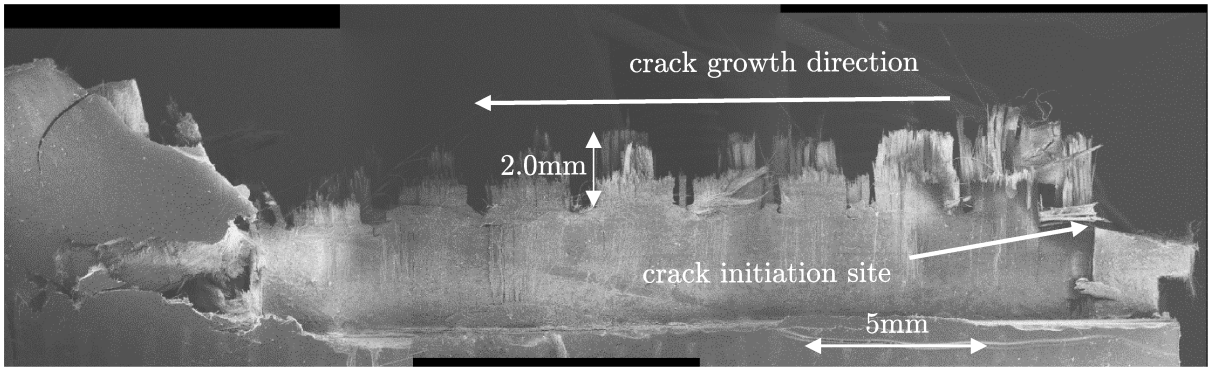


Figure 4.30: Electron micrograph of NCCT specimen, monolithic S2-glass composite

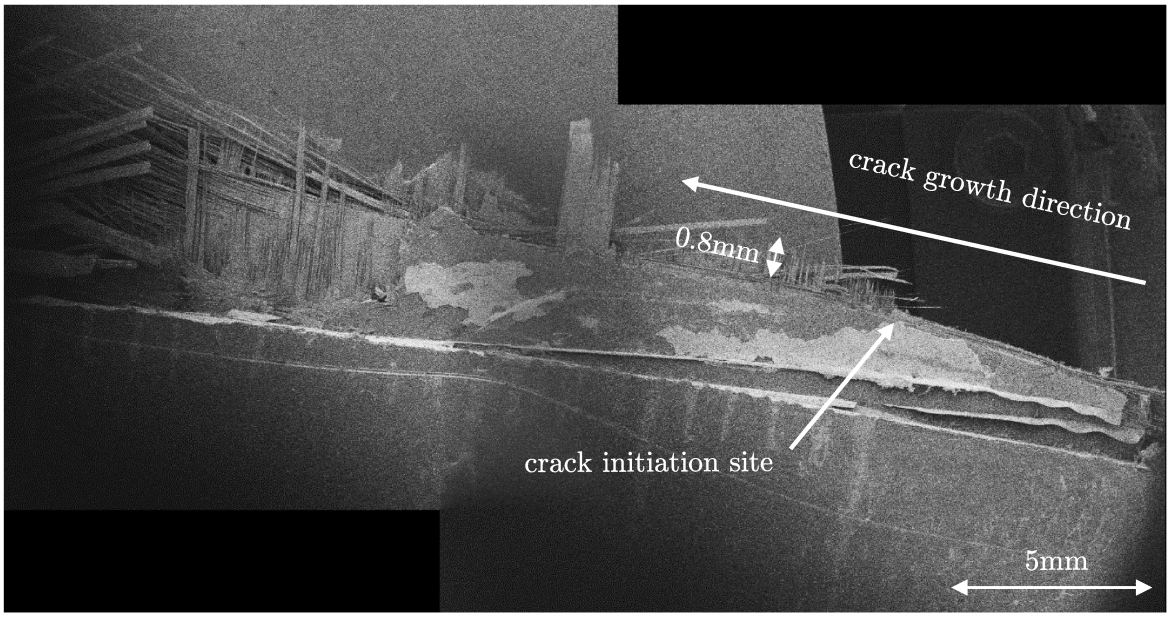


Figure 4.31: Electron micrograph of NCCT specimen, monolithic T700 carbon composite

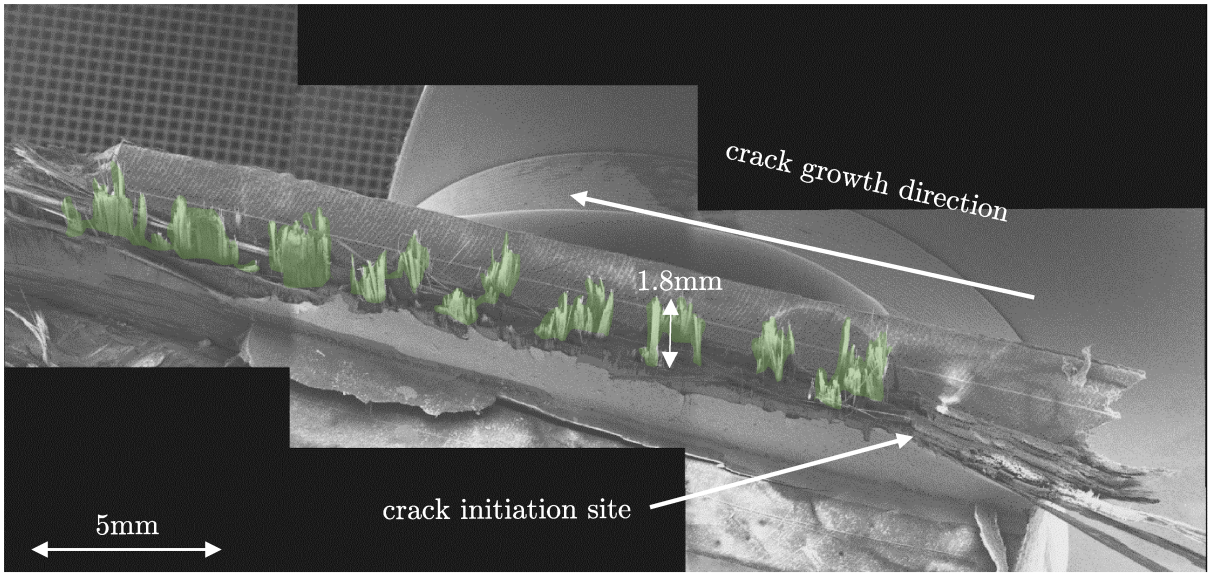


Figure 4.32: Electron micrograph of NCCT specimen, interlayer fibre hybrid T700 carbon/S2-glass composite (S2-glass fibres highlighted in green)

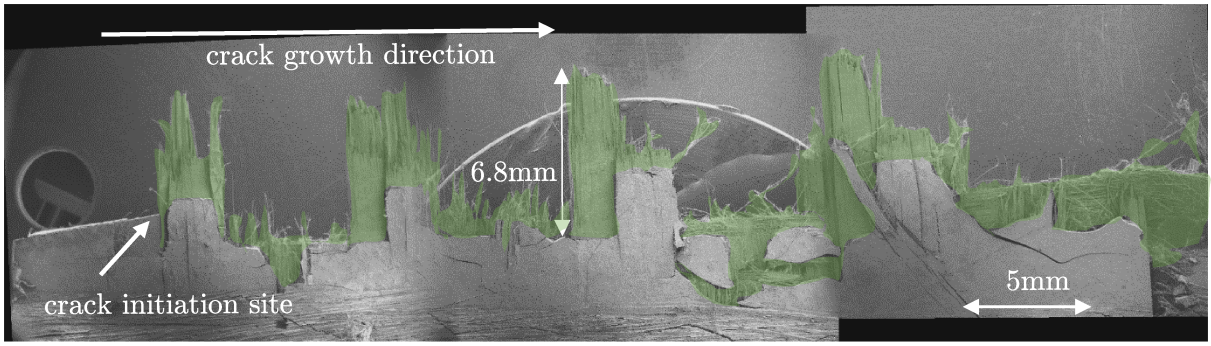


Figure 4.33: Electron micrograph of ENCCT specimen, intralayer fibre hybrid T700 carbon/Vectran composite (Vectran fibres highlighted in green)

Further testing is required to determine whether the NCCT and ENCCT specimen geometries are suitable for other materials and fibre architectures. However, due to the successful application of the NCCT specimen geometry regarding the extremely low compressive to tensile strength ratio (about 0.11) of Vectran composites [173], it is likely that the ENCCT geometry will suit the vast majority of fibre reinforced composites where premature compressive failure is an issue when adopting standard CT specimen types.

The calculation of the critical strain energy release rates were derived using an area method [90] which utilised multiple optical crack length measurements taken during testing. This negated the need for compliance calibration methods [171], which often rely heavily on the accuracy compliances derived from numerical modelling [87], [88], [172]. Both numerically FE-

based and experimental compliance calibration methods have however been used to support and verify the area method critical strain energy release rates, although the ENCCT method did present higher scatter within the results. This may be due to the T700 carbon/Vectrans' highly complex intrawoven fibre hybrid structure, but further work must be carried out with various material architectures to demonstrate this conclusively. Due to an accessible manufacturing approach and clear reduction of buckling and compressive failures, the ENCCT specimen geometry has become an attractive candidate for researchers facing similar premature compression/buckling failures when utilising the common CT type specimen geometries.

4.8. Summary

The research in this Chapter presented a wholly novel Compact Tension specimen design, developed to reduce the unwanted compressive failure that traditional CT specimens exhibited for materials with low compressive strengths relative to tensile strengths. The translaminar fracture toughnesses measured for the fibre hybrid composites were used in conjunction with the in-plane and interlaminar properties characterised in Chapter 3 to numerically model standard low velocity impact (Chapter 5) and structural component testing of the materials (Chapter 6), supporting the fracture toughness data determined within this Chapter.

The data proves the effect that the fibre architecture has upon the measured fracture toughnesses. Although the intralayer fibre hybrid T700 carbon/Vectran exhibited the largest fracture toughness, it also presented the highest amount of scatter, likely due to the 2x2 twill weave (promoting large pull-out bundles of Vectran fibres) as well as the fibrillous nature of the Vectran fibres themselves. The monolithic S2-glass composite presented the second largest fracture toughness, along with the monolithic T700 carbon spread tow composite presenting the lowest. The interlayer fibre hybrid T700 carbon/S2-glass presented a fracture toughness midway between its constituent monolithic composite counterparts, a phenomenon repeated elsewhere in the literature (see Section 2.3). It is advised that researchers experiencing the undesirable premature failure modes that traditional CT specimen geometries produce with high crimp and low compressive strength materials are urged to utilise the method presented in this chapter.

Chapter 4 publications and dissemination:

- **Journal papers:**
  - T. J. Katafiasz, L. Iannucci, and E. S. Greenhalgh, "Development of a novel compact tension specimen to mitigate premature compression and buckling failure modes within fibre hybrid epoxy composites," *Composite Structures*, vol. 207, 2019 [11]
- **Conference oral presentations:**
  - T. J. Katafiasz, "Interlaminar and Intralaminar Properties of Carbon Spread Tow and Glass Fibre Hybrid Composites for Cost Saving in the Mass Production of Automotive Components," in ECCM17 - 17th European Conference on Composite Materials, Munich, Germany, 2016 [14]
  - T. J. Katafiasz, "Development of a Novel Compact Tension Specimen for Fibre Hybrid Composites," in CompTest 2017: 8th International Conference on Composites Testing and Model Identification, Leuven, Belgium, 2017 [15]

5. Low velocity impact response characterisation of fibre hybrid composites

5.1. Introduction

The monolithic and fibre hybrid composites presented in Chapters 3 and 4 have been subjected to impacts on flat laminate plates following the ASTM D7136 [25] test standard using an Instron CEAST 9350 drop tower. To justify the feasibility of using fibre hybrid composites within structural automotive components, impact energies of 70J and 140J were chosen (to encompass both non-penetrative and penetrative impact through preliminary testing) using a 16mm tup diameter to represent a dropped tool or debris impact [118], [174], for comprehensive numerical model damage correlation. The following chapter outlines the experimental work undertaken to characterise the impact performance of the materials and correlation to a bilinear energy-based numerical modelling approach, providing support of the translaminar fracture toughnesses measured in Chapter 4 and the in-plane and interlaminar properties measured in Chapter 3.

5.2. Mechanical testing

5.2.1. Manufacture

A total of six 4mm nominally thick panels of 150mm x 100mm were waterjet cut from cured in panels of 600mm x 400mm for each of the monolithic and fibre hybrid composites under investigation (see Table 5.2 for layup). The panels were laid up to achieve the same volume fractions as those determined from the TGA burn-off and analytical microscopy in Section 3.1.4, and following the standard MTM57 epoxy resin curing cycle (ramping to 125°C, dwelled for 1 hour, and then an uncontrolled cool to room temperature of 23°C, under vacuum [159]). The panels were the C-scanned using a TechniTest NDT C-scanner to ensure that the panels were free of potential voids, inclusions, and delaminations, (see Figure 5.1, where the fibre architecture is visible without defects).

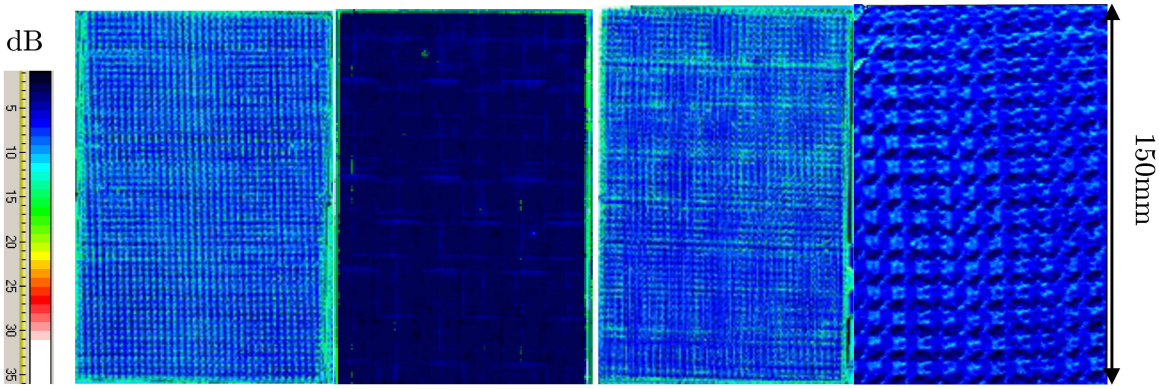


Figure 5.1: Impact panel representative pre-test C-scans plots, monolithic S2-glass composite, monolithic T700 carbon composite, interlayer fibre hybrid T700 carbon/S2-glass, intralayer fibre hybrid T700 carbon/Vectran (colour scale in dB)

5.2.2. Test set-up

The ASTM D7136 [25] test standard was used as a basis for the test rig set-up, where the flat laminates were held in place using four rubber tipped pins (Figure 5.2). The impact events were monitored using a Phantom v25.11 high speed optical camera at 100000 frames per second. Footage of the bottom face of each panel was recorded by placing a mirror underneath the impact panel, and lit using two Dedocool DC anti-flicker lights targeted at the panel face (Figure 5.3). A stand-alone data logger was used to record the camera footage and an Instron CEAST 9350 drop tower utilising a separate data logger was used to interpret the load cell located within the impactor tup. A calibrated 22kN load cell was used for all experiments.

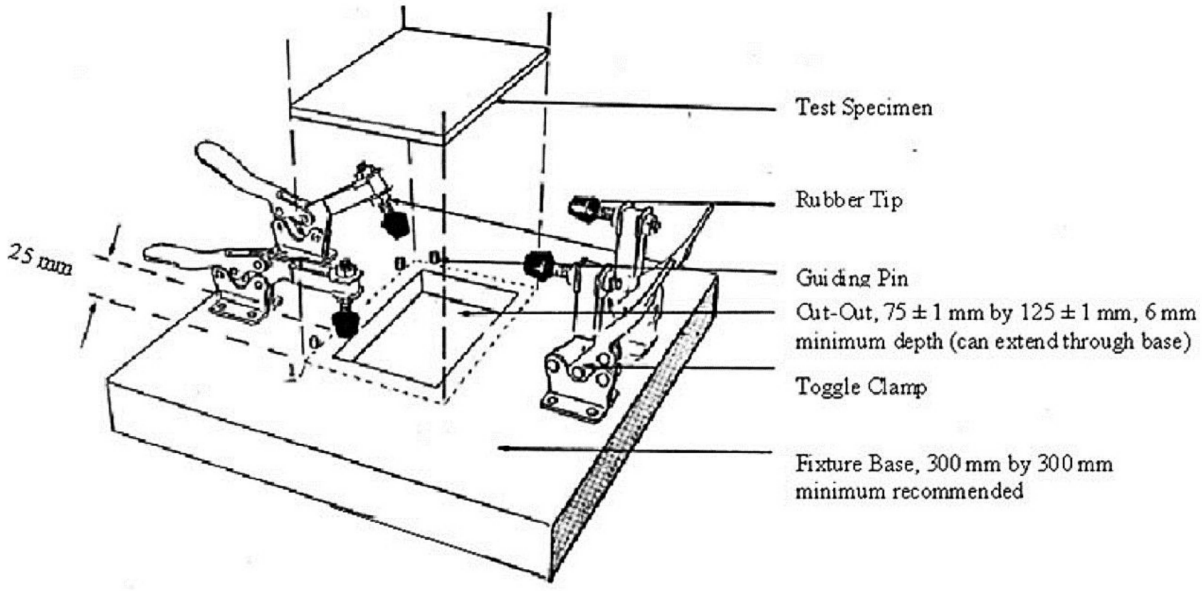


Figure 5.2: ASTM D7136 test fixture [25]

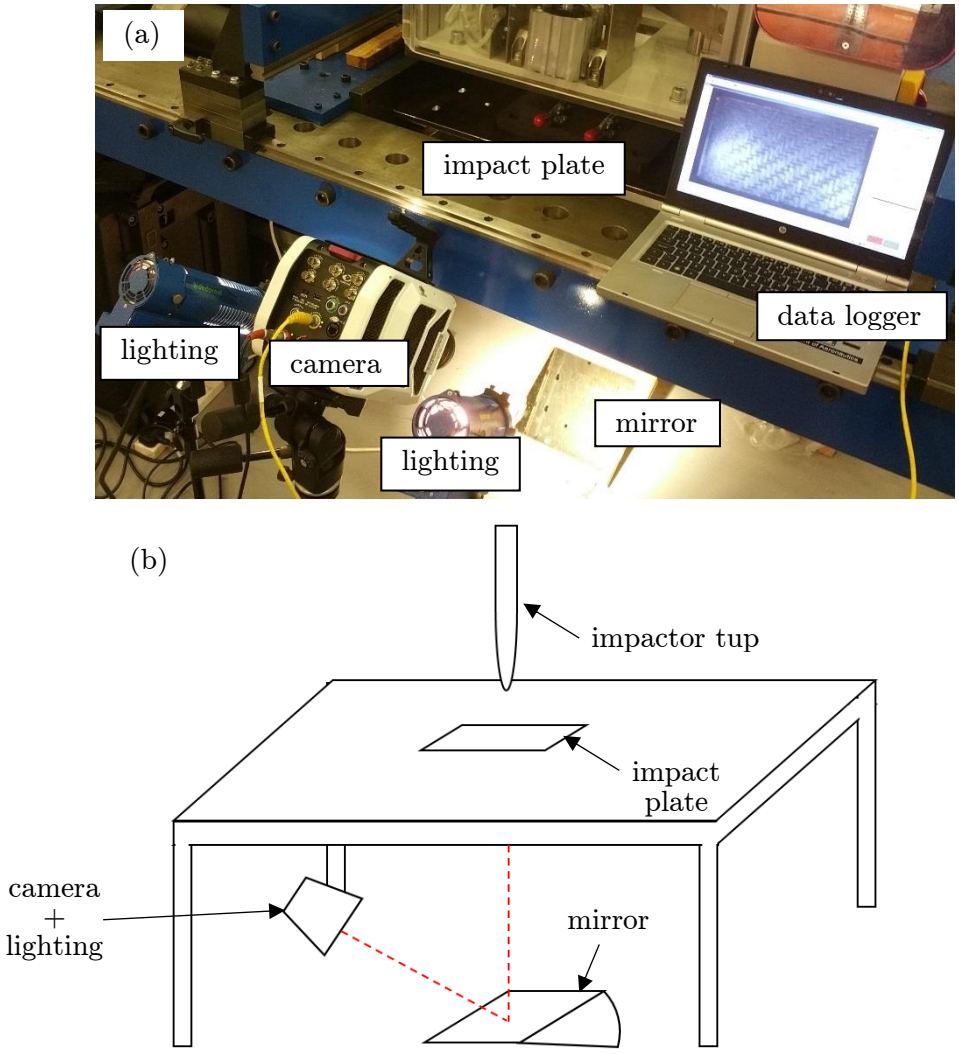


Figure 5.3: Low velocity impact plate test set-up: (a) photograph, (b) diagram

5.2.3. Data reduction

The Instron CEAST 9350 drop tower automatically integrated the 22kN load cell data to provide displacement and velocity readings of the impactor tup, since both the drop height and total drop mass were known for each event.

5.3. Finite element numerical modelling

5.3.1. Numerical model theory

Since four separate materials were tested, separate FE models using Abaqus 6.14 explicit were required for each test. Continuum shell elements (SC8R) were utilised for the in-plane composite ply properties as well as cohesive elements (COH3D8) for the interlaminar fracture

processes. A proprietary VUMAT (Abaqus user subroutine) material model was introduced to the models to be able to utilise the translaminar fracture toughness values determined in Chapter 4, since energy-based through-thickness composite failure material models were not available by default for Abaqus 6.14 explicit, as highlighted by Bogenfeld [109]. The subroutine was developed theoretically by Iannucci and Ankersen [122] and then ported to Abaqus using Fortran by Ankersen [163].

The in-plane damage modes considered in the material model include:

- Tensile failure in the (in-plane) 1-direction and the 2-direction
- In-plane shear failure in the 1-2 direction
- Compressive failure in the (in-plane) 1-direction and the 2-direction

The instantaneous moduli and strength (which are degraded as a function of their initial modulus and instantaneous stress respectively) for the damage modes were characterised by the following formulae:

$$E = (1 - d)E^0 \tag{5.1}$$

$$\sigma = \bar{\sigma}(1 - d) \tag{5.2}$$

where d=0 represents a wholly undamaged material, d=1 represents a fully damaged material, E is the instantaneous modulus in the desired mode, E^0 is the undamaged modulus, σ is the material strength, and $\bar{\sigma}$ is the effective stress (strain equivalence: a damaged volume of material under the nominal stress shows the same stress-strain response as a comparable undamaged volume under the effective stress $\bar{\sigma}$ [175])

Each of these components follow an energy-based bilinear plane stress-strain law (Figure 5.4). Once the integration point initiation strength (σ_c, ε_0) in the respective direction is reached, damage propagation is characterised using the following relationships until the maximum strain $\varepsilon_{max,}$ at which the material point is fully damaged (d=1) and the modulus E is degraded to zero.

Since:

$$\sigma(\varepsilon) = E\varepsilon$$

Substituting E from Eqn. (5.1):

$$\sigma(\varepsilon) = (1-d)E_0\varepsilon \tag{5.3}$$

$$\text{and,} \quad \sigma(\varepsilon) = \frac{\sigma_c}{\varepsilon_{max}-\varepsilon_0}(\varepsilon_{max}-\varepsilon) \tag{5.4}$$

Therefore equating (5.3) to (5.4):

$$d = \frac{\varepsilon_{max}}{(\varepsilon_{max}-\varepsilon_0)}\left[1-\frac{\varepsilon_0}{\varepsilon}\right] \tag{5.5}$$

Where:

$$\varepsilon_{max} = 2\frac{G_c}{\sigma_c l_x} \tag{5.6}$$

where d is the level of damage (between 0 and unity), ε_{max} is the maximum strain (d=1), ε_0 is the initiation strain, G_c in the translaminar fracture toughness (critical strain energy release rate), σ_c is the initiation strength, and l_x is the characteristic element length.

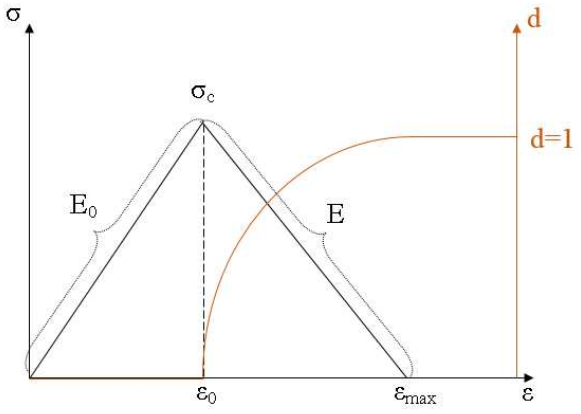


Figure 5.4: Bilinear energy-based stress-strain law with damage

By default, the characteristic element length is calculated by Abaqus as the square root of the area, which does not take into account the case of elements where the aspect ratio is not

constant, leading to a possible source of error. It is displayed as a user defined output variable where the characteristic length of each element in presented as a fraction of the maximum characteristic length. This law is also used to maintain mesh objectivity such that the damage propagation does not exceed the physical laws of energy conservation (ie the fracture toughness is not negative), whereby the maximum characteristic length [163] is given by rearranging Eqn. (5.6):

$$l_x < 2\frac{G_c E}{{\sigma_c}^2} \tag{5.7}$$

Since the in-plane shear load response curves of all the composites are non-linear (Section 3.1.3), the response of the stress-strain response was fully characterised using the following formula:

$$G_{12} = maximum\begin{Bmatrix} G_{ult} \\ G_{12init}e^{-\lambda(\gamma-\gamma_0)} - \lambda(\gamma-\gamma_0)G_{12init}e^{-\lambda(\gamma-\gamma_0)} \end{Bmatrix} \tag{3.1}$$

where γ is the shear strain, λ is a fitting constant, G_{12init} is the initial (linear) modulus, G_{ult} is the final (linear) modulus, S_{C0} is stress at which the response transitions from linear to non-linear, and $\gamma_0 = G_{12init}/S_{C0}$ is the strain at the linear-to-non-linear transition (Figure 5.5).

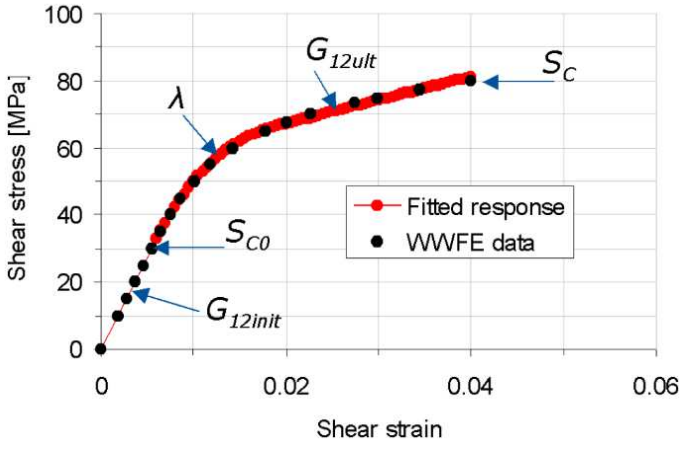


Figure 5.5: Non-linear in-plane shear curve fitting parameters [163]

The VUMAT material card required a total of twenty-nine user-defined input parameters, including the material properties, as shown in Table 5.1. The input deck material properties

were taken from the 0°/90° in-plane and translaminar fracture results presented in Chapters 3 and 4 where required, therefore all plies were assumed to be of equal modulus in 0° and 90° (directions 1 and 2). The β permanent strain constants were set to allow for permanent plastic strain post-impact, since much of the energy absorbed resulted in non-elastic rebound of partially degraded integration points, discussed in further detail in Section 5.3.2. The compressive fracture toughness was assumed to be equal to the tensile fracture toughness from the Compact Tension testing (Chapter 4), and since tensile fibre fracture dominated the impact event this assumption would not affect the resulting load response. The fibre and matrix compression 'debris' post failure strength was considered as the monolithic MTM57 matrix compression strength measured in Chapter 3, since any debris crushing would be a matrix dominated process. The failure flag was set to a value of '2', indicating material point deletion occurred at both failure in tension in the 1 and 2-directions. The other options available are as follows:

1. Fibre failure and non-zero matrix damage; or matrix failure and non-zero fibre damage (tension).

2. Both fibre failure and matrix failure (or fibre failure in woven/biaxial composites) (tension)

3. In plane shear failure

4. Fibre failure or matrix failure (tension)

5. Fibre failure. Deletion also occurs if matrix strain (direct or shear) exceeds ε_{del}

Table 5.1: VUMAT material input deck [163]

.cae entry	.inp entry	Parameter	Description
Line 1: Elastic constants			
1	1	E_{11}	Young's modulus in fibre direction
2	2	E_{22}	Young's modulus in matrix direction
3	3	ν_{12}	Major Poisson's ratio
4	4	G_{12init}	Initial in-plane shear modulus
5	5	G_{12ult}	Ultimate in-plane shear modulus
6	6		N/A
7	7		N/A
8	8		N/A
Line 2: Permanent set constants (must be >=1)			
9	1	β_1	Fibre tension
10	2	β_2	Matrix tension
11	3	β_3	In-plane shear
12	4	β_4	Fibre compression
13	5	β_5	Matrix compression
14	6		N/A
15	7		N/A
16	8		N/A
Line 3: Critical fracture energy per unit area			
17	1	G_{1CT}	Fibre tension
18	2	G_{2CT}	Matrix tension
19	3	$fact_{12}$	In-plane shear (γ_{ult} = $fact_{12}$ * γ_c) can be set to zero
20	4	G_{1CC}	Fibre compression
21	5	G_{2CC}	Matrix compression
22	6		N/A
23	7		N/A
24	8		N/A
Line 4: Initiation strength			
25	1	X_T	Fibre tension
26	2	Y_T	Matrix tension
27	3	S_C	In-plane shear
28	4	X_C	Fibre compression
29	5	Y_C	Matrix compression
30	6	$F_{interact}$	1 = S22-S12 interaction, 0 = no interaction (max stress)
31	7		N/A
32	8		N/A
Line 5: Debris strength, shear parameters and failure flag			
33	1	X_{CF}	Fibre compression post failure strength
34	2	Y_{CF}	Matrix compression post failure strength
35	3	λ	In-plane shear non-linearity parameter
36	4	κ	In-plane shear rate dependency factor
37	5	S_{C0}	In-plane shear stress where non-linear behaviour starts
38	6	F_{fail}	Failure flag
39	7	d_{max}	Maximum damage (fibre tension always one)
40	8	ε_{del}	Shear or matrix strain for material point deletion

5.3.2. Numerical model set-up

The FE models comprised of continuum shell stacks containing the composite material properties (each with three integration points, as required for bending), interspersed with cohesive element layers containing the interlaminar properties as presented in Table 5.2 and the material properties determined through the experimental testing in Chapters 3 and 4. The test rig was modelled using steel properties (Young's modulus = 200GPa, density = 8050kg/m^3) [176]. The impactor tup was modelled fully as a 16mm diameter hemi-spherical impact head using rigid shell elements (R3D4) with a point mass inertia of 2.392kg (as calculated by the Instron datalogger from the summation of the impactor components – load cell, drop-weight mass, and impact tup), encompassing the total experimental impactor geometry and mass. The test rig was fixed at the edges and the total model was one quarter of the experimental test with symmetry about the y-z and x-z planes to allow for faster computational time (Figure 5.6), since the fibre layups were 0°/90°, and hence symmetrical about both of these planes. The rubber-tipped location pins (ASTM D7136 [25]) were not modelled, since their constraining force was assumed to be negligible.

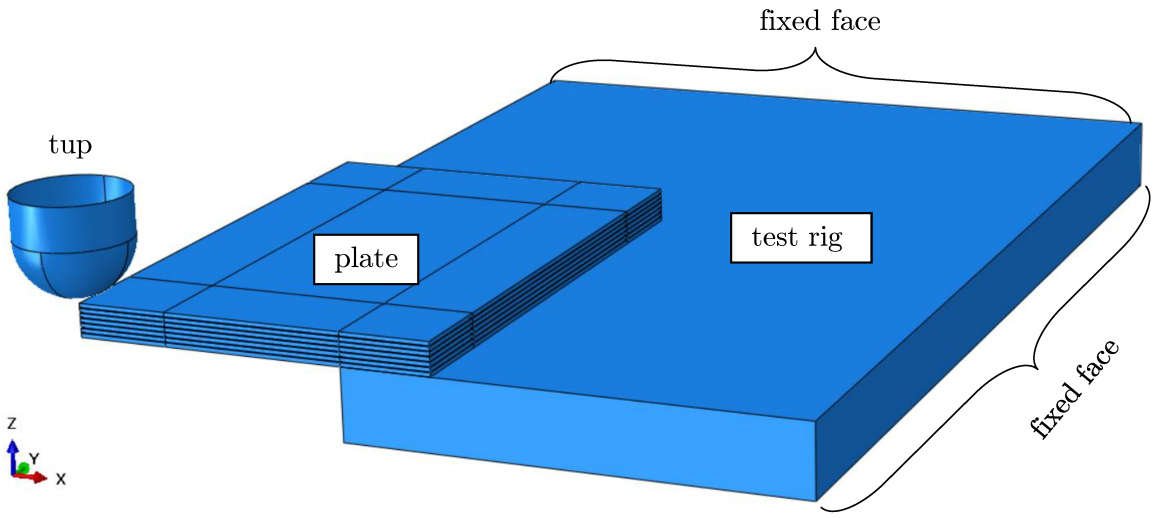


Figure 5.6: Impact plate FE quarter model set-up

Each of the models contained a minimum of six cohesive element layers given the physical layup in a sequence so as not split physical plies between element layers (Table 5.2). Six cohesive layers were utilised due to recommendation by Sun et al. [114], and also Ehrich [20]

who reported in his PhD thesis that a vast improvement in energy absorption and load response accuracy was noticed with an increase in cohesive layers, when using the same Abaqus VUMAT subroutine for monolithic composites. Each laminate was also modelled separately with no cohesive fracture to identify the effect of interlaminar failure upon energy absorption and load response. The contact for all parts was characterised using a global penalty-based interaction property, with a 'hard' normal contact criterion and a penalty tangential behaviour with a nominal friction coefficient of 0.3 [127].

Table 5.2: FE impact plate model thicknesses and continuum shell/cohesive element stacking sequences

Material (total cured thickness)	Layup, through-thickness (mm)
Monolithic S2-glass composite (5.408mm) (8 cohesive layers)	$\left[\overrightarrow{0.256\,G}\ \overrightarrow{0.256\,G}\ \overrightarrow{0.1\,coh}\right]_8\left[\overrightarrow{0.256\,G}\ \overrightarrow{0.256\,G}\right]$
Monolithic T700 carbon composite (4.596mm) (7 cohesive layers)	$\left[\overrightarrow{0.443\,5C}\ \overrightarrow{0.1\,coh}\ \overrightarrow{0.531\,6C}\ \overrightarrow{0.1\,coh}\right]_2\left[\overrightarrow{0.531\,6C}\ \overrightarrow{0.1\,coh}\ \overrightarrow{0.443\,5C}\ \overrightarrow{0.1\,coh}\ \overrightarrow{0.531\,6C}\ \overrightarrow{0.1\,coh}\ \overrightarrow{0.443\,5C}\right]$
Interlayer fibre hybrid T700 carbon/S2-glass (5.02mm) (8 cohesive layers)	$\left[\overrightarrow{0.089\,C}\ \overrightarrow{0.233\,G}\ \overrightarrow{0.1\,coh}\ \overrightarrow{0.089\,C}\ \overrightarrow{0.233\,G}\ \overrightarrow{0.089\,C}\ \overrightarrow{0.1\,coh}\ \overrightarrow{0.233\,G}\ \overrightarrow{0.089\,C}\right]_4$
Intralayer fibre hybrid T700 carbon/Vectran (4.618mm) (6 cohesive layers)	$\left[\overrightarrow{0.574\,CV}\ \overrightarrow{0.1\,coh}\right]_6\left[\overrightarrow{0.574\,CV}\right]$

$\overrightarrow{0.574\,CV}$ represents 1 x T700 carbon/Vectran continuum shell element that is 0.574mm thick, and $\overrightarrow{0.1\,coh}$ represents 1 x cohesive element that is 0.1mm thick

The continuum shell elements were assigned the composite material properties measured in Chapter 3. Each continuum shell element contained one composite ply which was allocated three integration points (to allow for bending), except for the monolithic T700 carbon composite model, which blocked composite plies into either 5 or 6 per element, due to their abundance. Abaqus continuum shell elements required through-thickness 'transverse shear stiffness' allocation, which was not physically measured. Due to this, the in-plane shear

properties were used in their place, since the out-of-plane shear moduli were assumed to be largely matrix-dominated. The interlayer fibre hybrid T700 carbon/S2-glass fibre ratios were kept equal to those determined through the TGA burn-off and the analytical microscopy as reported in Section 3.1.4.

The cohesive layers were set to a nominal thickness of 0.1mm for all of the models with the monolithic matrix strength providing the initiation strength of the layer. The monolithic matrix tensile modulus was used for the through-thickness direction and the initial in-plane modulus G_{12init} used for both the 1 and 2-directions (relating to the 't' and 's' directions), since this portion of the response was matrix dominated. A bilinear power law was used for the cohesive properties, where the Mode I and Mode II interlaminar toughnesses interacted together with quadratic power laws as follow for the stress-based initiation, and energy-based propagation [113]:

$$\left(\frac{\tau_n}{{\tau_n}^c}\right)^2 + \left(\frac{\tau_s}{{\tau_s}^c}\right)^2 + \left(\frac{\tau_t}{{\tau_t}^c}\right)^2 = 1 \tag{5.8}$$

$$\left(\frac{G_n}{{G_n}^c}\right)^\alpha + \left(\frac{G_s}{{G_s}^c}\right)^\alpha + \left(\frac{G_t}{{G_t}^c}\right)^\alpha = 1 \tag{5.9}$$

where the initiation strength τ^c and the fracture toughness (critical strain energy release rate) were represented in the 'n' (Mode I) and 's'/'t' (Mode II) directions (ie $G_n{}^c=G_{IC}$, and $G_s{}^c=G_t{}^c=G_{IIC}$), and α is a power indices used (with typical values of α usually between 1 and 2, and found by curve fitting to experimental data [177]).

Research by Camanho and Dávila [177] explored the behaviour associated with using the upper and lower bounds of α at 1 or 2. They noticed that at $\alpha=1$, thermoplastic PEEK composites tended to be predicted well through numerical analysis using the power law, whereas at $\alpha=1$ and $\alpha=2$ epoxy composites failed to accurately capture the response. It was suggested that the Benzeggagh and Kenane [178] criterion would be more suitable, but would require MMB (Mixed Mode Bending) tests to further determine the coefficients required. A value of $\alpha=1.5$ was utilised as a compromise using the power law, and for this analysis was considered acceptable, although further experimental testing would be required to conclusively verify this.

The global in-plane mesh size was set to 2.5mm and then refined around the impact region to capture the failure mode processes. Figure 5.7 shows the mesh generation scheme for the plate models, where 1mm mesh size was used at the origin of symmetry, around the x-z and y-z planes.

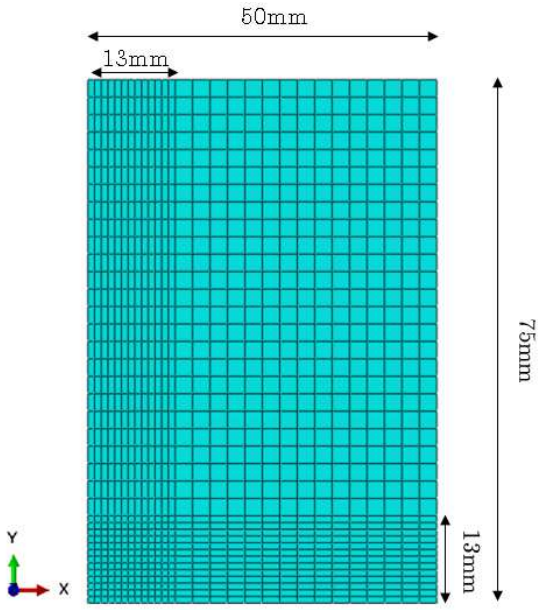


Figure 5.7: Mesh refinement and location in plate impact models (one quarter of the experimental test)

A mesh sensitivity study was employed using the monolithic S2-glass composite, since its unit cell was the smallest of the materials tested. A mesh size of 1mm was chosen since it was seen to be within the experimental scatter for maximum load, maximum deflection (Figure 5.8), and rebound velocity (Figure 5.9) (and therefore energy absorption, since they are directly proportional). There was also less noticeable distortion in the load response for the 1mm mesh size compared to the 4mm mesh size. A mesh refinement of 1mm around the impact site with 2.5mm globally elsewhere led to a total of 1064 elements per plate model layer.

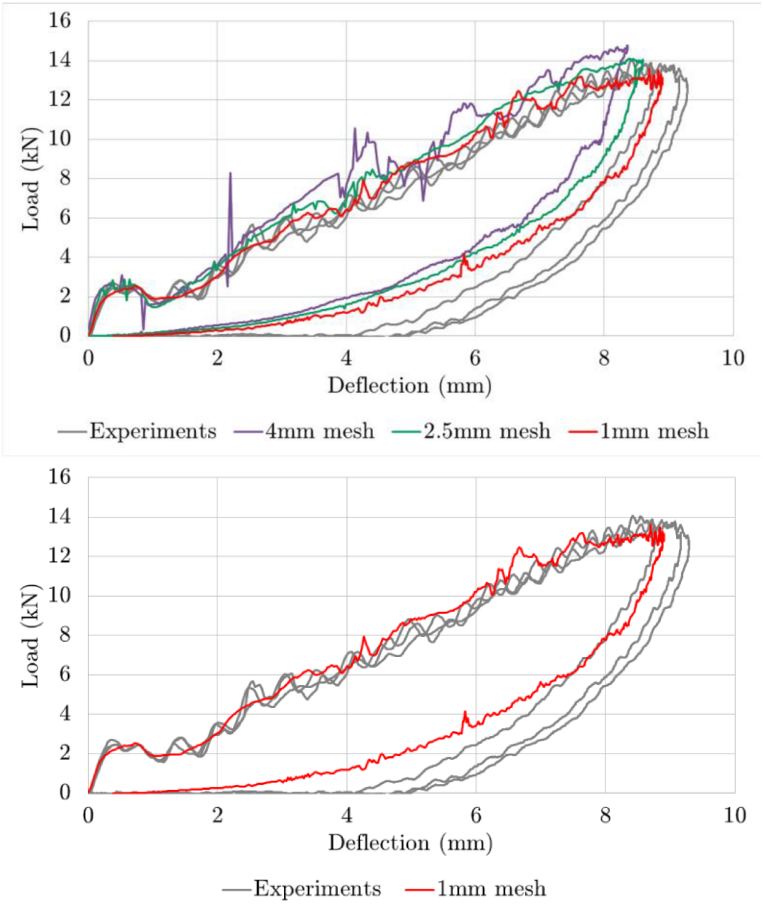


Figure 5.8: Mesh sensitivity study, 70J impact on monolithic S2-glass composite, load versus deflection

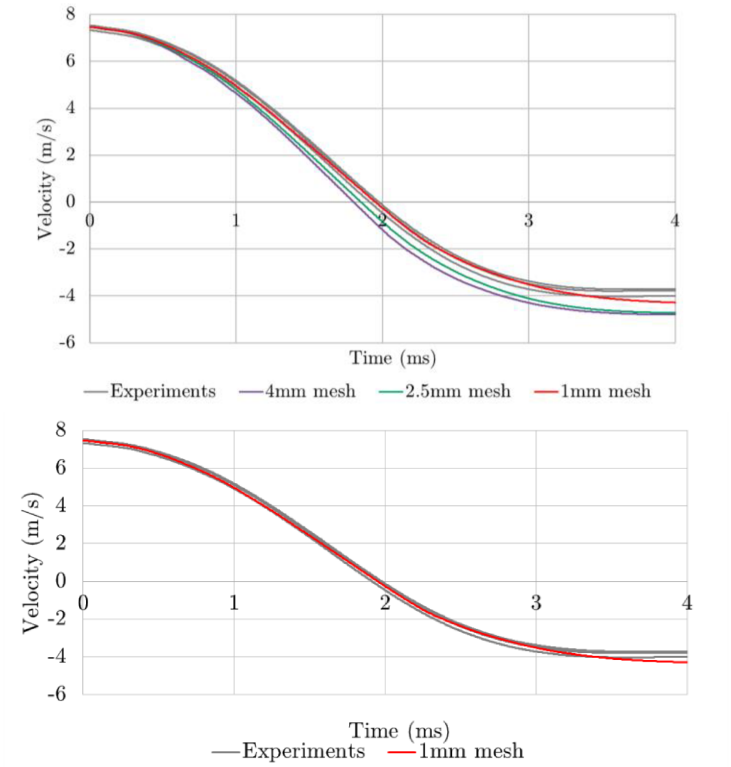


Figure 5.9: Mesh sensitivity study, 70J impact on monolithic S2-glass composite, velocity versus time

A mesh sensitivity study on the cohesive element thickness was conducted (Figure 5.10 and Figure 5.11). At a cohesive layer thickness of 0.5mm, the through-thickness comprising of cohesive elements was equal to that of the continuum shell elements. This resulted in an erroneous load response (Figure 5.10) and energy absorption (Figure 5.11), since the relatively low strength of the cohesive elements dominated the failure process by failing prematurely and hence reducing the overall stiffness of the plate. Where a cohesive layer thickness of 0.05mm was employed, the load response curve followed the experimental data except for the peak load, which was 9.56% higher than the average experimental peak load and thus outside of the experimental scatter. The 0.1mm thick cohesive layer model was closer to the experimental data for peak load and exit velocity (and thus absorbed energy) and was therefore chosen as the cohesive element thickness in the subsequent models.

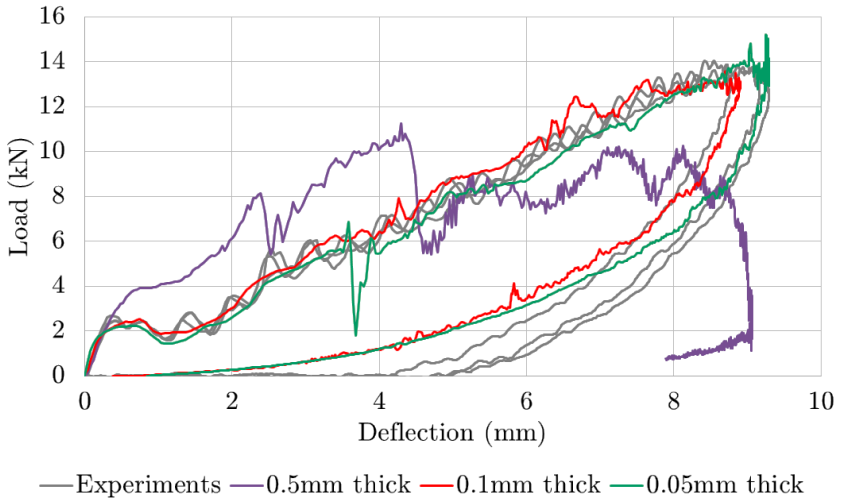


Figure 5.10: Mesh sensitivity study on cohesive thickness, 70J impact on monolithic S2-glass composite, load versus deflection

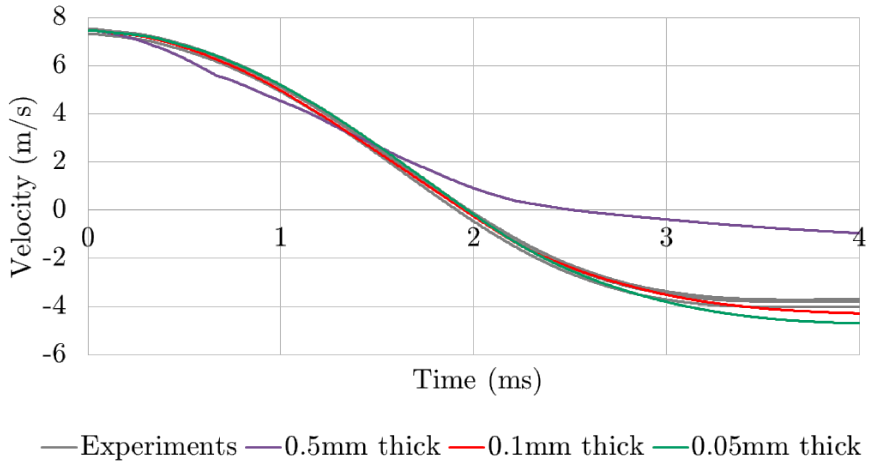


Figure 5.11: Mesh sensitivity study on cohesive thickness, 70J impact on monolithic S2-glass composite, velocity versus time

The tup was centred at the middle of the plate, 1mm above the top ply element layer. A predefined initial velocity of either -7.46m/s for a 70J or -10.66m/s for a 140J impact was applied in the z-direction to the impactor tups centre of mass, which was constrained to spatial movement in the z-direction. A gravity load card of -9.81m/s in the z-direction was applied throughout the entire model step and for all elements.

The numerical model was compared directly to the experimental testing by plotting the relative displacement, velocity, and load with respect to time taken from the centre of mass of the tup. The load was calculated by multiplying the total tup mass with the acceleration reported from the load cell.

Since glass fibres are known to be rate sensitive [149], a rate enhancement factor was employed by the Abaqus VUMAT subroutine. The subroutine allowed both the in-plane modulus and strength to be multiplied by the enhancement factor, which was governed by the following formula:

$$\alpha_{rate} = 2 - e^{-\frac{\dot{\gamma_{12}}}{k}} \tag{5.10}$$

where α_{rate} is the rate enhancement factor, $\dot{\gamma}_{12}$ is the shear strain rate, and k is a constant which determines where the enhancement occurs.

If $k = 0$, no enhancement factor was applied and the equation was ignored in the calculations. In-plane shear strain rate dependency for S2-glass/8552 epoxy composite was taken from the literature [148], and used with the above formula to estimate a suitable k value to be used for the S2-glass models. Figure 5.12 shows the literature value for a S2-glass/8852 composite with k values 10, 50, 100, and 500. A value of $k = 100$ was used for the S2-glass FE models, but the subroutine was not highly suitable due to its enforcement of a maximum enhancement factor of two. The range of strain rates in the experiment were much higher than those available within the model hence making the fit of the experimental data difficult without altering the subroutine directly. Highlighted in the literature survey (Chapter 2), a recent review by the research institution Swerea SICOMP [149] noted the scarcity of S2-glass in-plane shear rate sensitivity data, where the only experimentation available was seen to be that of Tsai and Sun [148]. The intralayer fibre hybrid T700 carbon/Vectran FE modelling was not

subjected to this enhancement factor since insufficient data in the literature was available for the hybrid regarding the effect that the Vectran fibres along with the T700 carbon interweave had upon the strain rate sensitivity (although the effect upon changing this sensitivity was seen to be negligible, see Appendix 10.2).

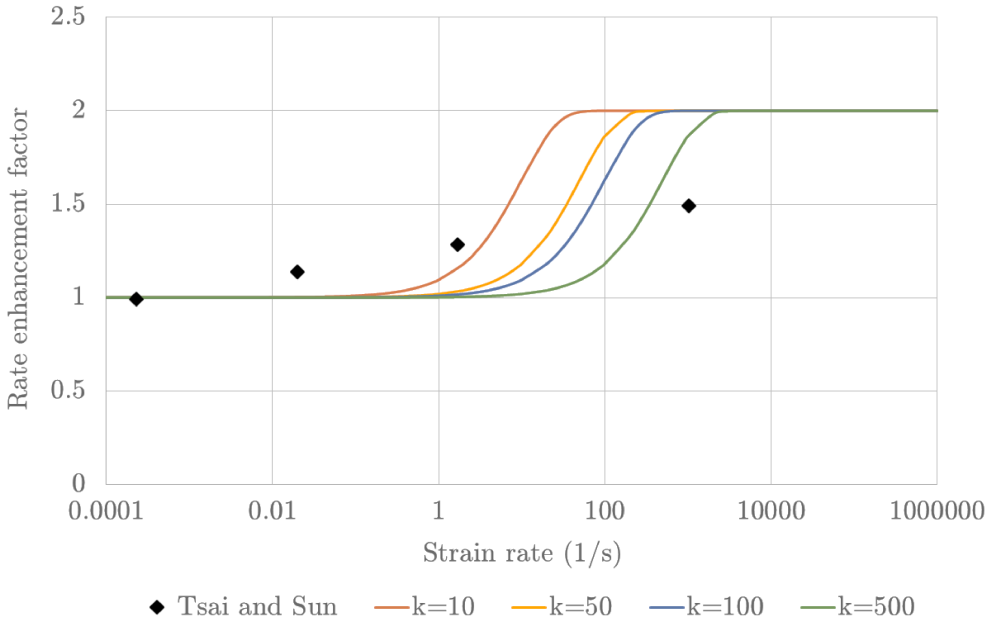


Figure 5.12: Strain rate enhancement, rate enhancement factor versus strain rate [148]

A permanent strain constant was utilised within the numerical model to allow for plastic strain to be permanently deformed upon damage of an element. The following formulae are derived from Hooke's Law, where a constant 'β' is introduced into the code to allow for permanent strain [122]:

$$\Delta\sigma = E\Delta\varepsilon + \Delta E_0\varepsilon \tag{5.11}$$

$$E = E_0(1-d) \tag{5.1}$$

$$\Delta E = -E_0 d \tag{5.12}$$

Substituting (5.1) into (5.11):

$$\rightarrow \Delta\sigma = E_0(1-d)\Delta\varepsilon + \frac{\Delta E}{(1-d)}\varepsilon \tag{5.13}$$

Substituting (5.12) into (5.13):

$$\rightarrow \Delta\sigma = E_0(1-d)\Delta\varepsilon - \frac{E_0 d}{(1-d)}\varepsilon \tag{5.14}$$

Incorporating permanent strain constant β and $\sigma = E_0\varepsilon$

$$\rightarrow \Delta\sigma = E_0(1-d)\Delta\varepsilon - \beta\frac{d\sigma}{(1-d)} \tag{5.15}$$

where σ is the stress, E_0 is the elastic modulus, E is the modulus after damage initiation, ε is the strain, d is the damage criteria (between zero and unity), β is the permanent strain constant.

To define the total plastic strain as a function of strain, Iannucci and Ankersen [122] provided a full analytical solution for the following relationship:

$$\Delta\varepsilon_{pl} = \left[1 - \frac{(1-A)\varepsilon + A\alpha\varepsilon_0(1-\beta)}{(1-d)\varepsilon} - \frac{\sigma A\alpha\varepsilon_0}{E_0(1-d)^2\varepsilon^2}\right]\Delta\varepsilon \tag{5.16}$$

where ε_{pl} is the total plastic strain, $A = \frac{\varepsilon_{max}}{\varepsilon_{max}-\varepsilon_0}$, and α is the strain rate enhancement factor

To verify the suitability of this constant and modelling approach, the largest value used for the beta constant (β =18.0) was applied to a single continuum shell element model containing the monolithic S2-glass composite properties using the VUMAT code with sufficient boundary conditions to allow for Poissons' ratio effects (Figure 5.13). The element was set to a cube of 1mm x 1mm x 1mm, being the same mesh size as that used at the impact site. A displacement in the z-direction (out of the page) of 1mm to ensure complete failure of the element (d=1), 0.125mm to reach d=0.25, and 0.3mm to reach d=0.6. It was noticed that at β=1, once the load was removed from the element, it returned back to its initial state, whereas when the load was removed before ultimate failure when β=18.0, some plastic strain was maintained permanently, as required by the model. The stress versus strain curves for these single element tests are shown in Figure 5.14. These stress versus strain plots were also verified by substituting the known variables into the analytical solution (Equation (5.16)).

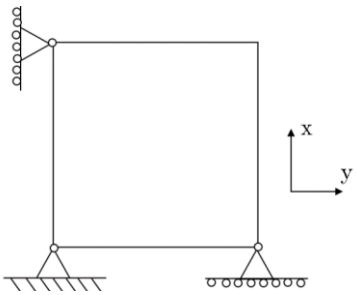


Figure 5.13: Single element boundary conditions

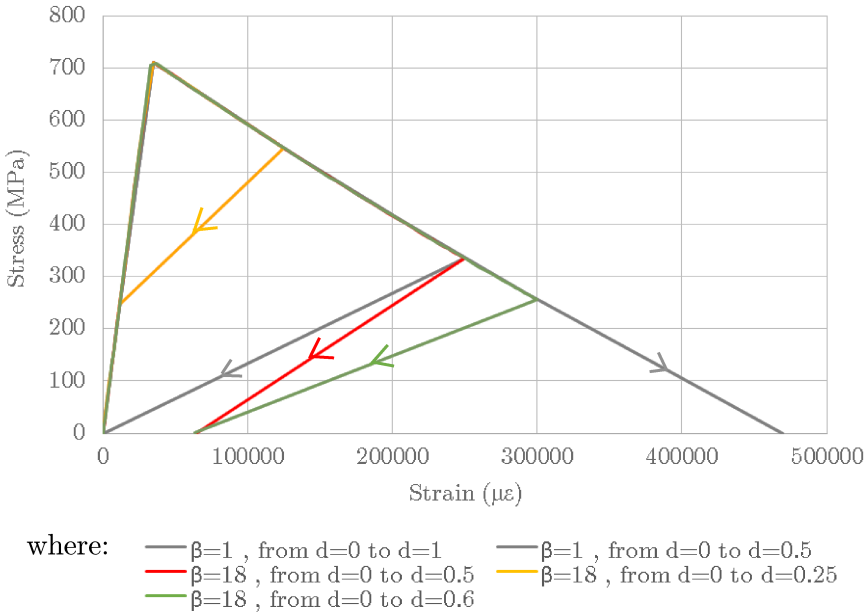


Figure 5.14: Loading and unloading of a single continuum shell element with permanent strain constants β=1 and β=18, in-plane stress versus strain

The translaminar fracture toughness was taken as the *R*-curve propagation values since the numerical model utilises a bilinear approach, requiring a single critical strain energy release rate. The numerical model's crack tip is inherently infinitesimally sharp, meaning that the experimental microcracks formed during the crack initiation could not be captured numerically. Furthermore, the length of the cracks produced during the impact are much longer than the initial crack region found within the *R*-curves and are thus dominated by the propagation fracture toughness. The intralayer fibre hybrid T700 carbon/Vectran fracture toughness used in the numerical models was lower than measured propagation value due to the large pull-out fibre lengths noticed within the failed ENCCT specimens, while still within the associated experimental scatter (see Appendix 10.3 for parametric study informing this value). These, as well as the other material properties are presented in Table 5.4.

The interlaminar properties used for the cohesive elements were taken from the mechanical testing (Chapter 3), presented in Table 5.3 with exception to the interlaminar fracture toughness of the carbon-carbon interface, which was taken from the literature [179] . The interlaminar out-of-plane elastic modulus were taken from the monolithic MTM57 resin testing whereas the in-plane modulus was taken from the respective initial in-plane shear modulus of the laminate being modelled (since it was matrix dominated). The interlaminar fracture toughnesses utilised the propagation values for the Mode I and Mode II tests (as with the

translaminar values). The density was taken as the monolithic MTM57 resin density found through experimental testing (Section 3.1.4). The initiation strengths in the shear directions were assumed to be equal to the normal direction, since the required experimental shear testing was not carried out.

Table 5.3: Interlaminar material properties used for FE modelling cohesive elements

	Monolithic S2-glass composite*[1]	Monolithic T700 carbon composite*[2]	Interlayer fibre hybrid T700 carbon/S2-glass	Intralayer fibre hybrid T700 carbon/Vectran
Elastic modulus out-of-plane (GPa), E_{nn}	2.68	2.68	2.68	2.68
In-plane shear modulus (GPa), E_{ss}, E_{tt}	5.68	4.25	5.57	2.48
Nominal initiation strength (MPa), τ_n^c, τ_s^c, τ_t^c	80.07	80.07	80.07	80.07
Mode I fracture toughness (kJ/m^2), G_n^c	1.15*[1]	0.70*[2]	0.80	1.74
Mode II fracture toughness (kJ/m^2), G_s^c, G_t^c	2.43*[1]	1.03*[2]	1.22	2.50
Power indices for energy-based power law, α	1.5	1.5	1.5	1.5
Density (kg/m^3), ρ	1202.8	1202.8	1202.8	1202.8

*[1]Monolithic S2-glass composite interlaminar fracture energies courtesy of S. Abdullah, Imperial College London [162]
*[2]Monolithic T700 carbon composite interlaminar fracture energies from literature [179]

Table 5.4: Material properties used for impact plate FE modelling, continuum shell elements

	Monolithic S2-glass composite	**Monolithic T700 carbon composite**	**Intralayer fibre hybrid T700 carbon/Vectran**
Elastic modulus (GPa), E_{11}/E_{22}	22.00	65.11	29.82
Poisson's ratio, ν_{12}	0.085	0.035	0.027
Initial in-plane shear modulus (GPa), G_{12init}	5.68	4.25	2.48
Ultimate in-plane shear modulus (GPa), G_{12ult}	0.20	0.21	0.09
Translaminar fracture toughness (kJ/m²), $G_{1CT}/G_{2CT}/G_{1CC}/G_{2CC}$	131.6	33.6	142.0
Initiation strength (MPa), tension, X_T/Y_T	719.77	1183.27	671.83
Initiation strength, in-plane shear (MPa), S_C	83.66	114.41	58.74
Initiation strength (MPa), compression, X_C/Y_C	371.81	762.00	165.78
Fibre/matrix post failure strength (MPa), X_{CF}/Y_{CF}	116.08	116.08	116.08
In-plane shear non-linearity factor, λ	51.0	33.5	24.0
In-plane shear rate dependency factor, κ	100.0	0.0	0.0
In-plane shear stress where non-linear behaviour starts (MPa), S_{C0}	2.67	0.74	1.77
Density (kg/m³), ρ	1904.6	1532.9	1574.9
Permanent strain constant, β	14.0	18.0	10.5

5.4. Non-destructive testing

To compare the degradation of the cohesive elements within the numerical modelling to the delamination extent from the experimental testing, C-scanning was employed. The post-tested panels were submerged within a water bath and an ultrasonic probe was used to conduct a 'mirror-echo' type analysis using a TechniTest NDT C-scanner, as shown diagrammatically in Figure 5.15. The echo of the beam on the back face was used to determine any potential voids, inclusions, and delaminations. The gate set-up at the back-face echo location was used to output an effective plot of the delaminated area. Fiji/ImageJ ver. 1.51h [166] was then used to measure the shape of the delamination as well as the affected area. From this, the failed cohesive plies within the FE model could be compared directly to the experimental tests to effectively deduce whether the interlaminar fracture toughnesses modelled were in the correct order of magnitude and shape.

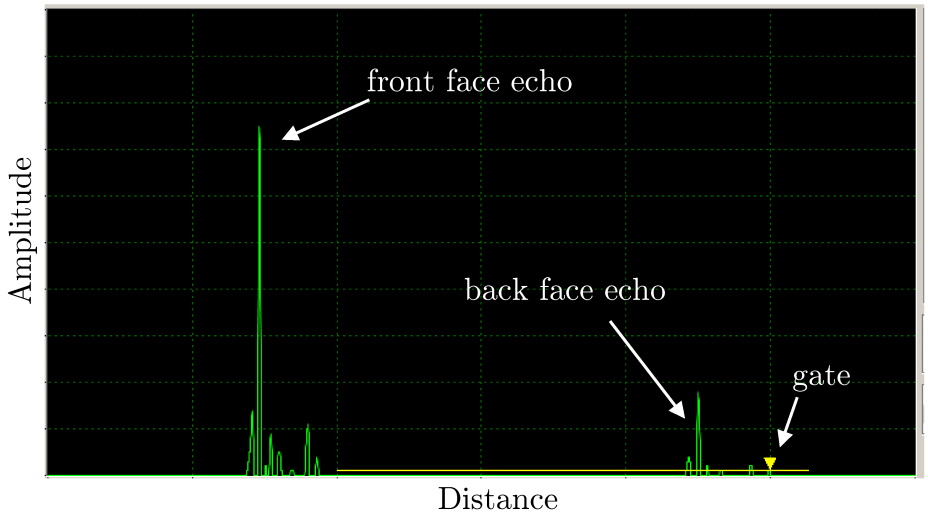


Figure 5.15: Ultrasonic C-scan of failed experimental specimens, back face delamination analysis

5.5. Experimental testing and numerical modelling of flat plate impacts

The following Section outlines the complete experimental testing and numerical modelling for the monolithic S2-glass composite, monolithic T700 carbon composite, interlayer fibre hybrid T700 carbon/S2-glass, and the intralayer fibre hybrid T700 carbon/Vectran impact panels following the ASTM D7136 [25] test standard. Table 5.5 and Table 5.6 present the translaminar damage by comparing the experimental and numerical tensile fibre fracture (on the models containing multiple cohesive layers) on the back-face of the impact panels for 70J and 140J impact energies respectively (although only one panel for each material was photographed, and the other panels were cut for microscopy). Table 5.7 and Table 5.8 present the experimental C-scans alongside the numerical cohesive layer degradation plots, comparing the areas produced through varying numbers of cohesive layers in the numerical models.

The back faces of one of each impact plate material was photographed and the image processing software Fiji/ImageJ ver. 1.51h [166] was used to optically determine the total tensile crack length by calibrating the scale to the plate edge dimensions (150mm x 100mm). This value was then compared to the corresponding FE model damage plots.

The load response curves for the experimental and numerical data are discussed, highlighting the advantages and drawbacks of the modelling approach. Optical microscopy along with the high speed camera footage is utilised to further understand the failure modes associated with the impact events and the effect of fibre hybridisation upon the responses.

Table 5.5: Back face damage for 70J plate impacts, experimental versus numerical

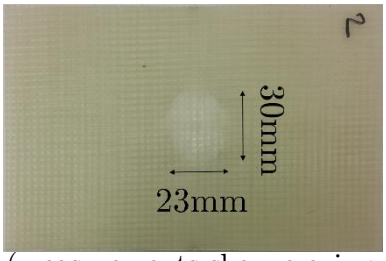
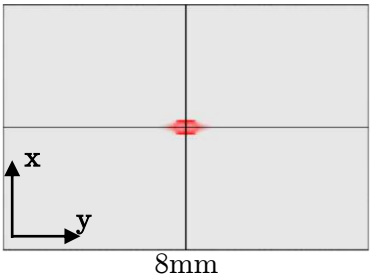
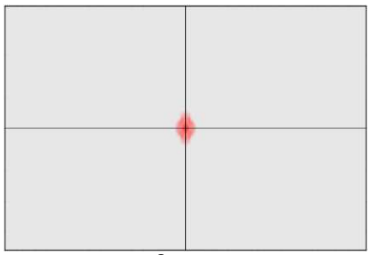
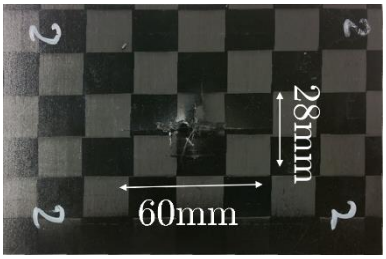
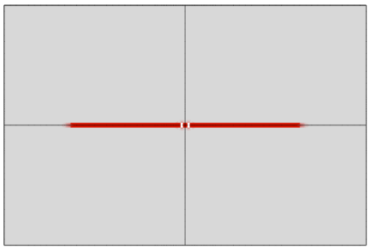
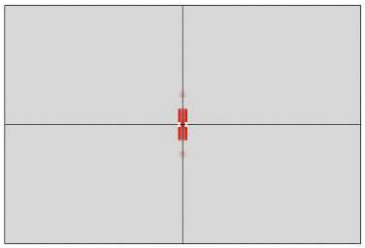
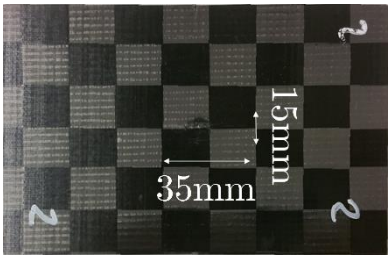
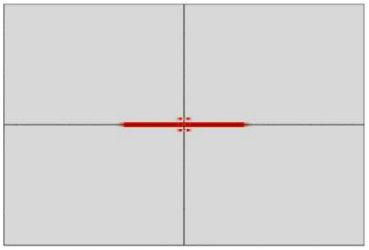
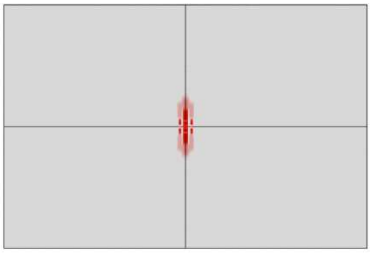
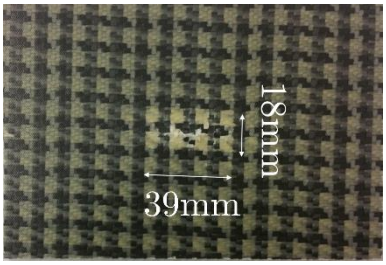
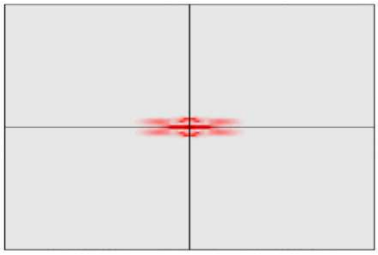
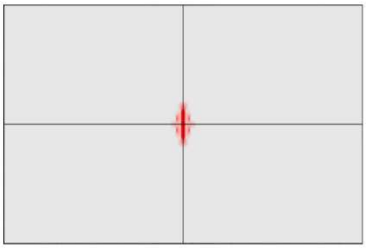
Experimental (representative)	Numerical (containing multiple cohesive layers)	
Visible back-face fibre damage	**Crack length (y-direction)**	**Crack length (x-direction)**
Monolithic S2-glass composite (8 cohesive layers)		
 (measurements show crazing, fibre fracture was negligible)	 8mm	 0mm
Monolithic T700 carbon composite (7 cohesive layers)		
	 95mm	 23mm
Interlayer T700 carbon/S2-glass (8 cohesive layers)		
	 50mm	 13mm
Intralayer T700 carbon/Vectran (6 cohesive layers)		
	 17mm	 12mm

Table 5.6: Back face damage for 140J plate impacts, experimental versus numerical

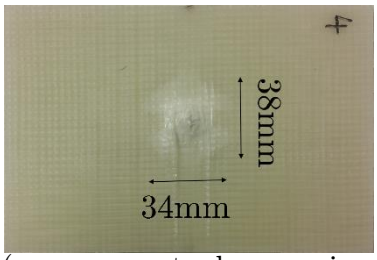
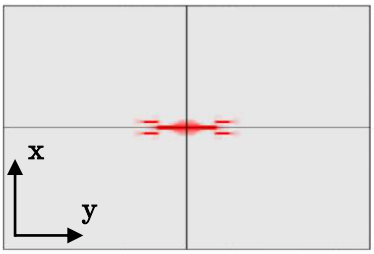
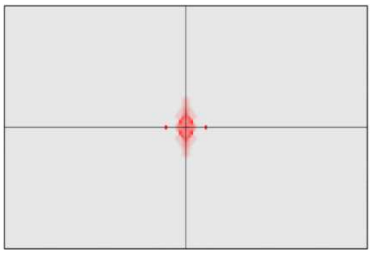
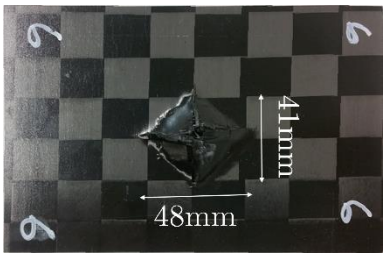
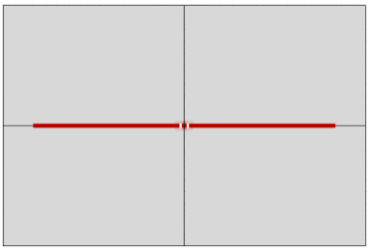
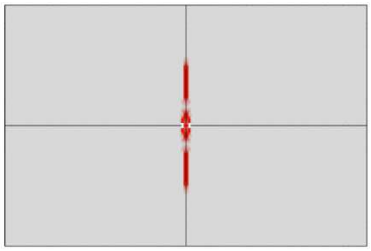
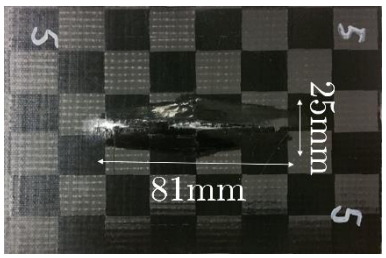
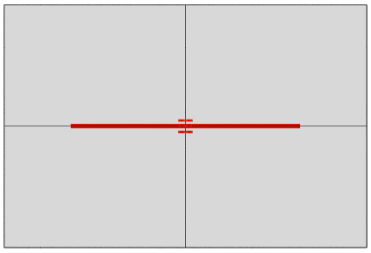
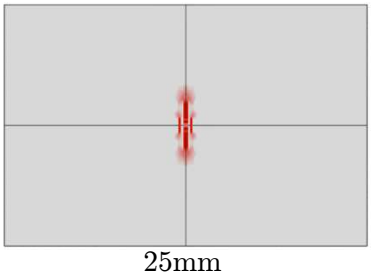
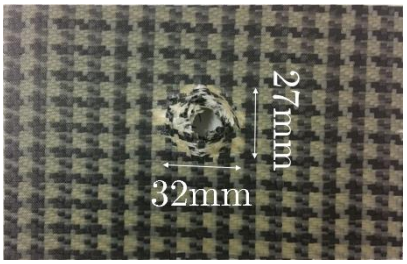
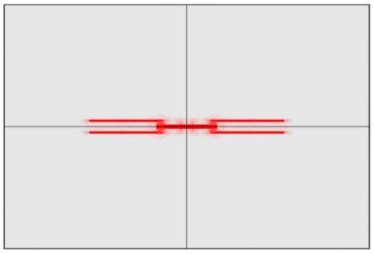
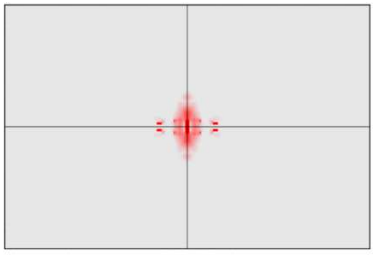
Experimental (representative)	**Numerical (containing multiple cohesive layers)**	
Visible back-face fibre damage	**Crack length (y-direction)**	**Crack length (x-direction)**
Monolithic S2-glass composite (8 cohesive layers)		
 (measurements show crazing, fibre fracture was difficult to distinguish optically)	 35mm	 6mm
Monolithic T700 carbon composite (7 cohesive layers)		
	 125mm	 50mm
Interlayer T700 carbon/S2-glass (8 cohesive layers)		
	 95mm	 25mm
Intralayer T700 carbon/Vectran (6 cohesive layers)		
	 80mm	 12mm

Table 5.7: Delamination (interlaminar) failure for 70J plate impacts, experimental versus numerical (not to scale)

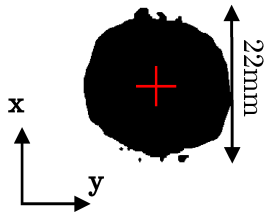
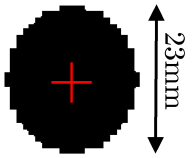
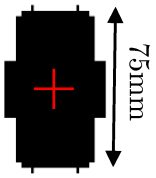
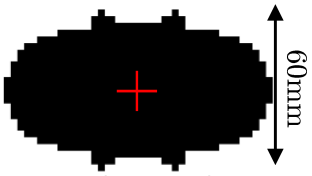
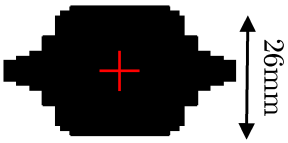
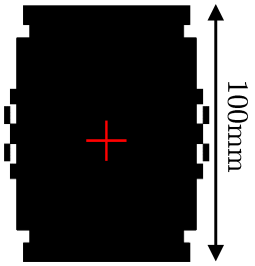
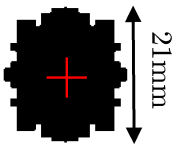
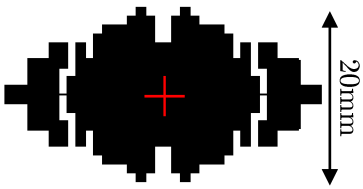
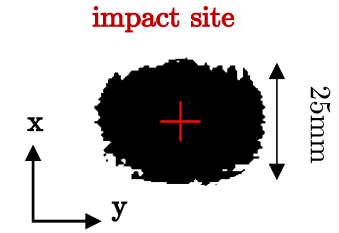
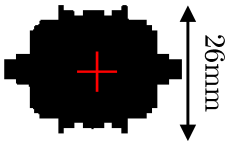
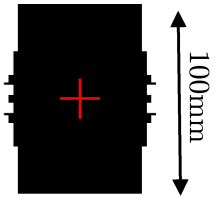
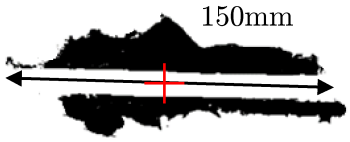
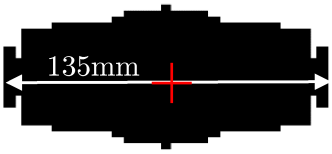
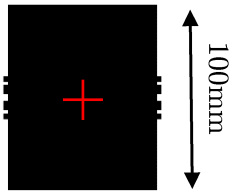
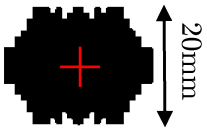
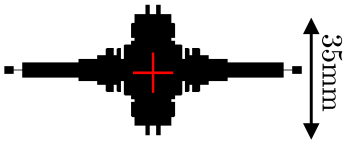
Experimental	**Numerical**	
Representative C-scan	**Multiple cohesive layers failure (total degradation)**	**Single cohesive layer failure (total degradation)**
	Monolithic S2-glass composite	
impact site  Area = 319mm^2 (CV not available)	 8 cohesive plies Area = 367mm^2	 1 cohesive ply Area = 2711mm^2
	Monolithic T700 carbon composite	
 Area = 1446mm^2 (CV=24%)	 7 cohesive plies Area = 1376mm^2	 1 cohesive ply Area = 4276mm^2
	Interlayer T700 carbon/S2-glass	
 Area = 1910mm^2 (CV=16%)	 8 cohesive plies Area = 783mm^2	 1 cohesive ply Area = 7038mm^2
	Intralayer T700 carbon/Vectran	
 Area = 958mm^2 (CV=10%)	 6 cohesive plies Area = 311mm^2	 1 cohesive ply Area = 382mm^2

Table 5.8: Delamination (interlaminar) failure for 140J plate impacts, experimental versus numerical (not to scale)

Experimental	**Numerical**	
Representative C-scan	**Multiple cohesive layers failure (total degradation)**	**Single cohesive layer failure (total degradation)**
Monolithic S2-glass composite		
 Area = 607mm^2 (CV not available)	 8 cohesive plies Area = 583mm^2	 1 cohesive ply Area = 6891mm^2
Monolithic T700 carbon composite		
 Area = 2092mm^2 (CV=35%) (plate split in two pieces)	 7 cohesive plies Area = 2761mm^2	 1 cohesive ply Area = 6066mm^2
Interlayer T700 carbon/S2-glass		
 Area = 2171mm^2 (CV=10%)	 8 cohesive plies Area = 1966mm^2	 1 cohesive ply Area = 8101mm^2
Intralayer T700 carbon/Vectran		
 Area = 1266mm^2 (CV=6%)	 6 cohesive plies Area = 390mm^2	 1 cohesive ply Area = 739mm^2

5.5.1. Monolithic S2-glass composite

Figure 5.16 presents the load response curves for the monolithic S2-glass composite impacts at 70J energy. The FE model response can be seen to follow the experimental response very well, with the numerical load curve falling closely within the experimental load curves during the majority of the impact event.

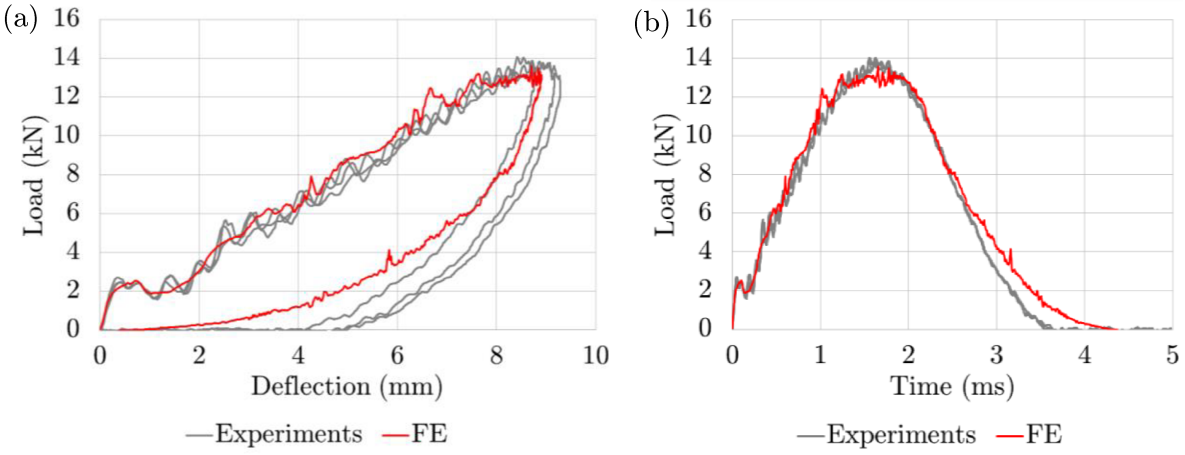


Figure 5.16: Monolithic S2-glass composite load response at 70J impact: (a) load versus deflection, (b) load versus time

The FE analysis that contained eight cohesive layers, as specified in Table 5.2, showed very good agreement with the observed fibre fracture (which was almost nil for the 70J impact), as shown in Table 5.5. The 70J impact exhibited crazing around the impact site (discolouration of the surrounding matrix), obscuring the back-face fibre fracture on the experimental panels, making correlation between the two difficult.

Figure 5.17 presents the through-thickness cross-section, which had been taken a few weeks post-test, with little indentation noticed since material relaxation may have occurred. The experimental data shown in Figure 5.16 presents the total deflection reaching about 4 to 5mm upon the load returning to 0N. Donckels, Y. et al [124] reported on this phenomenon where a drastic reduction in dent depth within the first 24 hours post-impact for biaxial AS4/8552 carbon fibre panels was noticed and although differing from the material tested in this Chapter, provides a possible reason for this discrepancy.

The cohesive damage behaviour within the numerical model presented degradation of 367mm^2 with the C-scanned experimental counterpart at 319mm^2 when all eight cohesive plies were

given damage initiation capabilities (Table 5.7). The same FE model with only one cohesive ply closest to mid-plane presented much larger delamination growth (2711mm^2), indicating that the failure of the cohesive layers depended largely upon their quantity and location within the through-thickness direction of the numerical model laminate. A microscopic through-thickness cross-section at the damage site provided crucial information regarding this phenomenon, indicating that the experimental specimens likely delaminated at two planes, as shown in Figure 5.17. This gives an indication why the numerical model with one cohesive layer vastly overestimated the cohesive damage.

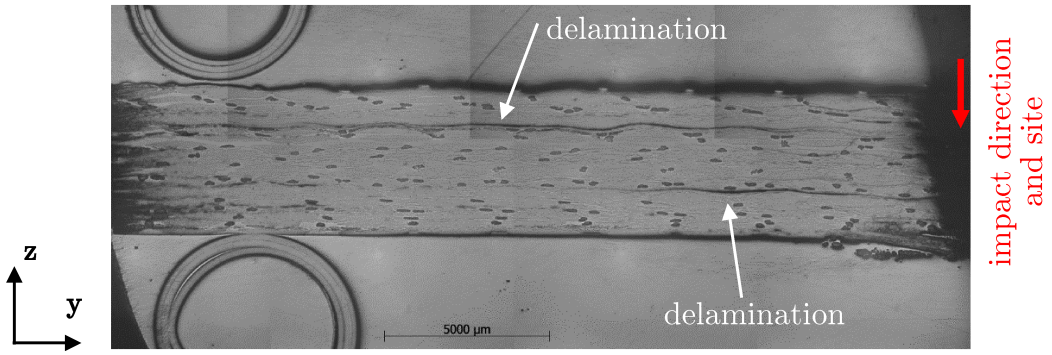


Figure 5.17: Monolithic S2-glass composite at 70J impact, through-thickness microscopic image of failed experimental specimen

Figure 5.18 presents the load response curves for the monolithic S2-glass composite panel at 140J impact. Good correlation was also seen between the numerical and experimental load curves. Table 5.6 displays the fibre fracture response of the plate both experimentally and numerically where the crack length fibre fracture within the numerical model appeared to be longer than that found experimentally. This discrepancy was indicative of 'shear plugging' [180], a phenomenon that occurs when a penetrating impactor tup produces through-thickness shear failure as opposed to tensile fibre damage on the back face of the panel. This results in a sudden load drop in the response since the energy required to propagate through-thickness shear is lower than that of tensile fibre fracture.

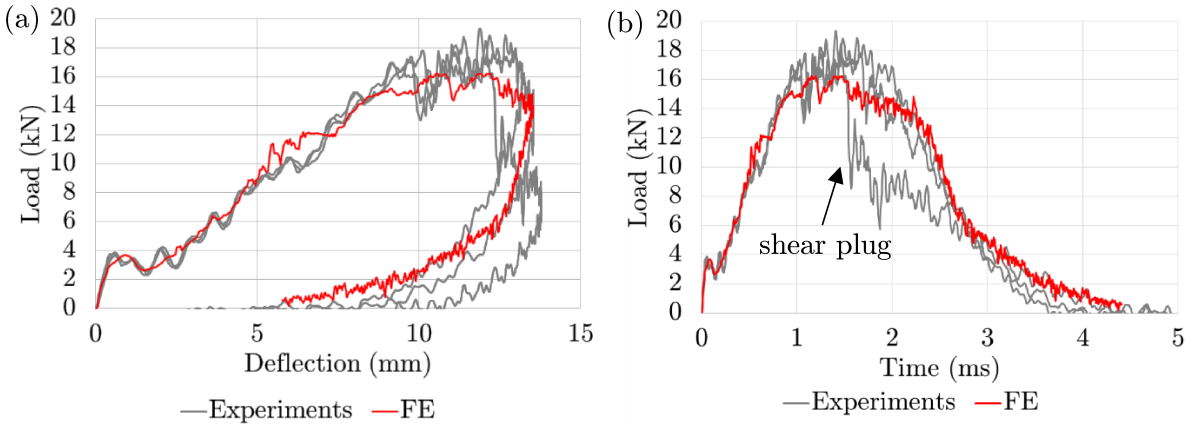


Figure 5.18: Monolithic S2-glass composite load response at 140J impact: (a) load versus deflection, (b) load versus time

Matrix crazing (and thus likely delamination formation and growth) was noticed to have occurred between 0.00ms and 0.79ms (Figure 5.19) from the high-speed camera footage. Subsequently, significant fibre fracture was then seen to have initiated and propagated on the back face of the specimen after 0.79ms. A load drop was noticed within the numerical model and one of the experiments at approximately 1.50ms, approximately 1mm (0.25ms) before the rebounding of the tup within the other two specimens. This load curve response feature for that particular specimen was likely due to the shear plugging phenomenon upon partial penetration, where the energy required to propagate through-thickness shear damage was lower than that of back-face fibre fracture. Localised fibre crushing was also noticed from post-test microscopy (Figure 5.20), akin to the tensile fibre fracture observed in the numerical model in Table 5.6.

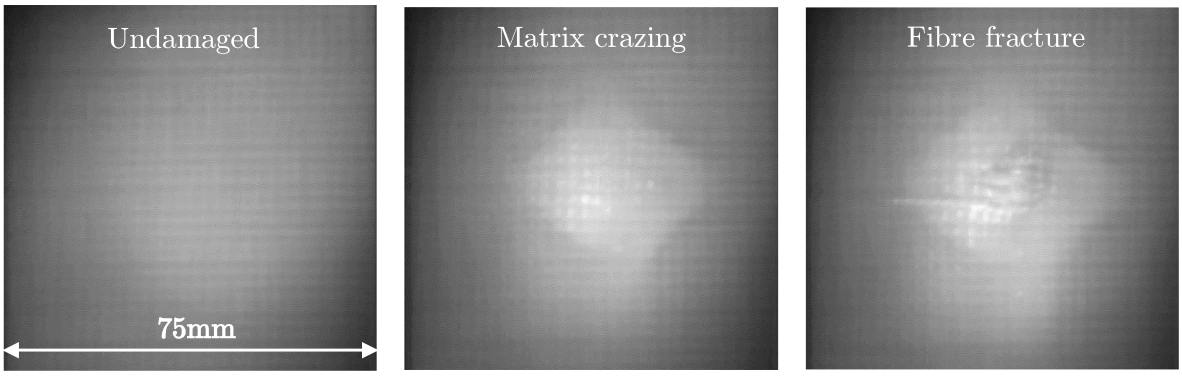


Figure 5.19: Damage progression on the back face of a monolithic S2-glass composite plate at 140J impact

The C-scanned image (Table 5.8) indicated an areal delamination of 607mm^2, much closer to the cohesive element degradation area of 583mm^2 for 8 plies than the 1 ply area of 6891mm^2 (where the delamination uncharacteristically grew to the edges of the plate).

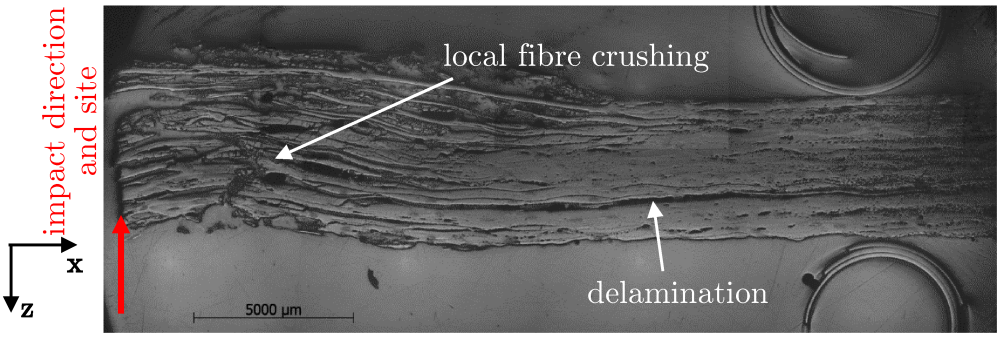


Figure 5.20: Monolithic S2-glass composite at 140J impact, through-thickness microscopic image of failed experimental specimen

5.5.2. Monolithic T700 carbon composite

Figure 5.21 presents the response curves for the monolithic T700 carbon composite plate impacts at 70J. The numerical model was noticed to have initially followed the experimental load response during the elastic phase, and then follow a higher load upon initial fibre fracture, possibly due to internal damage within the panel. Figure 5.22 illustrates the tup contact from 0.00ms until 0.44ms causing only elastic behaviour, with initial fibre fracture beginning at 0.46ms. This indicates that the 'step' in load that occurred between 0ms and 0.25ms was a purely elastic response, since no interlaminar or translaminar damage was noticed during that time period in the numerical model. It was expected that interlaminar damage would be followed by translaminar damage, as noticed in the S2-glass numerical models. Within two of the tested specimens, between approximately 1.60ms and 2.50ms, the initial crack was seen to have propagated quickly in an unstable and brittle manner, where a drastic drop in load had occurred. Subsequently, there was little damage whilst the tup impactor penetrated the plate and in one case rebounded in the opposite direction (Figure 5.21a).

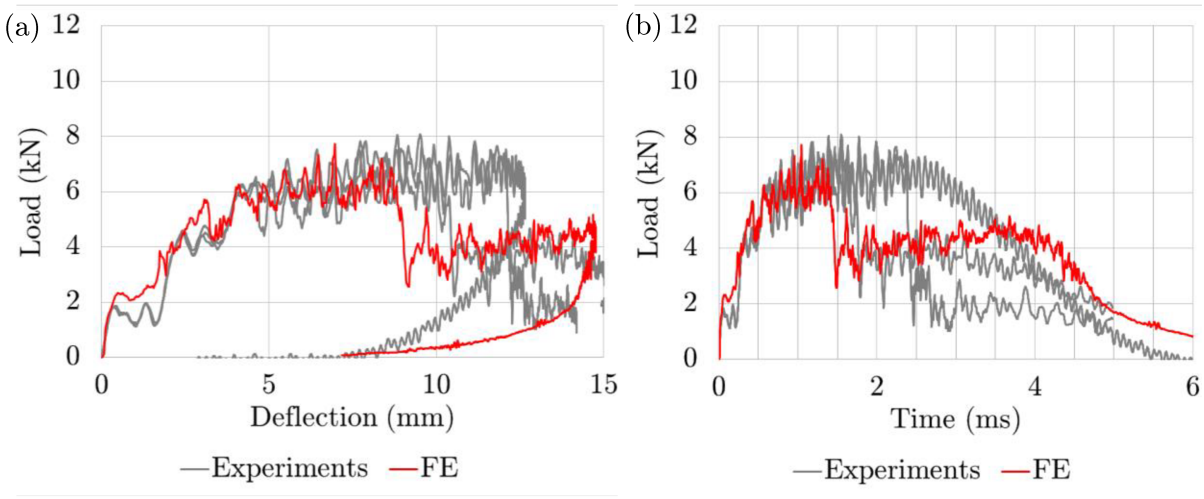


Figure 5.21: Monolithic T700 carbon composite load response at 70J impact: (a) load versus deflection, (b) load versus time

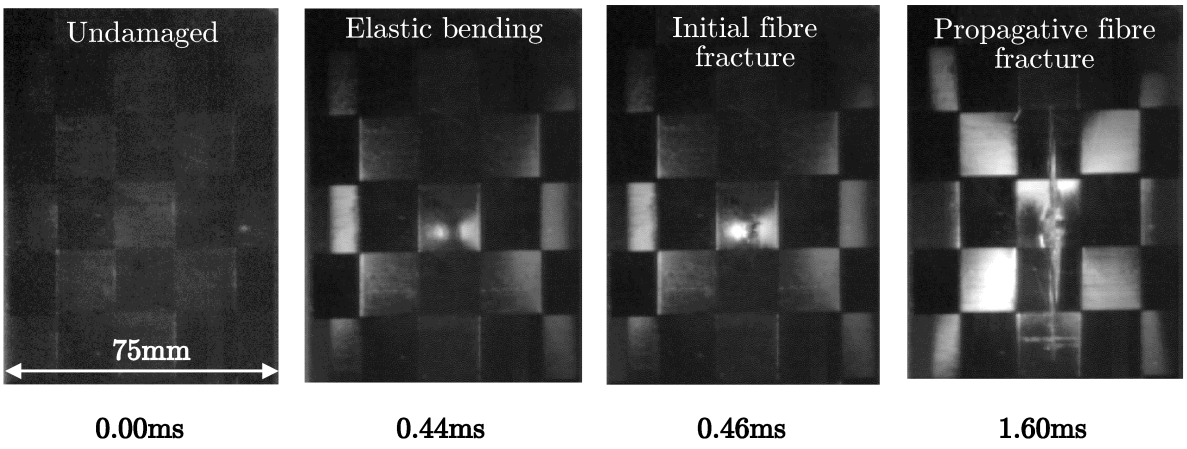


Figure 5.22: Damage progression on the back face of a monolithic T700 carbon composite plate at 70J impact

Post-test inspection showed reasonable agreement between the crack lengths recorded experimentally and through the numerical modelling. Because the experimental specimens presented high scatter in their responses, it was difficult to quantify how accurate the numerical models response was.

Where seven cohesive element layers were modelled, the interlaminar failure predicted by the numerical model showed good correlation with the experimental testing (Table 5.7 and Figure 5.23) and the damaged area of the cohesive element layers presented a similar pattern to that in the C-scan.

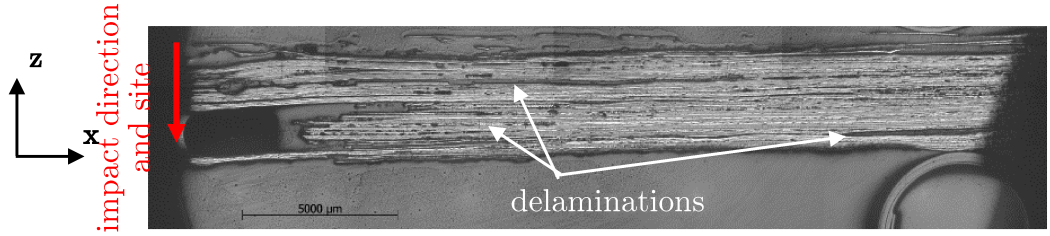


Figure 5.23: Monolithic T700 carbon composite at 70J impact, through-thickness microscopic image of failed experimental specimen

The 140J impact events for the monolithic T700 carbon composite specimens showed a similar load response to the 70J impacts up until the initiation of fibre fracture, and the 140J specimens exhibited a four-petal type failure (Table 5.6). This type of failure was noticeably similar to the shear-plugging observed within the monolithic S2-glass composite load response. Since the areal damage was limited locally to the region, it resulted in full penetration of the impactor tup. Due to this, the impactor did not rebound for any of the experimental specimens and four-petal type folds were seen to have extended from the impact site. Table 5.6 presents the experimental versus numerical crack length differences, where the numerical model did not capture the shear plugging (noticed experimentally after approximately 1.5ms), thus exhibiting larger crack lengths during the fibre fracture phase of the impact event.

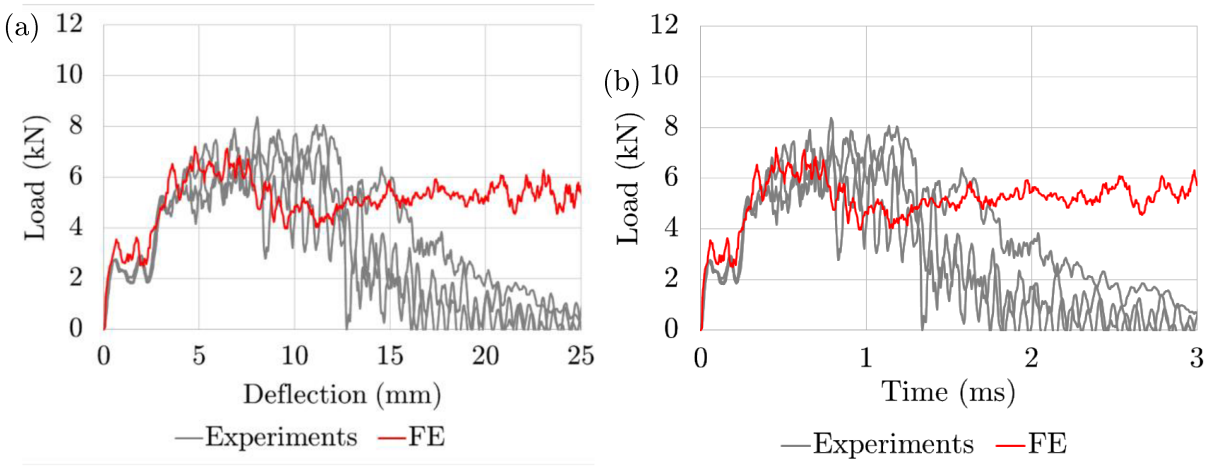


Figure 5.24: Monolithic T700 carbon composite load response at 140J impact: (a) load versus deflection, (b) load versus time

The numerical model with seven cohesive layers showed reasonably good agreement in delamination. Figure 5.25 presents this analytically and approximately seven interlaminar delaminations could be counted from the microscopic cross-section. The numerical model was

unable to account for the shear plugging effect caused by high impact energies since the through-thickness shear damage mechanism of the composite was not modelled.

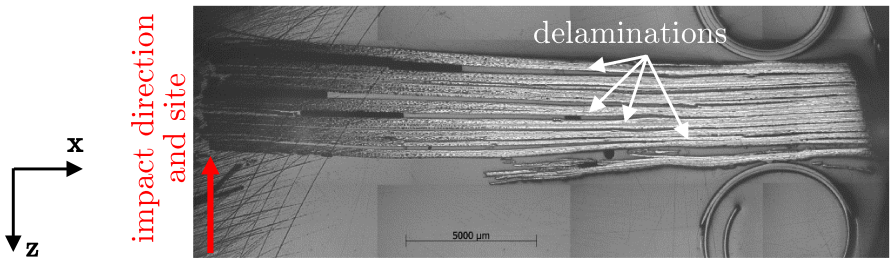


Figure 5.25: Monolithic T700 carbon composite at 140J impact, through-thickness microscopic image of failed experimental specimen

5.5.3. Interlayer fibre hybrid T700 carbon/S2-glass

Figure 5.26 displays the response curves for the interlayer fibre hybrid T700 carbon/S2-glass plate impacts at 70J. The numerical model followed the experimental response closely, falling within the scatter of the experimental test curves. The latter stage of the load response curve shows some variation from the testing, where tup rebound, the experimental load curve became indented at approximately 5mm, as shown in Figure 5.26a. This type of deformation was unaccounted for in the numerical model, and the same phenomenon was also exhibited by the hybrids main volumetric constituent, S2-glass, as discussed in Section 5.5.1.

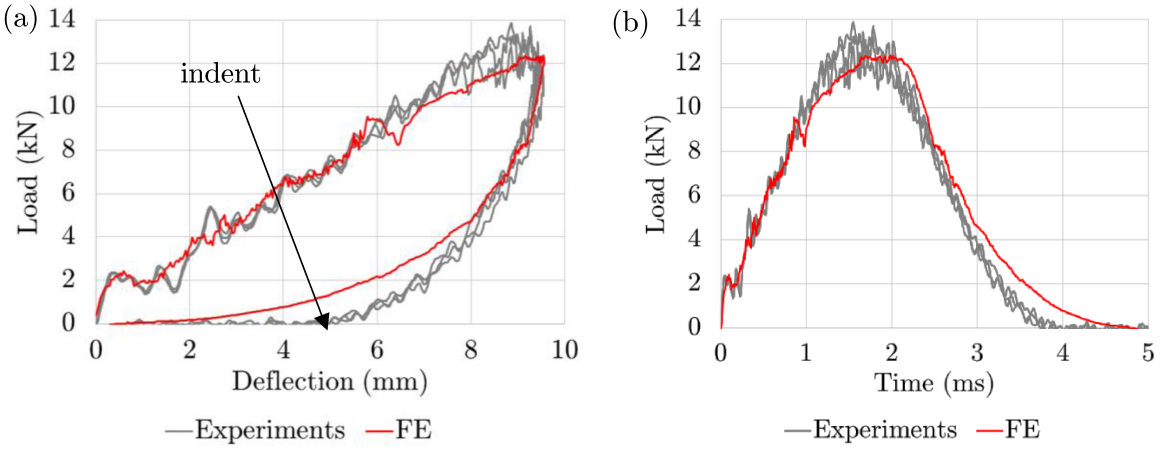


Figure 5.26: Interlayer fibre hybrid T700 carbon/S2-glass load response at 70J impact: (a) load versus deflection, (b) load versus time

The post-test analysis of the failed specimens and the numerical model damage presented some variation in the fibre fracture extent for each with the model over-estimating the fibre fracture in the x-direction, displayed in Table 5.5. The dent relaxation phenomenon mentioned earlier could be a possible explanation to the larger crack length recorded in the numerical model in

the x-direction, since the overall energy absorbed by the experimental tests and the numerical models were the same.

The cohesive element degradation for eight plies and one ply encompassed the range that the C-scan image area presented in Table 5.7. There were three delaminations that extended from the impact site as characterised by the microscopic cross-section of the laminate, Figure 5.27. Since a strain rate effect was not implemented within the numerical model for the cohesive element properties, it became difficult to quantify where the discrepancy between the model and experiment had originated. The experimental testing of the Mode II interlaminar fracture toughness only considered one orientation however (with the centremost carbon ply being in tension), which could account for this. Furthermore, the C-scan displayed in Table 5.7 highlights regions of delamination following the common 'peanut' shape associated with interlaminar impact damage, following the fibre directions (biaxially). The mesh geometry for the impact plates (Figure 5.7) made replicating these shapes inherently difficult, given the high elemental aspect ratio either side of the mesh refinement zone.

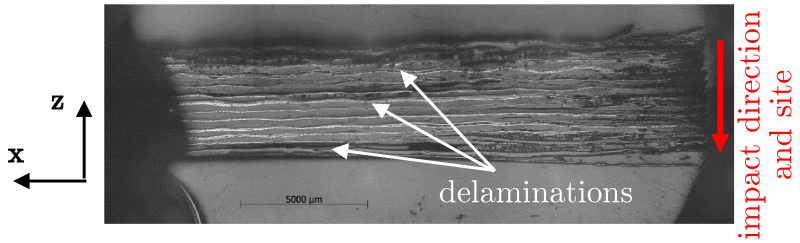


Figure 5.27: Interlayer fibre hybrid T700 carbon/S2-glass at 70J impact, through-thickness microscopic image of failed experimental specimen

The fibre fracture crack lengths were well predicted, given the complexity of the varying fibre types within the layup. The shear plugging effect noticed within the monolithic S2-glass composite (Section 5.5.1) was also captured within the interlayer fibre hybrid specimens, where the load dropped experimentally below the numerical model at about 1.8ms, after the relatively brittle initial T700 carbon fibre breakages at approximately 1.25ms. This was quantified from the high speed video capture footage of the back face (Figure 5.29) where the impactor tup did not rebound (Figure 5.28), resulting in full penetration. From Figure 5.28, it was deduced that the other two specimens did not undergo full penetration, but only partial penetration, since their load response curves can be seen to return to ˜12mm indentation.

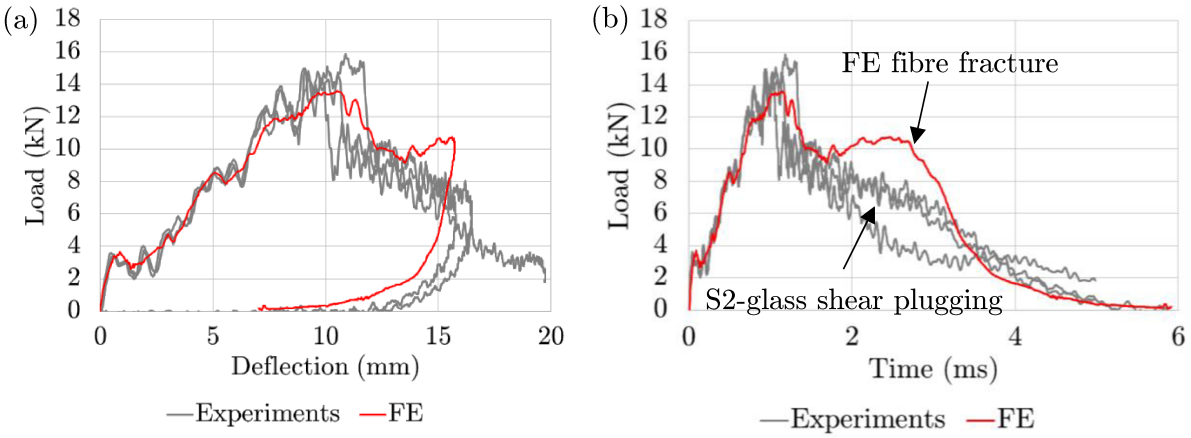


Figure 5.28: Interlayer fibre hybrid T700 carbon/S2-glass load response at 140J impact: (a) load versus deflection, (b) load versus time

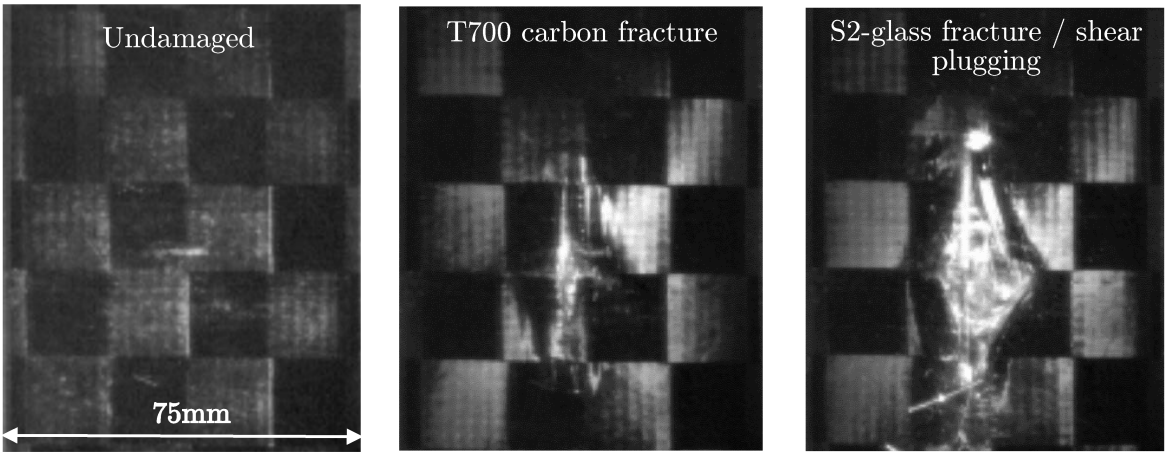


Figure 5.29: Damage progression on the back face of a interlayer fibre hybrid T700 carbon/S2-glass plate at 140J impact

Through-thickness cross-sectional microscopy (Figure 5.30) corroborated the shear plugging phenomenon, where local fibre crushing was noticed as well as multiple delaminations extending from the impact site. The delamination pattern presented a good correlation between the numerical model and experimental testing, where the delaminated area of the experiments fell within the scatter of the numerical models containing eight and one cohesive layers (Table 5.8). The bottom-most T700 carbon ply on the back-face of the specimen was also seen to delaminate due to the plugging effect exhibited by the S2-glass fibres and could be seen in the through-thickness microscopic image of a failed experimental specimen in Figure 5.30. The back-face ply was kept largely intact throughout the impact event, since the energy

required to delaminate it from the rest of the panel was lower than the carbon fibre's initiation tensile strength.

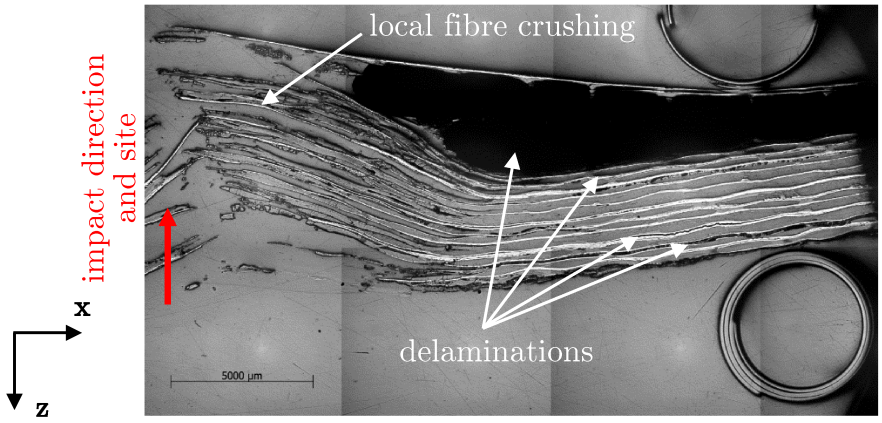


Figure 5.30: Interlayer fibre hybrid T700 carbon/S2-glass at 140J impact, through-thickness microscopic image of failed experimental specimen

5.5.4. Intralayer fibre hybrid T700 carbon/Vectran

Figure 5.31 presents the load response curves for the intralayer fibre hybrid T700 carbon/Vectran plate impacts at 70J. The numerical model accounted well for the fibre fracture crack lengths, as good correlation of the numerical model and the experiments was observed, Table 5.5.

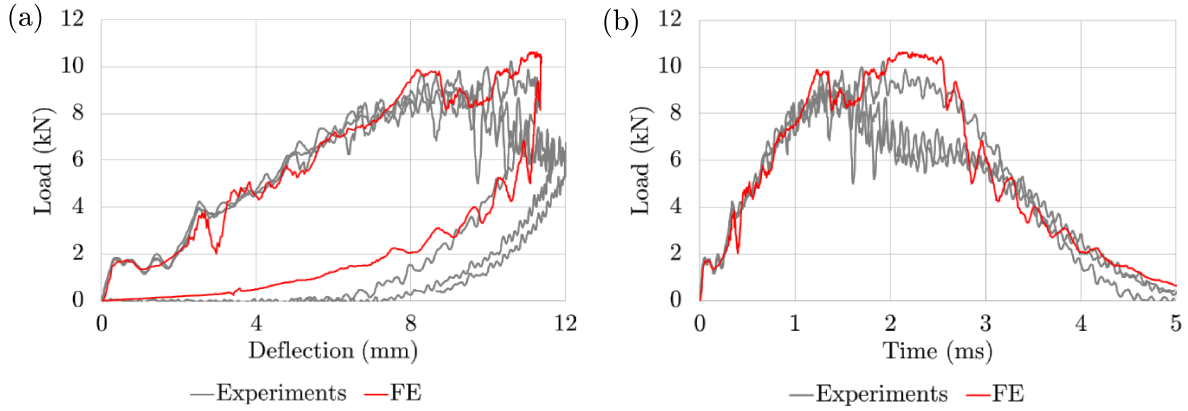


Figure 5.31: Intralayer fibre hybrid T700 carbon/Vectran load response at 70J impact: (a) load versus deflection, (b) load versus time

The numerical interlaminar failure did not however show good correlation for the 70J impact since the thickness and crimp angle of the undulations in the fibres within the intralayer weave caused erroneous back-face detection during the C-scanning. The pattern of the 2x2 twill weave was noticed within the C-scan, extending away from the impact site, and can be seen in Table 5.7.

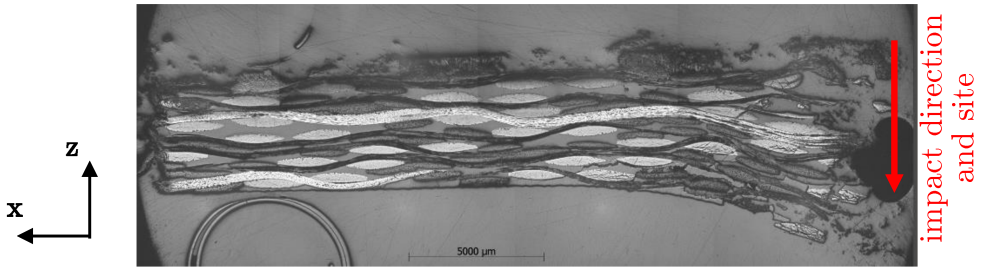


Figure 5.32: Intralayer fibre hybrid T700 carbon/Vectran at 70J impact, through-thickness microscopic image of failed experimental specimen

Figure 5.33 presents the load response curve for the 140J event of the intralayer fibre hybrid T700 carbon/Vectran panel impacts. Due to the extremely large shear plugging which was evident from the failed experimental section shown in Figure 5.34, the experimental tests presented shear plugging after approximately 1ms, whereas the numerical model failed to capture this and continued to undergo fibre fracture along the x-direction and y-direction, Table 5.6. The microscopic section (Figure 5.34) highlights the disintegration of the fibres at the impact site upon the full penetration of the impactor tup, caused by shear plugging. The shear plugging evident in the 140J impact energy for the intralayer fibre hybrid T700 carbon/Vectran plates can be attributed to the high fibre crimp within the weave, leading to poor through-thickness strengths.

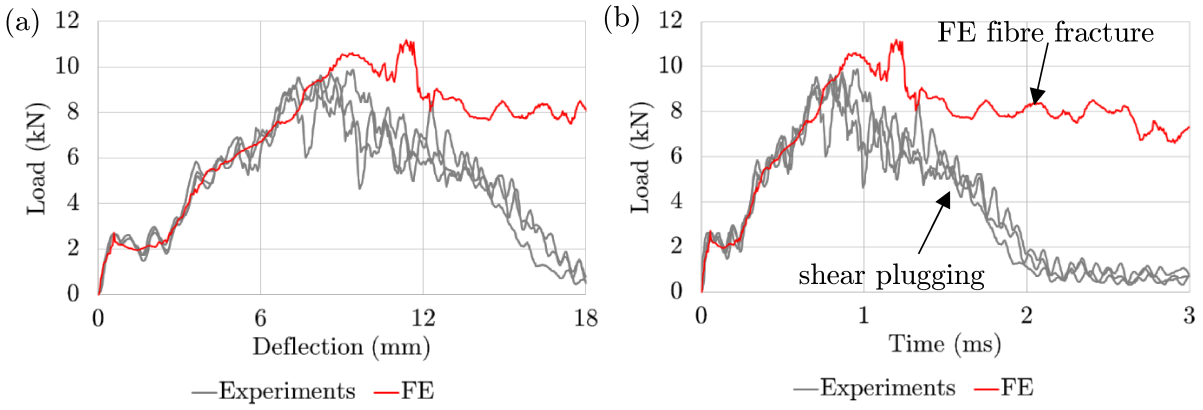


Figure 5.33: Intralayer fibre hybrid T700 carbon/Vectran load response at 140J impact: (a) load versus deflection, (b) load versus time

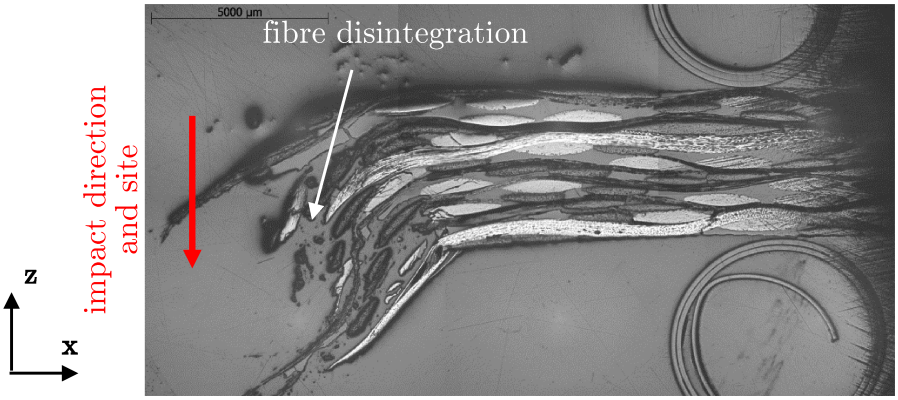


Figure 5.34: Intralayer fibre hybrid T700 carbon/Vectran at 140J impact, through-thickness microscopic image of failed experimental specimen

Because of the catastrophic effect that the 140J impact had upon the intralayer fibre hybrid T700 carbon/Vectran plate, the numerical model was unable to capture any relevant information beyond the peak load since the through-thickness shear damage mechanism was not modelled. Instead, the FE model underwent continuous fibre fracture and hence meant quantifying the energy absorbed through the impact event at this level and comparing to the other materials was difficult because the plate failed in its entirety, through-thickness.

5.6. Quantifying the numerical model's accuracy

By quantifying the peak loads and the energy absorbed through the impact events [20], it was possible that some conclusions may be drawn regarding the viability of the materials tested for the design of automotive sector structural components. Summary graphs for the peak loads (Figure 5.35, Figure 5.36, Figure 5.37, and Figure 5.38) and total absorbed energy (through the area encapsulated within the load response curves) (Figure 5.39, Figure 5.40, Figure 5.41, and Figure 5.42) were quantified for both the experimental data and numerical models per unit mass of the specimen and per unit through-thickness, as automotive component design prioritises material density [131]. The absorbed energy was calculated through the use of the trapezium rule, where the total energy was taken as the encapsulated area of the load versus deflection graphs. The numerical model data was presented with interlaminar damage and without interlaminar damage (the cohesive layers' strength and fracture energies were withdrawn from the simulation and thus interlaminar damage was not initiated). By doing this, the effect and the presence of damage within the cohesive layers was clearly defined. The experiments where full impactor tup penetration due to shear plugging occurred are labelled and can therefore be treated accordingly when comparing the results.

At the 70J impact events, the interlayer fibre hybrid T700 carbon/S2-glass presented the highest range of peak loads. This was not the case for the 140J impact events where the monolithic S2-glass composite and the interlayer fibre hybrid T700 carbon/S2-glass presented a similar magnitudes of peak load. The load response curves of the numerical models showed good agreement with the experiments where the impactor tup did not fully penetrate the plate, since the shear plugging failure mode was not implemented within the material model. The numerical modelling of the impact rig was conservative in its structural stiffness because the entire impact rig was not modelled and instead fixed rigidly, leading to inherently less compliant boundary conditions than the experimental test rig environment. This would manifest as longer load numerical response curves since the damping effects associated with the experimental rig were not captured. This was noticed particularly in the 70J load responses of the monolithic S2-glass and the interlayer fibre hybrid T700 carbon/S2-glass as the load responses took longer to return to zero (Figure 5.16 and Figure 5.26).

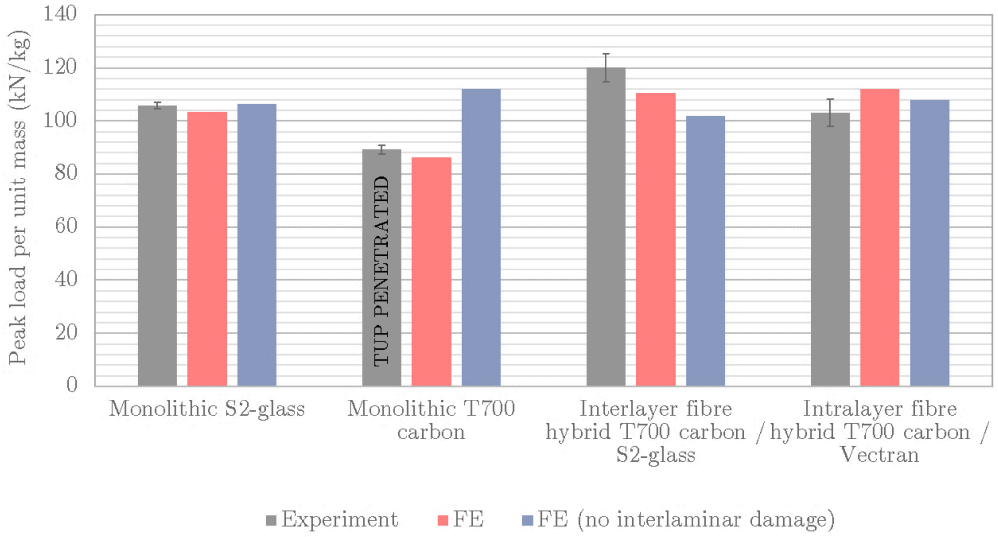


Figure 5.35: 70J composite plate impact, peak loads per unit mass

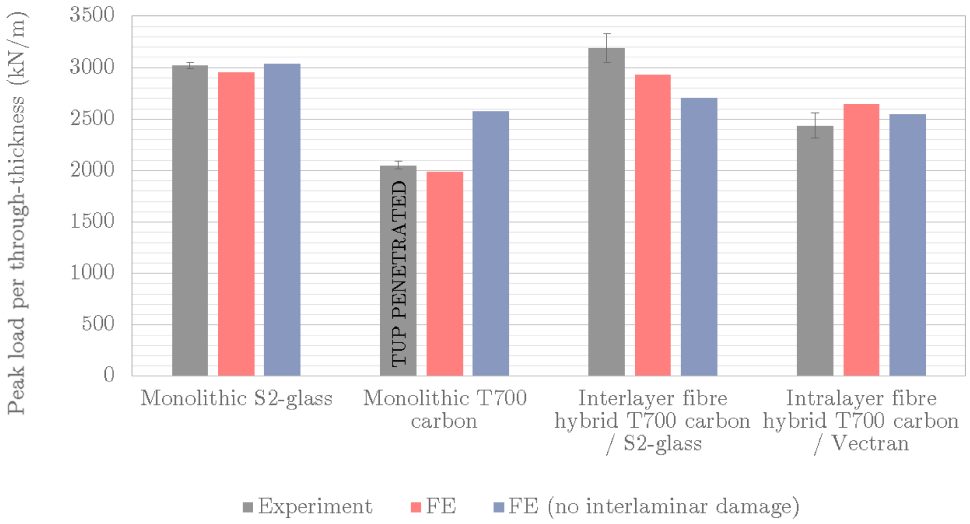


Figure 5.36: 70J composite plate impact, peak loads per through-thickness

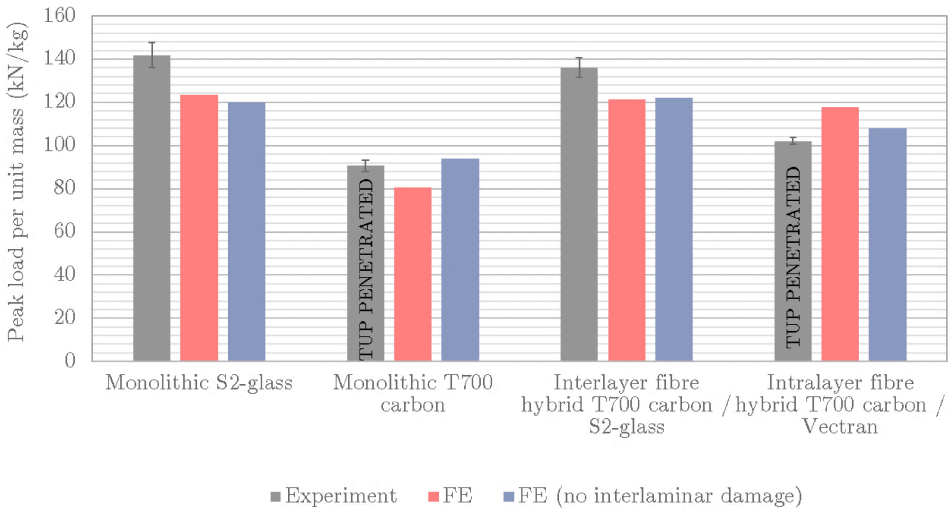


Figure 5.37: 140J composite plate impact, peak loads per unit mass

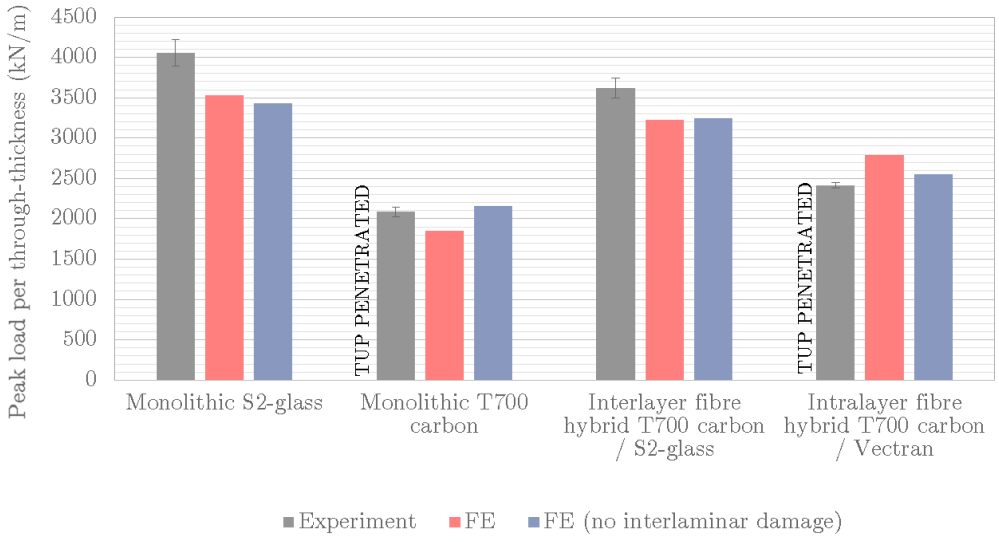


Figure 5.38: 140J composite plate impact, peak loads per through-thickness

Although superior in other material properties, such as modulus and strength, the monolithic T700 carbon composite presented the worst impact performance since the impactor tup was observed to fully penetrate the plates at both 70J and 140J. The fibre hybridisation of the S2-glass with the T700 carbon proved to be beneficial, since similar absorbed energies were noticed per unit mass, compared to that of the monolithic S2-glass composite. Therefore, due to the interlayer fibre hybrid's improved in-plane properties compared to the monolithic S2-glass composite, it presents beneficial properties for use in outer bodywork within the automotive sector, where structural and impact properties are integral to the materials required performance.

Where the impactor tup did not fully penetrate the plate, the absorbed energies determined through numerical modelling were seen to be lower than their experimental counterparts. This was likely due to the experimental impact rig absorbing some energy to the external surroundings, uncaptured by the numerical model due to its rigid boundary conditions.

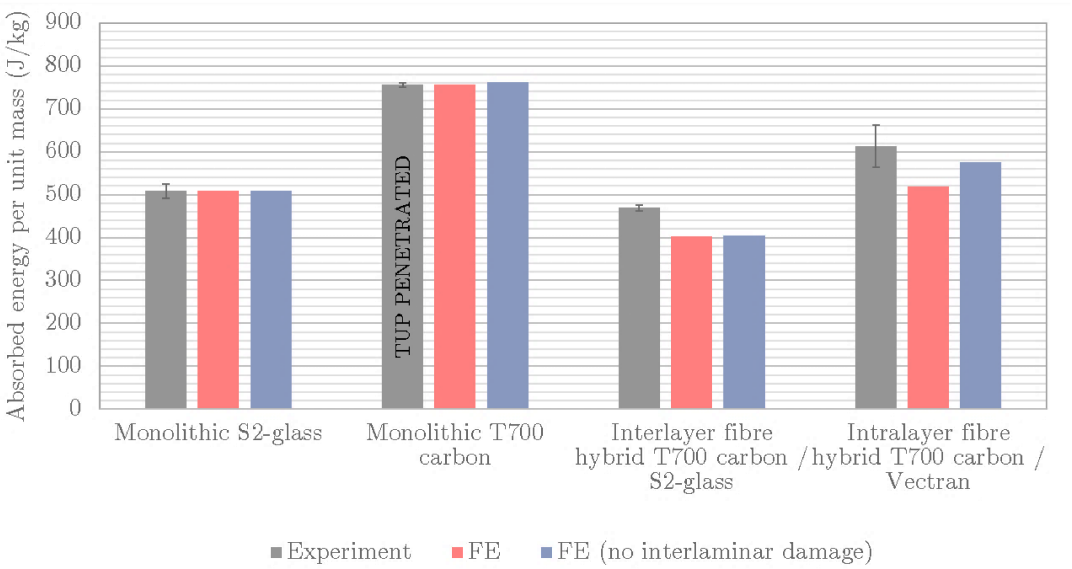


Figure 5.39: 70J composite plate impact, absorbed energies per unit mass

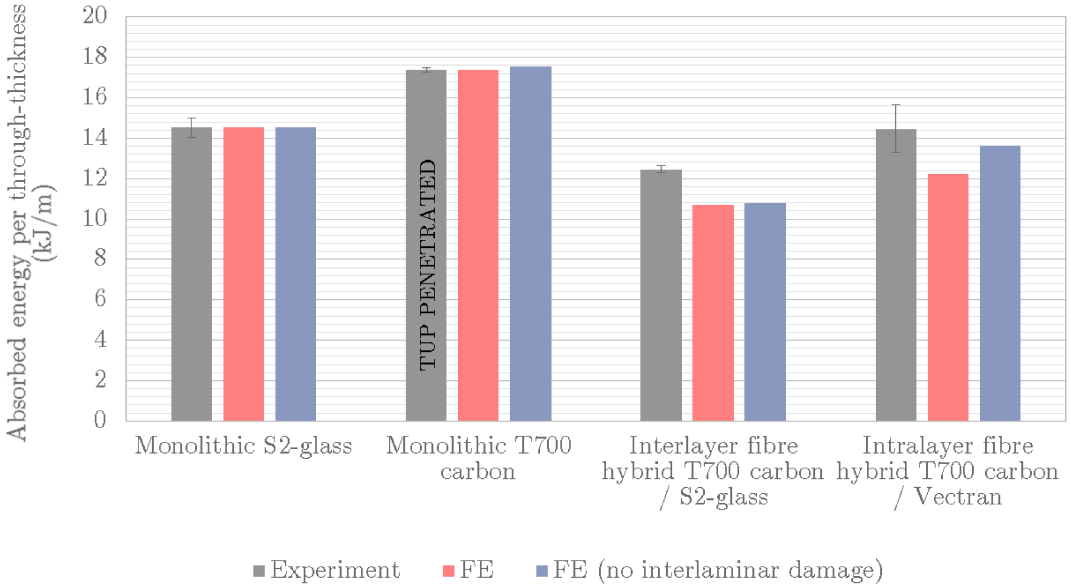


Figure 5.40: 70J composite plate impact, absorbed energies per through-thickness

The most consistent and accurate modelling was for the monolithic S2-glass composite, both in the load response curves in Section 5.5.1, and the peak loads and absorbed energies in Figure 5.39 and Figure 5.41 respectively. Because the materials were modelled as 0°/90° plies, the non-crimp fabric architecture of the S2-glass most suited this configuration of modelling. The thicker intralayer fibre hybrid T700 carbon/Vectran presented less desirable accuracy, since the fibre architecture was much more complex and hence became more dominated by the through-thickness properties such as shear plugging of the material which the (in-plane) numerical model failed to capture.

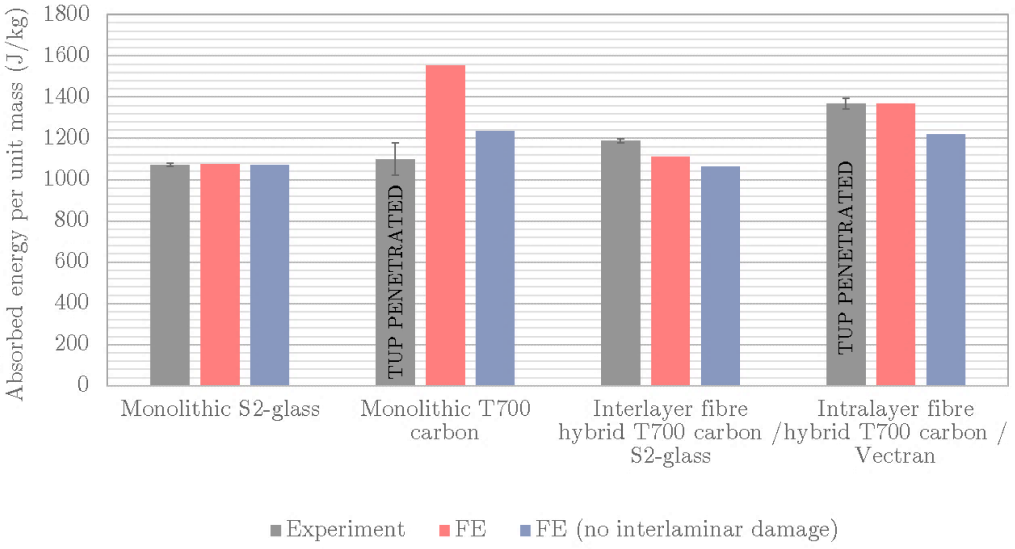


Figure 5.41: 140J composite plate impact, absorbed energies per unit mass

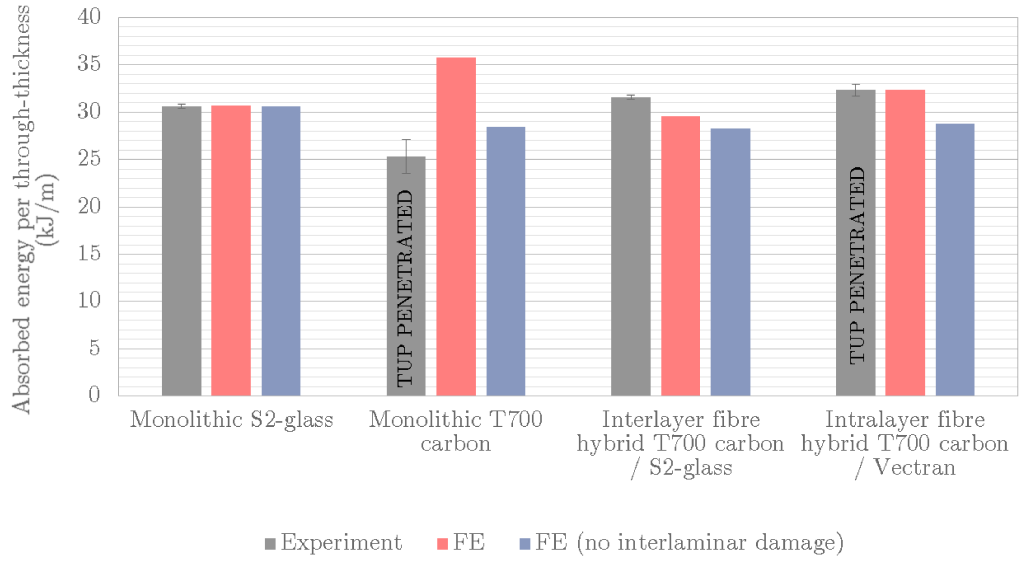


Figure 5.42: 140J composite plate impact, absorbed energies per through-thickness

5.7. Summary

Low velocity impact of two fibre hybrid composites and the T700 spread tow and S2-glass monolithic composites were characterised and showed agreement with an energy-based bilinear plane stress Abaqus VUMAT subroutine. The numerical model was able to capture the load responses of the interlayer and intralayer fibre hybrid composites at low velocities (without through-thickness shear plugging effects). There was a clear limitation of the numerical model, where full impactor tup penetration was observed for multiple instances at 140J due to shear

plugging which is due to a poor through-thickness shear strength, uncharacterised by the in-plane numerical model. These were highlighted in the peak load and absorbed energy graphs.

At the low impact energy, the intralayer fibre hybrid T700 carbon/Vectran composite exhibited the largest specific energy absorption properties, whilst at the higher impact energy the poor through-thickness shear strength of the intralayer fibre hybrid (due to the high crimp associated with the 2x2 twill weave) dominated the failure. Conversely, the interlayer fibre hybrid T700 carbon/S2-glass presented good energy absorption without full tup penetration at the higher impact energy where the fibre crimp in the carbon spread tow and non-crimp glass fabric layers was low. The interlayer fibre hybrid T700 carbon/S2-glass showed similar energy absorption to the monolithic S2-glass composite with no tup penetration at 140J, making it superior to the monolithic T700 carbon composite. This provides a good argument for use of the interlayer fibre hybrid over the intralayer fibre hybrid within the automotive industry, where low velocity impact resistance as well as structurally stiff material properties are integral to component design.

Chapter 5 publications and dissemination:

- **Invited webinar presentations:**
  - T. Katafiasz, "Bridging Characterization and Simulation: Materials Information Needs for Design," in *Granta Webinar,* Cambridge, UK, 2017 [16]
- **Conference oral presentations:**
  - T. J. Katafiasz, "Development of a Novel Compact Tension Specimen for Fibre Hybrid Composites," in CompTest 2017: 8th International Conference on Composites Testing and Model Identification, Leuven, Belgium, 2017 [15]

6. Low velocity structural impact response of fibre hybrid composites on a reduced scale car bonnet

6.1. Introduction

The fibre hybrid materials tested throughout this research, reported in the previous Chapters, have proven to be beneficial in both structural and impact performance compared to their monolithic composite counterparts. Low velocity impact numerical modelling has shown that the fibre hybrid composites can be accurately modelled at reasonably high energy level. This Chapter covers the steps taken to experimentally develop an impact rig which employed carefully controlled and therefore quantifiable boundary conditions for accurate correlation with numerical modelling of a reduced scale component. A 1:5 reduced scale Bentley Continental (Figure 6.1) car bonnet was impacted at 15J and 20J energies for direct comparison with numerical modelling in both load response and two independent strain gauges. Two low energy levels were chosen to provide what would produce a largely elastic response within the specimens, and a 5J variation to provide insight into the sensitivity of the numerical modelling.



Figure 6.1: Bentley Continental Supersports Convertible [181]

6.2. Mechanical testing

6.2.1. Manufacture using a Bentley bonnet mould

A reduced scale (1:5) Bentley Continental car bonnet mould (Figure 6.2) was supplied by Solvay [8] to manufacture fibre hybrid composite bonnets for mechanical testing and then numerical model correlation. A total of twelve bonnets were manufactured, with three for

each energy level and a total of six for each fibre hybrid composite. As with the previous material manufactured in Chapters 3, 4, and 5, RFI was employed to ensure a consistent layup and fibre volume fraction across all levels of testing for both the resin volume fractions and the interlayer fibre hybrid volume fractions, in accordance with the TGA and analytical microscopy conducted in Section 3.1.4.

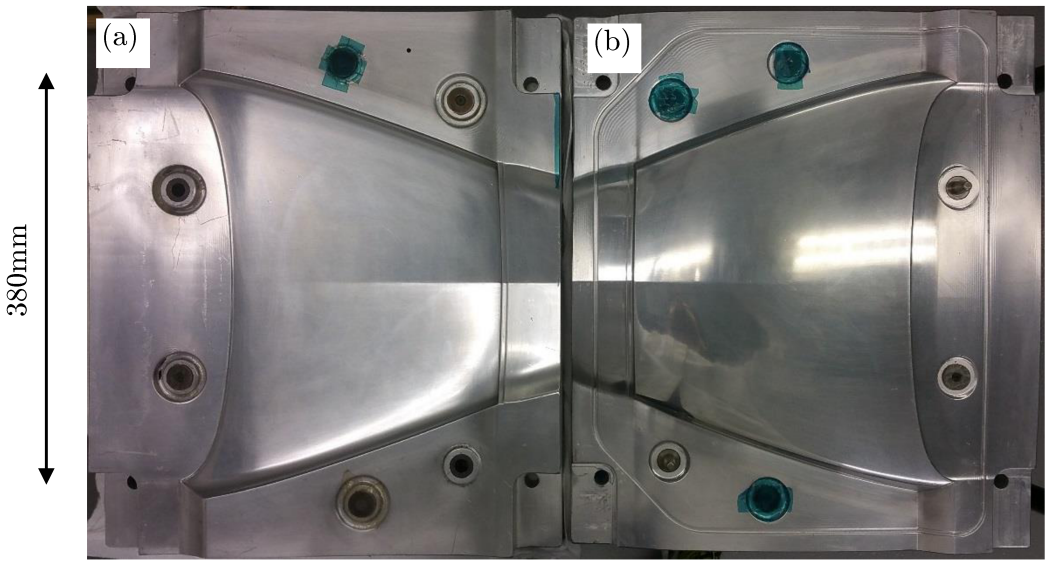


Figure 6.2: Bentley Continental car bonnet mould: (a) female side, (b) male side

Table 6.1 presents the nominal cured thicknesses of the fibre hybrid bonnets as well as their stacking sequences. A nominal thickness of 2mm was chosen as the minimum layup required for the interlayer fibre hybrid to maintain the four carbon to three glass fibre ply ratio. The numerical model's through-thickness element stacking sequence was included for completion, where each material ply contained three integration points to allow for bending, as with the plate impacts in Chapter 5. The homogenised material properties and numerical modelling approach are discussed in full in Section 6.3.

Table 6.1: Bonnet nominal cured thicknesses and stacking sequences

Material (total cured thickness)	Layup, through-thickness (mm)
Interlayer fibre hybrid T700 carbon/S2-glass (2.10mm)	$\left[\overbrace{\underbrace{0.089}_{\tilde{C}}\ \underbrace{0.231}_{\tilde{G}}}^{1\ element}\ \overbrace{\underbrace{0.089}_{\tilde{C}}\ \underbrace{0.231}_{\tilde{G}}}^{1\ element}\ \overbrace{\underbrace{0.089}_{\tilde{C}}\ \underbrace{0.231}_{\tilde{G}}\ \underbrace{0.089}_{\tilde{C}}}^{1\ element}\right]_S$ (0° 0° 45° 45°)
Intralayer fibre hybrid T700 carbon/Vectran (2.32mm)	$\left[\overbrace{\underbrace{0.580}_{\tilde{\tilde{CV}}}}^{1\ element}\ \overbrace{\underbrace{0.580}_{\tilde{\tilde{CV}}}}^{1\ element}\right]_S$ (0° 45°)

$\overset{0.580}{\tilde{\tilde{CV}}}$ represents 1 x T700 carbon/Vectran continuum shell element that is 0.580mm thick

The fibre plies and resin film plies were cut using an automated cutting machine to the desired shape of the bonnet (Figure 6.3). The bonnets were laid-up according to the layup presented in Table 6.1, where ±45° plies were also included as well as 0°/90° plies. The layup was constricted to keeping the ±45° plies closest to the mid-plane to ensure sufficient flexural stiffness about both the 0°/90° and ±45° axes.

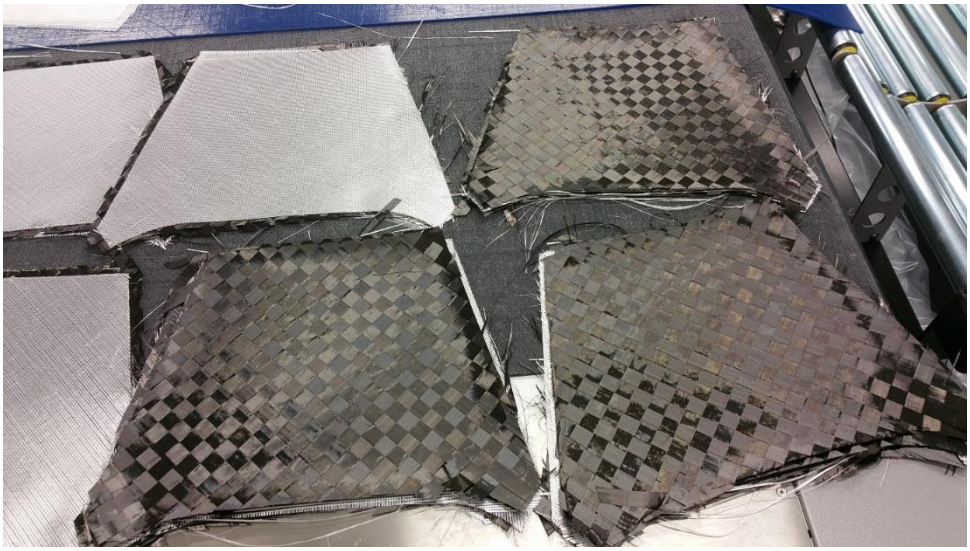


Figure 6.3: Dry fibre plies cut to bonnet shape, T700 carbon and S2-glass

Chemlease 41-90 EZ [182] release agent was applied to the mould using a lint-free cloth with six coatings before every third autoclave curing cycle since multiple releases between coatings were applicable to this type of agent.

Upon curing at 125°C for 1 hour within an autoclave under vacuum and cooling to room temperature [159], the bonnet parts were removed from the mould and a circular saw was used to remove the resin flash as well as extra fibres beyond the desired bonnet shape.

6.2.2. C-scanning of cured bonnets

To ensure that the bonnets did not contain delaminations, voids, or inclusions, ultrasonic C-scanning was employed using a TechniTest NDT system. The bonnets were submerged into a water bath and a 5MHz probe was used to undertake a transmission-echo ultrasound. Similar to the impact plate C-scanning in Section 5.4, non-destructive C-scanning was undertaken pre-test and post-test to capture defects. Because of the curvature of the bonnet surface, the automated scanning of the C-scanning machine could not be used alone, since a perpendicular ultrasonic pulse to the composite plies is imperative for the identification of possible delaminations. To solve this problem associated with the curvature, a proprietary in-house gimble was used (Figure 6.4). The gimble, developed at Imperial College London, allowed rotation about 2-axes, making it possible to follow the double curvature of the bonnet geometry. By keeping in contact with the bonnet surface using a 3-point fixture made from PTFE to avoid scratching the specimen, the surface of the bonnets were kept almost perpendicular to the probe head during scanning.

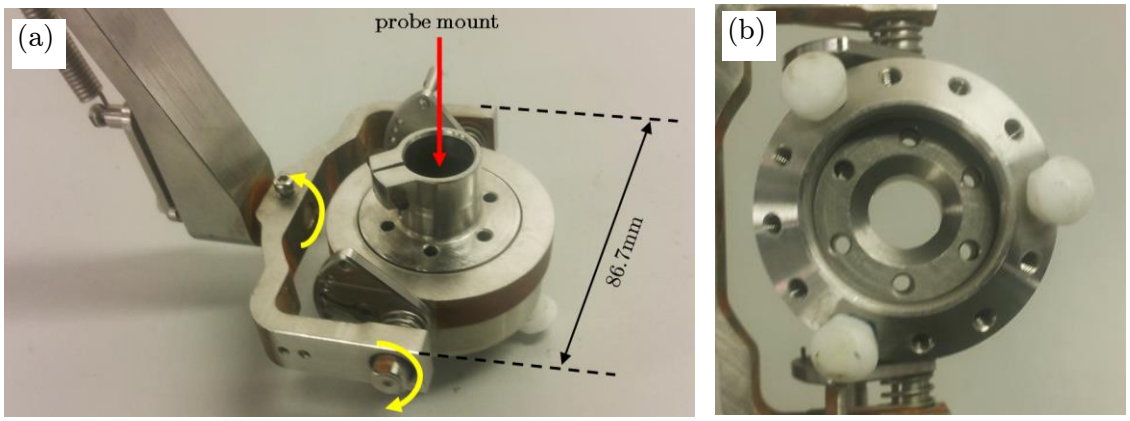


Figure 6.4: C-scanning gimble: (a) Isometric view, (b) bottom view with 3 PTFE contact points

The fibre hybrid bonnets were held in place using steel blocks to prohibit movement and an area of approximately 180mm x 180mm was scanned, with the corresponding locations shown in Figure 6.5 and representative C-scans presented in Figure 6.6. Clear C-scan plots show that the bonnets did not contain any delaminations at the intended impact site (see Section 6.2.3).

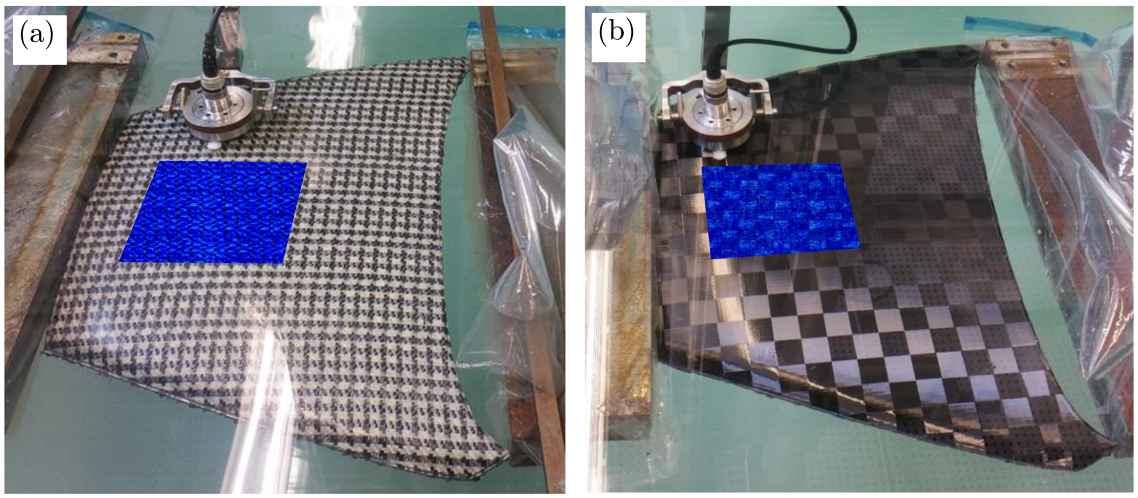


Figure 6.5: Bonnet C-scan configurations and approximate scanning locations: (a) Intralayer fibre hybrid T700 carbon/Vectran, (b) Interlayer fibre hybrid T700 carbon/S2-glass

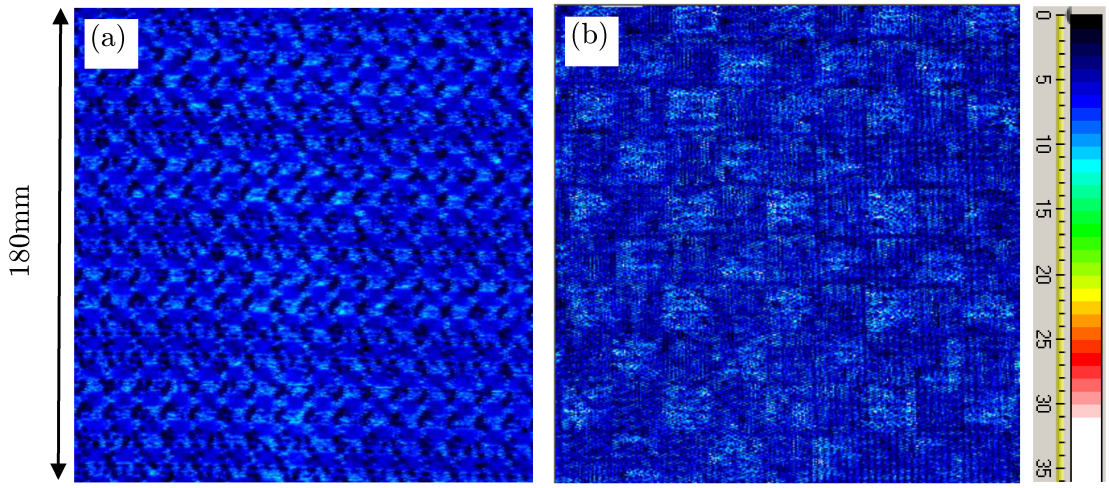


Figure 6.6: Representative C-scan plots pre-test (colour scale in dB): (a) Intralayer fibre hybrid T700 carbon/Vectran, (b) Interlayer fibre hybrid T700 carbon/S2-glass

6.2.3. Test rig development and set-up

The following outlines the development of an impact test rig designed to fix the scaled bonnets with repeatable and quantifiable boundary conditions. By developing a test rig with stringently quantifiable boundary conditions, the numerical model boundary conditions could be constructed to be representative of the experiment. Previous work in the Department of Aeronautics at Imperial College London [160] showed that the same reduced scale Bentley Continental car bonnet could be used to rank the structural performance of various composite materials. There was however an issue with the numerical modelling, since the bonnet was simply placed on an open section of steel plate, and the frictional effects as well as the damping effects of the system were unknown. It would also have been difficult to attach strain gauges to an object free to move so drastically without tearing from the connecting strain gauge wires, typically relatively fragile. Video footage of a preliminary impact test (Figure 6.7) shows the impactor tup striking a plain weave T700 carbon fibre/MTM57 reduced scale bonnet which was resting on a steel plate. Subsequent to impact, the bonnet was seen to spring away from the base plate in an unquantifiable manner since the boundary conditions were uncontrolled.

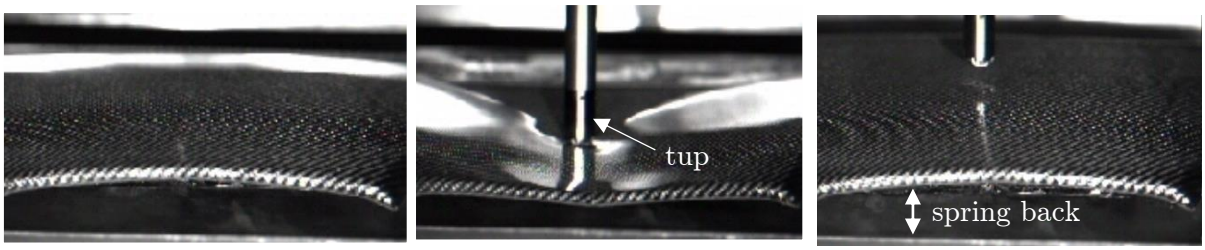


Figure 6.7: Preliminary bonnet impact testing exhibiting uncontrolled boundary conditions [160]

To control and therefore quantify the boundary conditions involved in the low velocity impact testing, either clamps or adhesive would need to be utilised to constrain its movement. End blocks were developed using PTC Creo Parametric 2.0 CAD software and manufactured from mild steel using a CNC machine. To minimise stress concentrations around the end blocks, rounded edges were incorporated as well as rounded chamfers between the connecting face and the mounting point. Appendix 10.7 presents the drawings of the end-blocks used, based upon the end blocks utilised with the DCB and 4-ENF testing conducted in Chapter 3.3.

The base rig of the impact fixture was also designed using Creo Parametric 2.0 CAD software and manufactured from mild steel, cut from a plate using a waterjet cutter. Countersunk impact resistant screws were used to connect the base rig together with the upright fixture points. The boundary conditions were developed to allow rotation at the rear of the bonnet, whilst being fully fixed at the front (representative of a full scale bonnet boundary conditions in service), as shown diagrammatically in Figure 6.8. The rear end blocks were pinned using 8mm diameter pins and loosely tightened with an M8 bolt to allow free rotation about the x-axis. The front-end blocks were spaced 42mm from each other, and the rear 82mm from each other, as shown in Figure 6.9. The front-end blocks were mounted using a hand wrench and torqued as tightly as possible by hand to minimise rotation about the y-axis. See Appendix 10.7 for drawings of the complete test fixture, including dimensions.

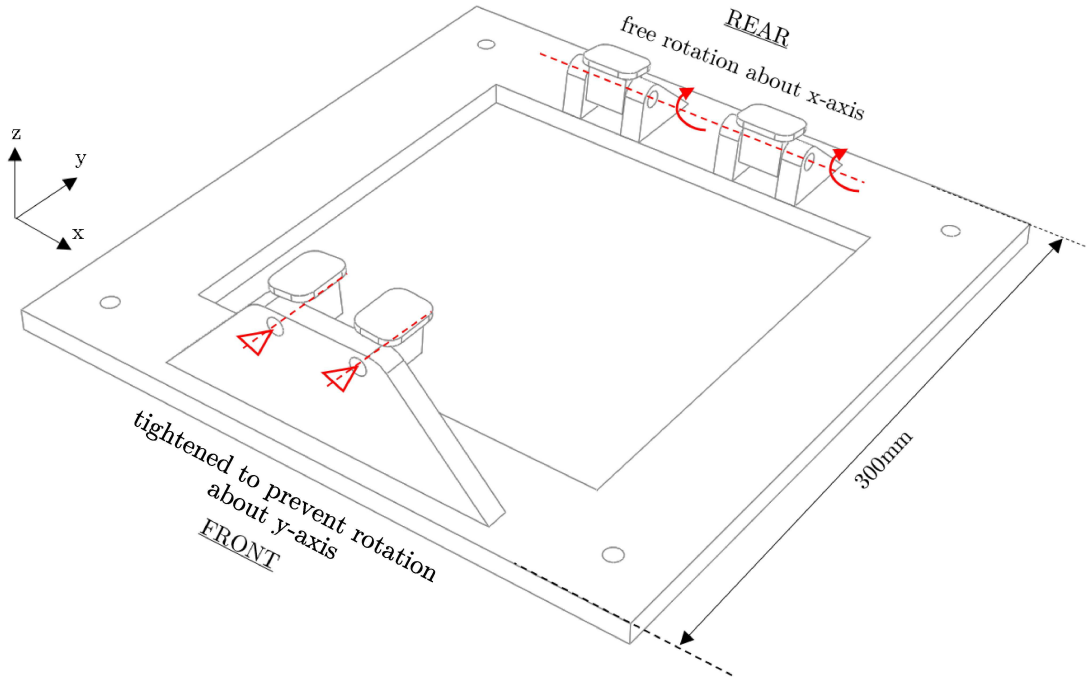


Figure 6.8: Base rig boundary conditions

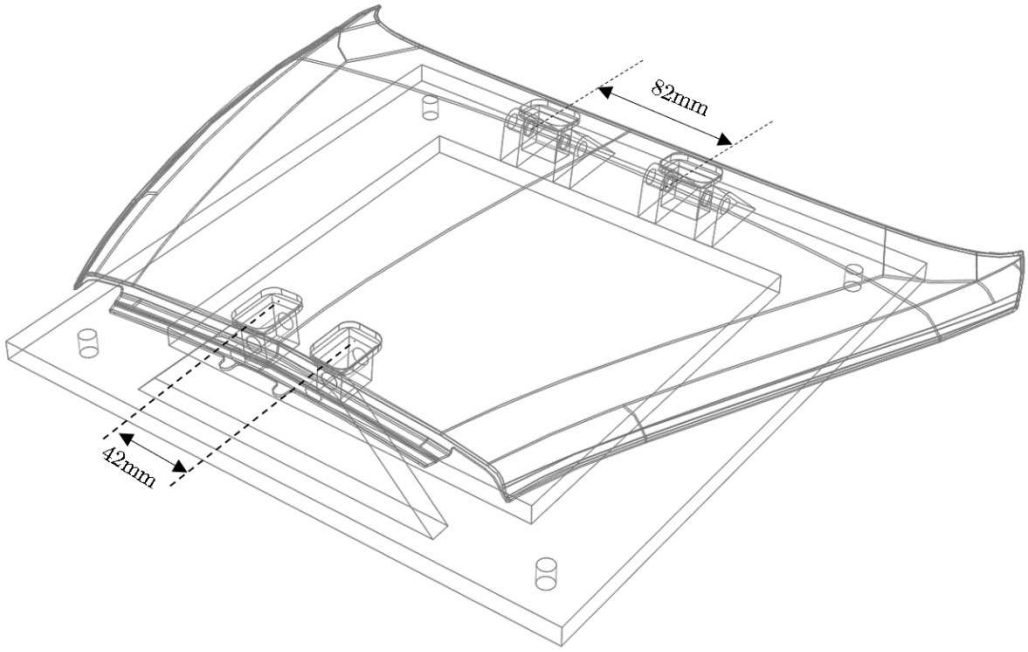


Figure 6.9: End block locale

The bonded region of the bonnet was sanded by hand and cleaned with isopropyl alcohol. The end blocks were then bonded to the bonnet surface using Araldite 2011 two-part epoxy due to its low shrinkage and good resistance to dynamic loading, as stated in its datasheet [183]. Each bonnet was clamped to the test rig fixture using three G-clamps, hand tightened and then left overnight to cure fully before removing the clamps for testing (Figure 6.10).

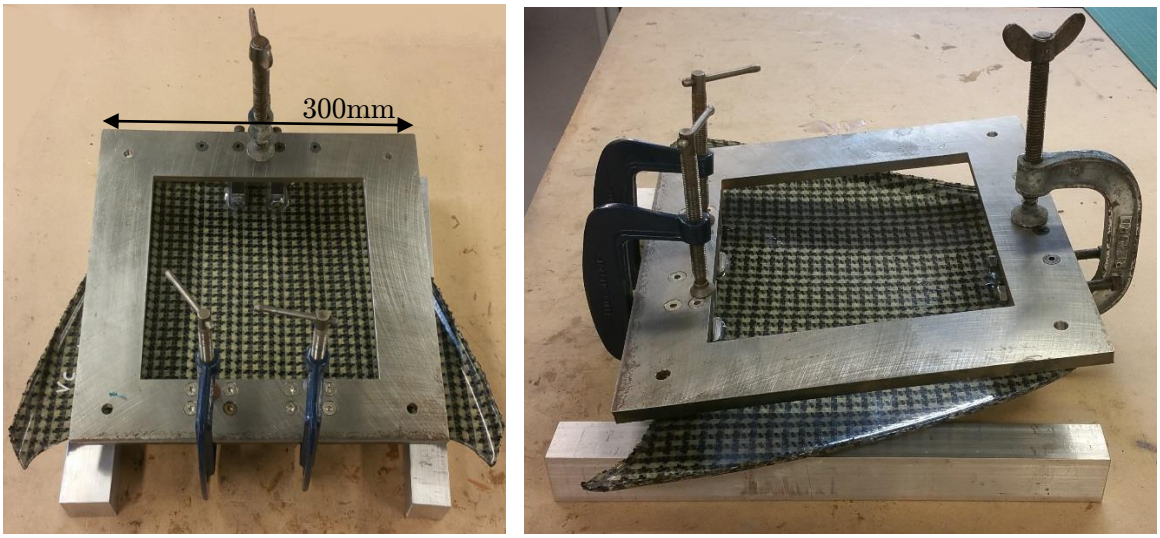


Figure 6.10: End block bonding set-up

Although the G-clamps were used primarily to aid in adhesion between the flat face of the end block and the bonnet surface, the pressure exerted produced adhesive flash, introducing a natural chamfer in the epoxy adhesive, alleviating a step change between the block and the bonnet surface and hence reducing the stress concentrations caused by the impact loading. By applying pressure to the end blocks and the surface of the bonnet, excess adhesive flash naturally built up around the sides of the block (held in place using screws during curing), an image of this is presented in Figure 6.11.

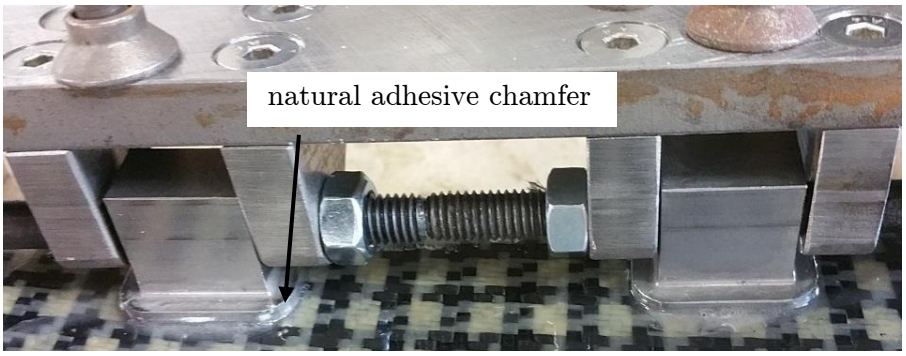


Figure 6.11: Natural adhesive chamfer between end block and bonnet surface (rear of bonnet)

The bonnet impact rig was loaded into the Instron CEAST 9350 drop tower and attached to the base plate using M8 bolts. The impactor tup was set centred at 120mm from the front of the bonnet with two FLA-3-11-1LJC 3mm 120Ω linear gauges (Figure 6.12) attached to the top and bottom of the bonnet, oriented in the x-direction and located 80mm in the x-direction from the impact site. The strain gauge connecting wires were held in place using masking tape to avoid breaking of the delicate wiring during impact, as shown in Figure 6.13. Dedocool anti-flicker DC lighting was used to illuminate the bottom of the bonnet and high-speed video footage was captured using a Phantom v25.11 camera at 100000fps via a mirror located beneath the test, so as to avoid damaging the camera lens from potential fragments or debris produced by the impact event.

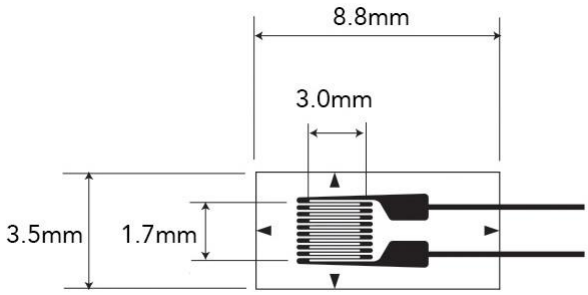


Figure 6.12: FLA-3-11-1LJC strain gauge dimensions [184]

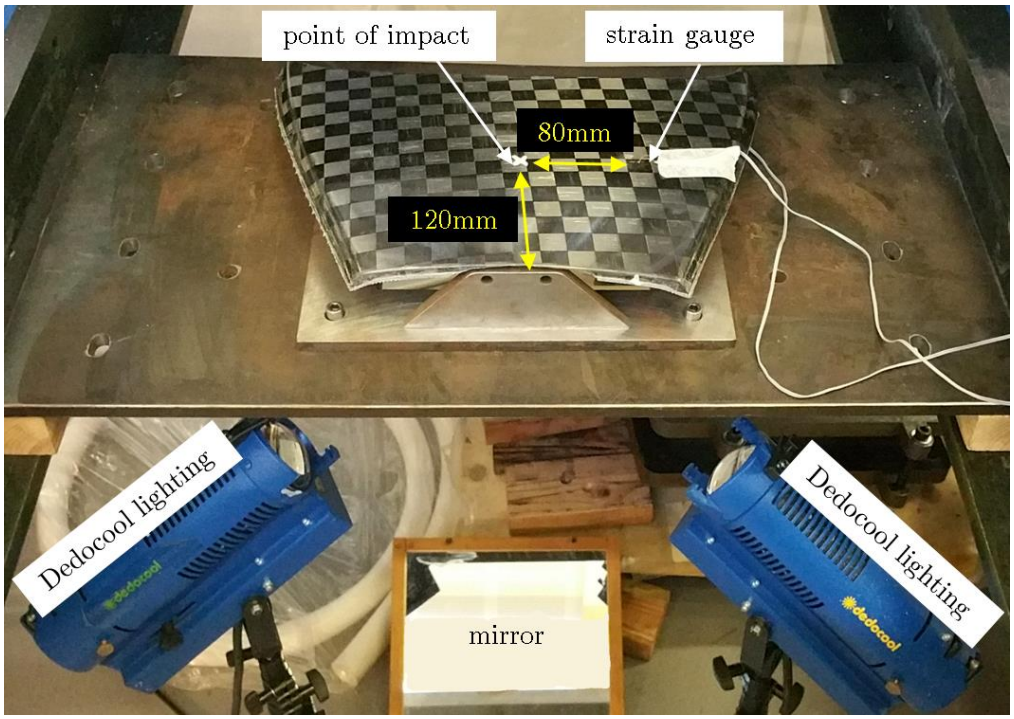


Figure 6.13: Bonnet impact test set-up

The strain gauges were connected to a DSO (Digital Storage Oscilloscope) at a sampling rate of 200000 points per second and triggered manually upon impact (by pressing the trigger by hand). The CEAST software supplied by Instron was used to capture the load cell data, which automatically integrated the load output to determine the velocity and displacement as well as the load, since the mass of the impactor was known to be 2.392kg. The tup diameter used was 16mm, identical to that used throughout the flat plate impacts presented in Chapter 5. Six bonnets made from each fibre hybrid composite were subjected to impact testing, three at 15J, and three at 20J, resulting in a total of six interlayer fibre hybrid T700 carbon/S2-glass bonnets and six intralayer T700 carbon/Vectran bonnets manufactured and tested. A 45J

impact energy was tested but resulted in end-blocks debonding prematurely and therefore invalidating the results.

6.3. Numerical model set-up

The numerical model of the bonnet impact testing was set up by considering the boundary conditions point of contact with the bonnet part. The CAD file of the bonnet was kindly supplied by Solvay [8] along with the mould, and a shell section was created. All minor facets and minute edges, artefacts of the original CAD model, were smoothed and removed using Abaqus 6.14 to enable automatic meshing. The mesh size was used from the mesh sensitivity study undertaken in Section 5.3.2 since it provided a good level of resolution in capturing the relevant failure modes in the same materials, using the same subroutine and element type. The bonnet impact numerical model consisted of 12126 continuum shell elements for the interlayer fibre hybrid T700 carbon/S2-glass model, and 8084 continuum shell elements for the intralayer fibre hybrid T700 carbon/Vectran model. The global mesh size was set to 14mm, with 1mm local refinement around the impact site and 1.5mm along the strain gauge length, shown diagrammatically in red, Figure 6.14.

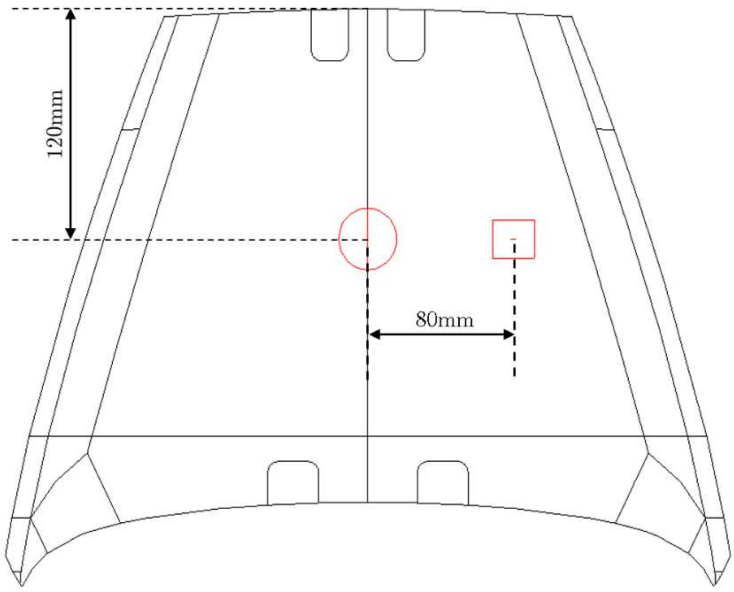


Figure 6.14: Part sectioning and mesh refinement zones, coloured red

The boundary conditions of the numerical model were constrained using MPCs (Multi Point Constraints). These are rigid element ties between one control point and multiple connecting

nodes, allowing for rotational moment and displacement of the control point, dependent upon its own boundary conditions. Figure 6.16 shows the location of the MPC control points which emulate the end block constraints of the physical experimental rig shown in Figure 6.8.

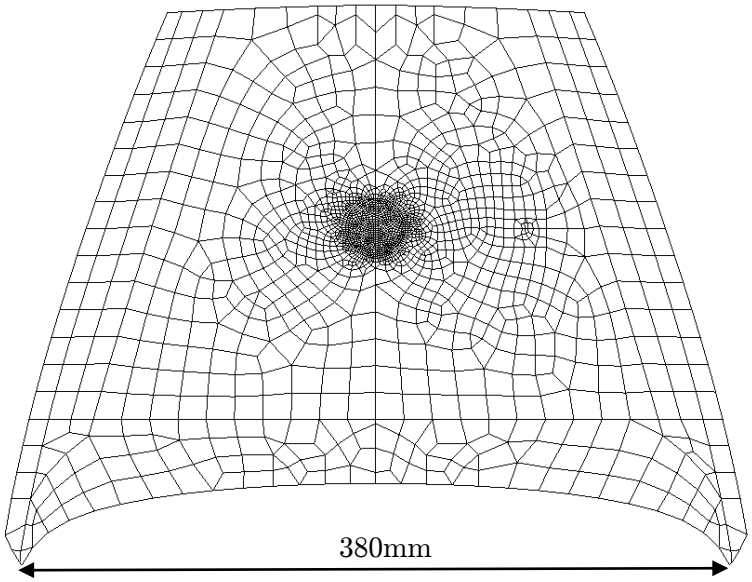


Figure 6.15: Bonnet mesh sizing

The 3-dimensional mesh was created using the Abaqus 6.14 'bottom-up' mesh tool, where an offset thickness and number of layers (plies) were specified. These layers were then assigned the material properties of the relevant fibre hybrid composite, as presented in Table 6.1.

The impactor tup was made up of rigid shell elements, identical to those used in Chapter 5, with an inertial mass at its centre of 2.392kg, resembling the total tup mass within the experimental set-up. A gravitational load card of -9.81m/s was applied in the z-direction throughout the model simulation and an initial predefined field of either -3.51m/s for the 15J impact or -4.05m/s for the 20J impact were applied directly to the centre of the impactor tup, which was in turn constrained solely to displacement within the z-direction. The acceleration output from the impactor tup was computed over the required time step and multiplied by the mass of the impactor (2.392kg) to calculate a load for the response curves displayed in Section 6.4. A global penalty-based interaction property was utilised, with a hard normal contact criterion and a penalty tangential behaviour with a nominal friction coefficient of 0.3 [127].

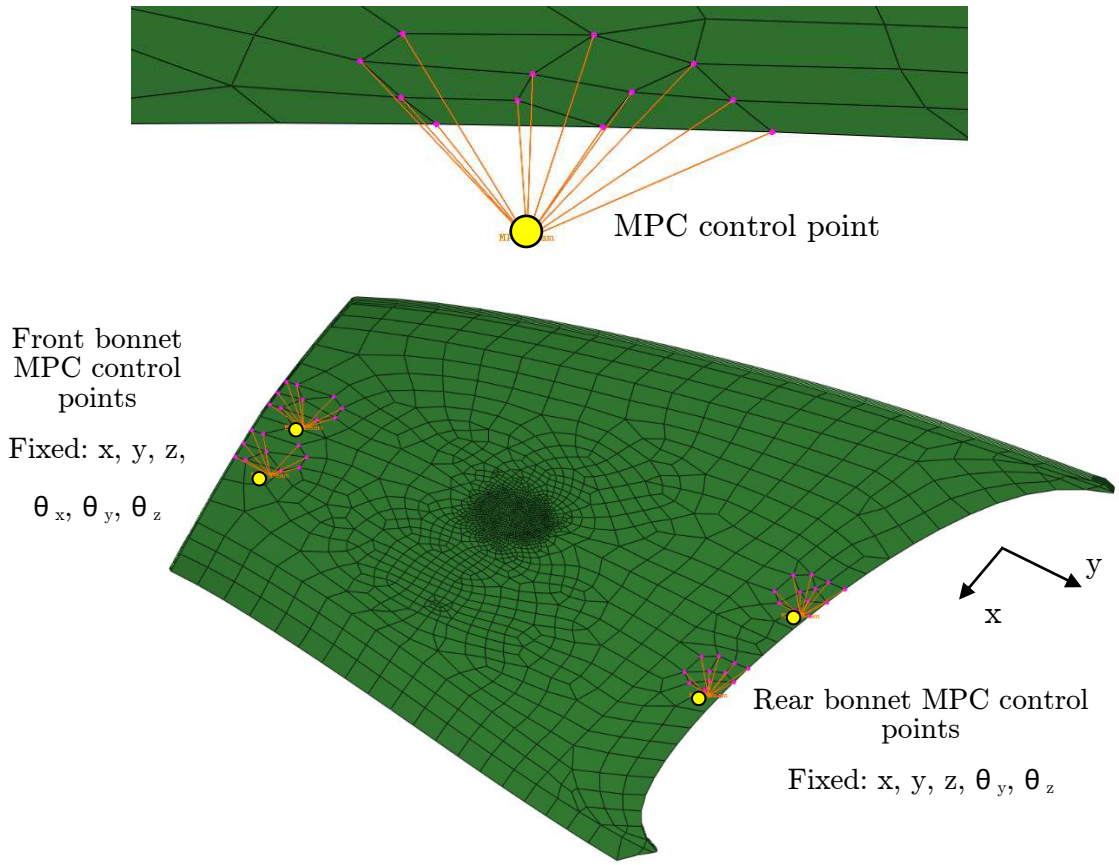


Figure 6.16: Bonnet impact model, MPC control points with boundary conditions

Cohesive surfaces were utilised instead of cohesive elements so that the cohesive element behaviour would not affect the through-thickness properties of the model, given the relative thinness of the bonnets. The Abaqus cohesive surface traction-separation energy-based power law (1.5) was utilised (as with the plate impacts in Chapter 5), where the midpoint surface for each model was given the following properties, determined from the material testing undertaken in Chapter 3, shown in Table 6.2. The interlaminar fracture toughnesses utilised the propagation values for the Mode I and Mode II tests, as with the plate impact models (see page 140 for reasoning). Both the interlayer and intralayer fibre hybrid models were split mid-plane through-thickness and the cohesive surface properties applied to the refined mesh region at the impact point. The underside of the top half was set to the master surface, and the top side of the bottom half was set to the slave surface. This was applied in Abaqus within the general contact dialogue, under individual property assignments. The remaining nodes outside of the refined area were then tied (allowing interlaminar damage to only occur within the

refined region). This is shown diagrammatically in Figure 6.17, where the cohesive surface locations are highlighted in red.

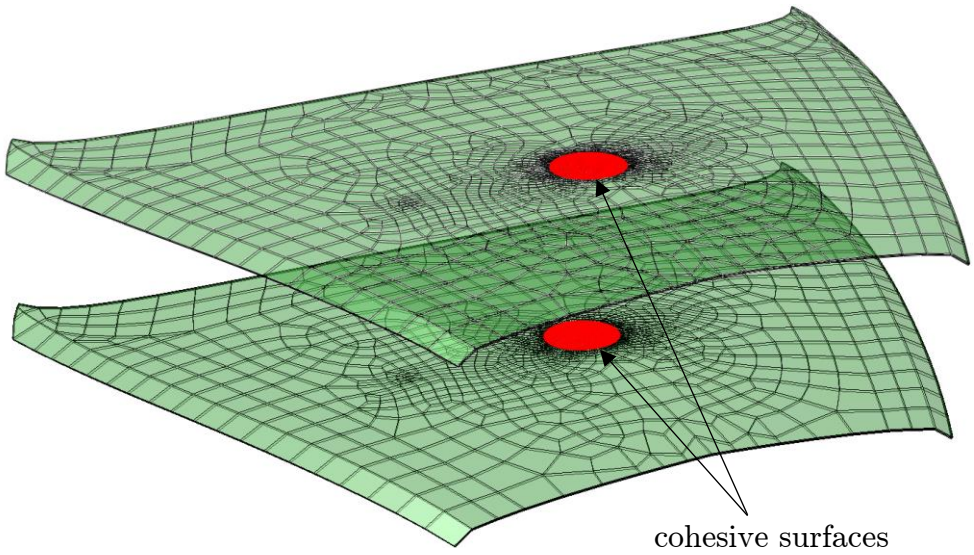


Figure 6.17: Structural bonnet model (exploded into two halves), cohesive surface locations

Table 6.2: Cohesive surface properties

	Interlayer fibre hybrid T700 carbon/S2-glass	**Intralayer fibre hybrid T700 carbon/Vectran**
Stiffness in normal direction (GPa), K_{nn}	2.68	2.68
In-plane shear stiffness (GPa), $K_{ss/tt}$	5.57	2.48
Initiation strength for resin (MPa), σ	80.07	80.07
Mode I interlaminar fracture toughness (kJ/m^2), G_{IC}	0.70*	1.74
Mode II interlaminar fracture toughness (kJ/m^2), G_{IIC}	1.03*	2.50

*Monolithic T700 carbon composite interlaminar fracture energies from literature [179], since the bonnet mid-plane was a carbon/carbon interface

The material properties used for the continuum shell elements were identical to those in the plate impact studies in Chapter 5 for the intralayer fibre hybrid T700 carbon/Vectran models. The interlayer fibre hybrid T700 carbon/S2-glass models however contained a homogenised form of material properties, determined from the testing of the fibre hybrid composite in Chapters 3 and 4, presented in Table 6.3. The flexural stiffness of the bonnet layup (i.e. $[C_0/G_0/C_{45}/G_{45}/C_0/G_0/\ C_{45}]_z$) using the homogenised material properties was calculated using classical laminate theory to be 36.0GPa and the using the individual ply properties was calculated to be 33.6GPa. It was assumed that since the difference between these was low (6.67%) it was sufficient for the structural analysis (although marginally larger than the experimental scatter of the in-plane modulus (5.01%)). Because it would be unlikely for the automotive industry to model each ply for a structural component due to computation efficiency, the homogenised properties provided an ample means of capturing what was a largely elastic response during impact of the bonnet. The permanent strain constant 'β' was not utilised for the bonnet models since there was very little fibre fracture noticed experimentally and therefore permanently deformed fibre fracture was not evident.

A virtual strain gauge was evaluated using the relative displacement between two local nodes, located at the same distance from the impact site as experimentally (80mm in the x-direction) as that shown in Figure 6.13 and Figure 6.14. This was due to the strain rate output from the FE model using the integration points within the elements (i.e. not on the surface of the model). The nodal displacements were output from the numerical models at a frequency of 5kHz to obtain an acceptably high resolution to compare with the experimental output of 200kHz. The following formulae were used to calculate an effective strain across the virtual strain gauge during impact:

$$u_x = x_1 - x_2 \quad , \quad u_y = y_1 - y_2 \quad , \quad u_z = z_1 - z_2 \tag{6.1}$$

$$u_T = \sqrt{{u_x}^2 + {u_y}^2 + {u_z}^2} \tag{6.2}$$

$$\varepsilon = \frac{u_T - u_{T0}}{u_{T0}} \tag{6.3}$$

where u is the distance between the nodes in a given axis, 'x, y, and z' denote the nodal co-ordinates in a given axes for node 1 and node 2, u_T is the total distance between the nodes, u_T

is the initial distance between the nodes, and ε is the overall strain between the two nodes (all for a given time step).

Table 6.3: Material properties used for structural bonnet impact FE modelling, continuum shell elements

	Interlayer fibre hybrid T700 carbon/S2-glass	**Intralayer fibre hybrid T700 carbon/Vectran**
Elastic modulus (GPa), E_{11}/E_{22}	40.56	29.82
Poisson's ratio, ν_{12}	0.049	0.027
Initial in-plane shear modulus (GPa), G_{12init}	5.57	2.48
Ultimate in-plane shear modulus (GPa), G_{12ult}	0.22	0.09
Translaminar fracture toughness (kJ/m^2), $G_{1CT}/G_{2CT}/G_{1CC}/G_{2CC}$	65.3	142.0
Initiation strength (MPa), tension, X_T/Y_T	661.78	671.83
Initiation strength, in-plane (MPa), S_C	80.00	58.74
Initiation strength (MPa), compression, X_C/Y_C	466.61	165.78
Fibre/matrix post failure strength (MPa), X_{CF}/Y_{CF}	116.08	116.08
In-plane shear non-linearity factor, λ	50.0	24.0
In-plane shear rate dependency factor, κ	100.0	0.0
In-plane shear stress where non-linear behaviour starts (MPa), S_{C0}	4.00	1.77
Density (kg/m^3), ρ	1772.2	1574.9
Permanent strain constant, β	1.0	1.0

6.4. Experimental testing and numerical modelling of structural bonnet impacts

The following outlines the complete experimental testing and numerical modelling for the interlayer fibre hybrid T700 carbon/S2-glass and the intralayer fibre hybrid T700 carbon/Vectran structural bonnet impacts with the following data:

- Graphs:
    - Load versus deflection [experimental + numerical]
    - Load versus time [experimental + numerical]
- Interlaminar fracture:
    - C-scanned images of discontinuities [experimental]
- Strain gauge and virtual strain gauge plots [experimental + numerical]

The results are presented alongside the discussion to allow for the reader to view the referenced Figures and Tables. It should be noted that since no fibre fracture occurred, the video capture did not provide any relevant information and is therefore omitted from the following Section.

6.4.1. Interlayer fibre hybrid T700 carbon/S2-glass

Figure 6.18 presents the structural bonnet numerical load responses for the interlayer fibre hybrid T700 carbon/S2-glass during the 15J impact event. The curve demonstrates that the impact event was largely elastic in response, since an overall half-sine wave was noticed in the load versus time curves. There was however some resonance due to underdamping noticed in the numerical models, manifesting as large variations in load throughout the impact event. The curves in the following Figures present the approximate frequencies of resonance associated with this response. A discrete Fourier transform (performed using the NumPy Python library [185] with Python 3.6.5 [186]) of the load versus time curve quantified this frequency at 329Hz to be predominant, Figure 6.19.

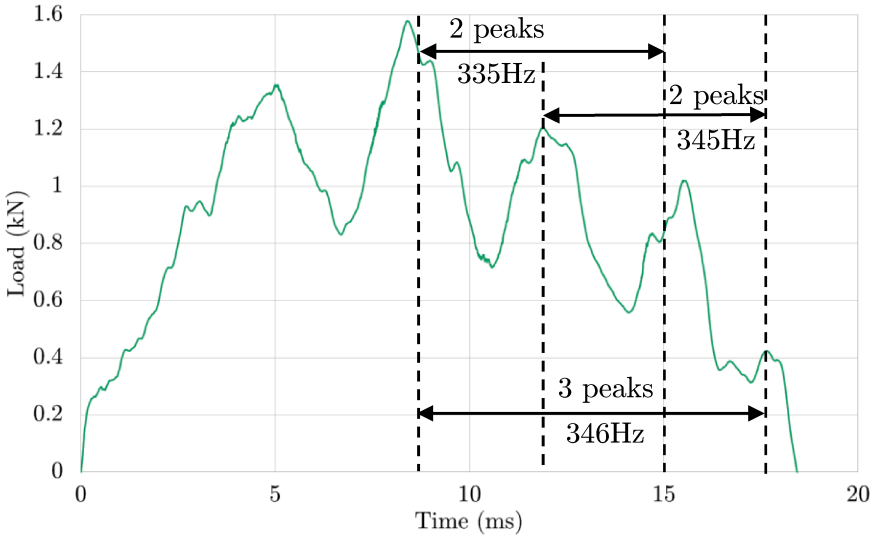


Figure 6.18: Interlayer fibre hybrid T700 carbon/S2-glass numerical FE (undamped) load response at 15J structural bonnet impact, load versus time

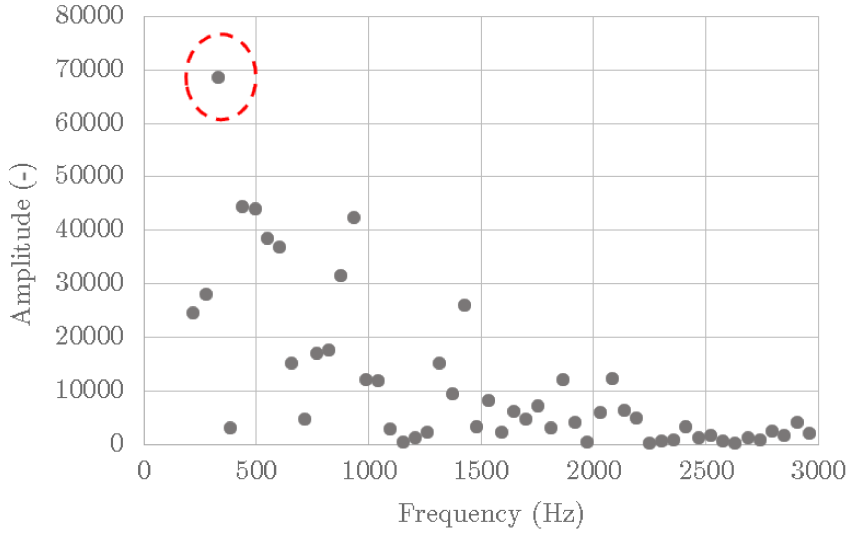


Figure 6.19: Discrete Fourier transform of the load versus time response curve (Figure 6.18), red dashed line encapsulates the frequency of interest = 329Hz, amplitude versus frequency

The initial portion of the 15J load response curve showed little harmonic resonance until approximately 5ms, where the load curve was seen to drop significantly (Figure 6.18). Subsequently, a full structural resonant response was observed throughout the remaining impact event. Upon examining the numerical model up until 5ms, the majority of the bonnets' deflection was largely seen to have been local, with most deformation having been around the impacted region. After 5ms, the bonnet was perceived to undergo a larger deformation with

a less local, more global response, where the rear of the bonnet engaged in larger deflections, shown in Figure 6.20.

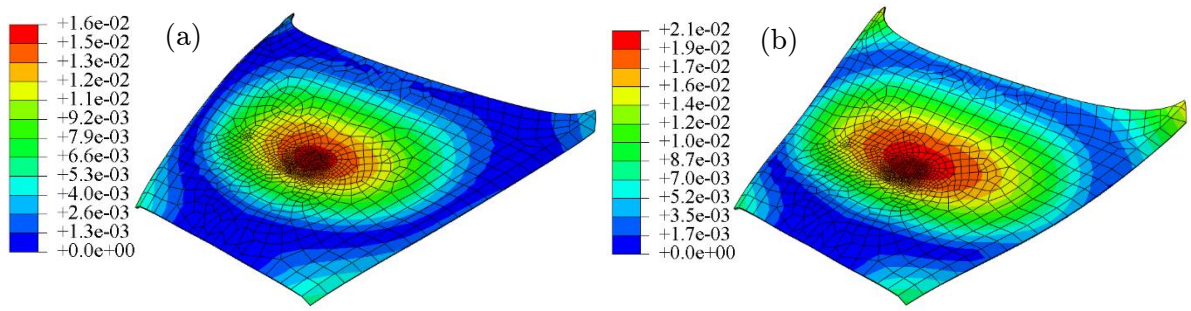
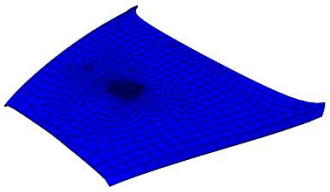
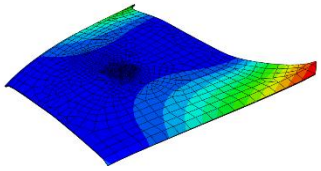
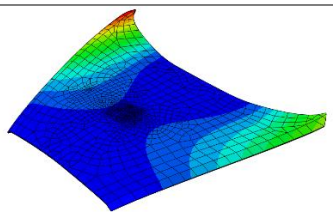
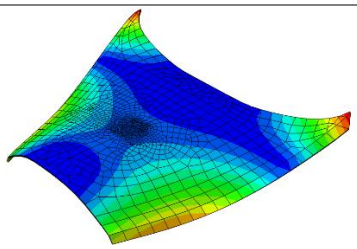
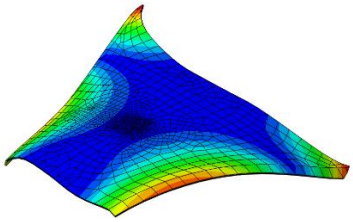
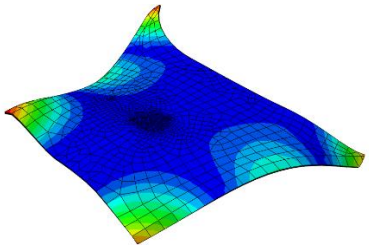
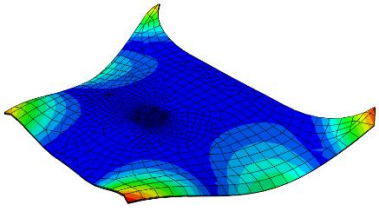


Figure 6.20: Interlayer fibre hybrid T700 carbon/S2-glass 20J structural bonnet impact deflection magnitude (m) at: (a) 5.0ms, (b) 7.4ms

To further understand the natural frequencies associated with the bonnet, an eigenvalue natural mode analysis was carried out. Table 6.4 shows the first six mode shapes of the numerical model along with their associated frequencies. The Abaqus Standard 6.14 linear frequency perturbation solver was employed, where the material was assigned the homogenised elastic properties and the density of the interlayer fibre hybrid T700 carbon/S2-glass composite. The boundary conditions were kept the same as with the explicit analysis and a total of 250 natural frequencies were requested using the Subspace convergence methodology [113]. The same model with a point mass of 2.392kg at the impact point was added to determine the effect of the tup mass on the natural frequencies (assuming a perfect contact during the impact event). Mode 6 appeared to be remarkably similar in shape to that presented in Figure 6.20b, as well as the frequency noted from the undamped numerical models in Figure 6.18 and Figure 6.19. This was difficult to quantify conclusively however, due to the complexity and overlapping of the natural frequencies. It was assumed that the numerical model did not capture a damping factor present within the material of the interlayer fibre hybrid T700 carbon/S2-glass structural bonnet impacts.

Table 6.4: Natural frequencies of the interlayer fibre hybrid T700 carbon/S2-glass numerical model

Mode number and associated frequency	Mode shape
Mode 0 (without tup mass): 0Hz Mode 0 (with tup mass): 0Hz	
Mode 1 (without tup mass): 86.0Hz Mode 1 (with tup mass): 85.8Hz	
Mode 2 (without tup mass): 87.1Hz Mode 2 (with tup mass): not present	
Mode 3 (without tup mass): 174.1Hz Mode 3 (with tup mass): 184.1Hz	
Mode 4 (without tup mass): 183.6Hz Mode 4 (with tup mass): 181.5Hz	
Mode 5 (without tup mass): 342.6Hz Mode 5 (with tup mass): 342.8Hz	
Mode 6 (without tup mass): 344.0Hz Mode 6 (with tup mass): 344.4Hz	

To counteract the resonance within the interlayer fibre hybrid numerical model, Rayleigh material damping was employed, with a damping factor of 0.3 (found through parametric modelling, Appendix 10.4). The reason for doing so was because the natural damping of the experimental set-up was not accounted for. The following equation presents the Rayleigh damping formulation, where the natural frequency found through the discrete Fourier transform of 329Hz was used. The β constant was set to zero since it is associated with damping higher frequencies.

$$\xi_i = \frac{\alpha_R}{2\omega_i} + \frac{\beta_R \omega_i}{2} \tag{6.4}$$

where ξ_i is the damping factor, α_R is the Rayleigh 'alpha' constant, ω_i is the natural frequency at a given mode, and β_R is the Rayleigh 'beta' constant.

The resulting numerically damped models, along with the experimental load response curves for the 15J and 20J impact events are presented in Figure 6.21 and Figure 6.22. Once Rayleigh damping was employed, good correlation was observed in both load versus deflection and also load versus time for the numerical models.

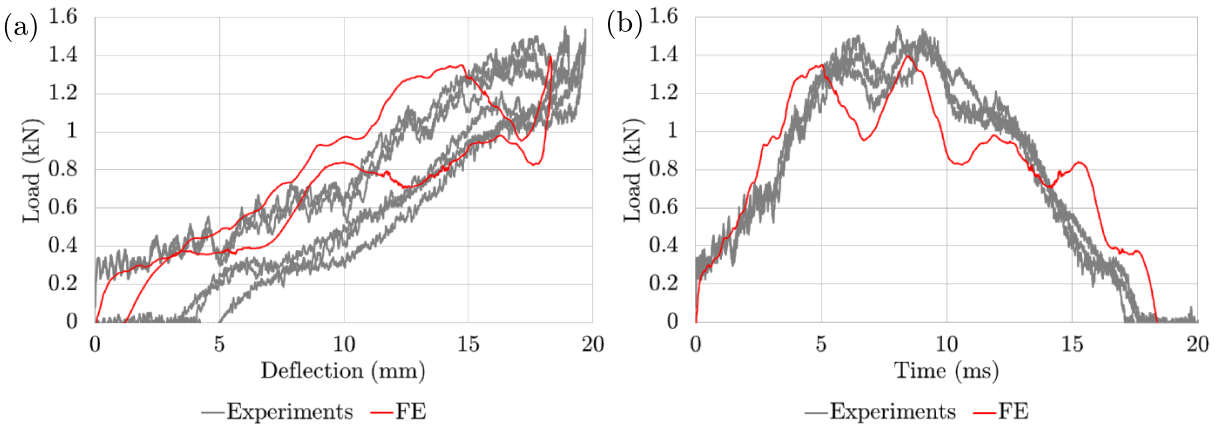


Figure 6.21: Interlayer fibre hybrid T700 carbon/S2-glass load response at 15J structural bonnet impact: (a) load versus deflection, (b) load versus time

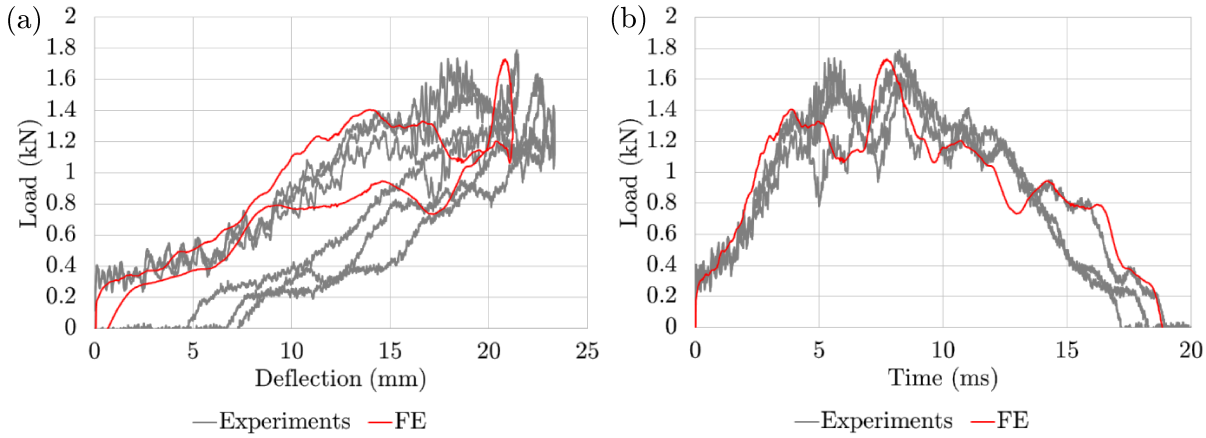


Figure 6.22: Interlayer fibre hybrid T700 carbon/S2-glass load response at 20J structural bonnet impact: (a) load versus deflection, (b) load versus time

Figure 6.23 and Figure 6.24 present the strain gauge responses for the structural bonnet impacts at 15J and 20J respectively. The first half of the sine wave for both numerical models were seen to compare well to the experimental tests, where both the magnitude of strain on the top and bottom side of the bonnet as well as the time phase were captured accurately. The second half of the sine wave was less well defined for the numerical models, and the second half of the wave was seen to have taken longer to dissipate than the experimental waves. The reason for this difference in rate of decay is difficult to quantify because of the complex interactions occurring between the various natural modes of the system, but also because of the rigidity of the numerical boundary conditions, which did not incorporate the elastic compliance within the test rig. Quantifying this however would require further testing regarding the damping characteristics of the drop tower structure and materials, outside the scope of this work due to time constraints. The experimental DSO appeared to truncate the strain readings at 1600με, but the reason for this was unknown. Aside from these, the numerical model captured the strain gauge readings extremely well given the complexity of the system.

The wave form captured both experimentally and numerically was in form due to the stress wave caused by the impactor tup, permeating across the bonnet's structure. The two strain gauges appear to be opposing in tension and compression due to their placement on either side of the bonnets surface, where the bonnet underwent flexure locally due to the stress wave.

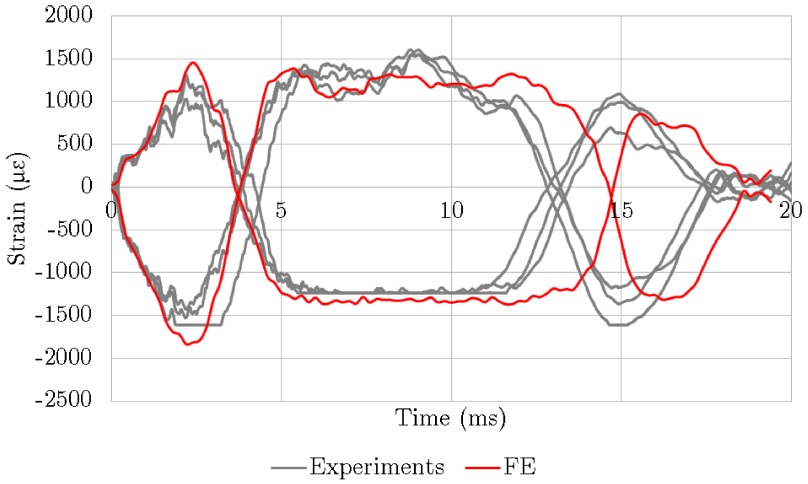


Figure 6.23: Interlayer fibre hybrid T700 carbon/S2-glass strain gauge response at 15J structural bonnet impact

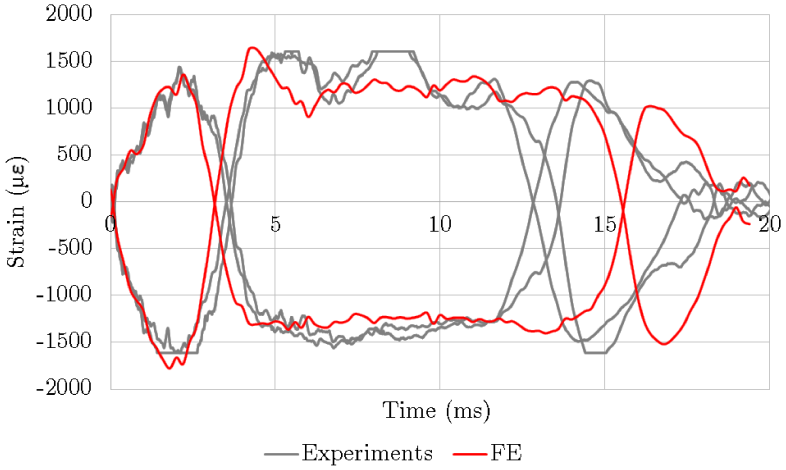


Figure 6.24: Interlayer fibre hybrid T700 carbon/S2-glass strain gauge response at 20J structural bonnet impact

When comparing the impact site cross-sections for both event energies, a clear mid-plane ply split could be seen in the 20J bonnet impact (Figure 6.25). C-scan plots also presented a discontinuity in the ultrasonic pulse in both the 15J and 20J impacts, presented in Figure 6.26.

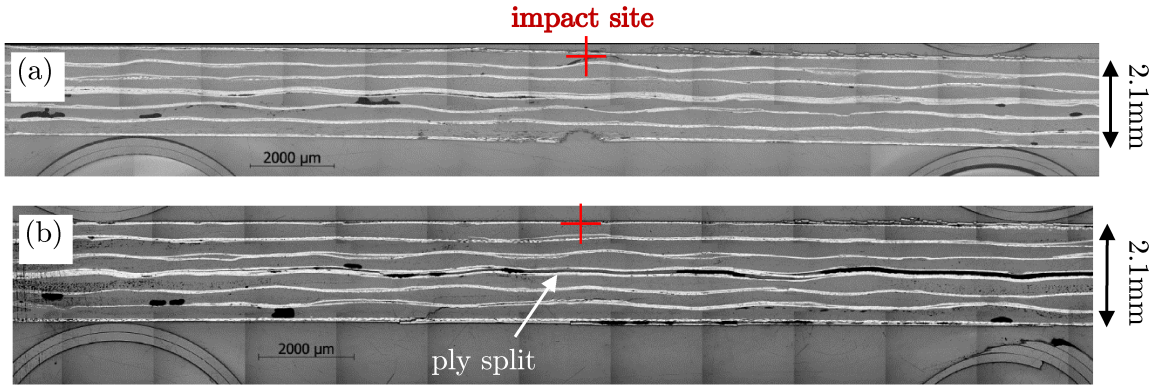


Figure 6.25: Micrographs of interlayer fibre hybrid T700 carbon/Vectran bonnet cross-section along the plane x-z at impact site: (a) 15J, (b) 20J

Given then that the cross-sectional micrographs and the numerical models both showed no evidence of delamination, especially at 15J, the fact that the C-scan plots showed 'damage' (Figure 6.26) was surprising. This was likely due to the local indentation of the material surface (noticed visually) rather than a potential delamination between neighbouring plies and is corroborated by the experimental load response curve returning to a non-zero deflection after the impact (Figure 6.21a and Figure 6.22a). It should be noted that the pixelated edges shown in the C-scans are attributed to the slight movement of the bonnets during scanning, despite the steel blocks used to prohibit movement (Figure 6.5). There was no damage associated with fibre fracture through tension or compression in either the 15J or 20J numerical models.

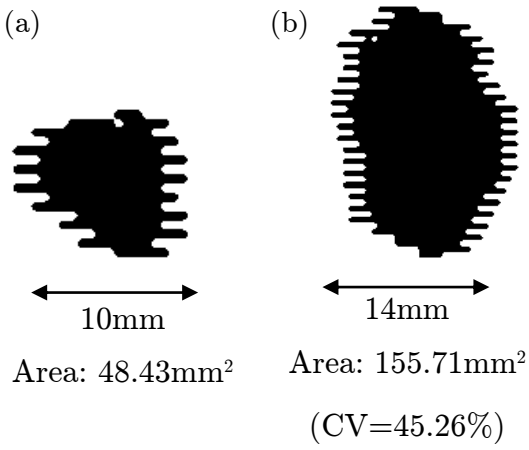


Figure 6.26: Representative C-scans for interlayer fibre hybrid T700 carbon/S2-glass bonnet experimental impacts: (a) 15J, (b) 20J

6.4.2. Intralayer fibre hybrid T700 carbon/Vectran

Figure 6.28 and Figure 6.27 present the experimental and numerical load response curves for both the 15J and 20J impact events. The 15J impact event showed reasonable correlation in what was largely an elastic response, except some load noise at the point of maximum deflection, where the tup began to rebound. This was due to compressive fibre failure occurring at 8.2ms, where one element fully degraded and its damage criterion reached unity. This was also the case for the load noise noticed within the 20J impact at 5.8ms, where the tup acceleration was affected by the compressive degradation of two 1mm x 1mm continuum shell elements at the surface of the bonnet, at the impact site. Figure 6.29 further validates this

numerical failure mode, where fibre failure on the top surface of the impact site was noticed through a cross-sectional micrograph at both 15J and 20J impact energies.

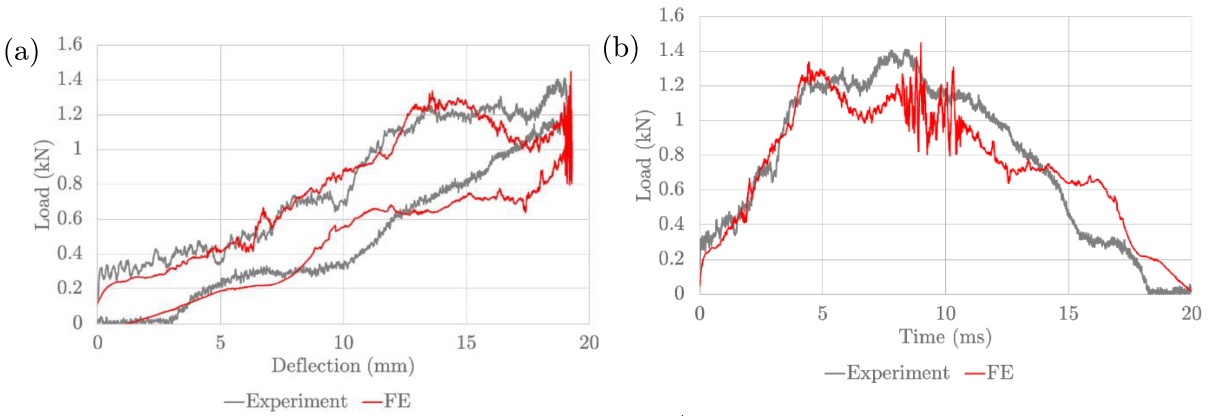


Figure 6.27: Intralayer fibre hybrid T700 carbon/Vectran load response at 15J structural bonnet impact: (a) load versus deflection, (b) load versus time

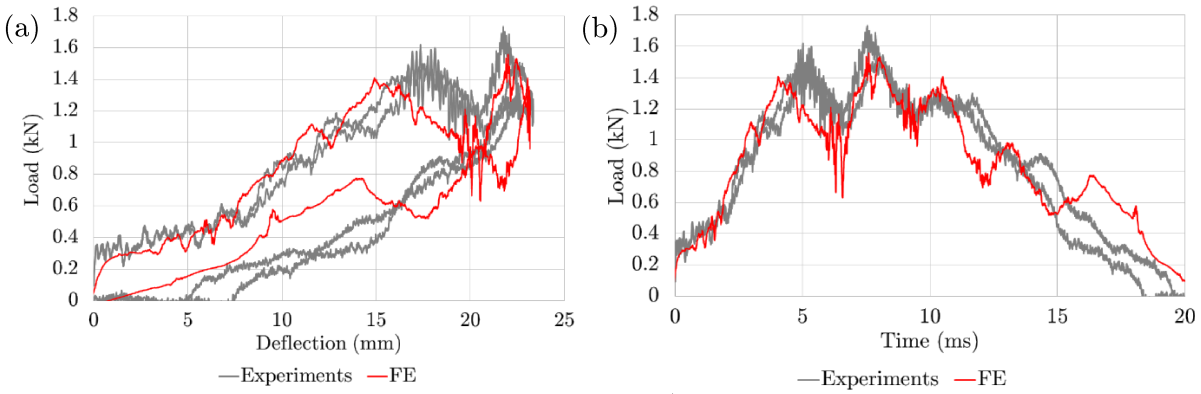


Figure 6.28: Intralayer fibre hybrid T700 carbon/Vectran load response at 20J structural bonnet impact: (a) load versus deflection, (b) load versus time

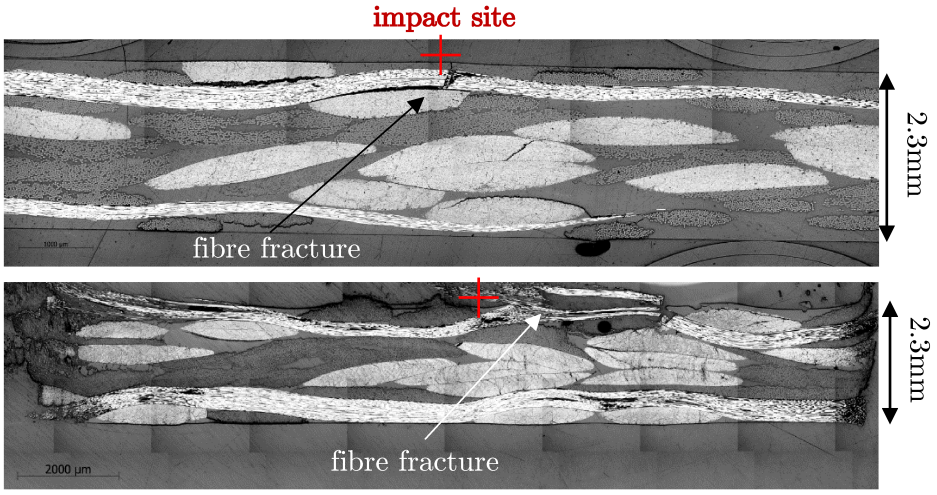


Figure 6.29: Micrographs of intralayer fibre hybrid T700 carbon/Vectran bonnet cross-section along the plane x-z at impact site: (a) 15J, (b) 20J

Aside from the noisy load signals experienced in the experimental model, a good correlation was noticed between the initial sine wave numerical and experimental load response curves. Rayleigh damping was not required because no natural mode was excited by the impactor tup in the numerical model. This implies that the material properties were correctly modelled (since the velocity of a wave is a function of the modulus and density of the material).

Figure 6.30 and Figure 6.31 present the experimental and numerical initial strain gauge responses for both the 15J and 20J impact events. Good correlation between the first half of the sine wave (between approximately 0-4ms) was noticed for both impact energies, which indicates that the modulus, volume, and density were correctly modelled (since the wave speed is directly proportional to the elastic modulus and density). The magnitude of the strain modelled was slightly larger numerically than experimentally recorded, although three of the six bonnets failed to capture data at all due to a timing fault within the drop tower software.

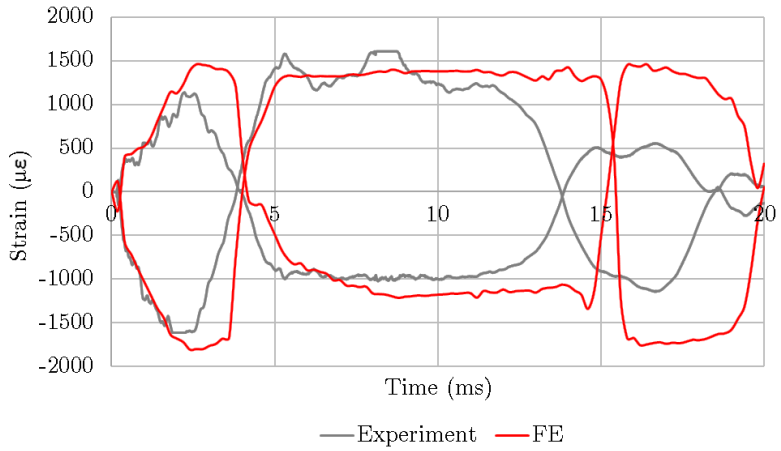


Figure 6.30: Intralayer fibre hybrid T700 carbon/Vectran strain gauge response at 15J structural bonnet impact

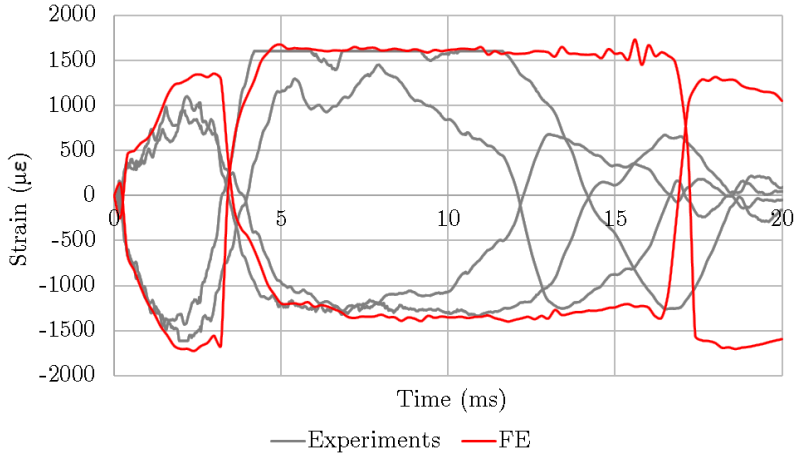


Figure 6.31: Intralayer fibre hybrid T700 carbon/Vectran strain gauge response at 20J structural bonnet impact

Similar to the interlayer fibre hybrid discussed in the previous Section 6.4.1, post-test C-scans showed discontinuities around the impact site whereas the numerical models showed no interlaminar failure and the damage plots were likely attributed to indentation effects. This theory was further validated through scarcity of delamination noticed in the cross-sectional micrographs in Figure 6.29. It should be noted that the areas associated with the C-scan plots also showed the pattern of the fibre architecture, where the undulations of the intralayer fibre hybrid 2x2 twill weave were noticed in Figure 6.32b.

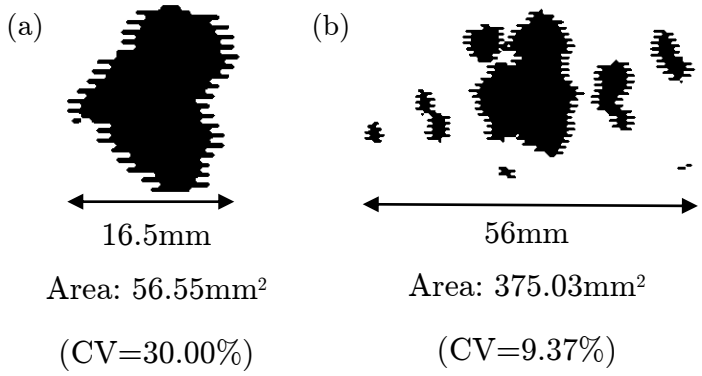


Figure 6.32: Representative C-scans for interlayer fibre hybrid T700 carbon/S2-glass bonnet experimental impacts: (a) 15J, (b) 20J

6.5. Quantifying the numerical model's accuracy

By quantifying the peak loads and maximum deflections throughout the range of the structural bonnet tests, the numerical models' effectiveness could be discussed. Figure 6.33 and Figure 6.34 present the structural bonnet impact peak loads per unit mass for each bonnet at 15J and 20J impact events respectively. It was interesting to notice that the 20J impact models showed closer correlation to the experimental data than the 15J counterparts, although due to lost data of three of the intralayer fibre hybrid T700 carbon/Vectran bonnets (due to the manual triggering and timing fault in the drop tower software), a good amount of scatter was not possible (see Figure 6.27 and Figure 6.28). Good correlation was noticed in the peak loads recorded between the numerical model and the experimental testing, which was consistent with the material properties and boundary conditions having been modelled correctly. Given the complexity of the resonant frequencies affecting the structural response of the system, the accuracy of the virtual strain gauges compared to the experimental strain gauges in the

previous section confirms that the material properties and boundary conditions were correctly numerically modelled.

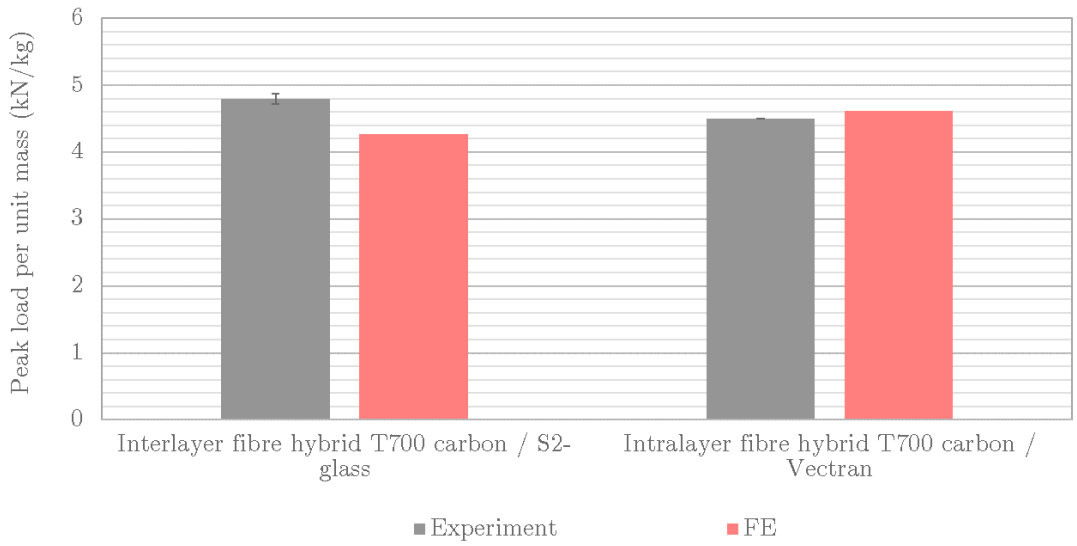


Figure 6.33: 15J structural composite bonnet impact, peak load per unit mass

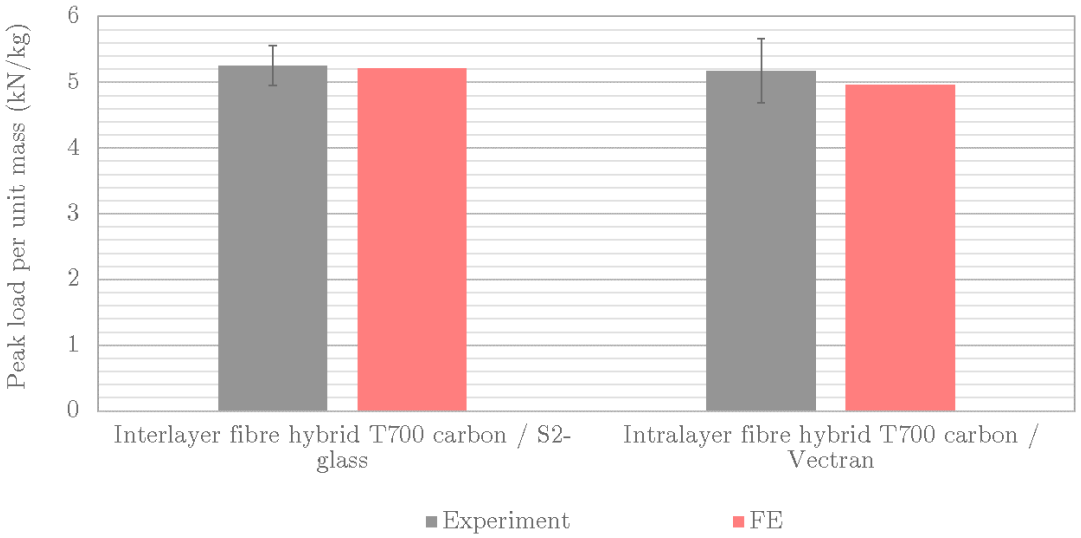


Figure 6.34: 20J structural composite bonnet impact, peak load per unit mass

The maximum deflection was quantified in Figure 6.35 and Figure 6.36, where good correlation was noticed between the numerical model and the experimental data. The numerical models showed lower deflection than that in the experiments across all test regimes which was attributed to the more compliant experimental boundary conditions, since the steel test fixture

was modelled as rigid points in the model. The maximum deflections quantified from the numerical model are conservative (since the compliance of the test rig was not modelled), since the boundary conditions are rigidly fixed (and thus less compliant than the experimental test rig).

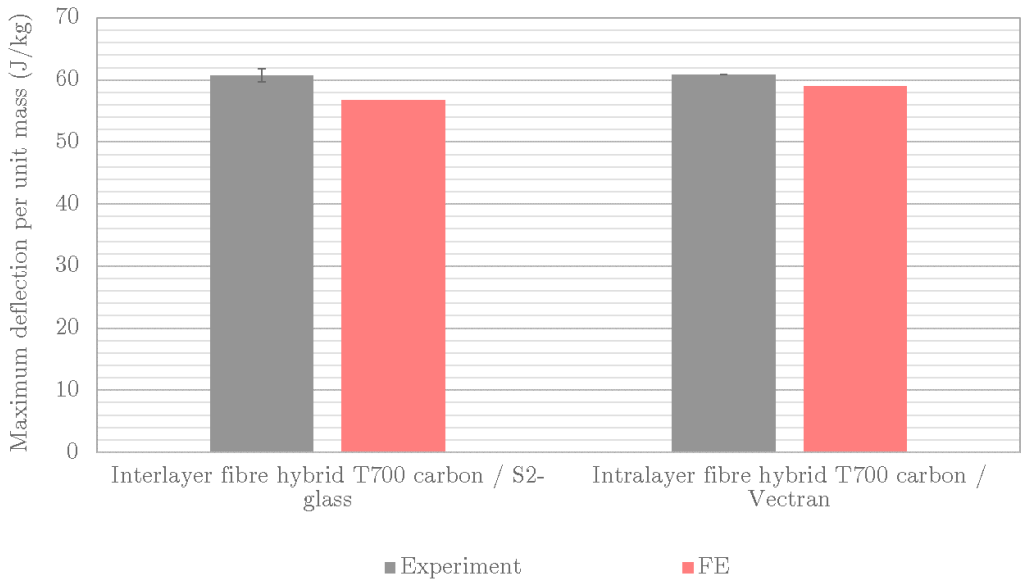


Figure 6.35: 15J structural composite bonnet impact, maximum deflection per unit mass

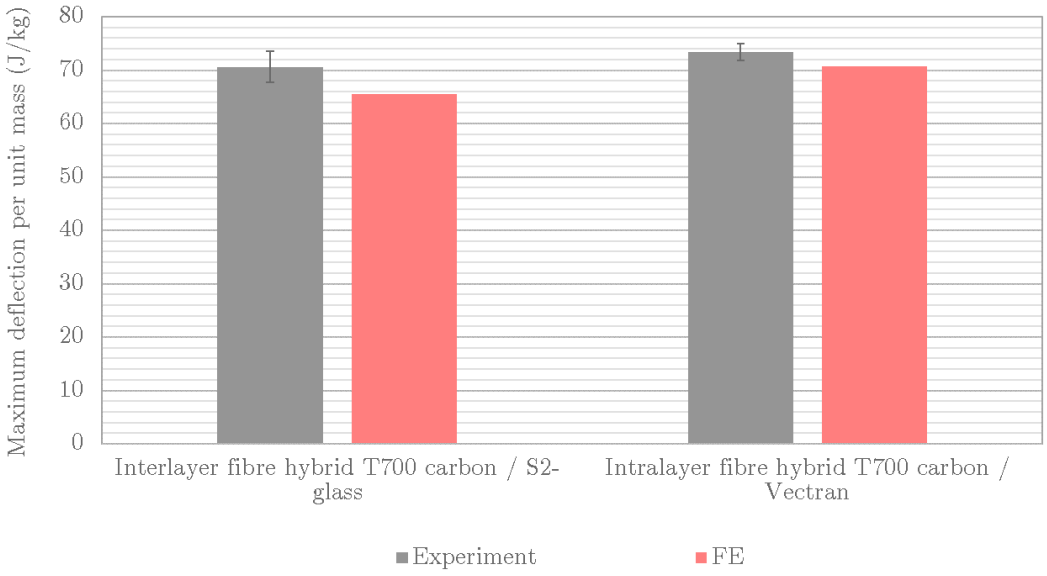


Figure 6.36: 20J structural composite bonnet impact, maximum deflection per unit mass

6.6. Summary

The research presented in this Chapter continues development from the in-plane, interlaminar, translaminar, and low velocity properties determined in Chapters 3, 4, and 5 to accurately numerically model low velocity impact events that compared well to the experimental testing of a reduced scale Bentley Continental car bonnet. A novel test-rig was developed and proved successful in providing quantifiable boundary conditions for the numerical model. The numerical model was seen to capture the elastic response of the system reliably, across two discrete energy levels. The interlaminar and translaminar failure modes were also captured, where interlaminar damage did not initiate (except for one anomaly in the interlayer fibre hybrid), and minimal compressive fibre fracture captured on the bonnet surfaces. The numerical model assumed rigid boundary conditions at the fixture points to the bonnet (although free rotation in given axes), which may have been the cause for the initial underdamped load response curve for the interlayer fibre hybrid T700 carbon/S2-glass numerical model, requiring Rayleigh damping to compensate.

Strain gauge data captured during the experimental impact compared well to virtual strain gauges within the numerical model given the complexity of the system. The utilisation of the Abaqus VUMAT subroutine proved successful since the structural component was modelled and compared well to the experimental testing. This novelty within the field shows a promising application for the modelling approach used in full-scale structural component testing, particularly concerning fibre hybrid composites, which exhibit a superior combination of structural and impact resistant properties compared to their monolithic composite counterparts.

Chapter 6 publications and dissemination:

- **Invited webinar presentations:**
    - T. Katafiasz, "Bridging Characterization and Simulation: Materials Information Needs for Design," in *Granta Webinar,* Cambridge, UK, 2017 [16]
- **Conference oral presentations:**
    - T. J. Katafiasz, "Development of a Novel Compact Tension Specimen for Fibre Hybrid Composites," in CompTest 2017: 8th International Conference on Composites Testing and Model Identification, Leuven, Belgium, 2017 [15]

7. Discussion

7.1. Introduction

The research topics explored in this thesis are as follows:

i. The in-plane and interlaminar characterisation of interlayer and intralayer fibre hybrid composites, and their monolithic composite counterparts (Chapter 3).
ii. The development of a novel Compact Tension specimen to mitigate premature compressive failure, hence determining the translaminar fracture toughness of the fibre hybrid composites (Chapter 4).
iii. Successfully employing an existing energy-based bilinear plane stress Abaqus VUMAT subroutine in numerically modelling the fibre hybrid composites, correlating accurately to low velocity experimental impact tests (Chapter 5).
iv. The development of a novel test rig for low velocity impact testing of a reduced scale Bentley Continental car bonnet, thus providing insight into the use of the Abaqus VUMAT subroutine for structural impact modelling of fibre hybrid composites (Chapter 6).

The following section discusses the key findings, the relationship between the different results, and their context regarding the background literature. The study's advancements as well as limitations regarding the testing, numerical modelling, and material selection are also discussed.

7.2. Key findings

The base level experimental testing provided coherent and specific mechanical properties for the materials tested. The successful numerical impact modelling in the latter two Chapters of this thesis is underpinned by the relevance and accuracy of the in-plane, interlaminar, and translaminar material properties measured in Chapters 3 and 4.

The tensile, compression, and in-plane shear testing proved highly repeatable with low levels of scatter within both the monolithic composite and fibre hybrids. The interlayer fibre hybrid T700 carbon/S2-glass tensile properties provided experimental indication of a rule of mixtures, where both the modulus of the hybrid was between those of its monolithic composite

counterparts. Linear [57] and bilinear [64] theoretical rule of mixture calculations used to estimate the interlayer and intralayer fibre hybrids tensile modulus and strength proved inaccurate. The same level of deviation between the experimental and theoretical values were however corroborated experimentally by Ribeiro et al. [64] and others [62], [65]. Regarding the interlayer fibre hybrid T700 carbon/S2-glass, the theoretical rule of mixture discrepancies were likely due to the alternating layup of the carbon spread tow plies, where previous research had suggested that alternating spread tow carbon fibres within interlayer fibre hybrid composites improved the tensile performance [55], [56] and also the penetration resistance [101]. This can be attributed to the suppression of fibre cluster breaks across multiple same-fibre type plies due to the alternating interlayer stacking sequence, where any fibre fracture would be limited to one ply layer growth [55]. Regarding the intralayer fibre hybrid T700 carbon/Vectran, the T700 carbon tensile data used for the rule of mixtures calculations was idealised and taken from the monolithic T700 carbon spread tow composite test data, and thus did not consider the crimp within the 2x2 twill weave of the fibres. This fibre crimp resulted in poor in-plane tensile and compressive moduli and strength. Of the materials tested, the monolithic Vectran composite provided the lowest compressive modulus and strength due to the kinking of the fibres at a microscopic level and thus proved to be highly matrix dominated by presenting a similar strength to the monolithic MTM57 resin. It also presented a non-linear response in both compression due to the kinking of its fibrillous microstructure and in tension due to the fibre crimp. This phenomenon also manifested in the tensile response of the intralayer fibre hybrid T700 carbon/Vectran, where the fibre crimp caused by the weave architecture at a macroscopic scale resulted in a non-linear in-plane load response.

The volume fraction measurements of the fibre hybrid composites showed low scatter whilst employing a TGA (Thermogravimetric Analysis) burn-off method that was further corroborated by analytical microscopy of the through-thickness cross-section. A drawback of the TGA analysis manifested where the unit cell of the intralayer fibre hybrid T700 carbon/Vectran weave proved to be too large for the maximum specimen size of the furnace. The analytical microscopy of the intralayer fibre hybrid T700 carbon/Vectran presented reasonable fibre to fibre volume fractions of 0.43 carbon to 0.57 Vectran, where the 2x2 twill weave idealistically contained equal tow volumes for each fibre type.

The interlaminar fracture of the fibre hybrids presented high levels of scatter, namely due to the varying 0° to 90° carbon fibre direction resulting from the plain weave architecture of the carbon spread tow. This manifested from the mid-plane 0°/90° carbon ply splitting and effectively becoming a carbon to carbon interface, rather than a carbon to glass interface. The intralayer fibre hybrid T700 carbon/Vectran presented higher interlaminar fracture toughness compared to that of the interlayer fibre hybrid T700 carbon/S2-glass in both Mode I and Mode II. This was due to the high level of fibre bridging within the Vectran [56] for the Mode I toughness, as noted in the post-test micrographs. The large undulations caused by the 2x2 twill weave (prohibiting interply fibre nesting and resulting in a tortuous crack path) accounted for the increased Mode II toughness within the intralayer fibre hybrid T700 carbon/Vectran [72], [73].

Translaminar fracture testing of the fibre hybrid composites (Chapter 4) was beneficial not only in the toughness values measured, but it also provided an insight into the failure processes involved during the low velocity impact testing (Chapter 5). Previous researchers' Compact Tension specimen geometries proved to be unsuitable for the materials tested because out-of-plane buckling and compressive failure occurred, namely whilst utilising the 2TCT specimen geometry [93]. Previous research had also failed to provide a solution to the out-of-plane buckling observed when CT testing the S2-glass composite and the fibre hybrid composites. The NCCT and ENCCT specimens were therefore developed to provide a solution to this problem, which frequently occurs throughout this field. The toughness values measured using these specimen geometries provided similar, if not lower, scatter than those acquired through the use of traditional CT specimens [87], [171], [172]. The interlayer fibre hybrid T700 carbon/S2-glass presented toughness values between its two monolithic composite counterparts. This rule of mixtures should be noted, and other researchers have also confirmed this phenomenon [101], [102] for similar interlayer fibre hybrid composites. The intralayer fibre hybrid T700 carbon/Vectran *R*-curve provided insight into the translaminar fracture processes involved in complex interwoven fibre hybrids, where the location of the constituent materials was seen to affect the fracture toughness at a (micro) local scale. This resulted in high scatter along the length of the crack during the propagation stage of the *R*-curve dependent upon the fibre type at the crack tip. The intralayer fibre hybrid T700 carbon/Vectran presented higher fracture toughnesses than the other materials tested, due to

the larger pull-out lengths promoted by the 2x2 twill weave architecture. A drawback of the ENCCT specimen geometry lies in its ability to allow for larger than 10mm x 10mm unit cell composites, where fibre pull-out would likely extend into the thickened portion of the specimen and hence alter the perceived toughness values.

The low velocity impact plate experimental testing provided valuable insight into the impact resistance of fibre hybrid composites. The in-plane, interlaminar, and translaminar material properties measured during the aforementioned testing proved vital in highlighting the complex failure modes required for low velocity impact numerical modelling. The monolithic T700 carbon composite presented poor penetration resistance, whereas the monolithic S2-glass composite did not penetrate at either the 70J or 140J energy level. These responses tended to be dictated by the translaminar fracture toughness values measured from the NCCT and ENCCT testing, where larger fibre pull-out lengths (resulting in high fracture toughness values) led to superior penetration resistance. By alternatingly stacking the T700 carbon and S2-glass fibre blankets to produce the interlayer fibre hybrid composite, the beneficial energy absorption capabilities of the monolithic S2-glass composite were achieved. The intralayer fibre hybrid T700 carbon/Vectran also presented good impact energy absorption properties at 70J, in accordance with the large pull-out lengths of the Vectran fibres noticed during the translaminar fracture toughness testing. However poor penetration resistance at 140J impact was noticed due to the high through-thickness fibre crimp angle governed by the weave architecture, resulting decreased through-thickness shear strength and thus localised shear plugging. This localisation of through-thickness failure was indicative of a high angle of fibre crimp resulting in more localised failure (i.e. shear plugging), as highlighted by Potluri et al. [117].

Commercially available material models do not provide non-linear in-plane shear load response fitting as well as permanent plastic deformation [109]. The Abaqus VUMAT subroutine energy-based bilinear plane-stress numerical modelling approach proved successful in capturing the elastic in-plane and through-thickness response of the fibre hybrid and monolithic composite laminates, as well as the delamination and back-face tensile fibre fracture from the interlaminar and translaminar fracture toughness testing respectively. The relative fibre volume fractions of the interlayer fibre hybrid T700 carbon/S2-glass were measured through TGA and analytical microscopy and represented in the numerical model, since each material

ply was modelled as a separate element with a nominal through-thickness. It was clear that the load responses for all materials tested were suitably within the scatter of the experimental testing where shear plugging was not apparent. Since the Abaqus VUMAT subroutine used for the numerical model was two-dimensional (in-plane), the permanent strain criterion did not account for the through-thickness direction and research by Tan et al. [125] provided a solution to this by developing a three-dimensional model. Herein lies the drawback of an in-plane numerical modelling approach, where the shear strength and permanent strain deformation in the through-thickness direction are not accounted for. An in-plane modelling approach would not capture the through-thickness shear strength for example, indicative of the shear plugging within the intralayer fibre hybrid T700 carbon/Vectran plate impacts, which the numerical model failed to capture.

Regarding the structural bonnet impact testing, in-plane continuum shell numerical modelling approach proved to be well suited in predicting the overall structural response of the system. This was quantified through load response curve correlation as well as strain gauge readings. It was however difficult to quantify the extent of damage associated with what was largely an elastic response, since the impact velocities were not large enough to produce any meaningful fibre fracture or delamination. When a higher impact energy of 45J was used, the adhesive at the fixture points debonded, leading to erroneous results. Due to this, no reasonable in-plane damage could be captured for numerical modelling to experimental correlation. Aside from this, the interlayer and intralayer fibre hybrids showed remarkably similar peak loads and maximum deflections across the two test energies despite their relatively different tensile, compressive, and in-plane shear moduli. The homogenisation of the material properties for both the interlayer and intralayer fibre hybrids proved acceptable for structural component numerical modelling (albeit during a largely elastic impact event), where good correlation was noted between the load response curves and strain gauge readings. This approach did however remove the ability to capture any delaminations between these plies however. This finding is integral to the progression of this particular in-plane numerical modelling approach for full scale components, where ply-by-ply models would be extremely costly in time and resources. A local-global numerical modelling approach would be beneficial for full scale componentry since computational power is currently insufficient to efficiently capture translaminar fracture throughout a full model, as highlighted by Bogenfeld et al. [109]. A ply-by-ply modelling

approach would also be inefficient since low velocity impact damage such as debris strike would be highly localised and unlikely to produce translaminar fracture throughout the whole component.

Concerning the material selection for automotive components, the interlayer fibre hybrid T700 carbon/S2-glass proved to be the most suitable. This was due to its higher in-plane stiffness relative to the monolithic S2-glass composite (promoted by the T700 carbon fibres), and superior low velocity impact resistance compared to the monolithic T700 carbon composite (due to the presence of the S2-glass fibres). High structural stiffness and strength, as well as good low velocity impact resistance (such as dropped tool impact or debris strike), are integral properties for load carrying automotive components. The intralayer fibre hybrid T700 carbon/Vectran utilising a 2x2 twill weave, although providing good drapeability for component manufacture, and high specific energy absorption, would present issues regarding compression after impact strength, where studies have shown that high fibre crimp reduces this [117].

Perhaps the most crucial outcome of this research is the ability to transfer the experimental testing of fibre hybrid composites presented, along with the numerical modelling approaches, into full scale industrial components. This work has proved accurate correlation between the experimental testing and numerical modelling for both interlayer and intralayer fibre hybrids, through both ply-by-ply interlayer, and homogenised interlayer and intralayer fibre hybrid material modelling. With ever increasing computation power, the ability to implement these techniques into larger components and structural models is becoming highly feasible. By conducting similar experimental and numerical studies on a full scale (1:1) structural bonnet, the associated natural frequencies would decrease, leading to a wholly different response. Vibrational analysis through experimentation or numerical modelling would be required to capture the relevant natural frequencies of the structural system and thus inform the damping characteristics. The ability to predict not only damage onset, but extent of damage through numerical analysis (as presented in the preceding chapters), is crucial to optimised component design. This is the overarching novelty presented in this thesis, since the automotive industry is increasingly coming under pressure both economically and technologically to utilise not only monolithic composites but fibre hybrid composites into the structural components of commercial products.

8. Conclusions and future work

8.1. Introduction

Fibre hybridisation proved beneficial for the in-plane material properties, where a rule of mixtures was noticed for the interlayer and intralayer fibre hybrid composites. The translaminar fracture toughness of the fibre hybrid composites also presented a rule of mixtures between the T700 carbon and S2-glass in the interlayer configuration. The intralayer fibre hybrid T700 carbon/Vectran provided insight into the drawbacks of woven composite translaminar toughness testing, particularly with two or more fibre types, where the local fibre configuration of the intralayer weave produced large amounts of scatter in the recorded values. The fibre crimp also reduced the penetration resistance of the intralayer fibre hybrid, making it a less attractive choice for structural components likely to suffer localised impact damage. The intralayer fibre hybrid T700 carbon/Vectran did however present large translaminar fracture toughness values due to the large fibre pull-out lengths noted during the translaminar testing, resulting from the 2x2 twill weave. The interlayer fibre hybrid T700 carbon/S2-glass provided the stiffness and impact resistance required for structural applications within commercial automotive products. Further development of fibre hybridisation for intralayer configurations would provide insight into their potential use in industrial components, where automated laydown and drapeability are prioritised manufacturing processes. If these can be achieved, the benefits of fibre hybridisation can be promoted at a larger scale within the automotive industry, reducing component mass whilst maintaining a high stiffness, strength, and impact resistance.

8.2. Conclusions

The main outcomes of the research are summarised as follows:

i. The experimental testing for the tension, compression, in-plane shear, interlaminar fracture toughness (Mode I and Mode II), and translaminar fracture provided novel data for the material systems tested. The Vectran fibres exhibited a non-linear tensile and compressive response in both the monolithic composite and the fibre hybrid composite due to the fibre crimp at microscopic and macroscopic scales respectively. The Mode I and Mode II interlaminar properties of the fibre hybrids were affected by

both the fibrillous nature (resulting in fibre bridging) of the Vectran fibres as well as the fibre architectures.

ii. Analytical microscopy and the TGA burn-off technique provided volume fraction measurements for the fibre hybrid composites. Correctly identifying the interlayer fibre hybrid volume fraction influenced the accuracy of the corresponding impact plate numerical model, where the thickness for each fibre type was required.

iii. The development of two novel Compact Tension specimens ('NCCT' and 'ENCCT'), by means of incorporating a curved rear to the standard specimen geometry as well as a through-thickness notch (pre-cure) to the fracture growth region, allowed for translaminar fracture measurement without the need for anti-buckling devices. The successful measurement of the translaminar fracture toughness of the fibre hybrids and the T700 carbon and S2-glass fibre monolithic composite counterparts were presented, proving novelty in the field of translaminar testing of materials that exhibit relatively low compressive strengths compared to tensile strengths. A rule of mixtures was noticed in the interlayer fibre hybrid T700 carbon/S2-glass translaminar fracture toughness. The intralayer fibre hybrid T700 carbon/Vectran presented high levels of scatter in its' translaminar fracture toughness due to the 2x2 twill weave, resulting in high levels of fibre pull-out.

iv. Chapter 5 presented the successful employment of an energy-based bilinear plane stress Abaqus VUMAT subroutine for the low velocity impact numerical modelling of both interlayer (ply-by-ply interlayer material modelling) and intralayer (homogenised ply blanket material modelling) fibre hybrid composites and their monolithic composite counterparts. The presence of the S2-glass fibres prohibited tup penetration in the interlayer fibre hybrid undergoing low velocity impact, and the intralayer fibre hybrid exhibited poor through-thickness local impact resistance due to the fibre crimp. The complex failure modes associated with the fibre hybrid composites were examined through high speed video capture and by comparing the experimental and numerical load responses.

v. The research in Chapter 6 presented the development of a novel test rig for the fixture of a reduced scale Bentley Continental car bonnet under low velocity impact. The same energy-based bilinear plane stress Abaqus VUMAT subroutine used for the plate

impacts was employed for structural testing and exhibited good correlation with the experimental testing. The homogenisation of the fibre hybrid properties proved acceptable for component scale modelling but a local-global approach would be needed to capture ply-by-ply damage. Although the correlation of experimental strain gauges to virtual strain gauges was already present in the literature, the use of an in-plane numerical modelling [122] approach for the low velocity impact of fibre hybrid composite structural components is currently novel in the field.

8.3. Future work

The research presented previously provides opportunity for future developments in the relevant fields as follows:

i. The failure modes associated with the tensile, compressive, and in-plane shear of the interlayer and intralayer fibre hybrid composites in Chapter 3 could be interrogated further by fractographic analysis. Although not a prerequisite for the impact testing and numerical modelling in Chapters 5 and 6, insight into the microscopic failure processes could lead to the development of highly optimised fibre hybrid material architectures, volume fractions, and layup orientations for specific industrial applications.

ii. The ENCCT specimen provided a fracture toughness measurement for the complex intralayer fibre hybrid T700 carbon/Vectran composite in Chapter 4, which was supported through the accurate numerical modelling of the low velocity plate impacts in Chapter 5. However, the specimen geometry could be improved further. For example, the in-plane area of the notched region could be enlarged to mitigate fibre pull-out or interaction with the stress fields of the thickened portion of the specimen. The length of the crack growth region could also be made longer to allow for longer *R*-curves to be measured, hence producing a more comprehensive propagation region.

iii. The interlayer fibre hybrid T700 carbon/S2-glass presented translaminar fracture toughness values between the two monolithic composite counterparts. This phenomenon has been studied for the in-plane material properties, namely tensile, but also is relatively new within the literature. The ENCCT geometry design now allows

for fibre hybrid testing without the need for anti-buckling devices, where research can be made into other fibre types and further insight into the translaminar toughness hybrid effect for different materials.

iv. The Abaqus VUMAT subroutine employed in the numerical impact modelling in Chapter 5 presented good correlation with the experimental testing. The strain rate effect for the 'kappa' constant could be made more suitable for the material systems tested. The subroutine used a fixed rate enhancement of a factor of two, whereas the literature data for the monolithic S2-glass composite suggested that a rate enhancement factor of 1.5 would be more suitable. Therefore, the numerical model used could be further developed to allow for variable rate enhancement factors, depending on the material being tested.

v. By incorporating the permanent strain associated with the non-linear in-plane shear response of the laminates into a three-dimensional numerical model, as proposed by Tan et al. [187], the indentation post-impact could be modelled across all impact energy figure figure levels. This would lend to more accurate energy absorption and therefore provide more suitable post-impact solutions for CAI (Compression After Impact) modelling.

vi. Shear plugging was observed in the majority of the 140J energy plate impacts. By experimentally capturing the through-thickness shear stiffness and strength for each composite, the numerical model could be modified to capture this phenomenon, hence providing a more robust and accurate solution where higher impact energies are employed.

vii. By reducing the fibre crimp within the intralayer fibre hybrid T700 carbon/Vectran composite (through incorporating a lower tow count or alternative weave architecture), the impact penetration resistance may be improved. The translaminar fracture toughness was seen to be improved by the large pull-out lengths of this fibre hybrid, but shear plugging was promoted by the high crimp angles. Further research into the fibre crimp angles' effect upon the through-thickness penetration susceptibility would allow for an optimised fibre hybrid, and also in-turn likely improve the in-plane structural material properties.

viii. The test rig fixture developed for the reduced scale Bentley Continental car bonnet low velocity impact testing in Chapter 6 proved to be successful since the fixture points to the bonnet allowed quantifiably accurate boundary conditions to be characterised in the numerical modelling. Unfortunately, impact energies higher than 20J proved unsuccessful. The bonding between the blocks and the bonnet surface failed when a 45J impact energy was used. Future work could incorporate an alternative bonding adhesive, stronger than the Araldite 2011 2-part epoxy, an alternative end-block design, or a mechanical joint, where debonding would not occur at such high energy levels. This would also allow for increased fibre damage for further numerical model and material property validation.

ix. Finally, although the damping factor of the intralayer fibre hybrid T700 carbon/Vectran bonnet numerical model was found through parametric modelling (Appendix 10.4), further experimental testing could also be used to validate the value used.

9. Bibliography

[1] Composites Leadership Forum, "Lightening the Load. The 2016 UK Composites Strategy," Hemel Hempstead, Hertfordshire, UK, Hertfordshire, UK, 2016.

[2] CiC, "Composites Innovation Cluster," 2015. [Online]. Available: http://www.the-cic.org.uk. [Accessed: 01-Oct-2014].

[3] Granta Design, "Granta Design," 2018. [Online]. Available: https://www.grantadesign.com/. [Accessed: 30-Jul-2018].

[4] S. N. A. Safri, M. T. H. Sultan, M. Jawaid, and K. Jayakrishna, "Impact behaviour of hybrid composites for structural applications: A review," *Composites Part B: Engineering*, vol. 133, pp. 112–121, 2018.

[5] Y. Swolfs, L. Gorbatikh, and I. Verpoest, "Fibre hybridisation in polymer composites: A review," *Composites Part A: Applied Science and Manufacturing*, vol. 67, pp. 181–200, Sep. 2014.

[6] E. Sevkat, B. Liaw, F. Delale, and B. B. Raju, "Drop-weight impact of plain-woven hybrid glass-graphite/toughened epoxy composites," *Composites Part A: Applied Science and Manufacturing*, vol. 40, no. 8, pp. 1090–1110, 2009.

[7] Sigmatex Ltd., "Sigmatex (UK) Ltd, Manor Farm Rd, Runcorn WA7 1TE, UK," 2015. [Online]. Available: http://www.sigmatex.com/. [Accessed: 14-May-2018].

[8] Solvay Composites, "Solvay Composites, Sinclair Cl, Heanor DE75 7SP, UK," 2018. [Online]. Available: https://www.solvay.co.uk/en/solvay-in/locations/Heanor.html. [Accessed: 15-May-2018].

[9] Department of Defense, "Composite Materials Handbook - MIL-HDBK-17-1F," 2002.

[10] J. Rouchon, "Certification of Large Aircraft Composite Structures, Recent Progress and New Trends in Compliance Philosophy," *17 th ICAS Congress*, vol. 2. pp. 1439–1447, 1990.

[11] T. J. Katafiasz, L. Iannucci, and E. S. Greenhalgh, "Development of a novel compact tension specimen to mitigate premature compression and buckling failure modes within fibre hybrid epoxy composites," *Composite Structures*, vol. 207, 2019.

[12] S. I. B. S. Abdullah, L. Iannucci, and E. S. Greenhalgh, "On the translaminar fracture toughness of Vectran/epoxy composite material," *Composite Structures*, vol. 202, no. March, pp. 1–12, 2018.

[13] T. Katafiasz, "Hybrid Fibre Composites for Delamination Resistance and Cost Saving," in *Cyclitech 2015*, 2015.

[14] T. J. Katafiasz, "Interlaminar and Intralaminar Properties of Carbon Spread Tow and Glass Fibre Hybrid Composites for Cost Saving in the Mass Production of Automotive Components," in *ECCM17 - 17th European Conference on Composite Materials*, 2016.

[15] T. J. Katafiasz, "Development of a Novel Compact Tension Specimen for Fibre Hybrid Composites," in *CompTest 2017: 8th International Conference on Composites Testing and Model Identification*, 2017.

[16] T. Katafiasz, "Bridging Characterization and Simulation: Materials Information Needs for Design," *Granta Webinar*, Granta, Cambridge, UK, 2017.

[17] CARBIO Project, "CARBIO - Carbon-Flax Hybrid Structures of Automotive Applications," 2018. [Online]. Available: https://carbioproject.com/. [Accessed: 08-Nov-2017].

[18] S. T. Pinho, "Modelling failure of laminated composites using physically-based failure models," PhD Thesis, Dept. of Aeronautics, Imperial College London, 2005.

[19] C. Lopes, Z. Gürdal, P. P. Camanho, Maimí, and E. V. González, "Simulation of low-velocity impact damage on composite laminates," *Collection of Technical Papers - AIAA/ASME/ASCE/AHS/ASC Structures, Structural Dynamics and Materials Conference*, no. May, 2009.

[20] F. Ehrich, "Low Velocity Impact on Pre-Loaded Composite Structures," Imperial College London, 2013.

[21] E. V. González, P. Maimí, P. P. Camanho, A. Turon, and J. A. Mayugo, "Simulation of drop-weight impact and compression after impact tests on composite laminates," *Composite Structures*, vol. 94, no. 11, pp. 3364–3378, 2012.

[22] E. V. González, P. Maimí, A. Turon, P. P. Camanho, and J. Renart, "Simulation of delamination by means of cohesive elements using an explicit finite element code," *Computers, Materials and Continua*, vol. 9, no. 1, pp. 51–92, 2009.

[23] J. M. Molina-Aldareguía, M. Rodríguez, C. González, and J. LLorca, "An experimental and numerical study of the influence of local effects on the application of the fibre push-in test (push-in)," *Philosophical Magazine*, vol. 91, no. 7–9, pp. 1293–1307, 2011.

[24] Altair Engineering, "Personal correspondance with Peter Snape (Altair Engineering, Imperial House, Holly Walk, Leamington Spa CV32 4JG)." .

[25] ASTM Int'l, "ASTM D7136: Standard Test Method for Measuring the Damage Resistance of a Fiber-Reinforced Polymer Matrix Composite to a Drop-Weight Impact Event," vol. i, pp. 1–16, 2005.

[26] A. Arteiro, G. Catalanotti, J. Xavier, and P. P. Camanho, "Notched response of non-crimp fabric thin-ply laminates: Analysis methods," *Composites Science and Technology*, vol. 88, pp. 165–171, Nov. 2013.

[27] S. W. Tsai and K. Kawabe, "Thin Ply Laminates," US 2006/0093802 A1, 2006.

[28] C. Borg, "Kiteboards perform better with TeXtreme reinforcement," *Reinforced Plastics*, vol. 55, no. 6, pp. 42–43, Nov. 2011.

[29] H. M. EL-Dessouky and C. A. Lawrence, "Ultra-lightweight carbon fibre/thermoplastic composite material using spread tow technology," *Composites Part B: Engineering*, vol. 50, pp. 91–97, Jul. 2013.

[30] K. Kawabe, S. Tomada, and T. Matsuo, "Technology for spreading tow and its application to composite materials Part 1: A new pneumatic method for spreading carbon tow," *Journal of the textile machinery society of Japan*, pp. 68–75, 1996.

[31] S. Sihn, R. Kim, K. Kawabe, and S. Tsai, "Experimental studies of thin-ply laminated composites," *Composites Science and Technology*, vol. 67, no. 6, pp. 996–1008, May 2007.

[32] K. Kawabe and T. Matsuo, "Technology for spreading tow and its application to composite materials Part 2: Spreading tow by roll method," *Journal of the textile machinery society of Japan*, vol. 51, no. 2, pp. 65–75, 1997.

[33] K. Kawabe, T. Matsuo, and Z. Maekawa, "New Technology for Opening Various Reinforcing Fiber Tows," 1998.

[34] S. W. Tsai and M. Cognet, "The amazing bi-angle thin-ply NCF," *JEC Composites Magazine*, vol. 68, 2011.

[35] A. Arteiro, G. Catalanotti, J. Xavier, and P. P. P. Camanho, "Large damage capability of non-crimp fabric thin-ply laminates," *Composites Part A: Applied Science and Manufacturing*, vol. 63, pp. 110–122, Aug. 2014.

[36] F. Ohlsson and N. Khokar, "Technical and economic advantages of continuous-length + α / - β spread tow fabrics," *Oxeon AB*, pp. 1–7, 2011.

[37] Chomarat, "Chomarat," 2018. [Online]. Available: http://chomarat.com/en/. [Accessed: 14-May-2018].

[38] Harmoni Indstry Co. Ltd., "Harmoni," 2018. [Online]. Available: http://harmoni.co.jp/. [Accessed: 14-May-2018].

[39] North Thin Ply Technology, "North Thin Ply Technology," 2015. [Online]. Available: https://www.thinplytechnology.com/. [Accessed: 14-May-2016].

[40] Oxeon AB, "Oxeon," 2018. [Online]. Available: http://oxeon.se/. [Accessed: 14-May-

2018].

[41] Sakai Ovex Co. Ltd., "Sakai Ovex," 2018. [Online]. Available: http://sakaiovex.co.jp/. [Accessed: 14-May-2018].

[42] Teknomax Corportation, "Teknomax," 2007. [Online]. Available: http://www.teknomax.jp/. [Accessed: 14-May-2018].

[43] G. Kretsis, "A review of the tensile, compressive, flexural and shear properties of hybrid fibre- reinforced plastics," vol. 18, no. 1, pp. 13–23, 1987.

[44] Y. Swolfs *et al.*, "Tensile behaviour of intralayer hybrid composites of carbon fibre and self-reinforced polypropylene," *Composites Part A: Applied Science and Manufacturing*, vol. 59, pp. 78–84, Apr. 2014.

[45] H. Ikbal, Q. Wang, A. Azzam, and W. Li, "GF/CF hybrid laminates made through intra-tow hybridization for automobile applications," *Fibers and Polymers*, vol. 17, no. 9, pp. 1505–1521, 2016.

[46] B. Vijaya Ramnath, V. M. Manickavasagam, C. Elanchezhian, C. Vinodh Krishna, S. Karthik, and K. Saravanan, "Determination of mechanical properties of intra-layer abaca-jute-glass fiber reinforced composite," *Materials and Design*, vol. 60, pp. 643–652, 2014.

[47] E. Selver, P. Potluri, C. Soutis, and P. Hogg, "Healing potential of hybrid materials for structural composites," *Composite Structures*, vol. 122, pp. 57–66, 2015.

[48] S. Dean, W. McDonough, J. Dunkers, K. Flynn, and D. Hunston, "A Test Method to Determine the Fiber and Void Contents of Carbon/Glass Hybrid Composites," *Journal of ASTM International*, vol. 1, no. 3, p. 12076, 2004.

[49] University of Bristol and Imperial College London, "HiPerDuCT," 2018. [Online]. Available: http://hiperduct.ac.uk/.

[50] M. R. Wisnom, G. Czél, Y. Swolfs, M. Jalalvand, L. Gorbatikh, and I. Verpoest, "Hybrid

effects in thin ply carbon/glass unidirectional laminates: Accurate experimental determination and prediction," *Composites Part A: Applied Science and Manufacturing*, vol. 88, pp. 131–139, 2016.

[51] M. Jalalvand, G. Czél, and M. R. Wisnom, "Numerical modelling of the damage modes in UD thin carbon/glass hybrid laminates," *Composites Science and Technology*, vol. 94, pp. 39–47, Apr. 2014.

[52] M. Jalalvand, G. Czél, and M. R. Wisnom, "Damage analysis of pseudo-ductile thin-ply UD hybrid composites - a new analytical method," *Composites Part A: Applied Science and Manufacturing*, vol. 69, pp. 83–93, 2014.

[53] M. Jalalvand, G. Czél, and M. R. Wisnom, "Parametric study of failure mechanisms and optimal configurations of pseudo-ductile thin-ply UD hybrid composites," *Composites Part A: Applied Science and Manufacturing*, vol. 74, pp. 123–131, 2015.

[54] H. Yu, M. L. Longana, M. Jalalvand, M. R. Wisnom, and K. D. Potter, "Pseudo-ductility in intermingled carbon/glass hybrid composites with highly aligned discontinuous fibres," *Composites Part A: Applied Science and Manufacturing*, vol. 73, pp. 35–44, 2015.

[55] Y. Swolfs, R. M. McMeeking, I. Verpoest, and L. Gorbatikh, "The effect of fibre dispersion on initial failure strain and cluster development in unidirectional carbon/glass hybrid composites," *Composites Part A: Applied Science and Manufacturing*, vol. 69, pp. 279–287, 2014.

[56] Y. Zhang, Y. Li, H. Ma, and T. Yu, "Tensile and interfacial properties of unidirectional flax/glass fiber reinforced hybrid composites," *Composites Science and Technology*, vol. 88, pp. 172–177, Nov. 2013.

[57] J. Summerscales, "The mechanical properties of carbon fibre with glass fibre hybrid reinforced plastics," PhD Thesis, Department of Mechanical Engineering, Plymouth

Polytechnic, 1983.

[58] T. Hayashi, "On the improvement of mechanical properties of composites by hybrid composition," *8th Reinforced Plastics Congress*, vol. Paper 22, pp. 149–152, 1972.

[59] P. W. Manders and M. G. Bader, "The strength of hybrid glass/carbon fibre composites," *Journal of Materials Science*, vol. 16, no. 8, pp. 2233–2245, Aug. 1981.

[60] G. Kretsis, "A review of the tensile, compressive, flexural and shear properties of hybrid fibre-reinforced plastics," *Composites*, vol. 18, no. 1, pp. 13–23, 1987.

[61] N. Pan and R. Postle, "The tensile strength of hybrid fibre composites: a probabilistic analysis of the hybrid effects," *Philosophical Transactions of the Royal Society A*, vol. 354, no. 1714, 1996.

[62] Y. Shan and K. Liao, "Environmental fatigue behavior and life prediction of unidirectional glass-carbon/epoxy hybrid composites," *International Journal of Fatigue*, vol. 24, no. 8, pp. 847–859, 2002.

[63] J. Aveston and J. M. Sillwood, "Synergistic fibre strengthening in hybrid composites," *Journal of Materials Science*, vol. 11, no. 10, pp. 1877–1883, 1976.

[64] F. Ribeiro, J. Sena-Cruz, F. G. Branco, and E. Júlio, "Hybrid effect and pseudo-ductile behaviour of unidirectional interlayer hybrid FRP composites for civil engineering applications," *Construction and Building Materials*, vol. 171, pp. 871–890, 2018.

[65] A. A. J. M. Peijs, P. C. A. Tsman, L. E. Govaert, and P. J. Lemstra, "Hybrid composites based on polyethylene and carbon fibres Part 2 : influence of composition and adhesion level of polyethylene fibres on mechanical properties," *Composites*, vol. 21, no. 6, pp. 513–521, 1990.

[66] A. A. Ravindra, R. Refai, A. Nigam, S. Kumar, and P. Krishnan, "Mode II shear behavior of a glass fabric/epoxy and a multi scale glass fabric/epoxy thick beam composite containing multiwalled carbon nanotubes," *Procedia Engineering*, vol. 97, pp.

449–458, 2014.

[67] V. Eskizeybek, A. Yar, and A. Avcı, "CNT-PAN hybrid nanofibrous mat interleaved carbon/epoxy laminates with improved Mode I interlaminar fracture toughness," *Composites Science and Technology*, vol. 157, pp. 30–39, 2018.

[68] S. S. Wicks, R. G. de Villoria, and B. L. Wardle, "Interlaminar and intralaminar reinforcement of composite laminates with aligned carbon nanotubes," *Composites Science and Technology*, vol. 70, no. 1, pp. 20–28, 2010.

[69] S. S. Wicks, W. Wang, M. R. Williams, and B. L. Wardle, "Multi-scale interlaminar fracture mechanisms in woven composite laminates reinforced with aligned carbon nanotubes," *Composites Science and Technology*, vol. 100, pp. 128–135, 2014.

[70] T. Li, M. Li, Y. Gu, S. Wang, Q. Li, and Z. Zhang, "Mechanical enhancement effect of the interlayer hybrid CNT film/carbon fiber/epoxy composite," *Composites Science and Technology*, pp. 1–7, 2018.

[71] B. Vijaya Ramnath, V. M. Manickavasagam, C. Elanchezhian, C. Vinodh Krishna, S. Karthik, and K. Saravanan, "Determination of mechanical properties of intra-layer abaca-jute-glass fiber reinforced composite," *Materials and Design*, vol. 60, pp. 643–652, 2014.

[72] K. Vallons, A. Behaeghe, S. V. Lomov, and I. Verpoest, "Impact and post-impact properties of a carbon fibre non-crimp fabric and a twill weave composite," *Composites Part A: Applied Science and Manufacturing*, vol. 41, no. 8, pp. 1019–1026, 2010.

[73] E. S. Greenhalgh, *Failure analysis and fractography of polymer composites*. Cambridge, UK: Woodhead Publishing Ltd., 2009.

[74] S.-F. Hwang and B.-C. Shen, "Opening-mode interlaminar fracture toughness of interply hybrid composite materials," *Composites Science and Technology*, vol. 59, no. 12, pp. 1861–1869, 1999.

[75] S.-F. A. Hwang and C.-C. Huang, "Sliding mode interlaminar fracture toughness of interply hybrid composite materials," *Polymer Composites*, vol. 19, no. 5, pp. 514–526, 1998.

[76] H. Miyairi and M. Wakabayashi, "Study on the Interlaminar Shear Strength by of CF / GF Hybrid Composites," *Zairyo/Journal of the Society of Materials Science*, vol. 33, pp. 67–72, 1984.

[77] C. Thanomsilp and P. J. Hogg, "Interlaminar fracture toughness of hybrid composites based on commingled yarn fabrics," *Composites Science and Technology*, vol. 65, pp. 1547–1563, 2005.

[78] R. Reeder and S. Whitley, "The Use of Doublers in Delamination Relative modulus material thickness," in *American Society of Composites 17th Technical Conference*, 2002.

[79] Z. Ouyang, G. Ji, and G. Li, "On Approximately Realizing and Characterizing Pure Mode-I Interface Fracture Between Bonded Dissimilar Materials," *Journal of Applied Mechanics*, vol. 78, no. 3, p. 031020, 2011.

[80] Z. Jiang, S. Wan, and Z. Wu, "Calculation of energy release rate for adhesive composite/metal joints under mode-I loading considering effect of the non-uniformity," *Composites Part B: Engineering*, vol. 95, pp. 374–385, 2016.

[81] R. G. Boeman, D. L. Erdman, L. B. Klett, and R. D. Lomax, "A practical test method for mode I fracture toughness of adhesive joints with dissimilar substrates," in *SAMPE-ACCE-DOE Advanced Composites Conference, Detroit, MI, September 27-28*, 1999.

[82] Z. Ouyang and G. Li, "Nonlinear interface shear fracture of end notched flexure specimens," *International Journal of Solids and Structures*, vol. 46, no. 13, pp. 2659–2668, 2009.

[83] C. Alía, J. M. Arenas, J. C. Suárez, R. Ocaña, and J. J. Narbón, "Mode II fracture

energy in the adhesive bonding of dissimilar substrates: Carbon fibre composite to aluminium joints," *Journal of Adhesion Science and Technology*, vol. 27, no. 22, pp. 2480–2494, 2013.

[84] J. M. Arenas, R. Ocaña, C. Alía, J. J. Narbón, and M. Islán, "Fracture energy in structural adhesive joints of composite-aluminum under adverse environments conditions," *Journal of Adhesion Science and Technology*, vol. 28, no. 2, pp. 201–214, 2014.

[85] Z. Ouyang and G. Li, "Nonlinear interface shear fracture of end notched flexure specimens," *International Journal of Solids and Structures*, vol. 46, no. 13, pp. 2659–2668, 2009.

[86] Z. Ouyang, G. Ji, and G. Li, "On Approximately Realizing and Characterizing Pure Mode-I Interface Fracture Between Bonded Dissimilar Materials," *Journal of Applied Mechanics*, vol. 78, no. 3, p. 031020, 2011.

[87] L. Gigliotti and S. T. Pinho, "Translaminar fracture toughness of NCF composites with multiaxial blankets," *Materials and Design*, vol. 94, pp. 410–416, 2016.

[88] R. F. Teixeira, S. T. Pinho, and P. Robinson, "Thickness-dependence of the translaminar fracture toughness: experimental study using thin-ply composites," *Composites Part A: Applied Science and Manufacturing*, vol. 90, pp. 33–44, 2016.

[89] G. Bullegas, S. T. Pinho, and S. Pimenta, "Engineering the translaminar fracture behaviour of thin-ply composites," *Composites Science and Technology*, vol. 131, pp. 110–122, 2016.

[90] M. J. Laffan, S. T. Pinho, P. Robinson, and A. J. McMillan, "Translaminar fracture toughness testing of composites: A review," *Polymer Testing*, vol. 31, no. 3, pp. 481–489, 2012.

[91] ASTM, "ASTM E399 - Standard Test Method for Linear-Elastic Plane-Strain Fracture

Toughness K1C of Metallic Materials," *ASTM International*, pp. 1–33, 2013.

[92] P. S. S. Gouda, S. K. Kudari, S. Prabhuswamy, and D. Jawali, "Fracture Toughness of Glass-Carbon (0/90)S Fiber Reinforced Polymer Composite – An Experimental and Numerical Study," *Journal of Minerals and Materials Characterization and Engineering*, vol. 10, no. 8, pp. 671–682, 2011.

[93] N. Blanco, D. Trias, S. T. Pinho, and P. Robinson, "Intralaminar fracture toughness characterisation of woven composite laminates. Part I: Design and analysis of a Compact Tension (CT) specimen," *Engineering Fracture Mechanics*, vol. 131, pp. 349–360, 2012.

[94] S. A. Tsampas, E. S. Greenhalgh, J. Ankersen, and P. T. Curtis, "On compressive failure of multidirectional fibre-reinforced composites: A fractographic study," *Composites Part A: Applied Science and Manufacturing*, vol. 43, no. 3, pp. 454–468, 2012.

[95] K. V. Arun, R. D. Kamat, and S. Basavarajappa, "Mechanism of Translaminar Fracture in Glass/Textile Fabric Polymer Hybrid Composites," *Journal of Reinforced Plastics and Composites*, vol. 29, no. 2, pp. 254–265, 2010.

[96] P. Prabhakar and A. M. Waas, "Micromechanical modeling to determine the compressive strength and failure mode interaction of multidirectional laminates," *Composites Part A: Applied Science and Manufacturing*, vol. 50, pp. 11–21, 2013.

[97] N. A. Fleck, "Compressive Failure of Fiber Composites," *Advances in Applied Mechanics*, vol. 33, no. C, pp. 43–117, 1997.

[98] S. A. Tsampas, E. S. Greenhalgh, J. Ankersen, and P. T. Curtis, "On compressive failure of multidirectional fibre-reinforced composites: A fractographic study," *Composites Part A: Applied Science and Manufacturing*, vol. 43, no. 3, pp. 454–468, 2012.

[99] S. A. Tsampas, E. S. Greenhalgh, J. Ankersen, and P. T. Curtis, "Compressive failure of hybrid multidirectional fibre-reinforced composites," *Composites Part a*, vol. 71, pp. 40–58, 2015.

[100] W. Cher, "Development of a test to measure energy absorption in fibre failure modes of woven composite laminates," 2006.

[101] Y. Swolfs, Y. Geboes, L. Gorbatikh, and S. T. Pinho, "The importance of translaminar fracture toughness for the penetration impact behaviour of woven carbon/glass hybrid composites," *Composites Part A: Applied Science and Manufacturing*, vol. 103, pp. 1–8, 2017.

[102] A. Ortega, P. Maimí, E. V Gonalez, J. R. S. de Aja, F. M. de la Escalera, and P. Cruz, "Translaminar fracture toughness of interply hybrid laminates under tensile and compressive loads," *Composites Science and Technology*, vol. 143, pp. 1–12, 2017.

[103] X. Li, S. R. Hallett, M. R. Wisnom, N. Zobeiry, R. Vaziri, and A. Poursartip, "Experimental study of damage propagation in Over-height Compact Tension tests," *Composites Part A: Applied Science and Manufacturing*, vol. 40, no. 12, pp. 1891–1899, 2009.

[104] H. Liu, B. G. Falzon, G. Catalanotti, and W. Tan, "An Experimental Method to Determine the Intralaminar Fracture Toughness of High Strength Carbon-Fibre Reinforced Composite Laminates," in *ECCM17*, 2016, no. June, pp. 1–22.

[105] M. V Donadon, B. G. Falzon, L. Iannucci, and J. M. Hodgkinson, "Intralaminar toughness characterisation of unbalanced hybrid plain weave laminates," vol. 38, pp. 1597–1611, 2007.

[106] R. Park and J. Jang, "Impact behavior of aramid fiber/glass fiber hybrid composite: Evaluation of four-layer hybrid composites," *Journal of Materials Science*, vol. 36, no. 9, pp. 2359–2367, 2001.

[107] M. Sayer, N. B. Bektaş, and O. Sayman, "An experimental investigation on the impact behavior of hybrid composite plates," *Composite Structures*, vol. 92, no. 5, pp. 1256–1262, Apr. 2010.

[108] G. Savage, "Composite materials technology in formula 1 motor racing," *SPE Automotive and Composites Division - 8th Annual Automotive Composites Conference and Exhibition, ACCE 2008 - The Road to Lightweight Performance*, vol. 1, no. July 2008, pp. 109–139, 2008.

[109] R. Bogenfeld, J. Kreikemeier, and T. Wille, "Review and benchmark study on the analysis of low-velocity impact on composite laminates," *Engineering Failure Analysis*, vol. 86, no. August 2017, pp. 72–99, 2018.

[110] Federal Ministry of Economic Affairs and Energy, "BMWi - Federal Ministry of Economic Affairs and Energy," 2018. [Online]. Available: https://www.bmwi.de. [Accessed: 28-Jun-2018].

[111] Airbus Group, "Airbus Helicopters," 2018. [Online]. Available: http://www.airbus.com/helicopters.html. [Accessed: 28-Jun-2018].

[112] P. Maimí, P. P. Camanho, J. A. Mayugo, and A. Turon, "Matrix cracking and delamination in laminated composites. Part I: Ply constitutive law, first ply failure and onset of delamination," *Mechanics of Materials*, vol. 43, no. 4, pp. 169–185, 2011.

[113] Dassault Systèmes Simulia, "Abaqus 6.14 Manual," *Abaqus 6.14*, 2014.

[114] X. C. Sun, M. R. Wisnom, and S. R. Hallett, "Interaction of inter- and intralaminar damage in scaled quasi-static indentation tests: Part 2 - Numerical simulation," *Composite Structures*, vol. 136, pp. 727–742, 2016.

[115] E. V. González, P. Maimí, J. R. Sainz de Aja, P. Cruz, and P. P. Camanho, "Effects of interply hybridization on the damage resistance and tolerance of composite laminates," *Composite Structures*, vol. 108, no. 1, pp. 319–331, 2014.

[116] A. Enfedaque, J. M. Molina-Aldareguia, F. Galvez, C. Gonzalez, and J. LLorca, "Effect of Glass Fiber Hybridization on the Behavior Under Impact of Woven Carbon Fiber/Epoxy Laminates," *Journal of Composite Materials*, vol. 44, no. 25, pp. 3051–

3068, May 2010.

[117] P. Potluri, P. Hogg, M. Arshad, D. Jetavat, and P. Jamshidi, "Influence of fibre architecture on impact damage tolerance in 3D woven composites," *Applied Composite Materials*, vol. 19, no. 5, pp. 799–812, 2012.

[118] J. M. Corum, R. L. Battiste, and M. B. Ruggles-Wrenn, "Low-energy impact effects on candidate automotive structural composites," *Composites Science and Technology*, vol. 63, no. 6, pp. 755–769, 2003.

[119] United States Government, "Vehicle Technologies Office — Department of Energy," 2018. [Online]. Available: https://www.energy.gov/eere/vehicles/vehicle-technologies-office. [Accessed: 08-Aug-2018].

[120] J. Corum, R. Battiste, and C. Brinkman, "Durability-based design criteria for an automotive structural composite: Part 2, background data and models," *Oak Ridge National Laboratory - 6931*, 1998.

[121] J. Poe CC, "Relevance of impactor shape to nonvisible damage and residual tensile strength of a thick graphite/epoxy laminate," *Composite Materials: Fatigue and Fracture, ASTM STP 1110, American Society for Testing and Materials*, pp. 501–26, 1991.

[122] L. Iannucci and J. Ankersen, "An energy based damage model for thin laminated composites," *Composites Science and Technology*, vol. 66, no. 7–8, pp. 934–951, 2006.

[123] S. Ying, T. Mengyun, R. Zhijun, S. Baohui, and C. Li, "An experimental investigation on the low-velocity impact response of carbon-aramid/epoxy hybrid composite laminates," *Journal of Reinforced Plastics and Composites*, vol. 36, no. 6, pp. 422–434, 2017.

[124] Y. Donckels, F. Matthews, and A. Foreman, "Impact dent depth relaxation in polymer matrix composites," in *The 9th European Conference on Composite Materials, ECCM-9*, 2000.

[125] W. Tan, B. G. Falzon, L. N. S. Chiu, and M. Price, "Predicting low velocity impact damage and Compression-After-Impact (CAI) behaviour of composite laminates," *Composites Part A: Applied Science and Manufacturing*, vol. 71, pp. 212–226, 2015.

[126] D. Muhammad *et al.*, "Experimental investigation on friction coefficient of composite materials sliding against SS 201 and SS 301 counterfaces," *Procedia Engineering*, vol. 105, no. Icte 2014, pp. 858–864, 2015.

[127] J. Schön, "Coefficient of friction for aluminum in contact with a carbon fiber epoxy composite," *Tribology International*, vol. 37, no. 5, pp. 395–404, 2004.

[128] P. yan Hung, K. tak Lau, L. kwan Cheng, J. Leng, and D. Hui, "Impact response of hybrid carbon/glass fibre reinforced polymer composites designed for engineering applications," *Composites Part B: Engineering*, vol. 133, pp. 86–90, 2018.

[129] M. M. Davoodi, S. M. Sapuan, A. Ali, D. Ahmad, and A. Khalina, "Thermoplastic impact property improvement in hybrid natural fibre epoxy composite bumper beam," *IOP Conference Series: Materials Science and Engineering*, vol. 11, p. 012013, 2010.

[130] T. Ishikawa *et al.*, "Overview of automotive structural composites technology developments in Japan," *Composites Science and Technology*, vol. 155, pp. 221–246, 2018.

[131] T. Ishikawa *et al.*, "Overview of automotive structural composites technology developments in Japan," *Composites Science and Technology*, vol. 155, pp. 221–246, 2018.

[132] FAR UK, "FAR Composites UK, Unit 29 Wilford Industrial Estate, Ruddington Ln, West Bridgford, Nottingham NG11 7EP, UK," 2016. [Online]. Available: http://www.far-uk.com/. [Accessed: 03-Jul-2016].

[133] Axon Automotive, "Axon Automotive." [Online]. Available: http://www.axonautomotive.com/. [Accessed: 22-Dec-2017].

[134] BMW Blog, "BMW 7 Series' Carbon Core more important than you might think," 2015. [Online]. Available: https://www.bmwblog.com/2015/09/01/bmw-7-series-carbon-core-more-important-that-you-might-think/. [Accessed: 02-Oct-2017].

[135] D. H. Kim, H. G. Kim, and H. S. Kim, "Design optimization and manufacture of hybrid glass/carbon fiber reinforced composite bumper beam for automobile vehicle," *Composite Structures*, vol. 131, pp. 742–752, 2015.

[136] F. Nunes, J. R. Correia, and N. Silvestre, "Structural behavior of hybrid FRP pultruded beams: Experimental, numerical and analytical studies," *Thin-Walled Structures*, vol. 106, pp. 201–217, 2016.

[137] F. Nunes, J. R. Correia, and N. Silvestre, "Structural behavior of hybrid FRP pultruded beams: Experimental, numerical and analytical studies," *Thin-Walled Structures*, vol. 106, pp. 201–217, 2016.

[138] A. Riccio, A. De Luca, G. Di Felice, and F. Caputo, "Modelling the simulation of impact induced damage onset and evolution in composites," *Composites Part B: Engineering*, vol. 66, pp. 340–347, 2014.

[139] M. Schwab, M. Todt, M. Wolfahrt, and H. E. Pettermann, "Failure mechanism based modelling of impact on fabric reinforced composite laminates based on shell elements," *Composites Science and Technology*, vol. 128, pp. 131–137, 2016.

[140] X. Zhang, "Impact damage in composite aircraft structures - experimental testing and numerical simulation," *Proceedings of the Institution of Mechanical Engineers, Part G: Journal of Aerospace Engineering*, vol. 212, no. 4, pp. 245–259, 1998.

[141] S. B. Unadkat, S. Kangde, M. Burkul, and M. Badireddy, "Development of Virtual Hood Slam Test," *SAE Technical Paper 2016-01-1365*, 2016.

[142] G. Savage, "Formula 1 Composites Engineering," *Engineering Failure Analysis*, vol. 17, no. 1, pp. 92–115, Jan. 2010.

[143] G. Savage, "Composite materials technology in formula 1 motor racing," *SPE Automotive and Composites Division - 8th Annual Automotive Composites Conference and Exhibition, ACCE 2008 - The Road to Lightweight Performance*, vol. 1, no. July 2008, pp. 109–139, 2008.

[144] G. Czel, J. Etches, I. P. Bond, and M. R. Wisnom, "Development and characterisation of pseudo-ductile hybrid carbon/glass-epoxy composites made of thin spread carbon tows," *ECCM15 - 15th European Conference on Composite Materials*, no. June, pp. 24–28, 2012.

[145] G. Czél and M. R. Wisnom, "Demonstration of pseudo-ductility in high performance glass/epoxy composites by hybridisation with thin-ply carbon prepreg," *Composites Part A: Applied Science and Manufacturing*, vol. 52, pp. 23–30, Sep. 2013.

[146] A. Franck, "Viscoelasticity and dynamic mechanical testing," no. 1, pp. 1–7.

[147] Y. Ou *et al.*, "Mechanical characterization of the tensile properties of glass fiber and its reinforced polymer (GFRP) composite under varying strain rates and temperatures," *Polymers*, vol. 8, no. 5, 2016.

[148] J.-L. Tsai and C. T. Sun, "Strain rate effect on in-plane shear strength of unidirectional polymeric composites," *Composites Science and Technology*, vol. 65, no. 13, pp. 1941–1947, 2005.

[149] V. Singh, "Literature survey of strain rate effects on composites," *Swerea SICOMP*, vol. 46, no. 31168, 2018.

[150] BSi, "BS ISO 527-4: 1997 Plastics — Determination of tensile properties - Part 4: Test conditions for isotropic and orthotropic fibre-reinforced plastic composites." 1997.

[151] BSi, "BS ISO 527-2:2012 Determination of tensile properties Part 2 : Test conditions for moulding and extrusion plastics," 2012.

[152] J. Haeberle and F. L. Matthews, "Studies on compressive failure in unidirectional CFRP

using improved test method," *Imperial College London*, 1990.

[153] BSi, "BS ISO 604:2003 Plastics — Determination of compressive properties," vol. 3, 2003.

[154] BSi, "BS ISO 14126:1999 Fibre-reinforced plastic composites — Determination of compressive properties in the in-plane direction," vol. 3. 1999.

[155] BSi, "BS ISO 14129:1998 Fibre-reinforced plastic composites — Determination of the stress / shear strain response , including the in-plane shear modulus and strength by the ffi 45 fl tension test method." 1998.

[156] ASTM Int'l, "ASTM D5528: Standard Test Method for Mode I Interlaminar Fracture Toughness of Unidirectional Fiber-Reinforced Polymer Matrix Composites," *American Standard of Testing Methods*, vol. 03, no. Reapproved 2007, pp. 1–12, 2014.

[157] R. H. Martin and B. D. Davidson, "Mode II fracture toughness evaluation using four point bend, end notched flexure test," *Plastics, Rubber and Composites*, vol. 28, no. 8, pp. 401–6, 1999.

[158] Micrometrics, "AccuPyc II 1340 Gas Displacement Pycnometer."

[159] Solvay Composites, "Communication with Mr Daniel Thompson at Solvay Composites, Heanor, UK." Heanor, Derby, UK, Derby, UK, 2016.

[160] S. Nguyen and T. J. Katafiasz, "Datacomp research for Composites Innovation Cluster." Imperial College London, London, 2015.

[161] R. Joffe, "FALCOM: Failure, Performance and Processing for Enhanced Design with Non-Crimp-Fabric Composites," 2004.

[162] S. Abdullah, "Communication with Mr Syed Abdullah, Imperial College London, UK," Imperial College London, 2018.

[163] J. Ankersen, "Abaqus laminated composite damage 2D VUMAT guide for input

parameters," London, 2011.

[164] M. Kinsella, D. Murray, and D. Crane, "Mechanical properties of polymeric composites reinforced with high strength glass fibers," *International Sampe Technical Conference Series*, vol. 33, pp. 1644–1657, 2001.

[165] Kuraray America Inc., "Vectran - Data Sheet," 2006.

[166] J. Schindelin *et al.*, "Fiji: an open-source platform for biological-image analysis," *Nature Methods*, vol. 9, p. 676, Jun. 2012.

[167] J. M. Hodgkinson, *Mechanical Testing of Advanced Fibre Composites*. Woodhead Publishing Series in Composites Science and Engineering, 2000.

[168] E. J. Barbero, *Finite Element Analysis of Composite Materials using Abaqus*. CRC Press, 2013.

[169] S. T. Pinho, "Personal correspondance with Silvestre Pinho (Imperial College London, London UK)." 2016.

[170] M. J. Laffan, S. T. Pinho, P. Robinson, and A. J. McMillan, "Translaminar fracture toughness: The critical notch tip radius of 0fl plies in CFRP," *Composites Science and Technology*, vol. 72, no. 1, pp. 97–102, 2011.

[171] M. J. Laffan, S. T. Pinho, P. Robinson, and L. Iannucci, "Measurement of the in situ ply fracture toughness associated with mode I fibre tensile failure in FRP. Part II: Size and lay-up effects," *Composites Science and Technology*, vol. 70, no. 4, pp. 614–621, 2010.

[172] N. Blanco, D. Trias, S. T. Pinho, and P. Robinson, "Intralaminar fracture toughness characterisation of woven composite laminates. Part II: Experimental characterisation," *Engineering Fracture Mechanics*, vol. 131, pp. 361–370, 2014.

[173] S. I. B. S. Abdullah, L. Iannucci, and E. S. Greenhalgh, "On the translaminar fracture toughness of Vectran/epoxy composite material," *Composite Structures*, no. March, pp.

1–12, 2018.

[174] J. Corum, R. Battiste, and C. Brinkman, "Durability-based design criteria for an automotive structural composite: Part 2, background data and models," *Oak Ridge National Laboratory - 6931*, 1998.

[175] D. Krajcinovic, "Damage mechanics: accomplishments, trends and needs," *Int J Solids Struct*, vol. 37(1–2), no. 267–77, 2000.

[176] MatWeb, "Steel, general properties," 2018. [Online]. Available: http://www.matweb.com/search/datasheet.aspx?bassnum=MS0001&ckck=1. [Accessed: 10-Jan-2018].

[177] P. P. Camanho and C. G. Dávila, "Mixed-Mode Decohesion Finite Elements for the Simulation of Delamination in Composite Materials," *NASA Technical Memorandum*, vol. TM-2002-21, no. June, 2002.

[178] M. L. Benzeggagh and M. Kenane, "Measurement of mixed-mode delamination fracture toughness of unidirectional glass/epoxy composites with mixed-mode bending apparatus," *Composites Science and Technology*, vol. 56, pp. 439–449, 1996.

[179] N. Alif, L. Carlsson, and J. Gillespie, "Mode I, Mode II, and Mixed Mode Interlaminar Fracture of Woven Fabric Carbon/Epoxy," *Composite Materials: Testing and Design 13th Volume*, pp. 82–106, 1997.

[180] K. S. Pandya, S. Shaktivesh, H. L. Gowtham, A. Inani, and N. K. Naik, "Shear Plugging and Frictional Behaviour of Composites and Fabrics Under Quasi-static Loading," *Strain*, vol. 51, no. 5, pp. 419–426, 2015.

[181] Bentley Motors, "Bentley Continental Supersports Convertible." [Online]. Available: https://www.bentleymotors.com/en/models/continental/continental-supersports-convertible.html. [Accessed: 21-Mar-2018].

[182] ChemTrend, "Chemlease 41-90 EZ Release Agent: Data sheet," 2004.

[183] Huntsman, "Araldite 2011 Data Sheet," Basel, Switzerland, 2007.

[184] Techni Measure, "Techni Measure FLA-3-11-1LJC Strain Gauge," 2017. [Online]. Available: https://store.technimeasure.co.uk/product/fla-3-11-1l/. [Accessed: 11-Nov-2017].

[185] NumPy developers - SciPy, "NumPy Scientific Python Package." 2018.

[186] Python Software Foundation, "Python 3.6.5." 2018.

[187] W. Tan, B. G. Falzon, L. N. S. Chiu, and M. Price, "Predicting low velocity impact damage and Compression-After-Impact (CAI) behaviour of composite laminates," *Composites Part A: Applied Science and Manufacturing*, vol. 71, pp. 212–226, 2015.

10. Appendices

10.1. Numerical model monolithic S2-glass composite impact plate fracture toughness sensitivity, 140J

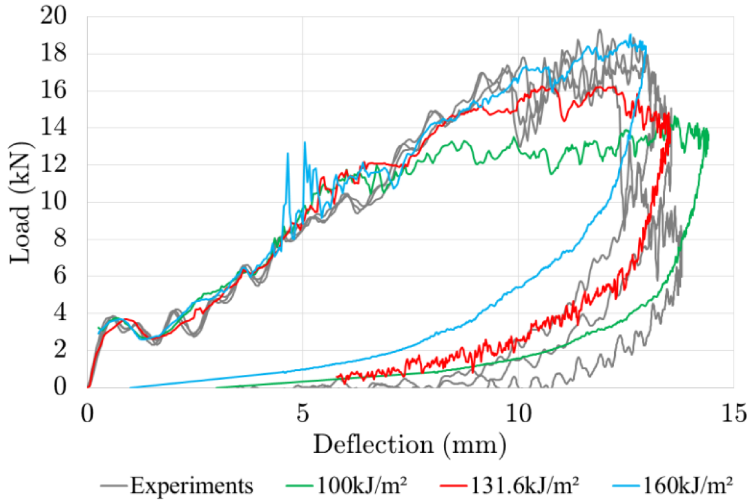


Figure 10.1: Monolithic S2-glass composite plate impact at 140J for various fracture toughness values (131.6kJ/m² used), load versus deflection

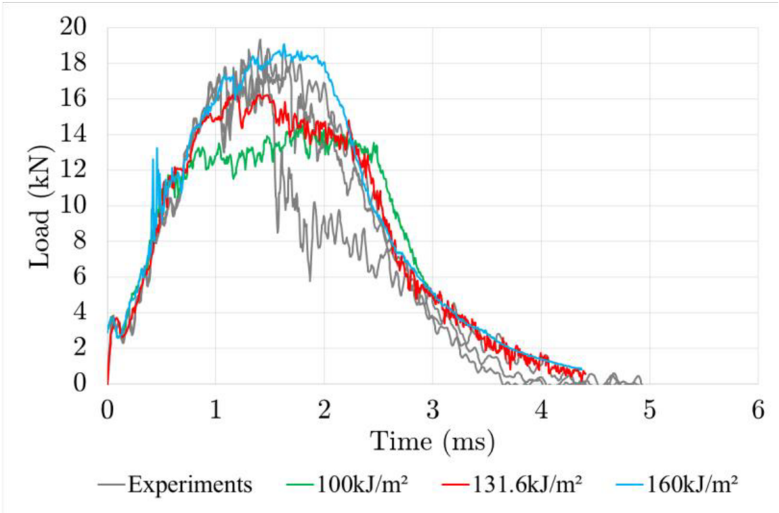


Figure 10.2: Monolithic S2-glass composite plate impact at 140J for various fracture toughness values (131.6kJ/m² used), load versus time

10.2. Numerical model monolithic S2-glass composite impact plate strain rate 'kappa' sensitivity, 140J

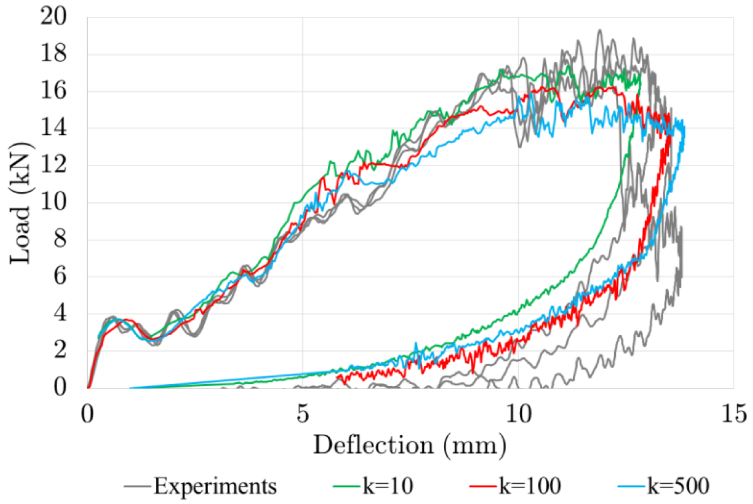


Figure 10.3: Monolithic S2-glass composite plate impact at 140J for various strain rate 'kappa' values (k=100 used), load versus deflection

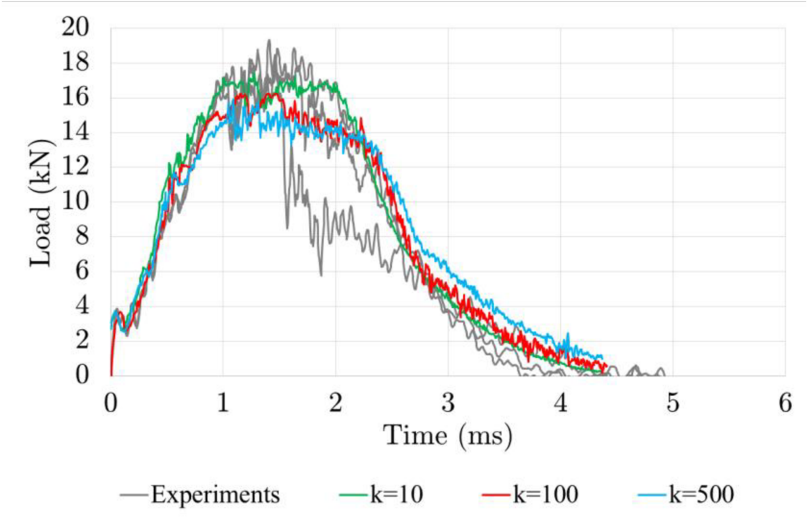


Figure 10.4: Monolithic S2-glass composite plate impact at 140J for various strain rate 'kappa' values (k=100 used), load versus time

10.3. Numerical model intralayer fibre hybrid T700 carbon/Vectran impact plate fracture toughness sensitivity, 70J

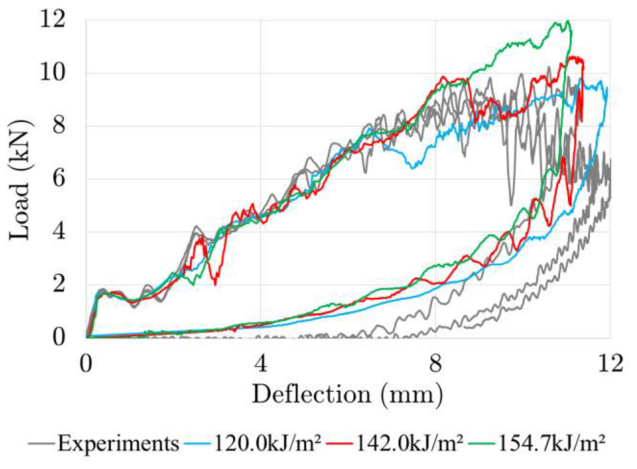


Figure 10.5: Intralayer fibre hybrid T700 carbon/Vectran plate impact at 70J for various fracture toughness values (G_{IC}=142.0 used), load versus deflection

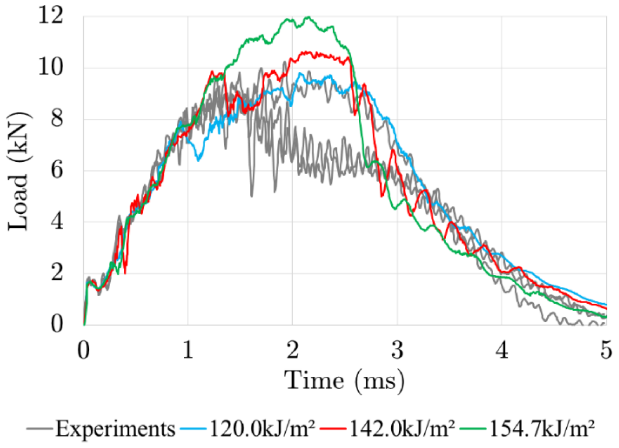


Figure 10.6: Intralayer fibre hybrid T700 carbon/Vectran plate impact at 70J for various fracture toughness values (G_{IC}=142.0 used), load versus time

10.4. Numerical model interlayer fibre hybrid T700 carbon/S2-glass structural bonnet impact damping factor sensitivity, 20J

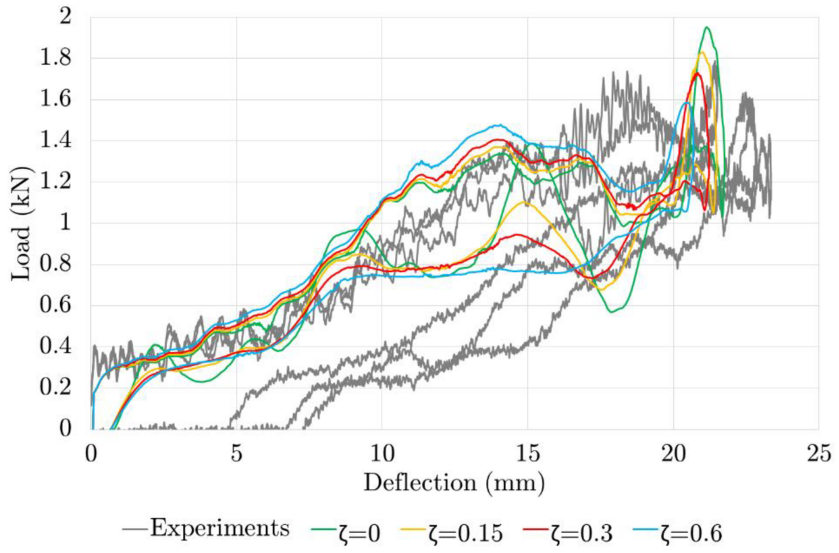


Figure 10.7: Interlayer fibre hybrid T700 carbon/S2-glass structural bonnet impact at 20J for various Rayleigh material damping (ζ=0.3 used), load versus deflection

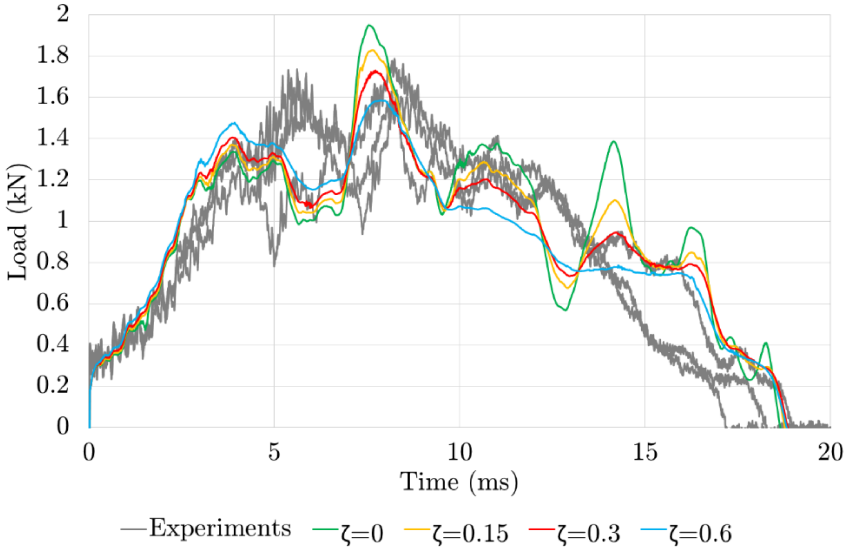


Figure 10.8: Interlayer fibre hybrid T700 carbon/S2-glass structural bonnet impact at 20J for various Rayleigh material damping (ζ=0.3 used), load versus time

```
********* Intralayer fibre hybrid T700 carbon / Vectran
*Material, name=MAT1
** Vectran/CF
*density
1574.9,
*user material, constants=40
** line 1: elastic constants
** E11, E22, nu12, G12_init, G12_ult
29.82e9, 29.82e9, 0.027, 2.475e9, 9.0e7
**
** line 2: permanent set constants (must be >=1)
** 11tens, 22tens, 12shear, 11compr, 22compr
10.5, 10.5, 10.5, 10.5, 10.5
**
** line 3: fracture energy per unit area (strain factor for shear)
** g1ct, g2ct, fact12, g1cc, g2cc
142e3, 142e3, 0., 142e3, 142e3
**
** line 4: strength
** xt, yt, sc, xc, yc, interaction flag
671.83e6, 671.83e6, 5.874e7, 165.78e6, 165.78e6, 1
**
** line 5: compression factors, shear param and failure flag
** xcf, ycf, lambda, kappa, Sc0, fail flag, max dmg, deletion strain
116.08e6, 116.08e6, 24., 0., 1.767e6, 2, 0.99, 2.0
*depvar, delete=9
21,
```

```
********* Monolithic S2-Glass
*Material, name=MAT1
** S2-Glass
*density
1904.6,
*user material, constants=40
** line 1: elastic constants
** E11, E22, nu12, G12_init, G12_ult
22.00e9, 22.00e9, 0.085, 5.68e9, 2.0e8
**
** line 2: permanent set constants (must be >=1)
** 11tens, 22tens, 12shear, 11compr, 22compr
14.0, 14.0, 14.0, 14.0, 14.0
**
** line 3: fracture energy per unit area (strain factor for shear)
** g1ct, g2ct, fact12, g1cc, g2cc
131.6e3, 131.6e3, 0., 131.6e3, 131.6e3
**
** line 4: strength
** xt, yt, sc, xc, yc, interaction flag
719.77e6, 719.77e6, 8.366e7, 371.81e6, 371.81e6, 1
**
** line 5: compression factors, shear param and failure flag
** xcf, ycf, lambda, kappa, Sc0, fail flag, max dmg, deletion strain
116.08e6, 116.08e6, 51., 100., 2.671e6, 2, 0.99, 2.0
*depvar, delete=9
21,
```

```
********* Monolithic T700 carbon spread tow
*Material, name=MAT2
** spread tow t700
*density
1532.9
*user material, constants=40
** line 1: elastic constants
** E11, E22, nu12, G12_init, G12_ult
65.11e9, 65.11e9, 0.035, 4.253e9, 2.1e8
**
** line 2: permanent set constants (must be >=1)
** 11tens, 22tens, 12shear, 11compr, 22compr
18.0, 18.0, 18.0, 18.0, 18.0
**
** line 3: fracture energy per unit area (strain factor for shear)
** g1ct, g2ct, fact12, g1cc, g2cc
33.6e3, 33.6e3, 0., 33.6e3, 33.6e3
**
** line 4: strength
** xt, yt, sc, xc, yc, interaction flag
1183.27e6, 1183.27e6, 114.41e6, 762.00e6, 762.00e6, 1
**
** line 5: compression factors, shear param and failure flag
** xcf, ycf, lambda, kappa, Sc0, fail flag, max dmg, deletion strain
116.08e6, 116.08e6, 33.5, 0., 7.388e5, 2, 0.99, 2.0
*depvar, delete=9
21,
```

```
********* Interlayer fibre hybrid T700 carbon / S2-glass homogenised
*Material, name=MAT1
** STS2
*density
1772.2,
*user material, constants=40
** line 1: elastic constants
** E11, E22, nu12, G12_init, G12_ult
40.56e9, 40.56e9, 0.049, 5.569e9, 2.2e8
**
** line 2: permanent set constants (must be >=1)
** 11tens, 22tens, 12shear, 11compr, 22compr
1.0, 1.0, 1.2, 1.0, 1.0
**
** line 3: fracture energy per unit area (strain factor for shear)
** g1ct, g2ct, fact12, g1cc, g2cc
65.3e3, 65.3e3, 0., 65.3e3, 65.3e3
**
** line 4: strength
** xt, yt, sc, xc, yc, interaction flag
661.78e6, 661.78e6, 8.00e7, 466.61e6, 466.61e6, 1
**
** line 5: compression factors, shear param and failure flag
** xcf, ycf, lambda, kappa, Sc0, fail flag, max dmg, deletion strain
116.08e6, 116.08e6, 50., 100., 4.00e6, 2, 0.99, 2.0
*depvar, delete=9
21,
```

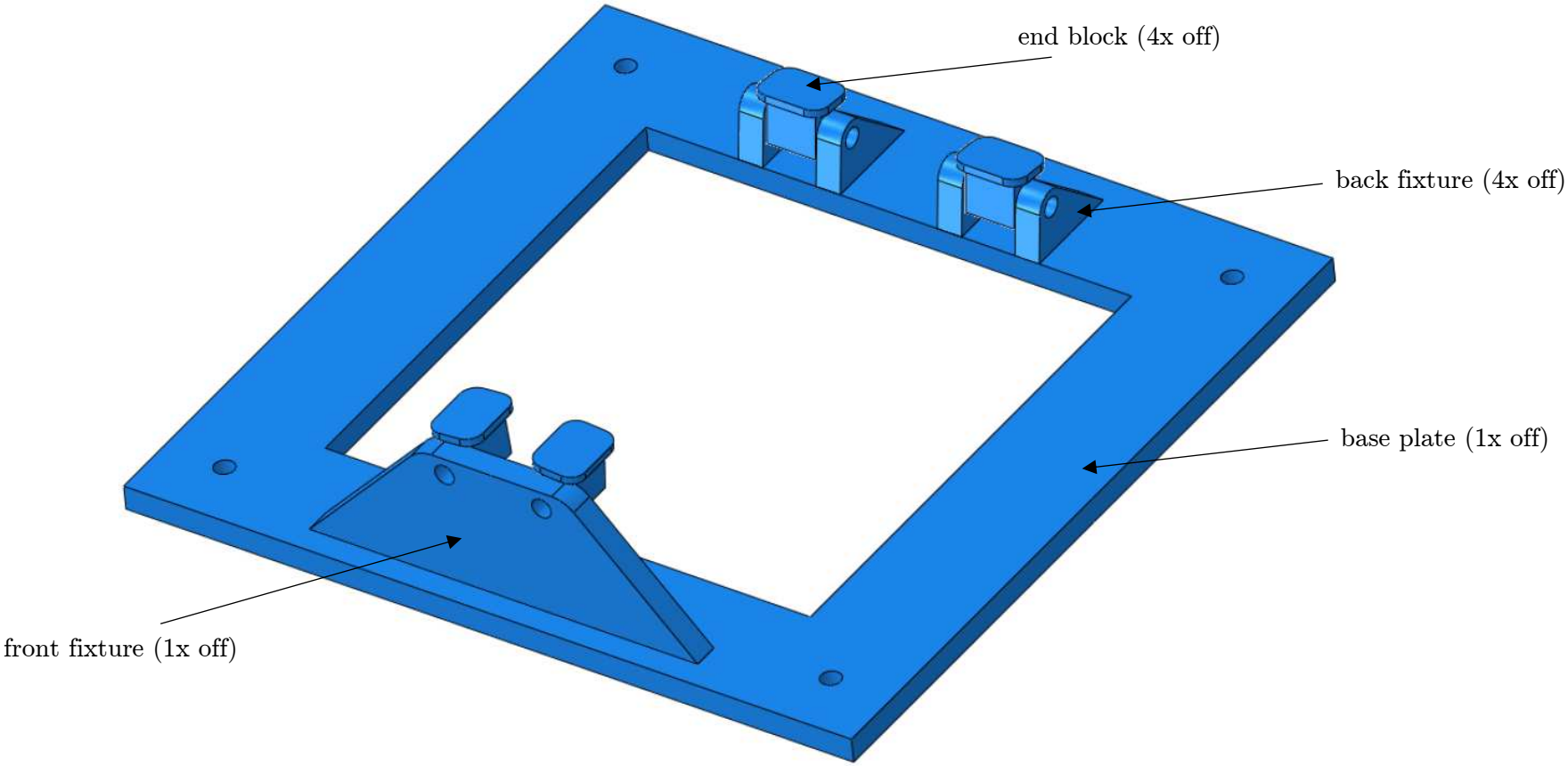
```
********* S2-S2 COHESIVE
*Material, name=coh
*Damage Initiation, criterion=QUADS
 8.007e+07, 8.007e+07, 8.007e+07
*Damage Evolution, type=ENERGY, mixed mode behavior=POWER LAW, power=1.5
1150.,2430.,2430.
*Density
 1202.8,
*Elastic, type=TRACTION
 2.68+09, 5.68e+09, 5.68e+09

********* ST-S2 COHESIVE
*Material, name=coh
*Damage Initiation, criterion=QUADS
 8.007e+07, 8.007e+07, 8.007e+07
*Damage Evolution, type=ENERGY, mixed mode behavior=POWER LAW, power=1.5
800.,1200.,1200.
*Density
 1202.8,
*Elastic, type=TRACTION
 2.68e+09, 5.569e+09, 5.569e+09

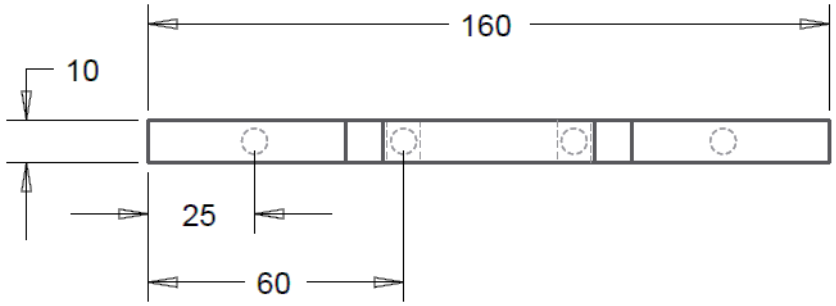
********* VCF COHESIVE
*Material, name=coh
*Damage Initiation, criterion=QUADS
 8.007e+07, 8.007e+07, 8.007e+07
*Damage Evolution, type=ENERGY, mixed mode behavior=POWER LAW, power=1.5
1750.,2500.,2500.
*Density
 1202.8,
*Elastic, type=TRACTION
 2.68e+09, 2.475e+09, 2.475e+09
```

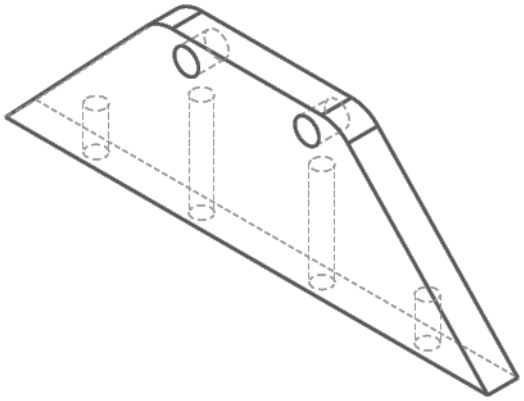
```
********* ST T700 COHESIVE
** Damage evolution values taken from:
**
** Mode I, Mode II, and Mixed Mode Interlaminar Fracture of Woven Fabric
** Carbon/Epoxy (1997)
** Alif, Nidal
** Carlsson, Leif
** Gillespie, John
*Material, name=coh
*Damage Initiation, criterion=QUADS
 8.007e+07, 8.007e+07, 8.007e+07
*Damage Evolution, type=ENERGY, mixed mode behavior=POWER LAW, power=1.5
700.,1030.,1030.
*Density
 1202.8,
*Elastic, type=TRACTION
 2.68e+09, 4.253e9, 4.253e9
```

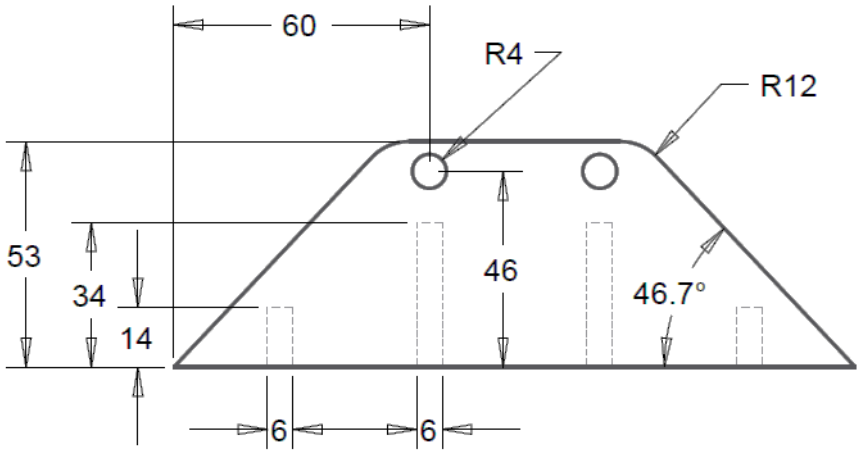
10.7. Bonnet rig test fixture drawings

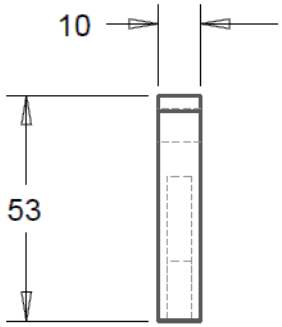


Front fixture (1x off). All dimensions in mm

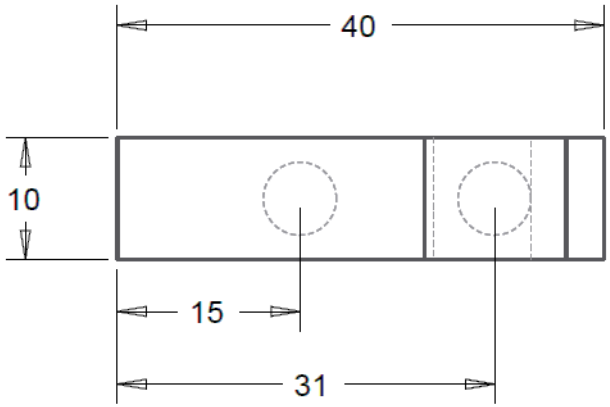


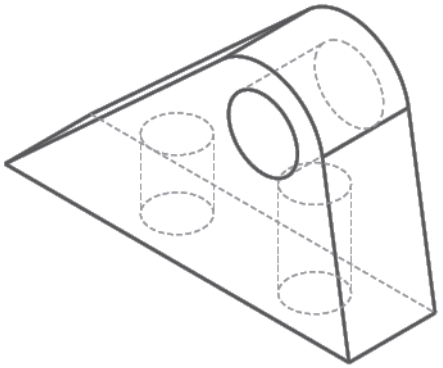


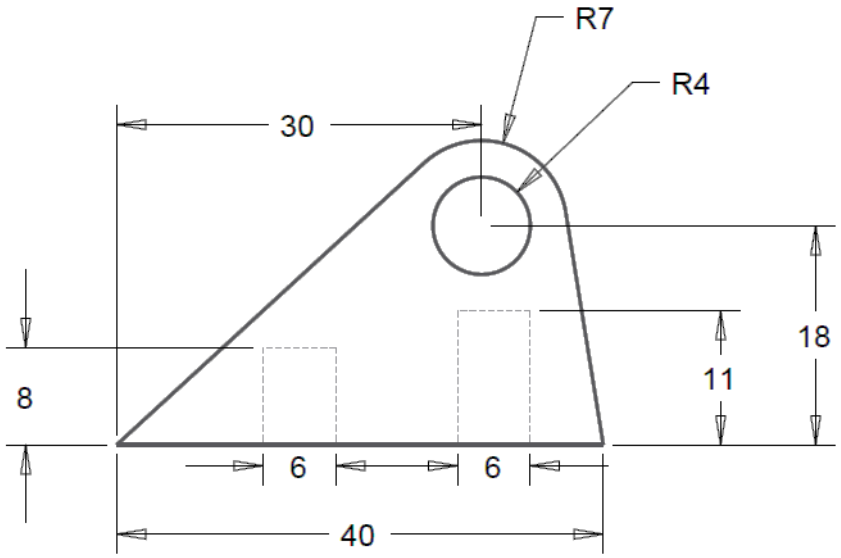


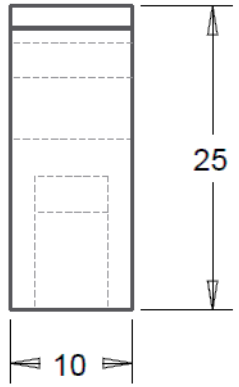


Back fixture (4x off). All dimensions in mm

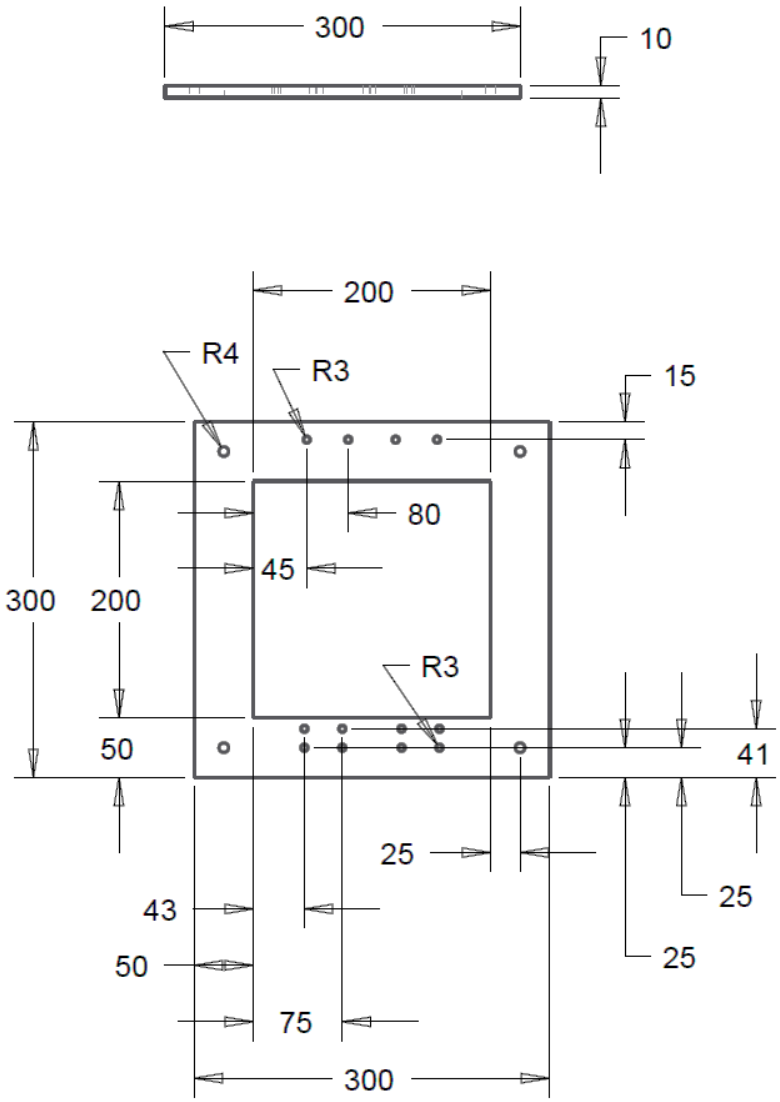


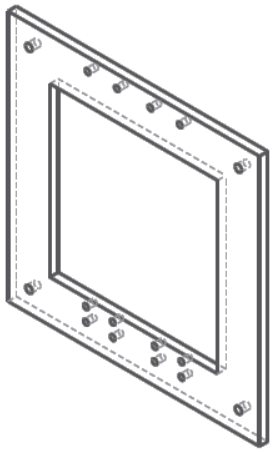


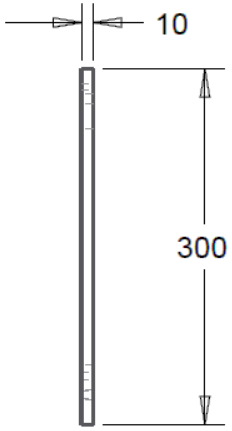




Base plate (1x off). All dimensions in mm







End block (4x off). All dimensions in mm:

